REPORT NUMBER 137
NOVEMBER 1963

WIND TUNNEL TEST REPORT
IFT FAN-POWERED SCALE MODEL

DISCLAIMER NOTICE

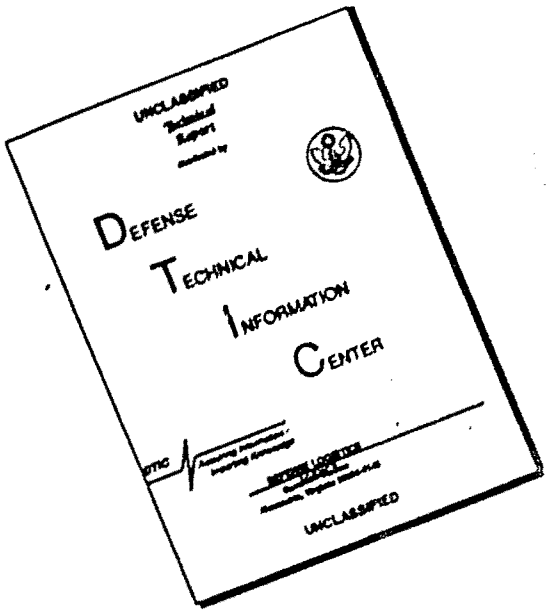

THIS DOCUMENT IS BEST QUALITY AVAILABLE. THE COPY FURNISHED TO DTIC CONTAINED A SIGNIFICANT NUMBER OF PAGES WHICH DO NOT REPRODUCE LEGIBLY.

DDC AVAILABILITY NOTICES

1. Distribution of this document is unlimited.

2. This document is subject to special export controls and each transmittal to foreign governments or foreign nationals may be made only with prior approval of US Army Aviation Materiel Laboratories, Fort Eustis, Virginia 23604.

3. In addition to security requirements which must be met, this document is subject to special export controls and each transmittal to foreign governments or foreign nationals may be made only with prior approval of USAAVLABS, Fort Eustis, Virginia 23604.

4. Each transmittal of this document outside the agencies of the US Government must have prior approval of US Army Aviation Materiel Laboratories, Fort Eustis, Virginia 23604.

5. In addition to security requirements which apply to this document and must be met, each transmittal outside the agencies of the US Government must have prior approval of US Army Aviation Materiel Laboratories, Fort Eustis, Virginia 23604.

6. Each transmittal of this document outside the Department of Defense must have prior approval of US Army Aviation Materiel Laboratories, Fort Eustis, Virginia 23604.

7. In addition to security requirements which apply to this document and must be met, each transmittal outside the Department of Defense must have prior approval of US Army Aviation Materiel Laboratories, Fort Eustis, Virginia 23604.

8. This document may be further distributed by any holder only with specific prior approval of US Army Aviation Materiel Laboratories, Fort Eustis, Virginia 23604.

9. In addition to security requirements which apply to this document and must be met, it may be further distributed by the holder only with specific prior approval of US Army Aviation Materiel Laboratories, Fort Eustis, Virginia 23604.

DISCLAIMER

10. The findings in this report are not to be construed as an official Department of the Army position unless so designated by other authorized documents.

11. When Government drawings, specifications, or other data are used for any purpose other than in connection with a definitely related Government procurement operation, the United States Government thereby incurs no responsibility nor any obligation whatsoever; and the fact that the Government may have formulated, furnished, or in any way supplied the said drawings, specifications, or other data is not to be regarded by implication or otherwise as

in any manner licensing the holder or any other person or corporation, or conveying any rights or permission, to manufacture, use, or sell any patented invention that may in any way be related thereto.

12. Trade names cited in this report do not constitute an official endorsement or approval of the use of such commercial hardware or software.

DISPOSITION INSTRUCTIONS

13. Destroy this report when no longer needed. Do not return it to originator.

14. When this report is no longer needed, Department of the Army organizations will destroy it in accordance with the procedures given in AR 380-5.

Report No. 132

Wind Tunnel Test Report
Lift Fan Powered Scale Model

XV-5A Lift Fan

Flight Research Aircraft Program

November 1963

ADVANCED ENGINE AND TECHNOLOGY DEPARTMENT
GENERAL ELECTRIC COMPANY
CINCINNATI, OHIO 45215

CONTENTS

(Continued)

TABLES

LIST OF FIGURES

(Continued)

(Continued)

(Continued)

(Continued)

(Continued)

1.0 SUMMARY

This report presents the results of wind tunnel tests of a 1/6 scale powered model of the U. S. Army XV-5A Lift Fan Research Aircraft. The tests were conducted in the 16 x 20 foot test section of the General Dynamics/Convair Low Speed Wind Tunnel facility.

Data were obtained to define the static characteristics in and out of ground effect; aerodynamic characteristics in forward flight for the transition, conversion, and low speed conventional flight modes; and flight characteristics at low translational speeds near hovering in vertical, lateral, and rearward directions. In addition, wing surface static pressures and wing fan inlet closure door hinge moments were measured.

The data indicate an adverse ground effect on static lift at heights less than 2 wing fan diameters with a reduction of approximately 6% at 1.0 diameter. A corresponding reduction in fan power at constant fan RPM compensates for the lift reduction if operation at constant power is considered.

The effects of wing fan and nose fan operation are destabilizing with respect to angle of attack. Nose fan operation is slightly destabilizing in yaw, but the data indicate positive lateral-directional stability for the entire range of thrust coefficient in fan-powered flight.

A favorable ground effect on lift is obtained with increasing forward speed as would occur during short take-off operation, with an increase of approximately 22% above the out-of-ground effect lift at a thrust coefficient of .885. The data obtained in ground effect were uncorrected for wall effects but this correction is believed to be small compared with the lift increase shown.

Opening the exit louvers with power off and with the wing fan inlets closed results in a decrease in maximum lift coefficient, ΔC_L, of approximately .12. The associated longitudinal trim changes due to opening the exit louvers and the nose fan duct are small.

A decrease in lift coefficient of approximately 5% from the static value at low forward speeds is believed to be largely caused by negative static pressures on the wing lower surface. This lift loss was regained by utilizing large span trailing edge flaps, which extend outboard of the fan, or by drooping the ailerons to effectively obtain full span flaps.

The control effectiveness of the conventional flight control surfaces in fan-powered flight is essentially unaffected by fan operating conditions and exit louver position.

Tests conducted to represent low translational speeds near hovering indicate a rolling moment variation with lateral translation indicative of a high level of speed stability similar to that obtained in symmetrical flight.

2.0 INTRODUCTION

This report presents a summary of the results obtained from wind tunnel tests of a 1/6-scale powered model of the U.S. Army XV-5A Lift-Fan Flight Research Aircraft. The 1/6-scale powered model was used to determine fan-powered aerodynamic characteristics in the hovering transition, and conversion flight modes.

The 1/6-scale model incorporated electrically powered, gear driven, counter-rotating lift fans in the wing and a pitch control fan in the fuselage nose section. The nose fan to wing fan static thrust ratio was approximately .24 compared with the full scale value of the order of .15. Therefore, the nose fan was operated to determine interference and stability effects rather than to obtain full-scale nose fan performance and control effectiveness.

The wing fans were equipped with butterfly type closure doors and exit louvers. The nose fan installation included fixed inlet louvers and adjustable thrust modulator doors. The model was fitted with movable trailing edge flaps, ailerons, horizontal stabilizer and rudder.

The model was tested in the General Dynamics/Convair 16 x 20 foot low-speed wind tunnel facility, which is especially suited for testing models of this type. The tests were conducted in two phases from June 29 through July 12, 1962, and from August 27 through October 16, 1962. This report presents the principal findings of the test program arranged under headings of particular interest. References 1 and 2, which were prepared by the testing facility, contain in either graph or tabular form all of the test data obtained during the two test periods.

The model was instrumented to measure 6-component model force and moment data, 5-component data on the right-hand wing fan unit, static pressures on the wing and fuselage surfaces, static and total pressures at the wing and nose fan exits, and hinge moments of the right-

hand wing fan inlet doors. Fan balance data are not included in this report, but plots of selected runs are included in References 1 and 2.

The 1/6-scale test data have been used as a basis for stability and control, performance, and loads analyses of the XV-5A in fan-powered flight, together with unpublished full-scale data obtained at the NASA Ames Research Center 40 x 80 wind tunnel. The methods of utilization of this data to derive XV-5A characteristics will be covered in subsequent aircraft reports.

Photos of the model installed in the wind tunnel are shown in Figures 2.1 and 2.2. A 3-view sketch of the model is shown in Figure 2.3 and the model geometric characteristics are given in Table 6.1.

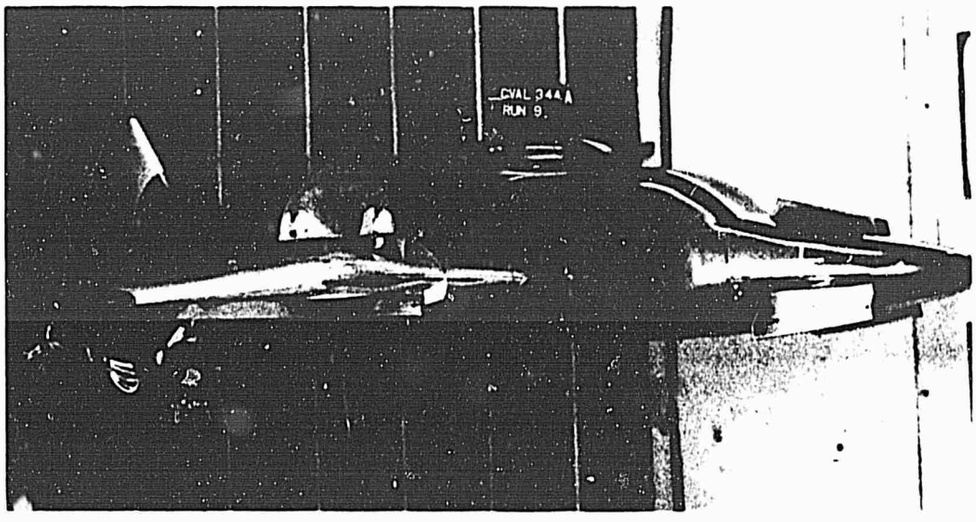

Figure 2.1 XV-5A 1/6 Scale Model in Fan-Powered Flight Configuration

Figure 2.2 XV-5A 1/6 Scale Model in Conventional Flight Configuration

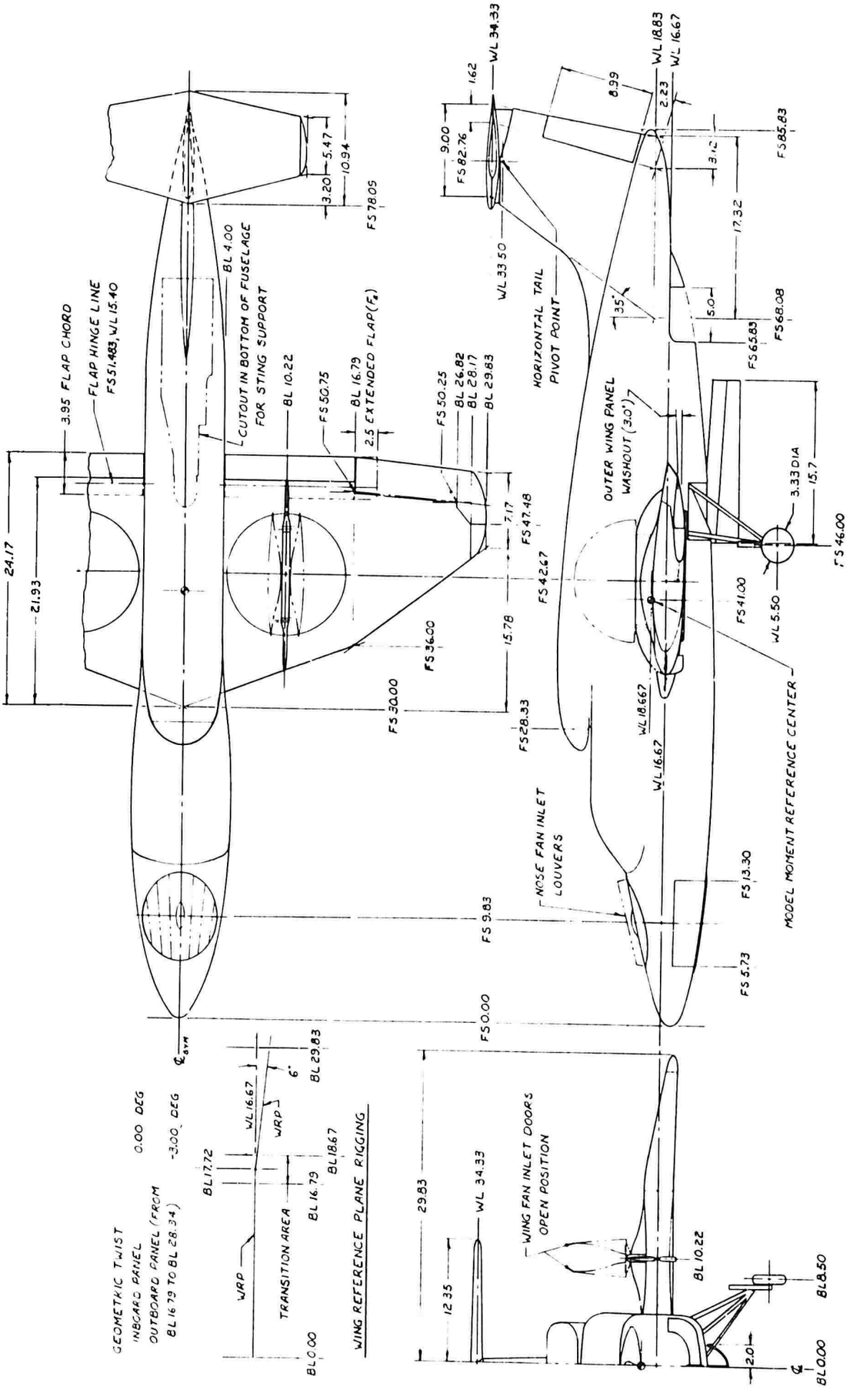

Figure 2.3 3-View Drawing of 1/6 Scale Wind Tunnel Model

3.0 MODEL DESCRIPTION AND TEST PROCEDURES

3.1 MODEL AND INSTALLATION

The basic model strueture consisted of a steel beam which supported the wing and nose fan drive assemblies, wing, and tail surfaces. The fuselage shell was of Fiberglas construetion and housed the wing fan and nose fan drive motors, exit louver aetuators and pressure measuring system. Sections of the fuselage were removable for inspection and servieing of the model. The wing and tail surfaces were of aluminum alloy construction; the wing incorporated ailerons outboard and single slotted trailing edge flaps inboard.

In order to aecommodate the lift fan units within the wing contour during model construction, it was neeessary to modify the wing airfoil seetion. This was aceomplished by inereasing the airfoil ordinates normal to the wing ehord plane by 20% and resulted in a wing thickness (at the fan axis) to fan diameter ratio of .28 compared with the full-scale value of .234. Due to the wing expansion it was necessary to adjust the model flap hinge line to maintain the same gap to ehord ratio (at $\delta_f = 45°$) of the aircraft. Some minor loeal fairing was also done at the wing-fuselage intersection to house the fans and gear boxes.

Eaeh of the two wing lift fan units consisted of a 36-blade 10.4 ineh diameter rotor, a 55-blade exit stator, a bellmouth inlet, and gear box driven by an external shaft from the motor gear box within the fuselage. The wing fans were driven with 32 horsepower electrie motors. The overall motor to fan gear ratio was 1.46:1.0. An exit louver assembly with 13 louvers was attached to the lower frame of the fan units, and butterfly-type elosure doors hinged from a ehordwise strut were attached to the wing upper surface at the fan centerlines.

The nose fan unit eonsisted of a 10-blade 6 inch diameter rotor, a 9-blade stator, and a 0.74:1.0 ratio gear box driven by a 15 horsepower nose fan drive motor. The nose fan inlet eonsisted of 7 fixed-position louvers and a hub fairing mounted on the bellmouth inlet whieh were replaceable by a flat faired cover for the elosed eonfiguration.

Variable position nose fan thrust modulator doors were hinged below the fan unit and, in the closed position, the doors contoured and sealed the lower fuselage nose opening.

The wing fan and nose fan drive motors were water cooled by an external water circulating system. The wing fan motor gear boxes and the fan hub gear boxes were cooled by a pressurized feed and scavenging oil system. All water, oil, and electrical lines entered the model through the lower aft portion of fuselage along the model support sting. The lines were flexibly mounted across the model main and wing fan balances. A photograph showing the internal arrangement of the model instrumentation is shown in Figure 3.1.

Variable control positions were provided for the nose fan thrust reverser doors, ailerons, trailing edge flaps, horizontal stabilizer, and rudder. Wing fan exit louver stagger angle was set manually by means of various size links and wing fan exit louver vector angle was remotely controlled. The wing fan closure door angular position could be manually set in 5° increments from fully open to fully closed. It should be noted that the horizontal tail was constructed with a sweep angle of the quarter chord line of 8.44° compared with a sweep of 13.7° for the aircraft.

3.2 INSTRUMENTATION

The instrumentation arrangement is shown in Figure 3.1. The model forces and moments were recorded by an internal six-component strain gage balance and digital readout system. The balance center of moments was transferred to a moment reference center corresponding to a full-scale c.g. position at Station 246, Waterline 112.

The right hand wing fan unit was isolated from the surrounding structure and mounted on a 5-component strain gage balance to measure the normal force, axial force, pitching moment, rolling and yawing moments experienced by the fan unit. The moment center of the fan balance was referenced to the fan axis in the plane of the rotor.

The odd-numbered wing fan exit louvers were driven by screw-jack actuators with position potentiometers for remote actuation of the exit louvers. The even-numbered louvers were slaved to the driven louvers by means of various sized links calibrated for variable stagger. A predetermined calibration of louver position for each stagger setting was used for setting the desired vector angle.

Electrical input power to the wing fan drive motors was recorded for each data point and motor rotational speed was recorded for each fan.

Pressure instrumentation consisted of surface static pressure taps located on the fuselage surface and left hand wing surface, and total and static pressure taps at the nose fan and wing fan exits. Pressures were recorded with five 2.5 psi Scanivalve units located within the fuselage. The locations of the pressure taps are shown in Figures 6.1 through 6.3. In addition to the above, temporary pressure instrumentation was also available for measurement of left hand wing fan inlet static pressures and fan strut surface pressures using manometry. A 16 probe, 4 element rake was used for inlet pressure measurements. Four orifices were added later in the program for measurement of wing fan longitudinal strut pressures.

The right hand wing fan closure doors were equipped with strain gage balances for recording the hinge moments of each door panel. These data were taken during the second test phase.

3.3 TEST PROCEDURES

The model was tested in the 16 x 20 foot test section located in the diffuser of the Convair low speed wind tunnel. The dynamic pressure in the test section is a calibrated function of the main 8 x 12 foot test section q, with special screens installed in the diffuser required for dynamic pressure values at the model of 9.3 and 1.5 lbs/ft^2. A few runs were made at a q of .50 lbs/ft^2, which was not calibrated, but was believed to be reasonably accurate. The corresponding test Reynolds Numbers based on the wing mac for standard atmospheric conditions were .885, .356 and .206 million. Figure 3.2 shows the range of test thrust coefficients available for the RPM range of the wing fan motors for each value of test dynamic pressure.

Calibration checks of the main and wing fan balances were made prior to and after assembly of the model before installation of the model in the wind tunnel. These measurements indicated that interference tares were in all cases less than 2 per cent of limit calibration values. A similar procedure was used for calibration of the wing fan closure balances. Subsequent calibration checks were made following installation of the model in the test section.

Angle of attack runs were conducted by bringing the wind tunnel and model fan speeds up to the desired level and then rotating the model

in pitch. Physical limits of the support sting restricted the model angle of attack range from -4° to 24°. Yaw data were obtained by yawing the entire model support system in its curved track to predetermined locked positions and then varying model angle of attack.

For runs conducted in ground effect, the wind tunnel facility main ground board was locked in the raised position and a portable ground board mounted on the main ground board. The model support sting could be remotely raised and lowered to locate the model at desired heights above the ground board.

For tail-off runs, the vertical and horizontal tails were usually removed as a unit.

3.4 DATA REDUCTION PROCEDURES

A data reduction technique has been utilized which expresses the power-on data in the form of slipstream coefficients -- a variation of the method developed by NASA for wind tunnel tests of V/STOL aircraft models. The method used to normalize the data for the 1/6-scale XV-5A model tests makes use of the total model static lift measured with zero exit louver vector and stagger angle. This method has the advantage of requiring only one thrust calibration curve and yields a lift coefficient of unity for the static condition, which is equal to the thrust coefficient. Moreover, data in this form can be more conveniently compared with full-scale lift fan data wherein the actual fan thrust is not separated from the over-all system lift.

All of the wind-on main balance force data (except static runs, runs made with the ground board, and runs made at $\pm 90^\circ \alpha$, $-90^\circ \psi$, and $180^\circ \psi$) have been corrected for wind tunnel wall effects by a method developed by Convair from NASA procedures. Deflection corrections to angle of attack and yaw angle were determined prior to the tests by statically loading the model. No corrections were applied for tunnel flow inclination or for model support interference.

The main balance longitudinal force and moment slipstream coefficients are based on wing fan area and diameter, whereas the lateral-directional coefficients are based on wing area and span. Wing geometry is a more appropriate base for coefficients when studying the effects of aileron deflection and yaw angle but fan geometry is perhaps a better choice for low speed tests near the hovering condition, where the fan forces are predominant.

All of the main balance data, except for the hovering translational tests, are referenced to a stability axes system with origin at Model Station 41.000, W. L. 18.667. The hovering translational data are referenced to a system of body axes with the same origin.

The slipstream coefficients were reduced to sea level standard conditions by correcting the slipstream dynamic pressure to the tunnel operating conditions of temperature and static pressure for each run.

Power-off coefficients were computed on the basis of both fan and wing geometries, but usually presented in the latter form.

Pressure coefficients were nondimensionalized by the slipstream dynamic pressure for the purpose of data reduction to avoid infinities at zero wind tunnel speed.

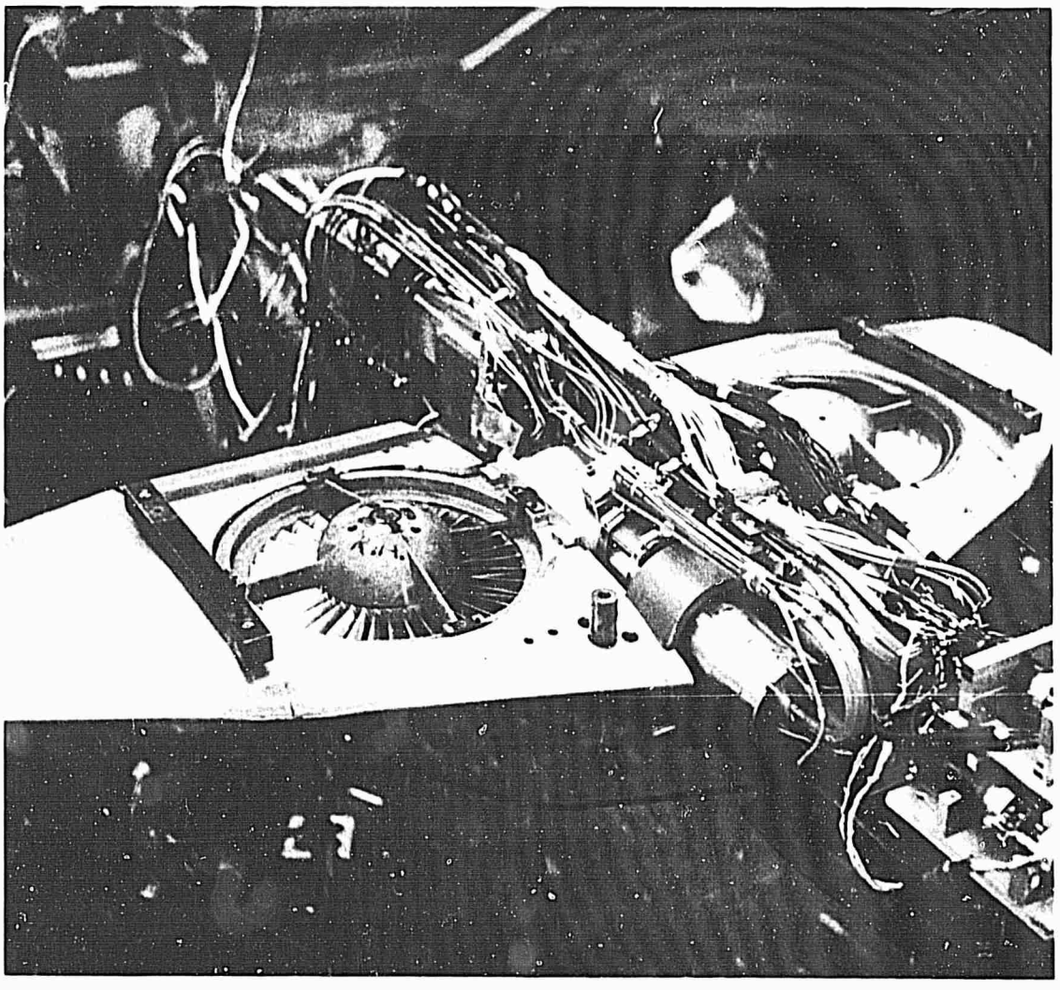

Figure 3.1 XV-5A 1/6 Scale Model Instrumentation Arrangement

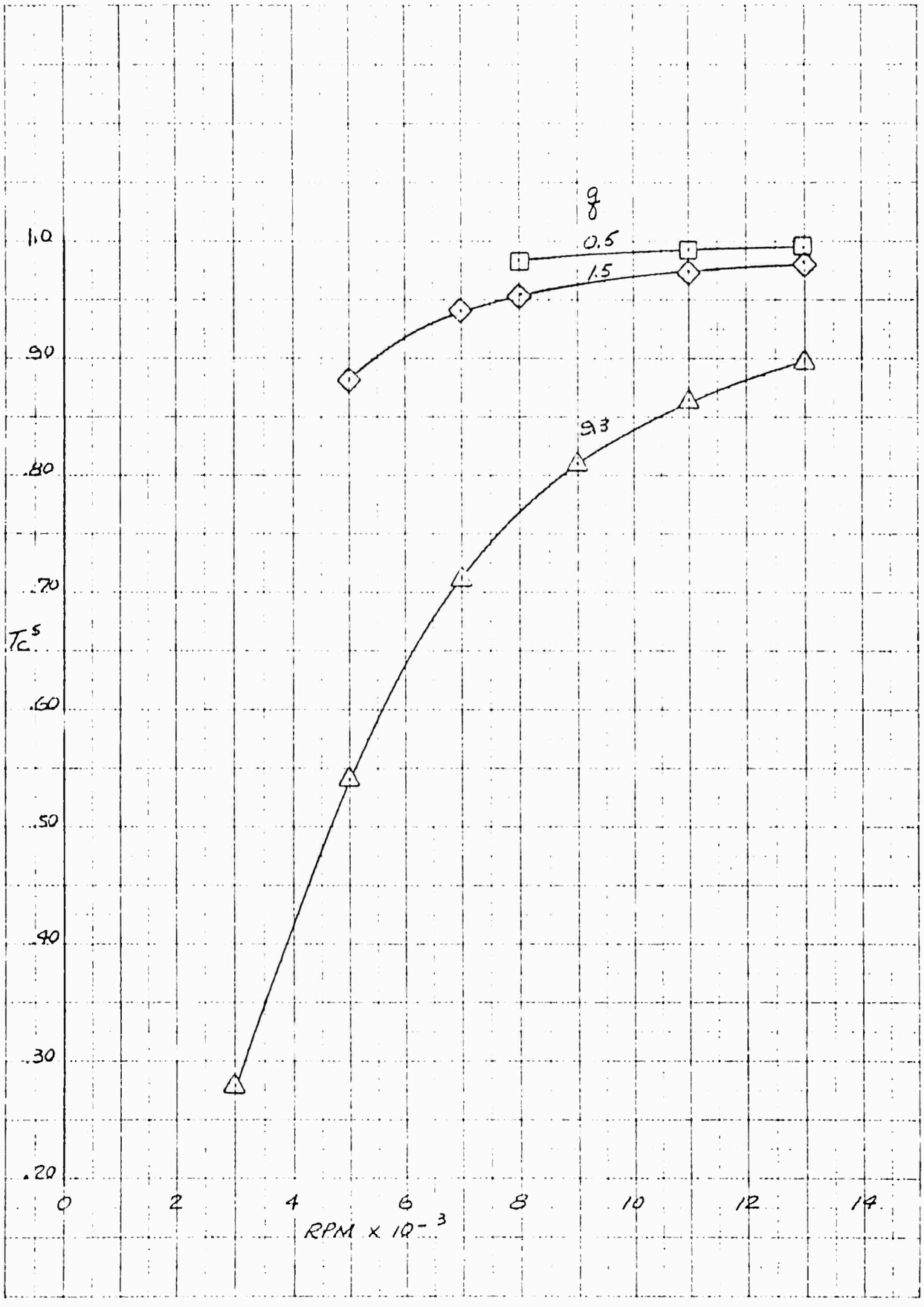

Figure 3.2 Available Range of Thrust Coefficient for Various Values of Tunnel Dynamic Pressure

4.0 TEST RESULTS

4.1 MODEL FORCE AND MOMENT CHARACTERISTICS

Results of the model main balance force and moment measurements are discussed in the following sections. The nose fan is off unless otherwise indicated.

4.1.1 Static Characteristics

4.1.1.1 Wing Fan Thrust Calibration

The variation of static lift, drag, and pitching moment with motor RPM is shown in Figure 4.1. The lift curve served as the wing fan static thrust calibration for use in reducing the force and moment data to the nondimensional slipstream coefficients, as illustrated by Figure 4.2. The nonlinear variation of the power coefficient with RPM is discussed in Section 4.1.8.

4.1.1.2 Ground Effect

Results of testing the model at various heights above the ground board are shown in Figure 4.3 with the nose fan on and off. Reductions in model lift and wing fan power at constant fan speed occur at about two wing fan diameters above the ground board with a lift reduction of approximately 6% at 1.0 diameter with the wing fans only operating. This lift loss is reduced slightly with the nose fan also operating.

4.1.1.3 Nose Fan Thrust and Door Calibration

Static measurements obtained with the nose fan only operating are shown in Figure 4.4 as functions of nose fan RPM and thrust modulator door position. Data are shown for door configurations with and without trip strips located on the door outer surface at the door hinge line. The relatively large yawing moments developed at the higher fan speeds are significant and are evident in data taken with wind on in the transition speed range.

4.1.1.4 Effect of Wing Fan Exit Louver Deflection

Exit louver vector and stagger effectiveness are presented in and out of ground effect in Figures 4.5 and 4.6, respectively, for a constant motor RPM.

4.1.1.5 Wing Fan Inlet Configuration

The effects of separately installing the wing fan closure doors and the fixed inlet vanes representative of the full-scale fan inlet configuration, are shown in Figure 4.7. No lift change resulted from the door installation, but the vanes caused a lift reduction of approximately 7%. The sudden variation in the coefficients at the high RPM settings was apparently due to some flow separation, but was not prevalent for all runs at these motor speeds.

4.1.1.6 Static Effect of Landing Gear

The effect of installing the main landing gear in the forward (conventional take-off and landing) position on the static characteristics is shown in Figure 4.8. No significant change in the coefficients occurs due to the landing gear from these tests.

4.1.2 Longitudinal Characteristics in the Transition Speed Range

4.1.2.1 Effect of Angle of Attack

Lift, drag, and pitching moment coefficients are shown for constant-thrust coefficient angle of attack polars in Figure 4.9 for $\beta_V = 0°$ and in Figures 4.10 and 4.11 for $\beta_V = 50°$. These data represent the basic model tail-off longitudinal characteristics for the range of $T_c{}^S$ from near hovering through transition and conversion to the power-off condition with wing fan inlet doors open. These data show the increasing lift curve slope, $\frac{dC_L{}^S}{d\alpha}$, increasing drag coefficient, and increasing nose-up pitching moment coefficient, all with decreasing values of $T_c{}^S$. For $\beta_V = 50°$, the pitching moment reaches a maximum at a $T_c{}^S$ of .896 and becomes negative with further decreases in $T_c{}^S$.

4 1.2.2 Horizontal Stabilizer Effectiveness

Static longitudinal stability characteristics and horizontal stabilizer effectiveness are shown for various thrust coefficients and stabilizer incidence settings for $\beta_V = 0^\circ$ in Figures 4.12 through 4.15 and for $\beta_V = 50^\circ$ in Figures 4.16 through 4.19. The horizontal stabilizer effectiveness parameter, dCm^S/di_t is a linear function of T_c^S and is, therefore, independent of the fan operating conditions. The data indicate a slightly negative static stability with angle of attack in the transition speed range of thrust coefficient for the model moment center which corresponds to the full-scale airplane aft c.g. location. Exit louver vector angle has no significant effect on the static stability level.

4.1.2.3 Effect of Nose Fan Operation

Longitudinal characteristics with the nose fan on are shown in Figures 4.20 through 4.23 for nose fan thrust modulator settings of 48° and 68°, which provide negative and positive nose fan thrust increments, respectively. Nose fan operation is destabilizing with respect to angle of attack for the values of thrust coefficient tested. Figures 4.22 and 4.23 provide a comparison of the effect of the nose fan with the tail on and off at a thrust coefficient of .956. The 68° door setting results in a somewhat larger destabilizing effect than the 48° setting.

4.1.2.4 Wing Fan Exit Louver Vector and Stagger Effectiveness

The effects of exit louver vector angle and angle of attack for constant values of exit louver stagger angle are shown in Figures 4.24 through 4.28 for a thrust coefficient of .956. Figure 4.29 shows the effects of vector angle and angle of attack for zero stagger and a thrust coefficient of .975. Figure 4.30 shows the variation in longitudinal coefficients with vector and stagger angle for a thrust coefficient of .896 at zero angle of attack.

4.1.2.5 Effect of Flap Deflection

The incremental lift and moment coefficients for a flap deflection of 45° and thrust coefficient of .885 are shown in Figure 4.31. Improvement in flap effectiveness is noted with increasing vector angle.

4.1.3 Lateral Directional Characteristics in The Transition Speed Range

4.1.3.1 Effect of Yaw Angle

Lateral-directional coefficients as functions of angle of attack and yaw angle, with the nose fan inoperative, are shown in Figures 4.32 through 4.37. Figure 4.32 shows the influence of exit louver vector angle on the lateral-directional characteristics in yaw for a thrust coefficient of .897. The data of Figures 4.33, 4.36, and 4.37 were obtained with the ailerons drooped 15°. Comparison of Figures 4.32 and 4.33 shows little effect of aileron droop on the lateral-directional data. Positive lateral-directional stability for the model is indicated for all values of thrust coefficient.

Figure 4.38 illustrates the coupling effect of pitching moment due to yaw angle. The magnitude of this pitching moment coefficient change was found to be independent of fan thrust level and, therefore, equivalent to the power-off moment coefficient.

4.1.3.2 Effect of Nose Fan Operation

Figures 4.39 through 4.41 show the effect of the nose fan with a thrust modulator door angle of 48° for several values of thrust coefficient. The increment in yawing moment coefficient at zero yaw angle is apparently due to the asymmetric yawing moment measured during the nose fan static calibration. (See Figure 4.4.) The major effect of nose fan operation on lateral-directional characteristics appears to be a slight reduction in directional stability, $\frac{dC_n^s}{d\psi}$.

4.1.3.3 Aileron and Rudder Control Effectiveness

The effect of aileron deflection on rolling moment, yawing moment, and sideforce coefficients is presented in Figures 4.42 through 4.47. Data are shown for both conventional aileron deflections with respect to the wing trailing edge, and for differential aileron deflections from the 15° droop position. Figures 4.46 and 4.47 are for the power-off conventional flight configurations with 0° and 45° flap deflections. The relatively small sideforce variations due to aileron deflection are not discernible due to excessive sideforce data scatter and these data are presented unfaired.

The effect of rudder deflection on the lateral-directional characteristics is shown in Figures 4.48 and 4.49 for two values of thrust coefficient. From comparisons made with the 1/8-scale model data of Reference 3, both aileron and rudder effectiveness appear to be unaffected by fan operation.

4.1.4 Ground Effect in Fan-Powered Flight

A limited amount of testing was conducted with fans operating with the model located just above the ground board to simulate powered flight in ground effect. These tests were run to determine if changes occur in the aerodynamic characteristics for STOL operation in ground proximity which are predictable by powered model tests. The results of these tests are presented in the following sections.

4.1.4.1 Effect of Angle of Attack

Basic tail-off longitudinal characteristics at a ground height of 1.36 wing fan diameters are shown in Figure 4.50 for several values of thrust coefficient. Effect of the ground board on lift at a T_e^S of .975 shows no change but at a T_c^S of .881 the lift is approximately 22% higher than that obtained out of ground effect. No wall corrections have been applied to these data due to the use of the partial ground board, but the wall effects are believed to be small relative to the change in lift shown.

4.1.4.2 Horizontal Stabilizer Effectiveness

Static longitudinal stability and horizontal tail effectiveness are shown in Figures 4.51 and 4.52 in ground effect. Increases in longitudinal stability level above those obtained out of ground effect are apparently due to reduced downwash at the horizontal tail.

4.1.4.3 Effect of Nose Fan Operation

Figures 4.53 and 4.54 show the longitudinal characteristics in ground effect with the nose fan on at nose fan thrust modulator door settings of 68° and 48°. The variation of pitching moment coefficient due to door position appears unchanged from the out of ground effect data, whereas the destabilizing effect of the nose fan is greater, particularly at the lower value of thrust coefficient.

4.1.4.4 Wing Fan Exit Louver Vector Effectiveness

Figure 4.55 shows the effect of vector angle for two values of thrust coefficient in ground effect. The incremental changes in the lift and drag coefficients due to vectoring appear to be slightly reduced from the increments measured out of ground effect.

4.1.4.5 Effect of Tunnel q in Ground Effect

Figure 4.56 shows longitudinal data obtained at different values of tunnel q and wing fan motor speed selected to give approximately the same thrust coefficient. The flat drag curve and sudden increase in drag between angles of attack of 4 and 8 degrees for the 5000 RPM, 1.5 q condition was consistent throughout the tests and appeared to be peculiar to this motor speed-tunnel speed combination. The higher RPM-tunnel speed combination shows a smooth variation of drag coefficient with α.

4.1.5 Representation of Translational Flight Near Hovering

A specialized series of tests were conducted by orienting the model at several attitudes with respect to the tunnel free stream flow to investigate the region of translational flight at very low speeds near hovering. The model was oriented at effective angles of attack of +90° and -90° to represent vertical ascent and descent; at -90° yaw for lateral translation to the right; and at 180° yaw for rearward translational flight. These test results were obtained out of ground effect and are briefly discussed in this section. All data in this section are referenced to a system of body axes.

4.1.5.1 Vertical Ascent

The effect of velocity in vertical ascent, obtained by varying tunnel q and wing fan RPM is shown in Figure 4.57 as variations of the longitudinal body axes coefficients with thrust coefficient. The increment in lift due to the vertical drag of the model is also shown and was determined by measuring the normal force with model fan-power off. The fan thrust change, or damping, is small compared to the model vertical drag. Figure 4.58 shows nose fan lift and moment for several nose fan door positions measured with the wing fans inoperative at a tunnel q of .50 lb/ft^2. The equivalent wing fan thrust coefficients for the RPM settings tested are shown in the figure. The nose fan lift data may be used in conjunction with the static data of Figure 4.4 to determine nose fan thrust damping.

Figure 4.59 shows the effect of all three fans operating in vertical ascent and the effect of variable exit louver stagger is shown in Figure 4.60.

4.1.5.2 Vertical Descent

The effect of velocity in vertical descent is shown in Figure 4.61 along with the power-off vertical drag increment measured at +90° angle of attack. The power-on data is unreliable due to extreme vibration of the model caused apparently by poor fan inlet recovery. Nose fan only data, presented in Figure 4.62, is reasonably smooth, however.

4.1.5.3 Lateral Translation

The effect of speed in lateral translation on the longitudinal and lateral-directional coefficients is shown in Figure 4.63. These data were obtained by varying model roll angle at constant values of thrust coefficient. Rolling moment and sideforce variations with thrust coefficient are similar to pitching moment and drag variations with thrust coefficient at low forward speeds, indicating similar center of pressure shifts and momentum drag for the two model attitudes.

The effect of the nose fan in lateral translation for two values of thrust coefficient is shown in Figures 4.64 and 4.65 and the relative effect of the vertical and horizontal tail is shown in Figure 4.66.

4.1.5.4 Rearward Translation

Longitudinal characteristics in rearward translational flight are shown in Figures 4.67 through 4.72 for various thrust coefficients. For these tests the model was rotated in pitch from -8° to +10°. The effect of speed is illustrated in Figure 4.67 and the effect of the tail is shown in Figures 4.68 and 4.69 for two values of thrust coefficient. The thrust coefficients of .992 and .982 correspond to approximate full-scale velocities of 20 and 55 knots. As would be expected, the model is unstable in pitch in rearward flight and the horizontal tail, which acts as a canard surface, is mildly destabilizing.

Nose fan operation is shown in Figure 4.70 with two nose fan door settings and shows good linearity of control effectiveness.

The effect of negative vectoring to reduce the longitudinal (drag) force coefficient is presented in Figure 4.71. For the vector angles

and thrust eoeffieients tested, the longitudinal foree eoeffieient remains positive, indicating a requirement of a nose-up attitude to rotate the normal forec to achieve trimmed flight to the rear.

The effeet of flap defleetion, as shown in Figure 4.72, shows little ehange in the longitudinal eharaeteristies for 0 and 45 degrees flap defleetion in rearward flight.

4.1.6 Power-Off Charaeteristies

Suffieient power-off data were obtained on the fan-powered model to enable comparisons to be made with test results of the 1/8-scale unpowered model reported in Referenee 3. In addition, the ineremental effeets of opening the wing fan and nose fan duet enelosures were determined to establish the airplane characteristies in the eonversion eonfiguration of the eonventional flight mode. The power-off data are presented in conventional aerodynamie eoefficient form, based on wing geometry.

4.1.6.1 Flap Effectivencss

The results of deflecting the wing trailing edge flap are given in Figures 4.73 and 4.74 for both tail-off and tail-on eonfigurations. The nonlinear variation of pitehing moment eoeffieient with angle of attack for the tail-on configuration is due to a nonlinear downwash variation with α and beeomes more pronounced with inereasing flap defleetion.

4.1.6.2 Horizontal Stabilizer Effectiveness

Angle of attack polars with various horizontal tail ineidenee angles are shown in Figures 4.75 and 4.76 for 0° and 45° flap defleetions.

4.1.6.3 Conversion Configuration

The effects of opening the wing and nose fan ducts are shown in Figure 4.77. The eurves are labeled aecording to the sequence in whieh the various configurations were tested. Opening the exit louvers results in a loss of lift, ($\Delta C_{L_{max}} = -.12$), a positive moment increment, and a reduetion in drag at moderate angles of attaek due probably to a reduetion in flap effeetiveness. Opening the nose fan duet produees a small lift and drag inerease and a negligible ehange in pitehing moment. The eonfiguration with the wing fan inlet doors open is of aeademie interest as it does not represent a true flight eondition with fan power off.

Figure 4.78 shows the effect of retracting the flap with the exit louvers at 25° vector angle and with the wing fan inlet closure doors closed.

4.1.6.4 Ground Effect

A series of tests were conducted with the 1/6-scale model in the "clean" conventional flight configuration with the model positioned over the ground board to determine conventional take-off and landing characteristics in ground effect. Longitudinal data are presented in Figures 4.79 and 4.80 for flap deflections of 30° and 45°. The most significant effects of ground proximity are an increase in lift curve slope, a small increase in lift at zero α and an increase in longitudinal stability level due to reduced downwash at the horizontal tail.

In order to define the angle of attack for stall, it was necessary to increase the model ground height due to an interference limitation between the ground board and model support sting at higher angles of attack. Twenty degrees angle of attack were obtainable at a ground height of .975 wing mac. Figure 4.81 shows the effect of testing at various ground heights and indicates the same stall angle of attack either in or out of ground effect.

4.1.7 Model Modifications

Tests of the 1/6-scale model have indicated a reduction in lift of approximately 5% from the static hovering value, at moderately low forward speeds corresponding to the range of thrust coefficients from approximately .95 to .99. See, for example, Figure 4.9. A portion of this lift reduction is attributed to regions of negative static pressure measured on the wing lower surface, particularly in the region of the flap aft of the fans. The existence of this negative pressure field is characteristic of wing-fan combinations and has been observed in tests of other models of wing-lift fans.

Several modifications to the model were tested in an attempt to improve the lift characteristics by increasing the wing lower surface static pressures and are discussed in this section. The most promising configurations were flap span extensions and aileron droop.

4.1.7.1 Flap Span Extension

A few tests were conducted with a revised flap configuration, formed by using a portion of the ailerons to effectively increase each

flap span by 2.5 inches or 15 inches full scale. Figure 4.82, which is a comparison of the modified flap effectiveness with that of the original flap, shows a substantial lift increase for the modified flap at a thrust coefficient of .94, but at T_c^S = .975 the lift increment is not as large as that obtained from moderate aileron droop angles.

The data of Figure 4.82 were obtained with wax fairings at the wing lower surface-fuselage juncture, installed to reduce the lower surface wing area between the fuselage and fan exit, as on the full-scale aircraft. No change in the data was noted due to the fairing and it was left in place for the remainder of the tests.

4.1.7.2 Effect of Aileron Droop

A relatively simple modification, which effectively provides a full-span trailing edge flap, was that of collectively deflecting, or drooping, the ailerons. Figure 4.83 shows the effect of various amounts of aileron droop on the longitudinal characteristics at a thrust coefficient of .976. Positive lift increments are obtained for aileron droop angles up to 30° but the greatest change in lift per degree of droop occurs between droop angles of 10° and 20°. Small drag increases are noted and a favorable nose down pitching moment increment is obtained with the ailerons drooped.

Some relief of the negative pressures on the flap lower surface are illustrated in Figure 4.84 which shows an improvement in flap effectiveness with the ailerons drooped.

Figure 4.85 shows the effect of exit louver vector angle on flap effectiveness with the ailerons drooped 15°. Improvement in flap lift at the higher vector angle arises from directing the high pressure fan efflux toward the flap lower surface. Again, the flap lift increment is larger for the zero vector condition with drooped ailerons than for zero droop at the same thrust coefficient (see Figure 4.31).

Effects of aileron droop on the power-off characteristics are given in Figures 4.86 through 4.88. Combined droop and flap deflection curves are shown in Figure 4.87 which could be incorporated on the full-scale airplane such that the droop is removed with flap retraction for high-speed flight.

Conversion sequence configuration data with 15° aileron droop and with the tail on are shown in Figure 4.89. The incremental effects

of opening the wing and nose fan ducts are similar to those obtained earlier in the test without droop and with tail off, as shown in Figure 4.77.

Basic tail-off longitudinal characteristics with 15° drooped ailerons are presented in Figure 4.90 through 4.92 for 0° and 50° exit louver vector angles and for the range of thrust coefficient through transition flight into conversion flight. As shown in Figure 4.90 for the 0° vector setting, the lift coefficient is maintained greater than unity for all values of thrust coefficient.

Static longitudinal stability and horizontal tail effectiveness with aileron droop are shown in Figures 4.93 through 4.97 for several values of thrust coefficient and for 0° and 50° vector angle. Compared with the zero droop data of Figures 4.13 through 4.18, the drooped aileron data indicate a slight increase in downwash at the horizontal tail, but no change in $d\epsilon/d\alpha$ as evidenced by the same stability level for the two configurations.

4.1.8 Wing Fan Power Data

The measured electrical input power to the wing fan drive motors was corrected to motor shaft output power by means of motor power calibration curves prior to computation of the fan power coefficients for data reduction. However, the power coefficient includes the frictional power of the fan drive gear boxes. As mentioned in Section 4.1.1 and indicated in Figure 4.2 the fan power coefficient varies with RPM due to these frictional losses.

If the total frictional power is assumed to be a linear function of RPM^2 and the fan power as a linear function of RPM^3, the total power coefficient may be expressed in the form

$$C^{s}_{P_{TOTAL}} = \frac{K_1}{N} + K_2$$

where K_1 represents the friction coefficient, K_2 the fan power coefficient, and N is motor speed in revolutions per minute. Multiplying both sides by N,

$$C^{s}_{P_{TOTAL}} N = K_1 + K_2 N.$$

A plot of the product $C_P{}^S N$ versus motor RPM is a straight line over the range of test RPM with intercept K_1 and slope K_2. Evaluating these terms,

$$K_1 = 2420$$

$$K_2 = .553$$

The quantity K_1/N represents the frictional power coefficient increment for correcting the computed values of $C_P{}^S$ and is plotted in Figure 4.98.

Typical corrected power coefficient variations with thrust coefficient and exit louver vector and stagger angles are also shown in Figure 4.98. Fan power tends to increase with cross flow velocity and to decrease with either vector or stagger angle. Power coefficient remains essentially constant with angle of attack (and yaw angle) indicating no tendency for fan stall within the unstalled range of angle of attack for the wing.

All of the power data presented in this report, other than that of Figure 4.98, are uncorrected for the friction increment discussed above.

4.2 WING PRESSURE DISTRIBUTIONS

Figures 4.99 through 4.107 are isometric representations of pressure distributions on the left hand wing panel. Although there were insufficient pressure orifices to precisely determine the distributions, general trends are indicated and several interesting features of the complex flow field around the wing are illustrated. Among these are the favorable pressure gradient on the wing upper surface created by the fan inflow, negative pressures on the wing and flap lower surfaces aft of the fan, and the possible existence of stagnation pressures on the wing upper surface aft of the fan. The wing surface pressure orifice locations are given in Figure 6.1.

Figures 4.99 and 4.100 provide a comparison of pressure distributions for power-off and power-on conditions for 0° and 16° angle of attack. The power-off configuration had the fan inlet doors closed and the exit louvers closed; the power-on configuration was with zero vector and stagger angle and the nose fan was operating. The corresponding lift coefficients determined from the force data are indicated. Pressure peaks induced over the wing leading edge due to fan operation are

illustrated and spanwise stations well outboard of the fan are seen to be influenced by the fan. The flap lower surface pressures and wing lower surface pressures aft of the fan are negative for the power-on condition and result in a reduction in flap effectiveness. The negative pressures in this region are believed to be caused by poor pressure recovery of the free stream flow due to the blanketing effect of the column of air created by the fan efflux.

Figures 4.101 through 4.103 show pressure distributions for several values of thrust coefficient in the transition speed range for 0° angle of attack. The exit louver vector angle was set for each thrust coefficient to balance out the drag force in order to represent approximate trim flight conditions. Gradual improvement in the flap pressure distribution is noted with increasing vector angle, particularly for the spanwise stations just inboard and outboard of the fan.

Pressure data are shown in Figures 4.104 through 4.106 for several values of aileron droop, discussed in Section 4.1.7. The principal effect of drooping the ailerons is to increase the loading over the wing tip region although the force data indicate a slight improvement in flap effectiveness with the ailerons drooped.

Pressure data obtained with the extended flap span are shown in Figure 4.107. Compared with the original flap configuration of Figure 4.104, for the same test conditions, the pressure distributions are similar and only a small increase in lift coefficient is indicated for the modified flap at this thrust coefficient.

4.3 WING FAN DOOR HINGE MOMENT COEFFICIENTS

Curves of wing door hinge moment coefficients were constructed from tabulated data of the second series low speed wind tunnel tests (Reference 2). The figures are presented to show the variation of the wing-fan door hinge moment coefficients ($C_H{}^s$) with thrust coefficient, angle of attack, flap position, yaw angle, exit louver vector angle, and door position. Although complete data for all parameters are not available, a sufficient latitude of test conditions is available to establish major trends.

The right hand wing fan doors were instrumented for the tests and all hinge moment data presented are with respect to these doors. The sign convention established for the hinge moment data is such that a moment tending to open the door is positive.

The curves of Figure 4.108 show the trends of the hinge moment coefficient with T_e^s, α, and to some extent with δ_f. As would be expected, the hinge-moments for both the inboard and outboard doors tend toward a common value at a T_e^s of 1.0. The diminishing effect of α upon the coefficient, with increasing value of T_e^s, is also apparent from the curves.

Figure 4.109 shows that varying the angle of yaw produces significant changes in the hinge-moment coefficient. Although the data are limited to the higher values of T_e^s, the trends established in Figure 4.108 for this parameter are probably valid. Only negative angles of yaw could be tested.

The effects of door position are shown in Figures 4.110 and 4.111. The doors in the fully open position are considered at zero degrees. The curves of Figure 4.110 are applicable for both a 0 and a -10 degree yaw angle as indicated. Figure 4.111 summarizes the data of the previous two figures.

The variation of the hinge-moment coefficient with louver vector angle is also shown in Figure 4.111. For clarity, only one curve has been drawn through the data points for the inboard door although the slight variation with α is apparent in Figure 4.108.

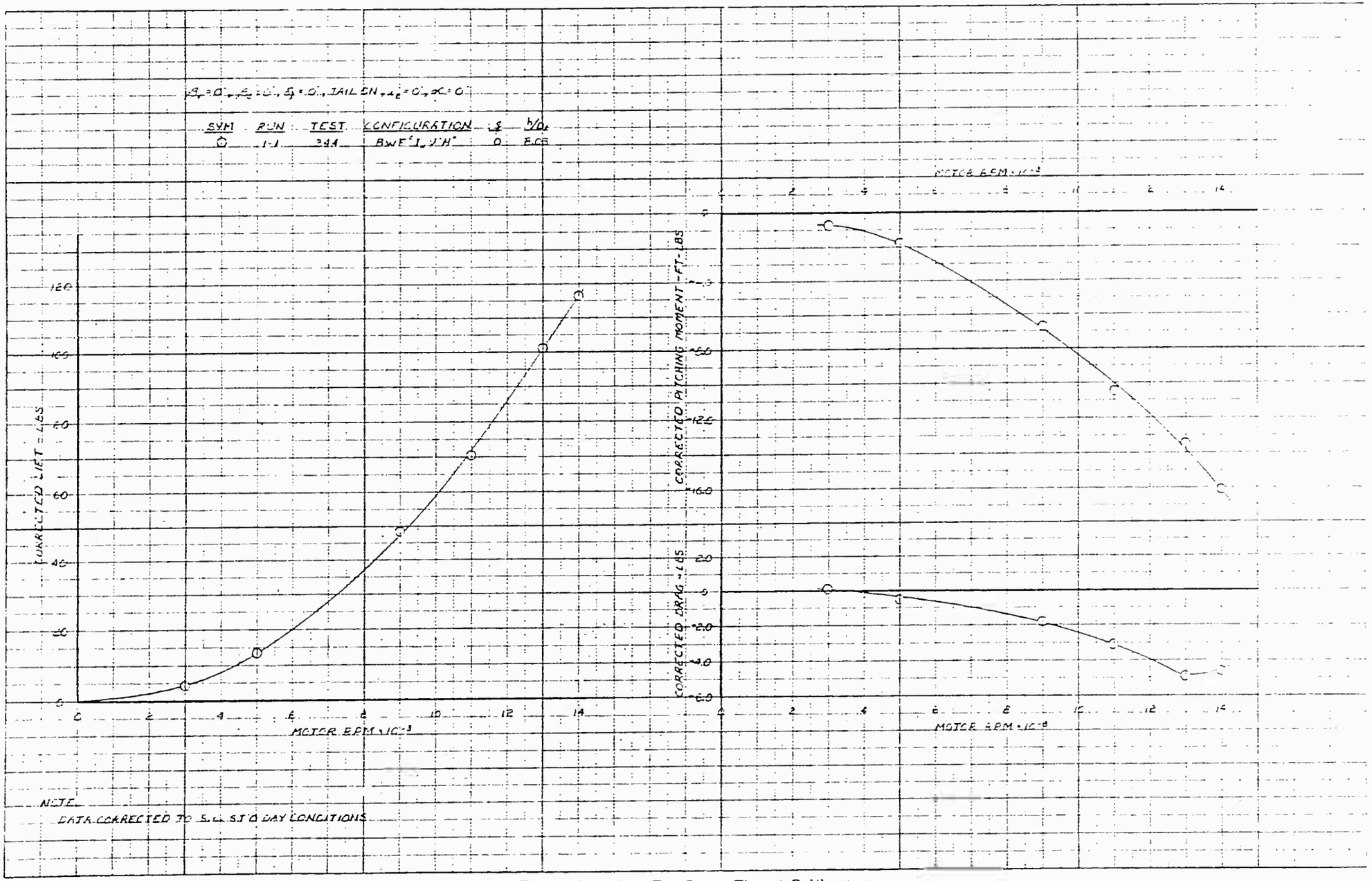

Figure 4.1 Wing Fan Static Thrust Calibration

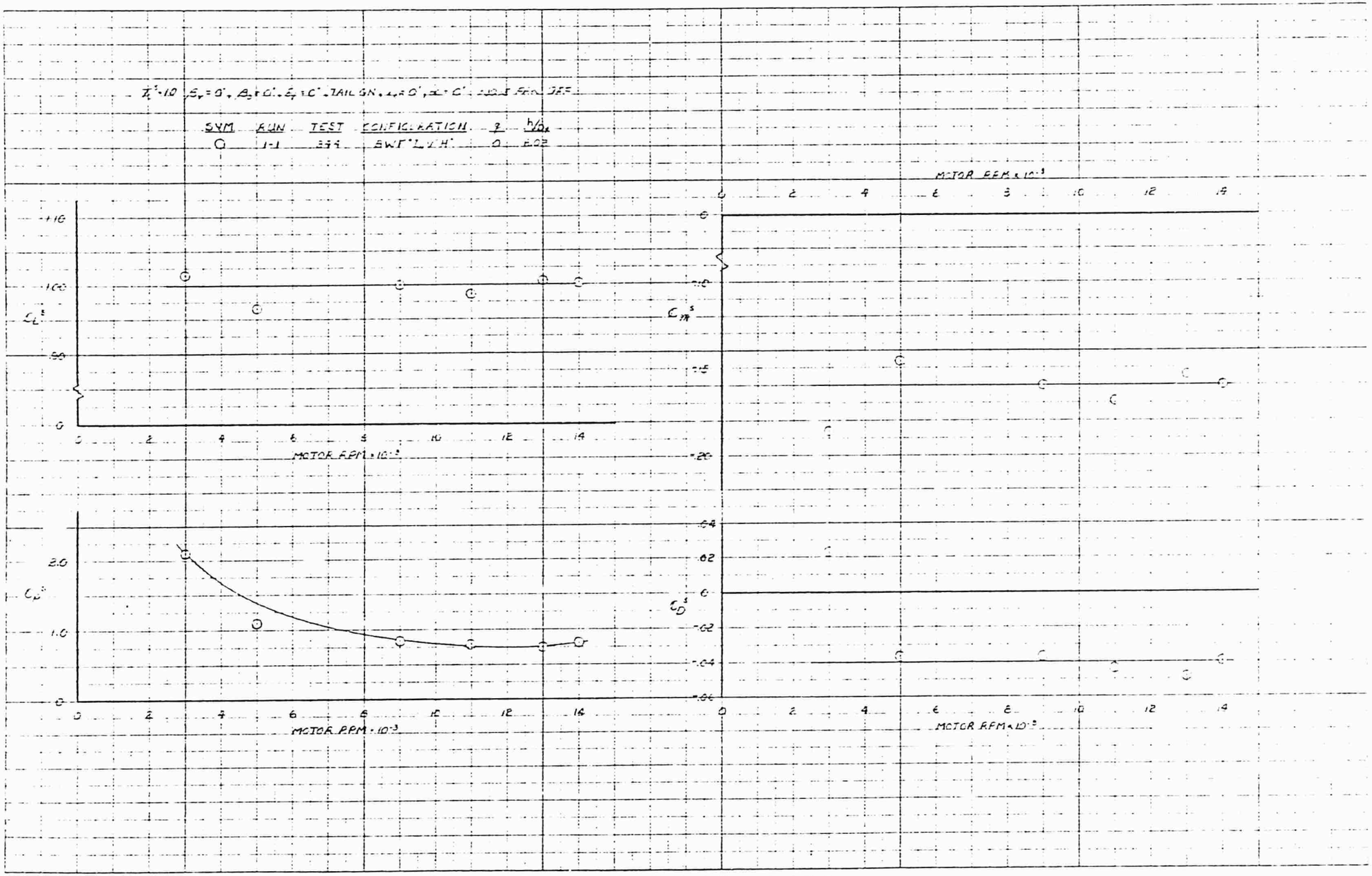

Figure 4.2 Basic Static Longitudinal Characteristics

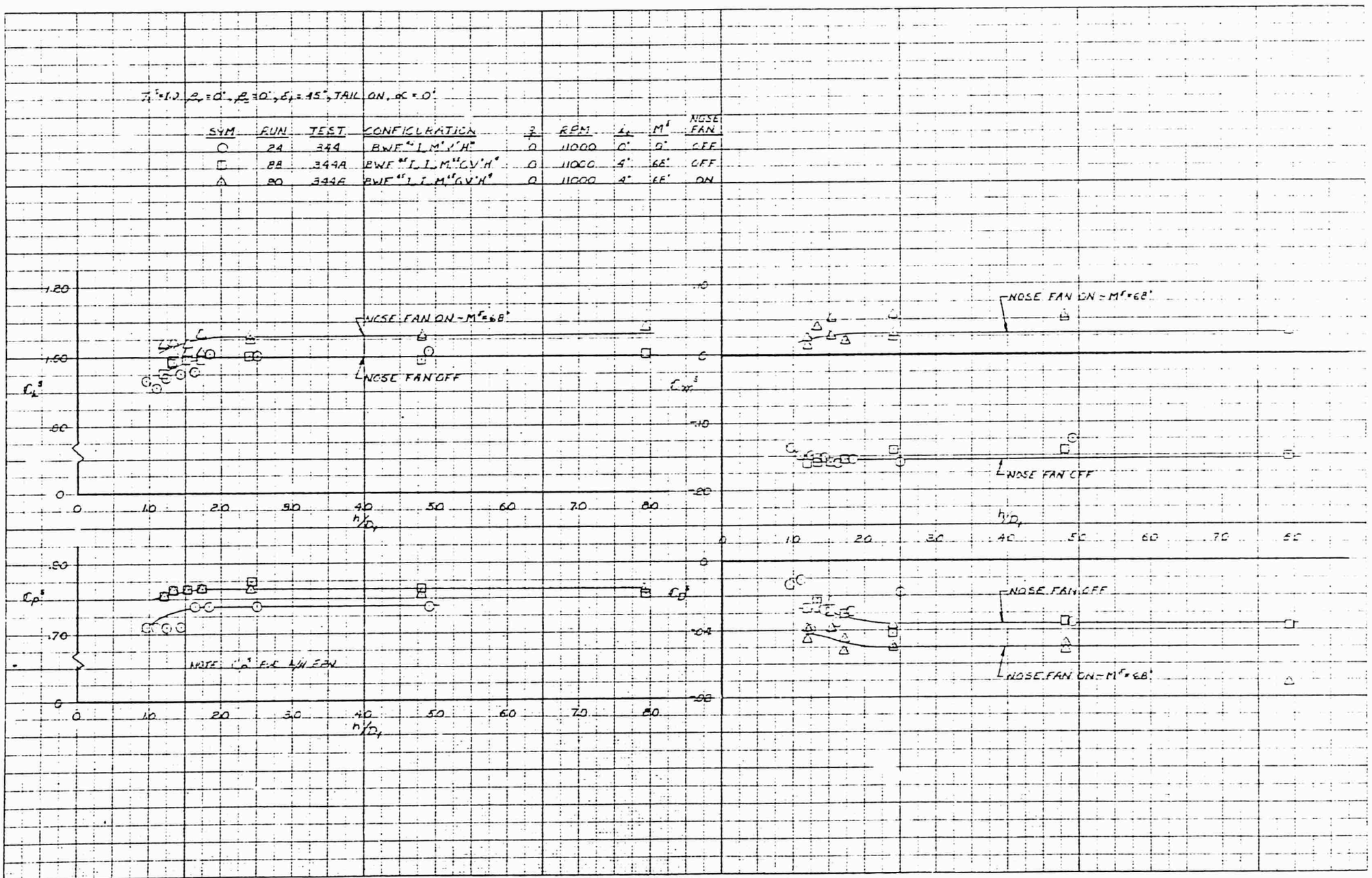

Figure 4.3 Effect of Ground Porximity on Static Characteristics

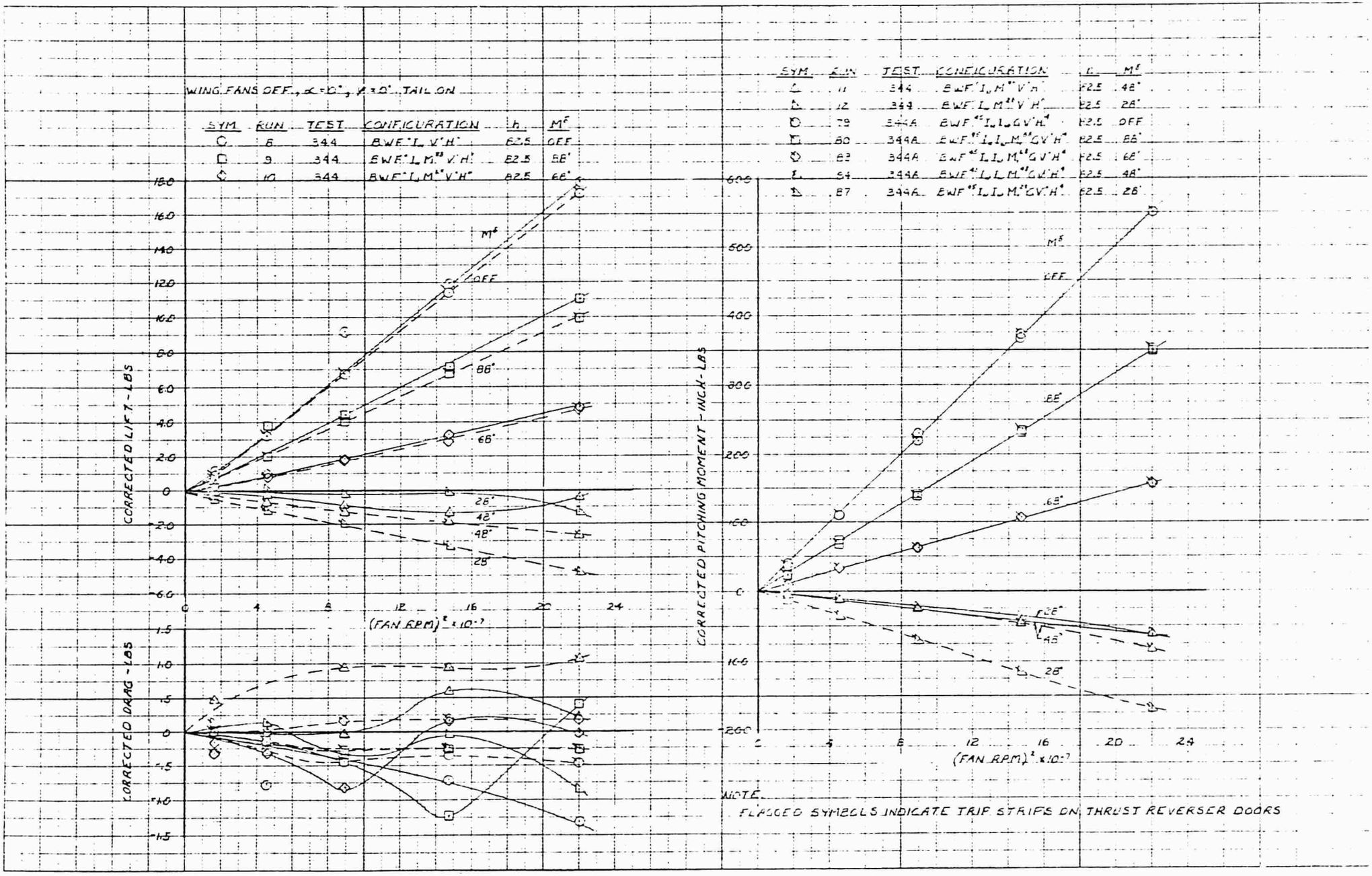

Figure 4.4 Nose Fan Static Thrust Calibration (Continued)

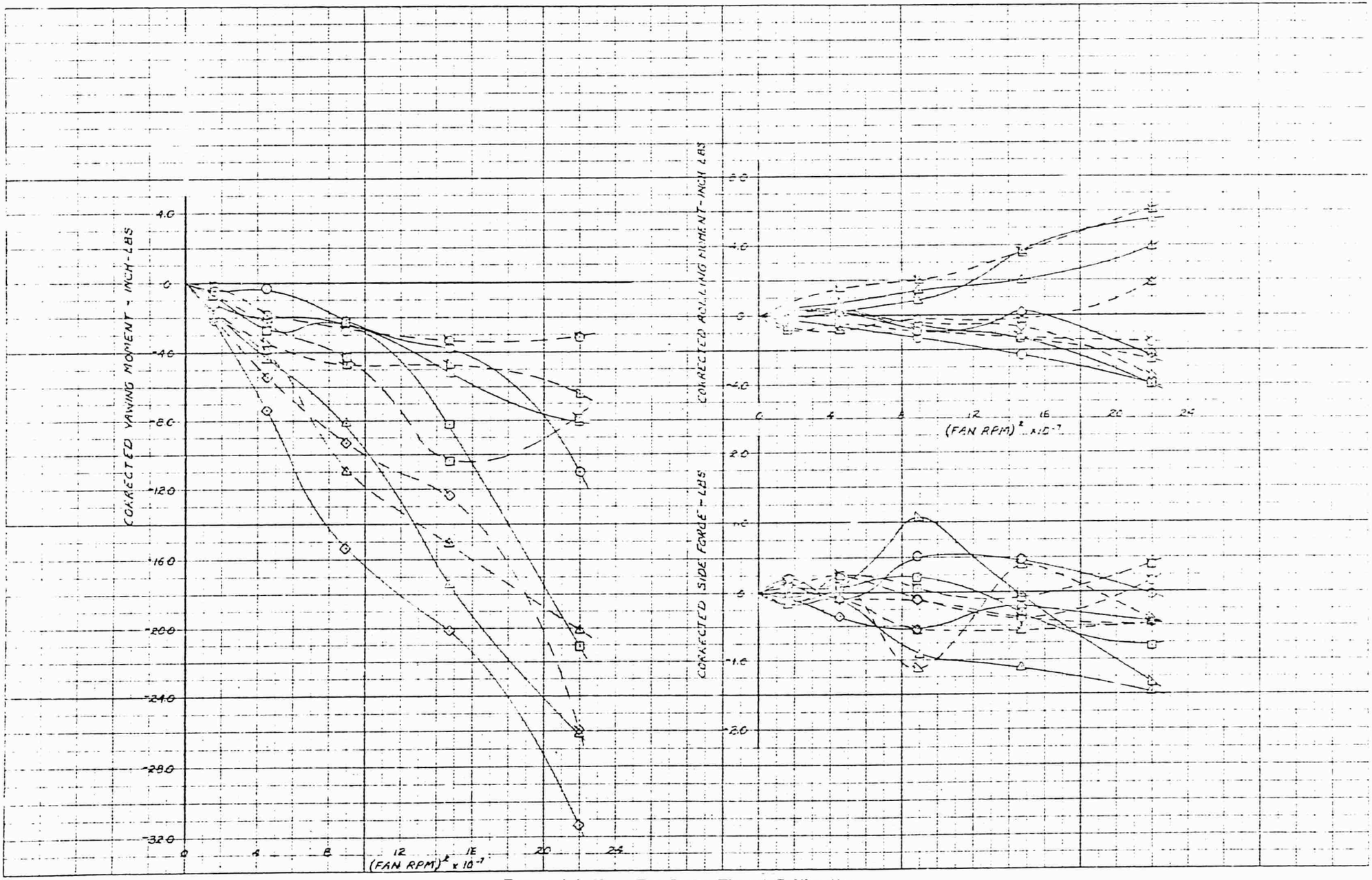

Figure 4.4 Nose Fan Static Thrust Calibration

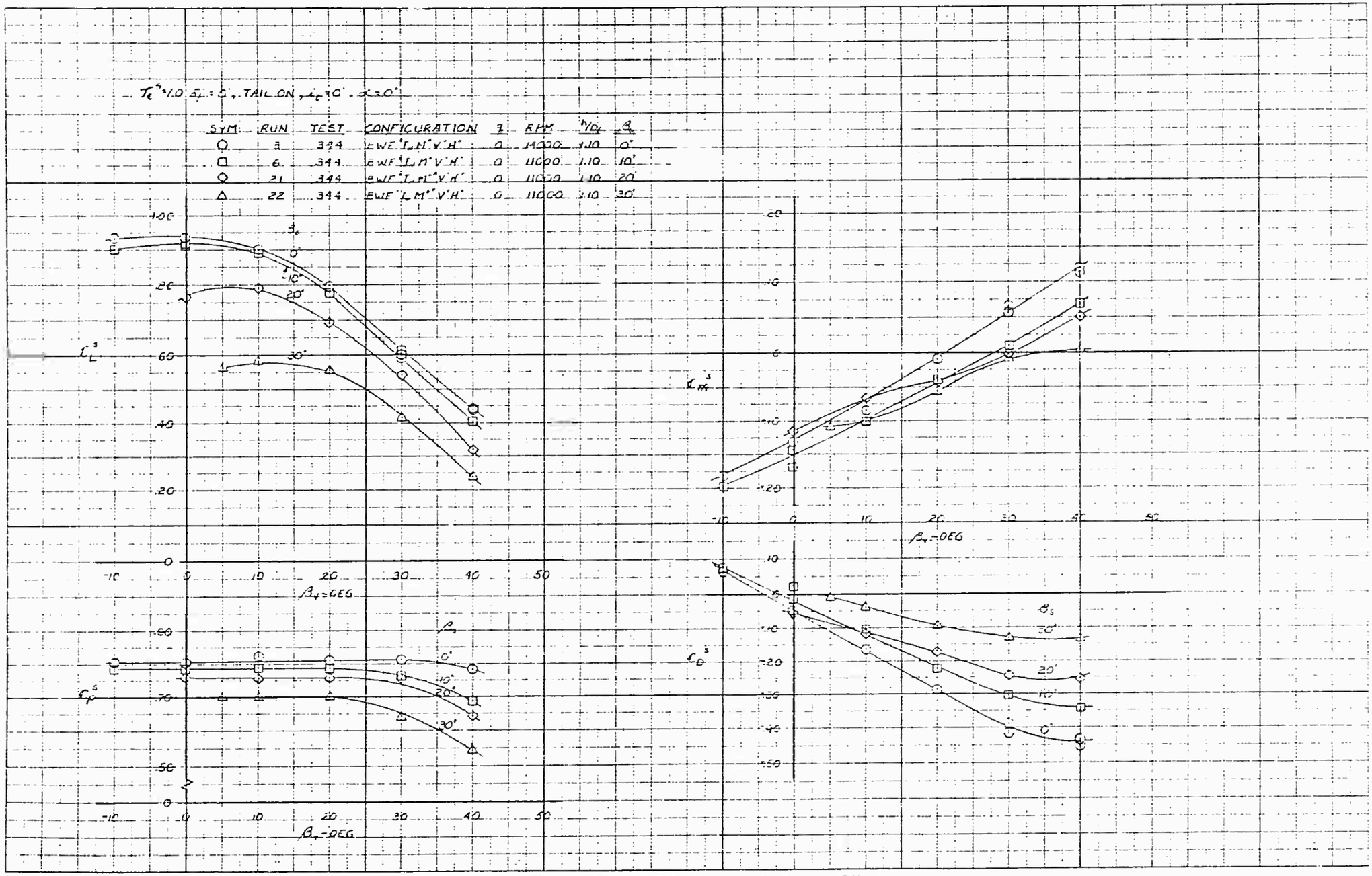

Figure 4.5 Vector-Stagger Effectiveness in Ground Effect

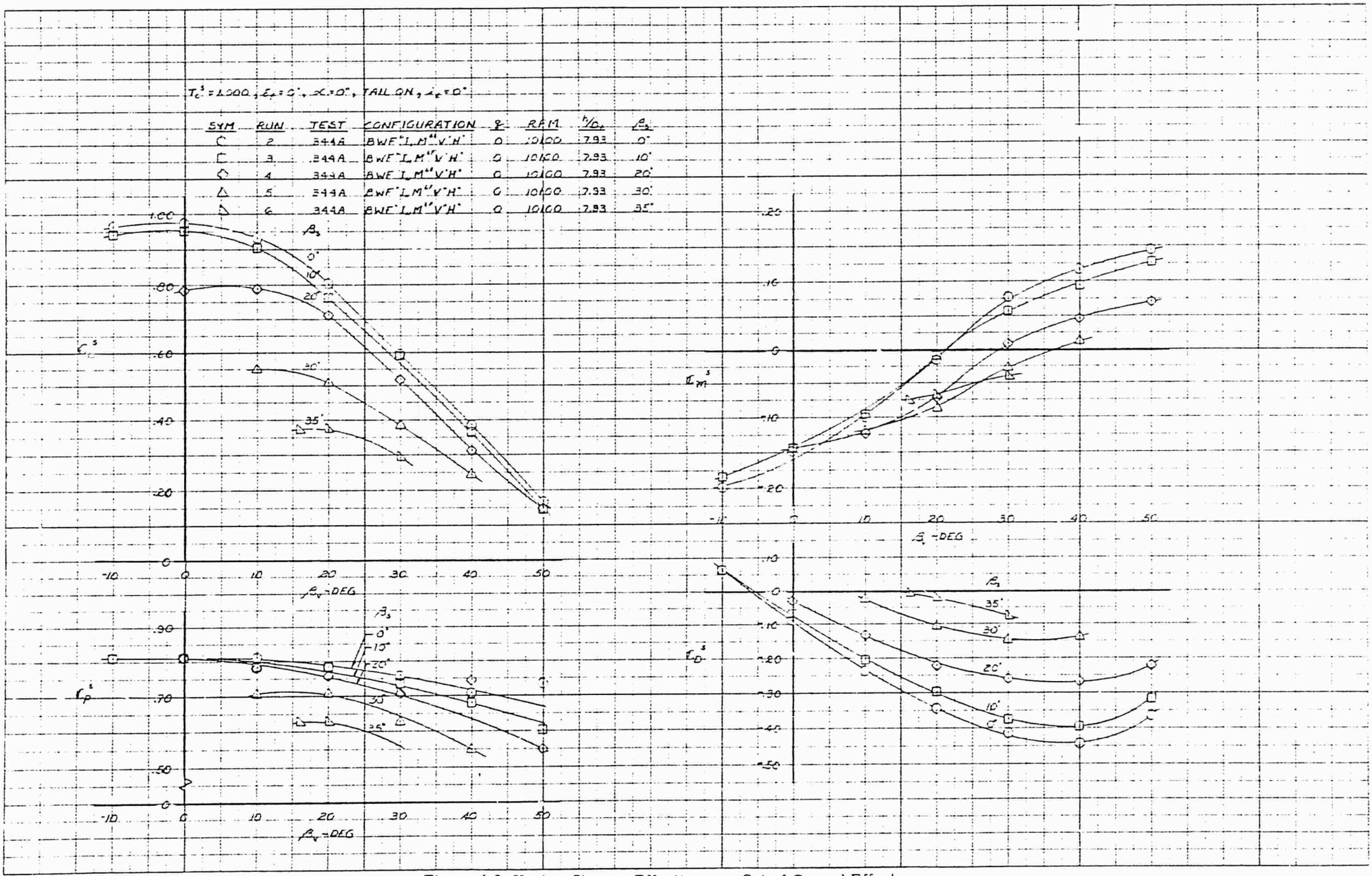

Figure 4.6 Vector-Stagger Effectiveness Out of Ground Effect

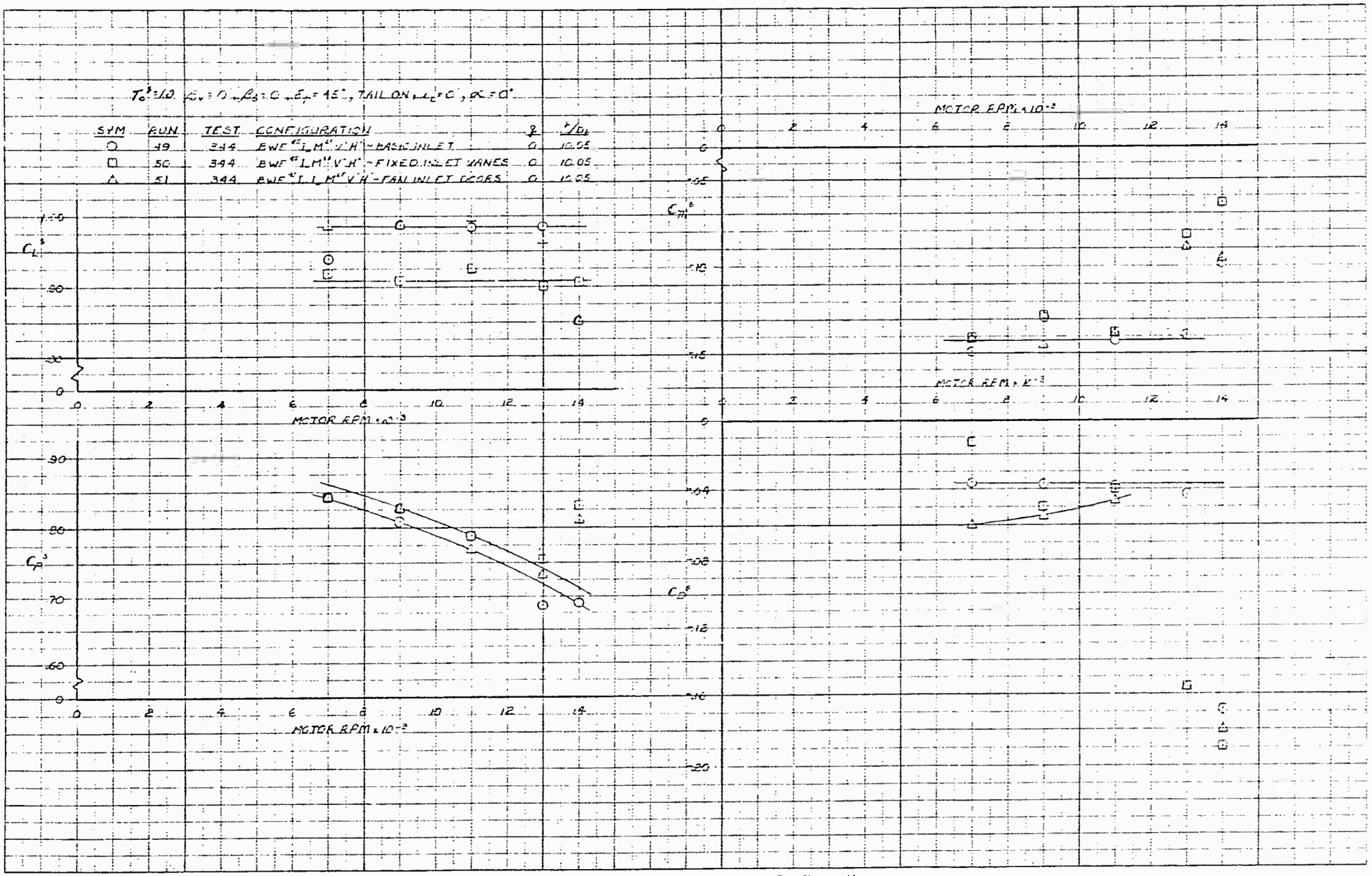

Figure 4.7 Static Effect of Wing Fan Inlet Configuration

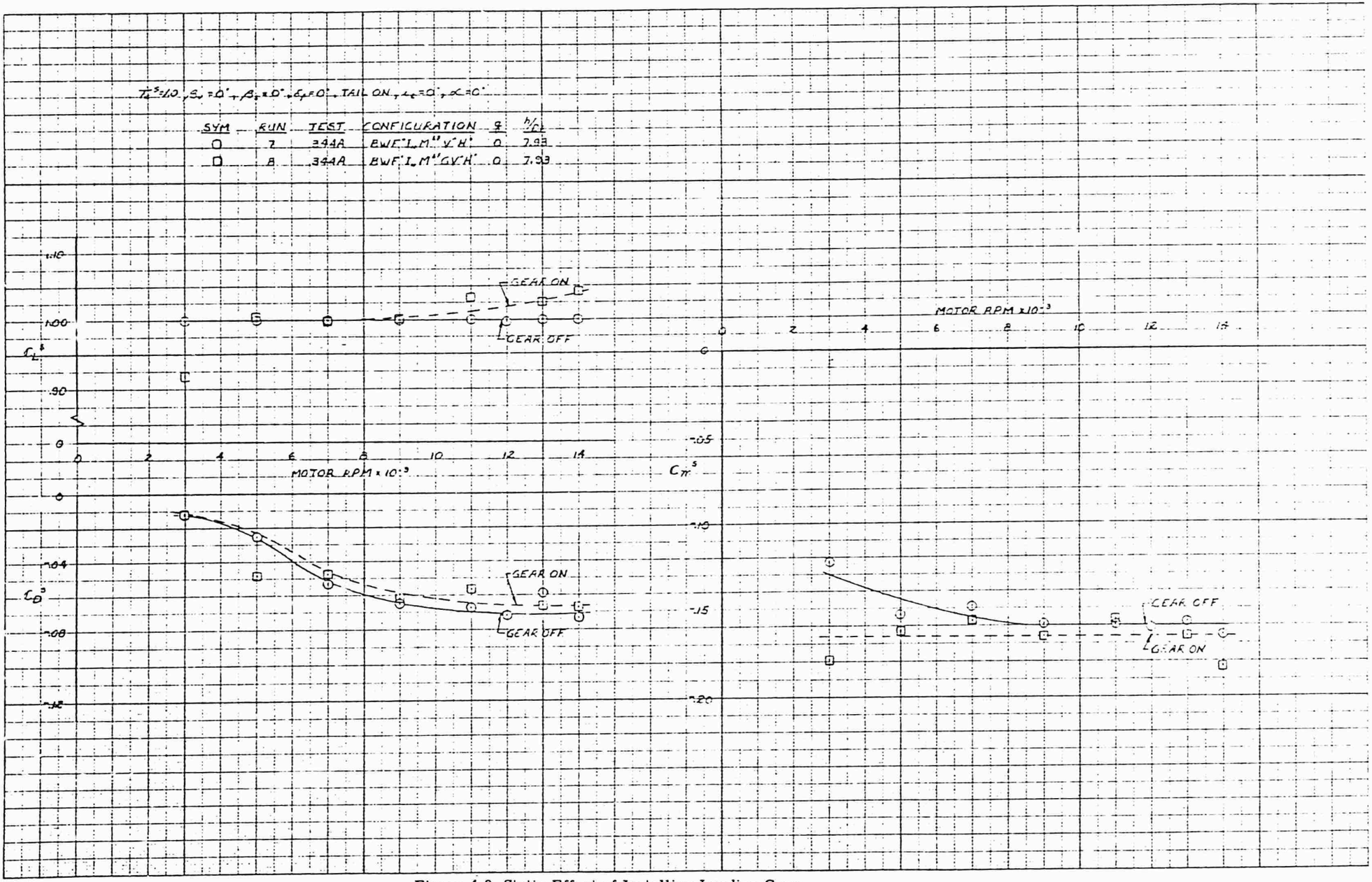

Figure 4.8 Static Effect of Installing Landing Gear

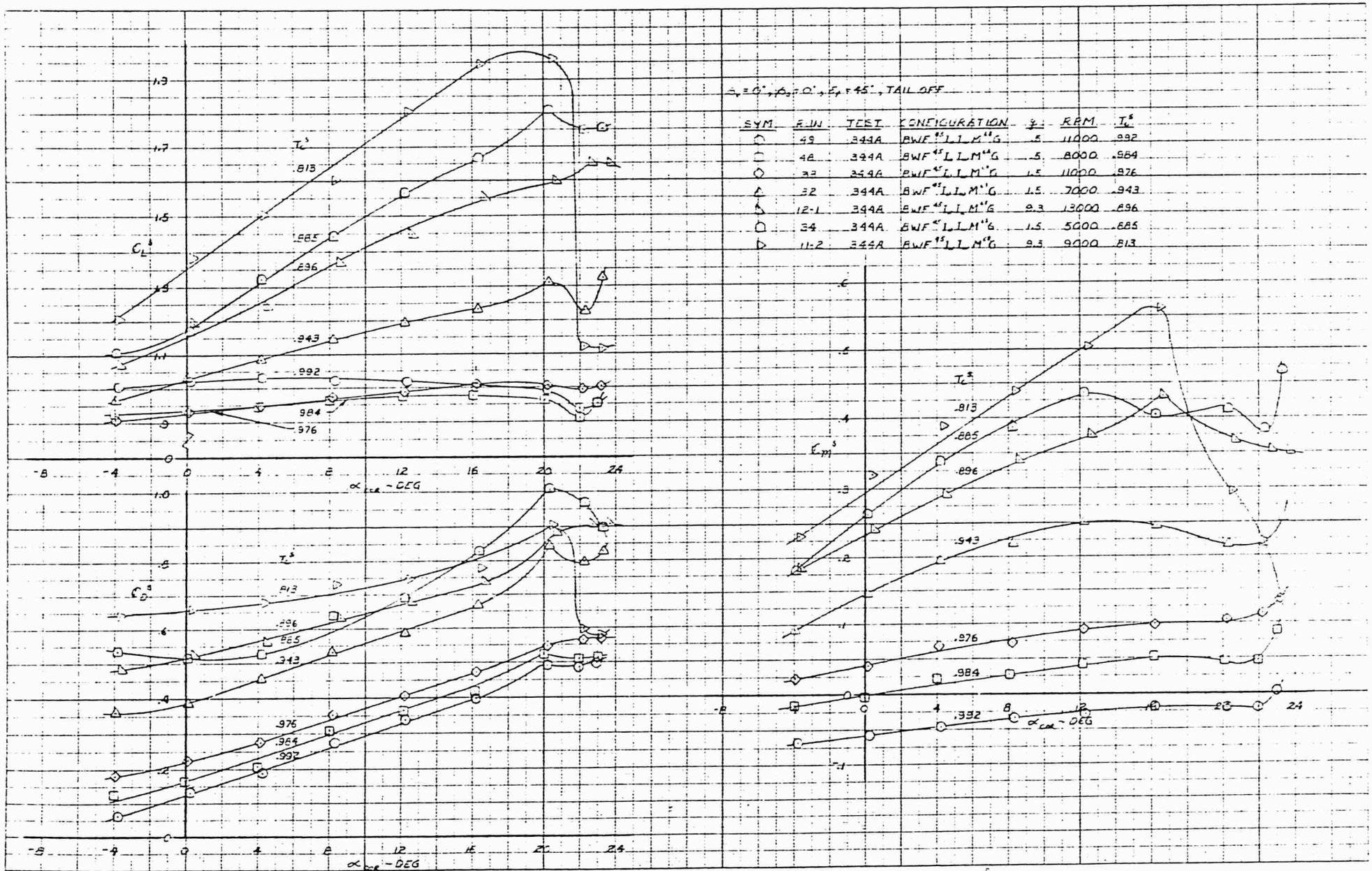

Figure 4.9 Effect of Thrust Coefficient on Longitudinal Characteristics, $\beta_v = 0°$

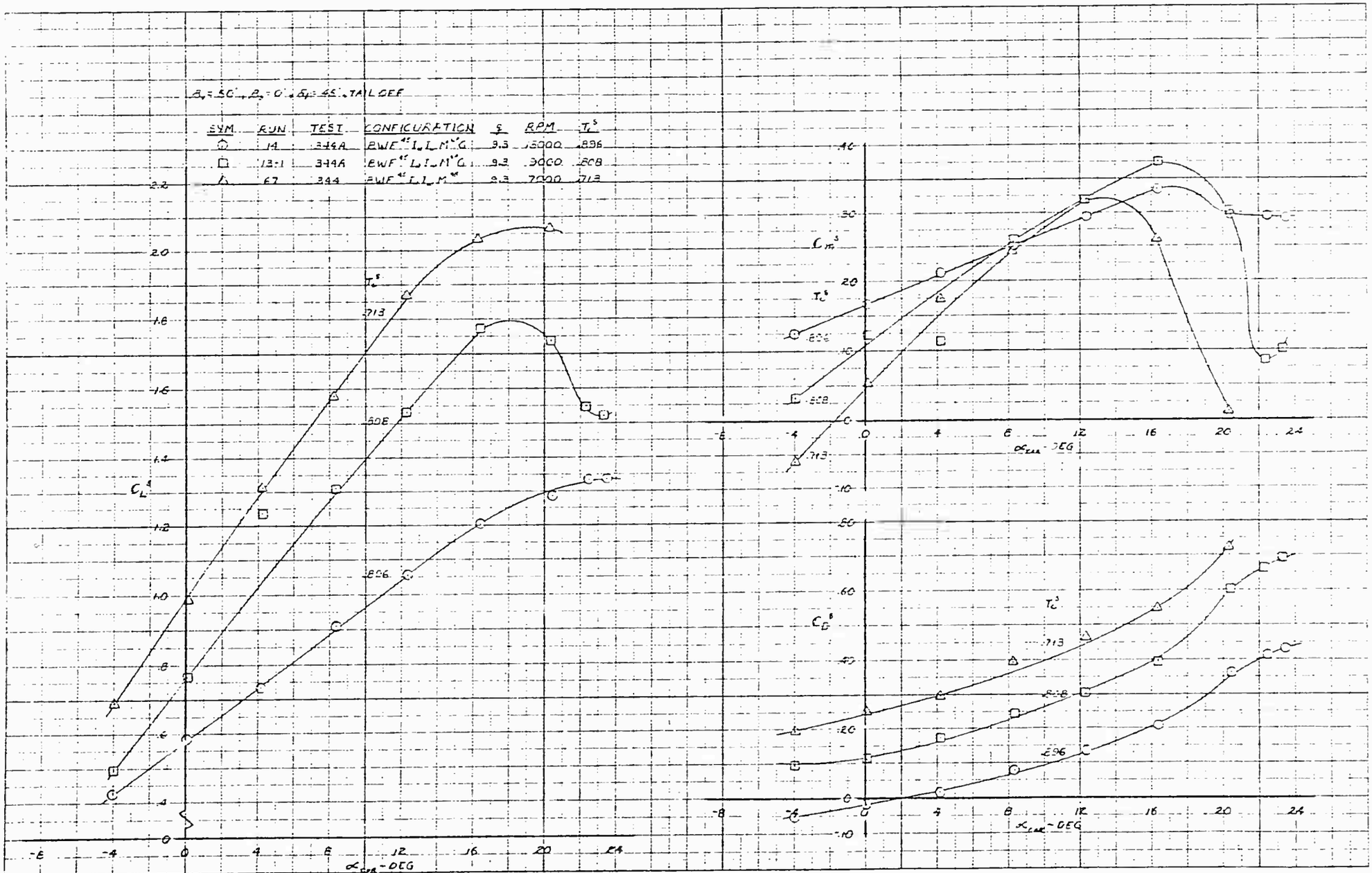

Figure 4.10 Effect of Thrust Coefficient on Longitudinal Characteristics,

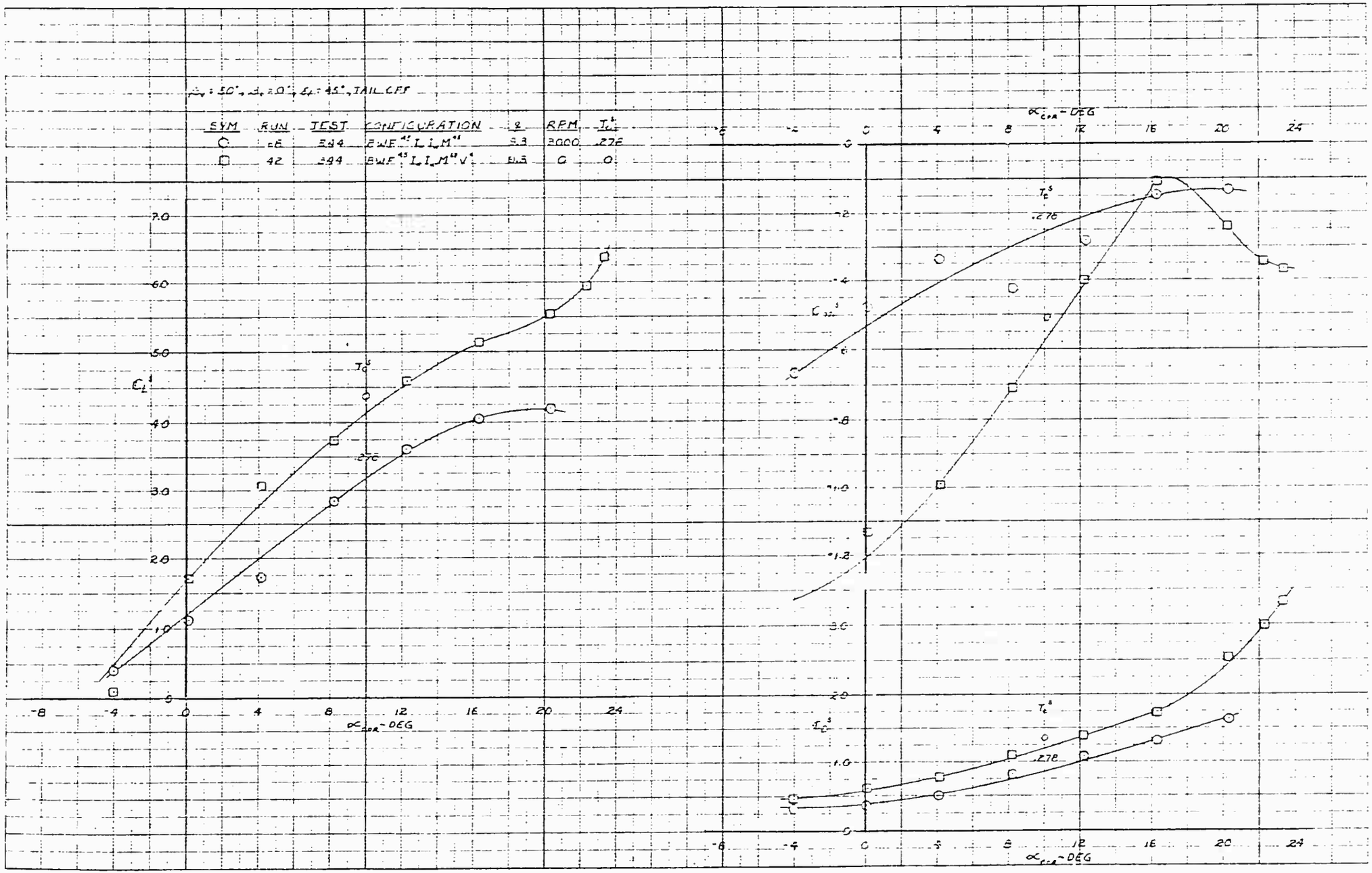

Figure 4.11 Effect of Thrust Coefficient on Longitudinal Characteristics,

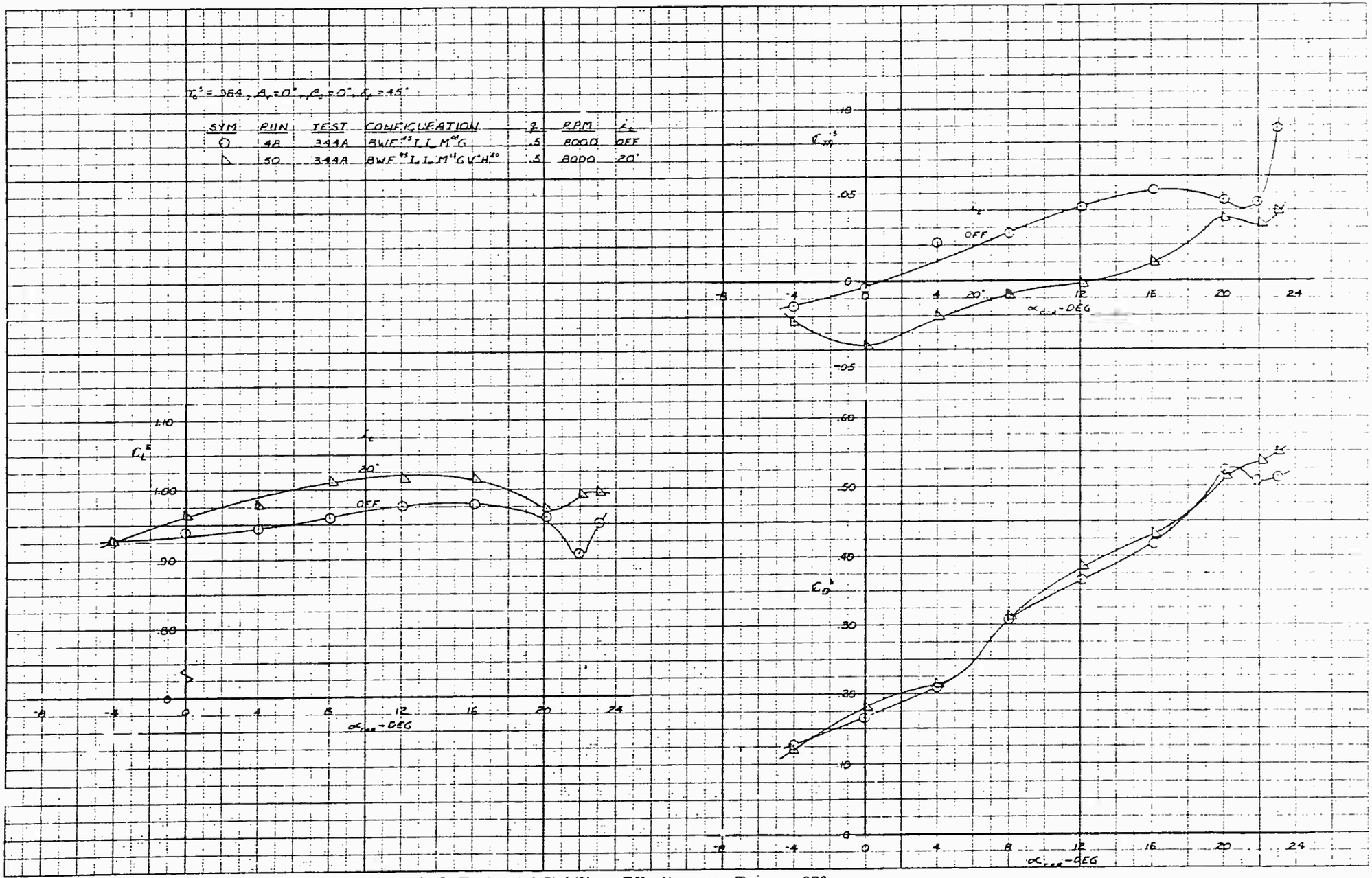

Figure 4.12 Horizontal Stabilizer Effectiveness, T_c' = .976

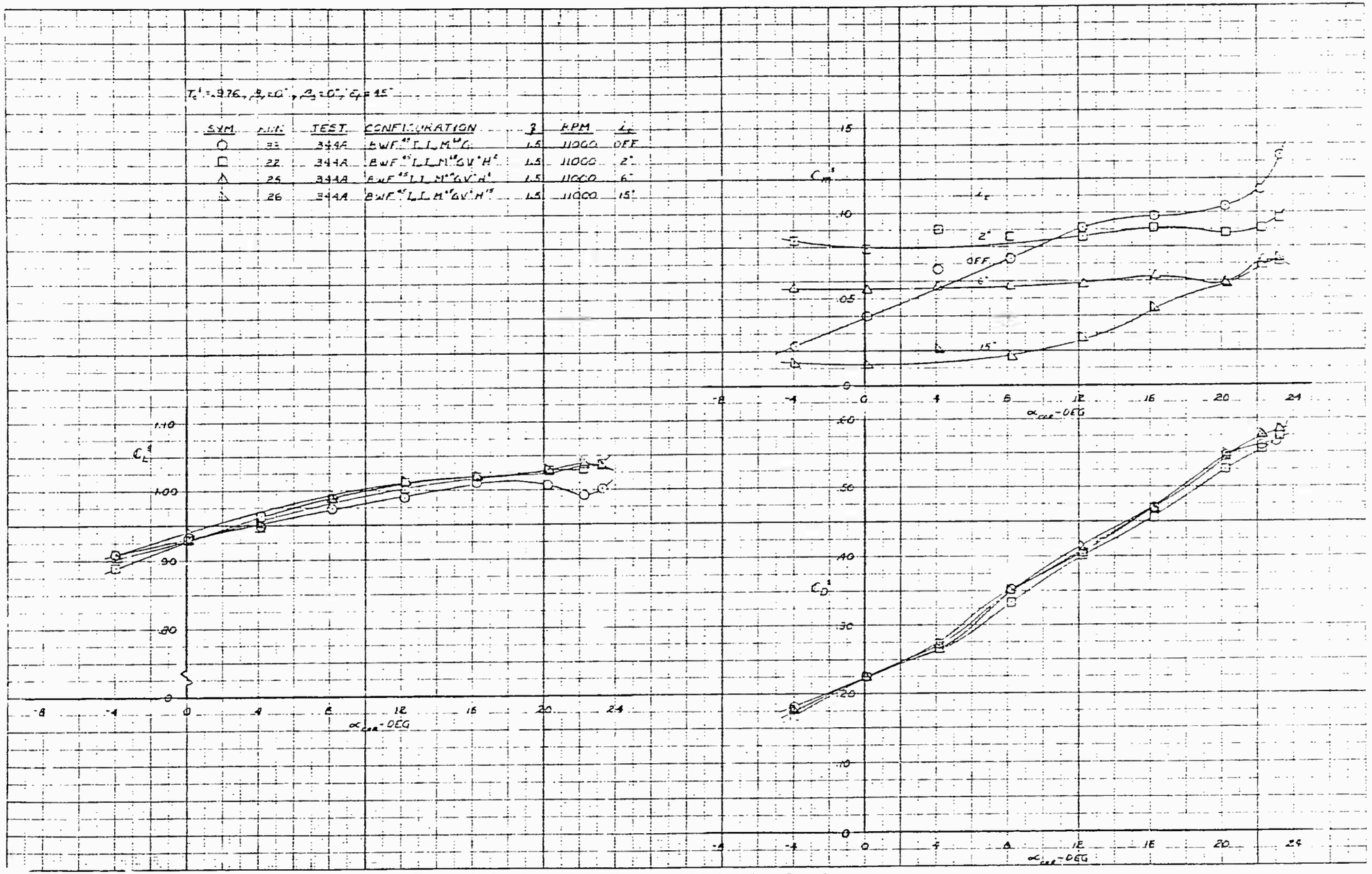

Figure 4.13 Effect of the Horizontal Tail at Low Speed

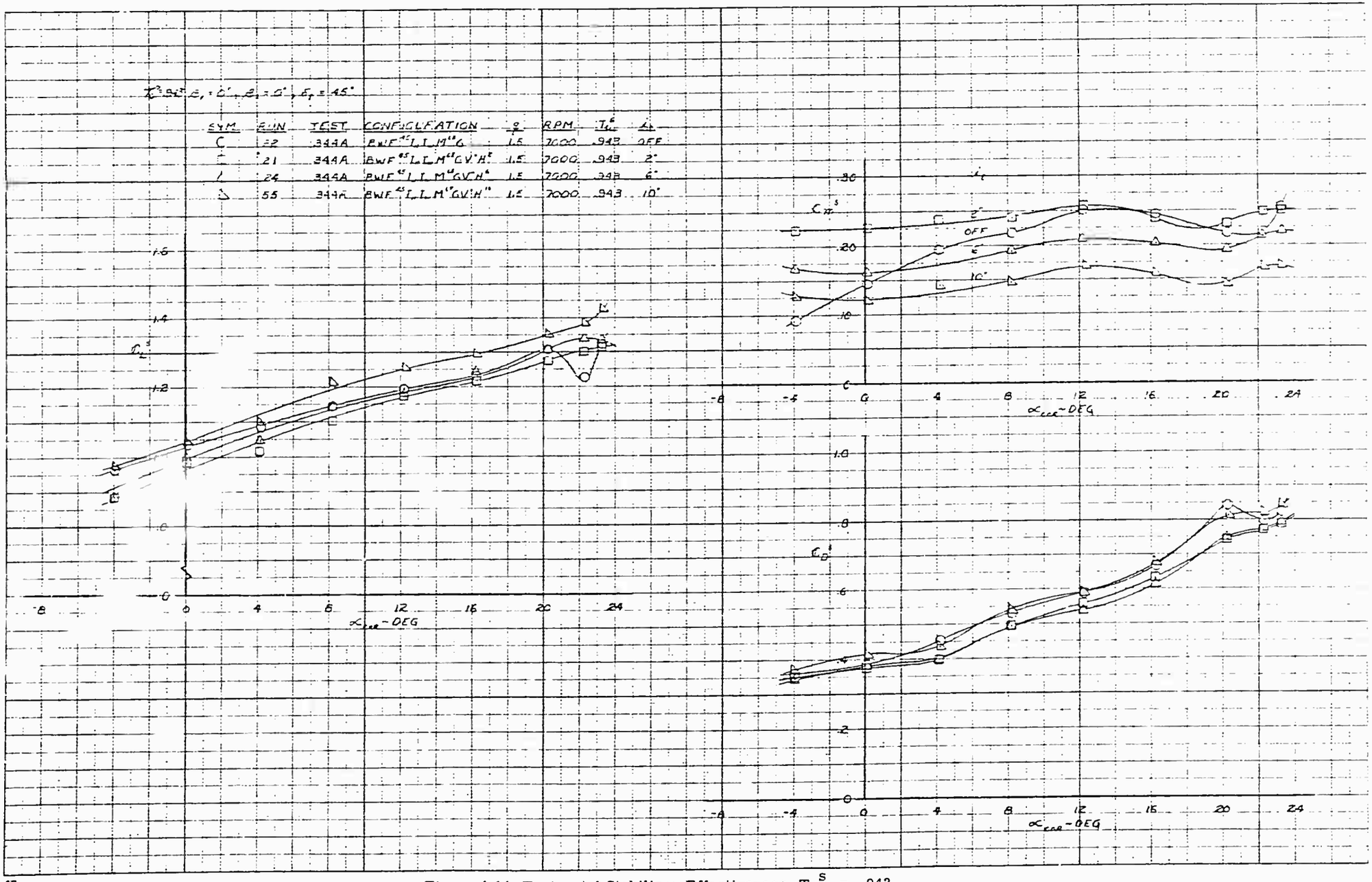

Figure 4.14 Horizontal Stabilizer Effectiveness, T_c^s = .943

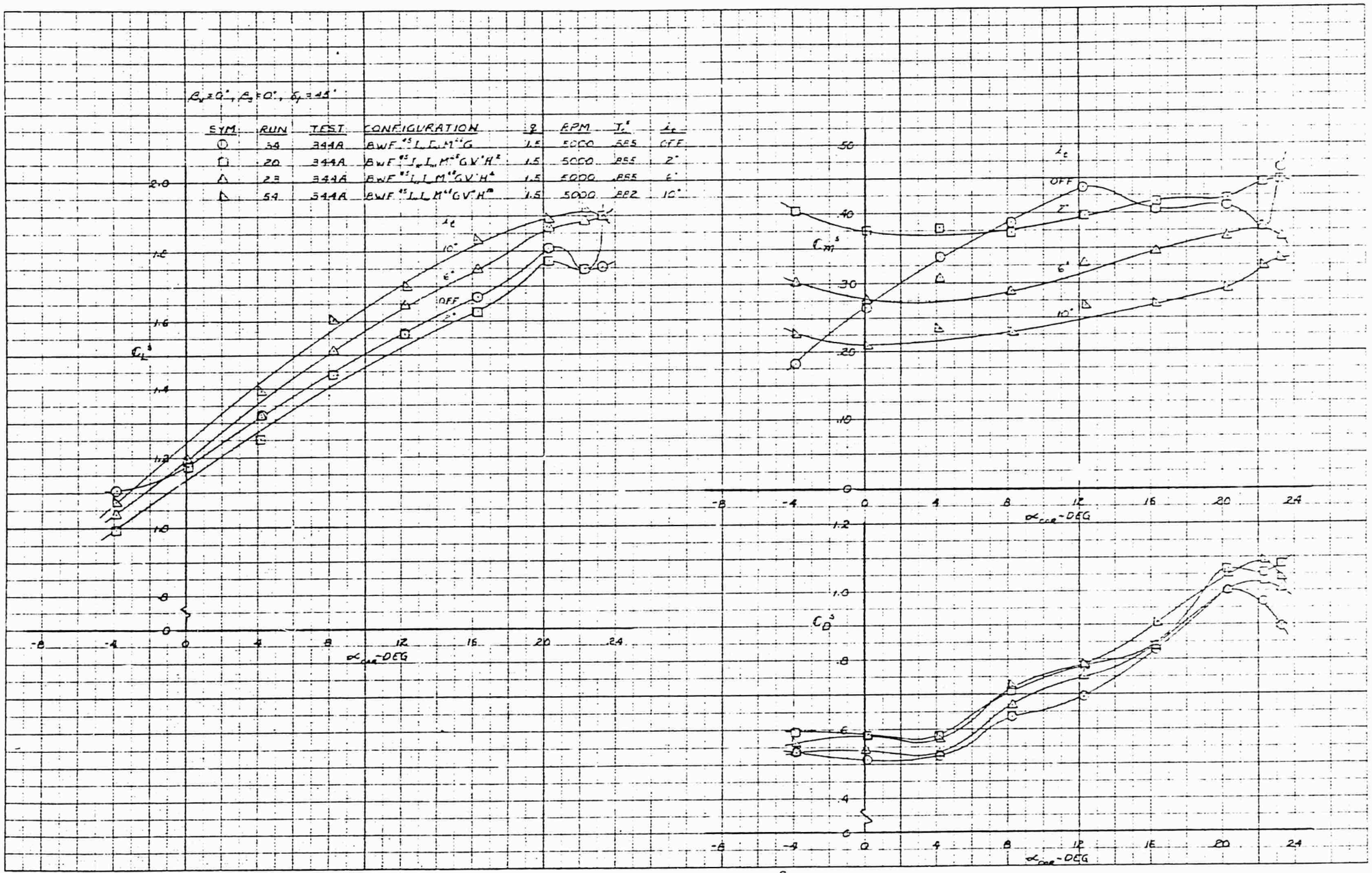

Figure 4.15 Horizontal Stabilizer Effectiveness, T_c^S = .885

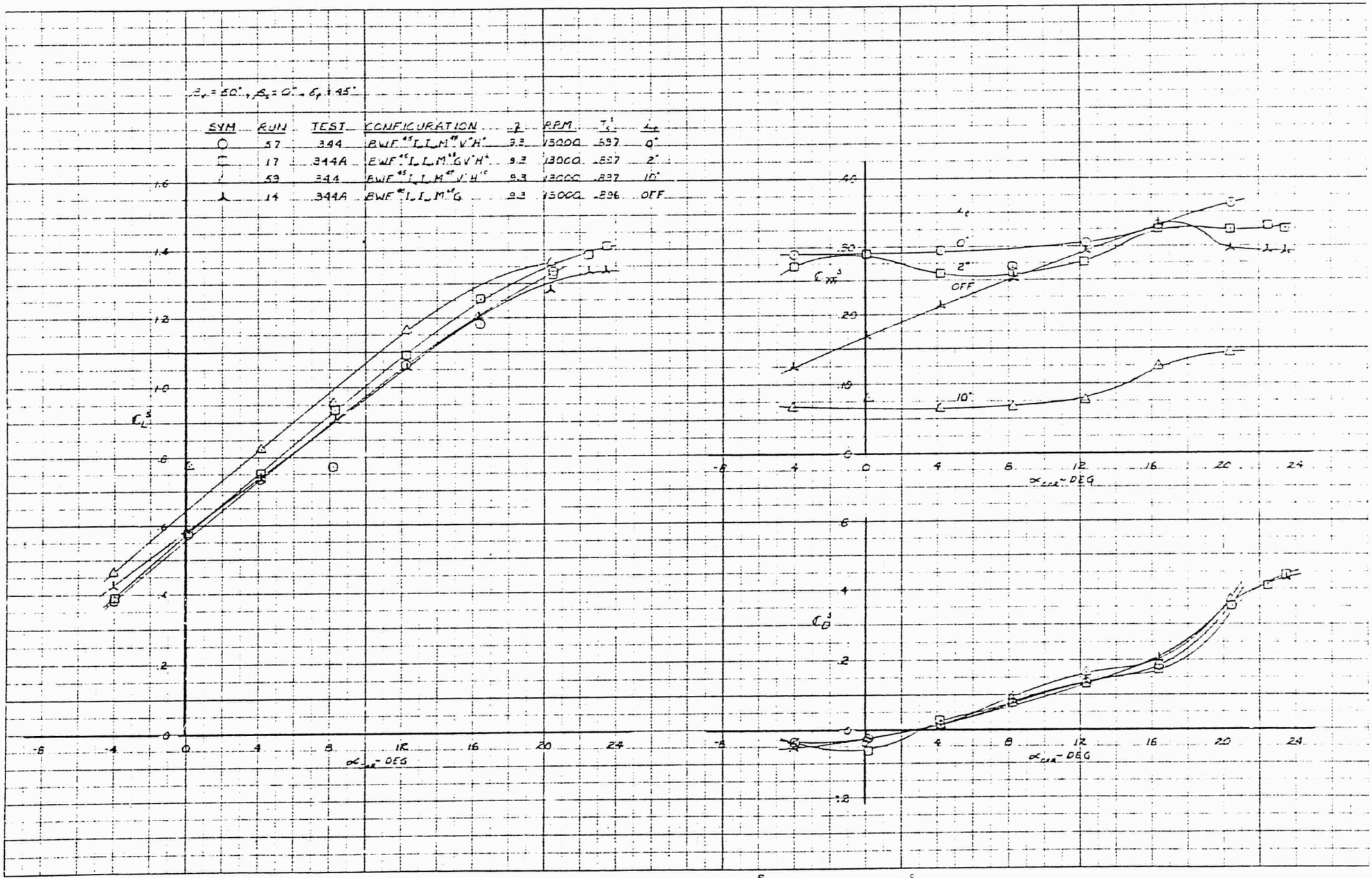

Figure 4.16 Horizontal Stabilizer Effectiveness, T_c^s = .897, β_v = 50°

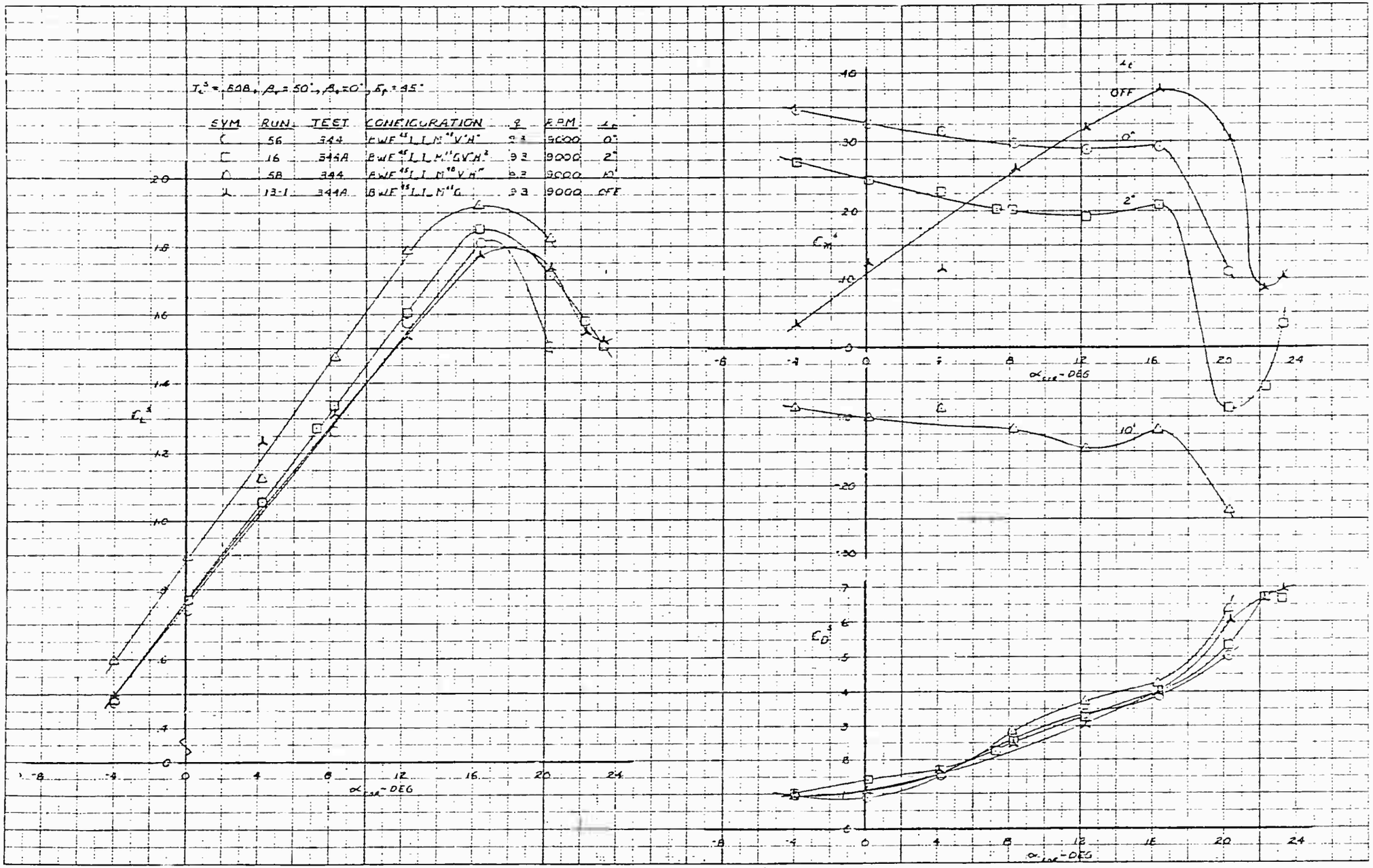

Figure 4.17 Horizontal Stabilizer Effectiveness, T_c^s = .808, β_v = 50°

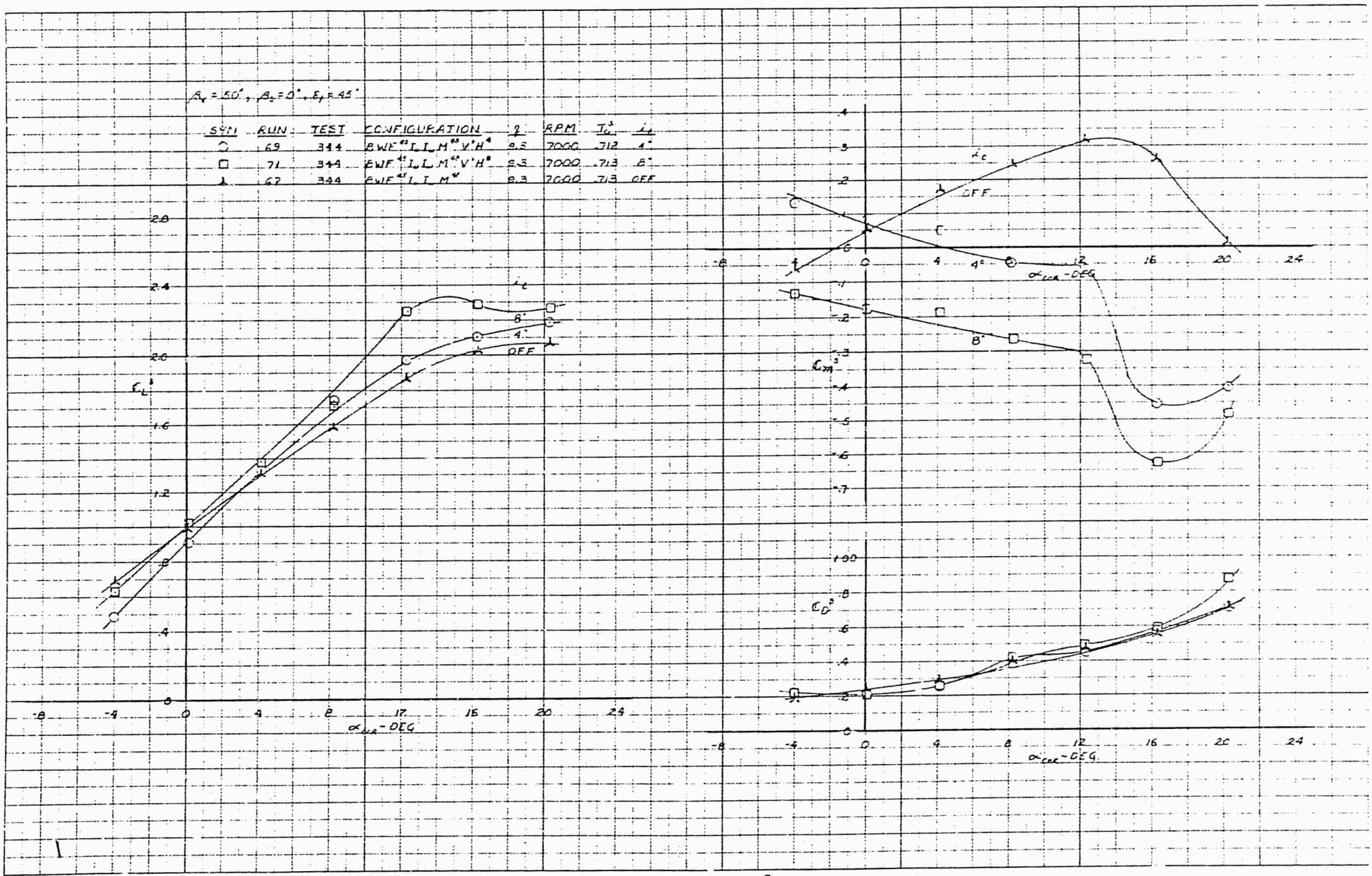

Figure 4.18 Horizontal Stabilizer Effectiveness, $T_c^s = .713, \beta_v = 50°$

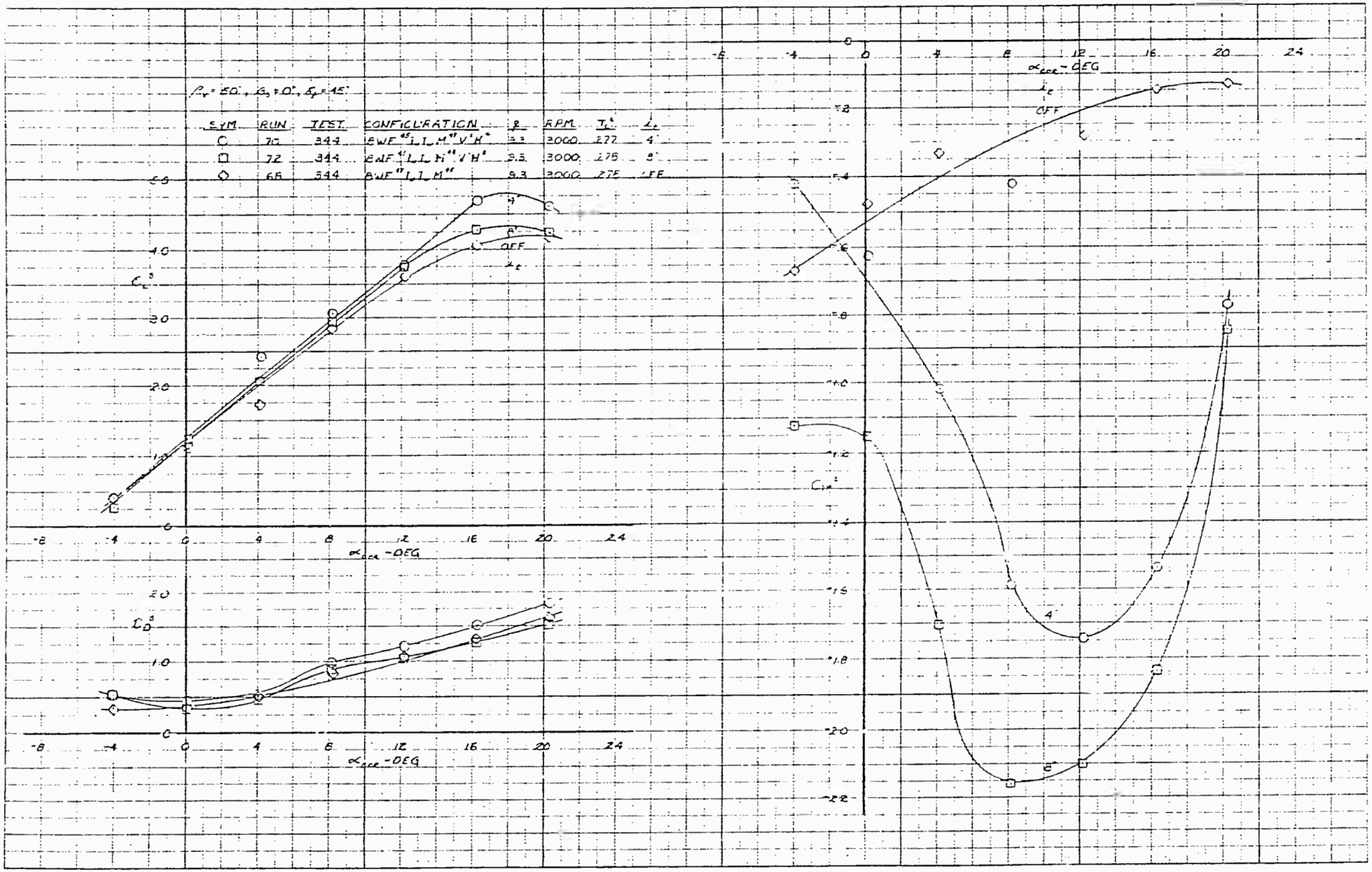

Figure 4.19 Horizontal Stabilizer Effectiveness, T_C^S = .278, β_V = 50°

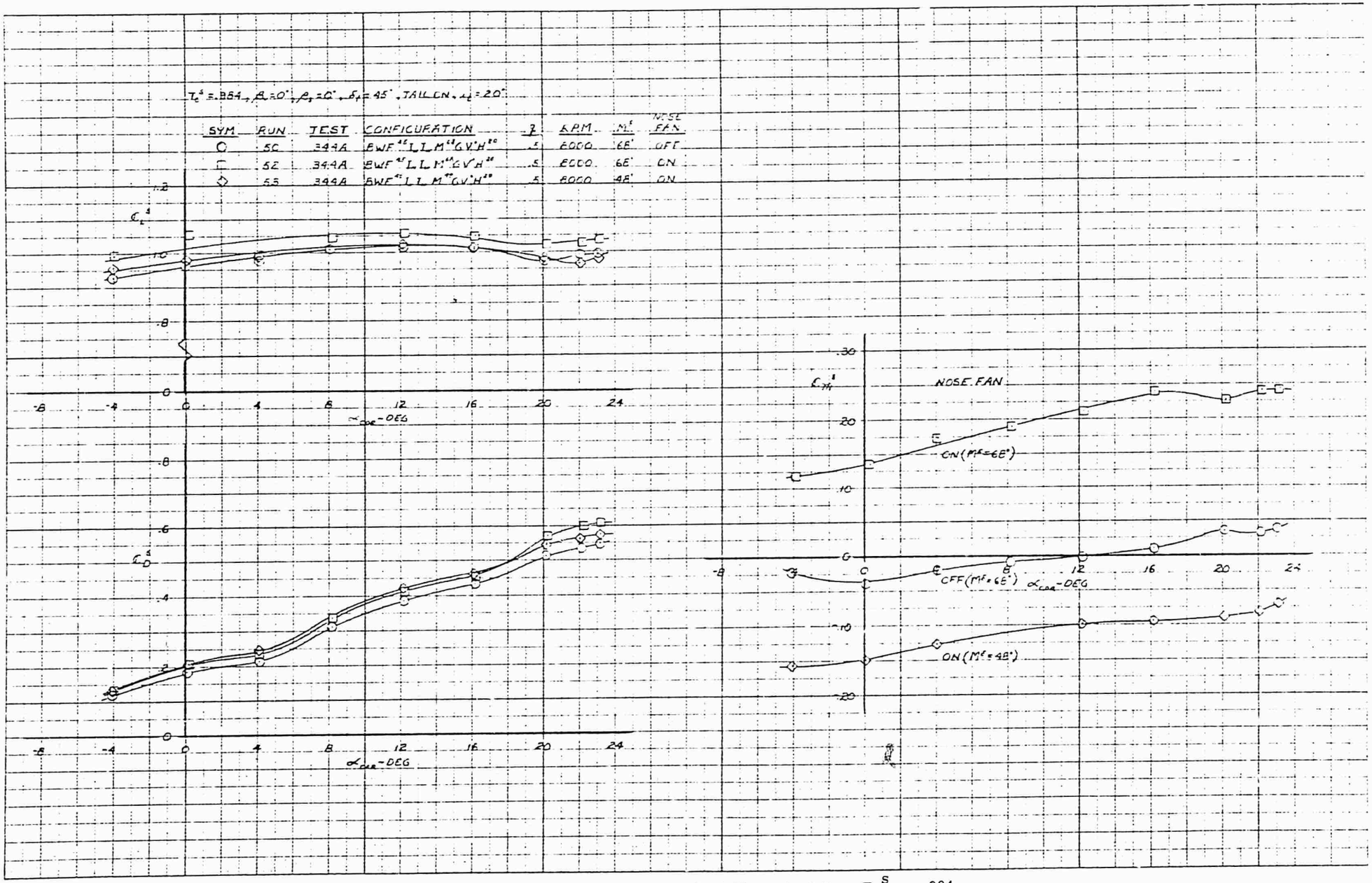

Figure 4.20 Effect of the Noae Fan on Longitudinal Characteristics, T_c^s = .984

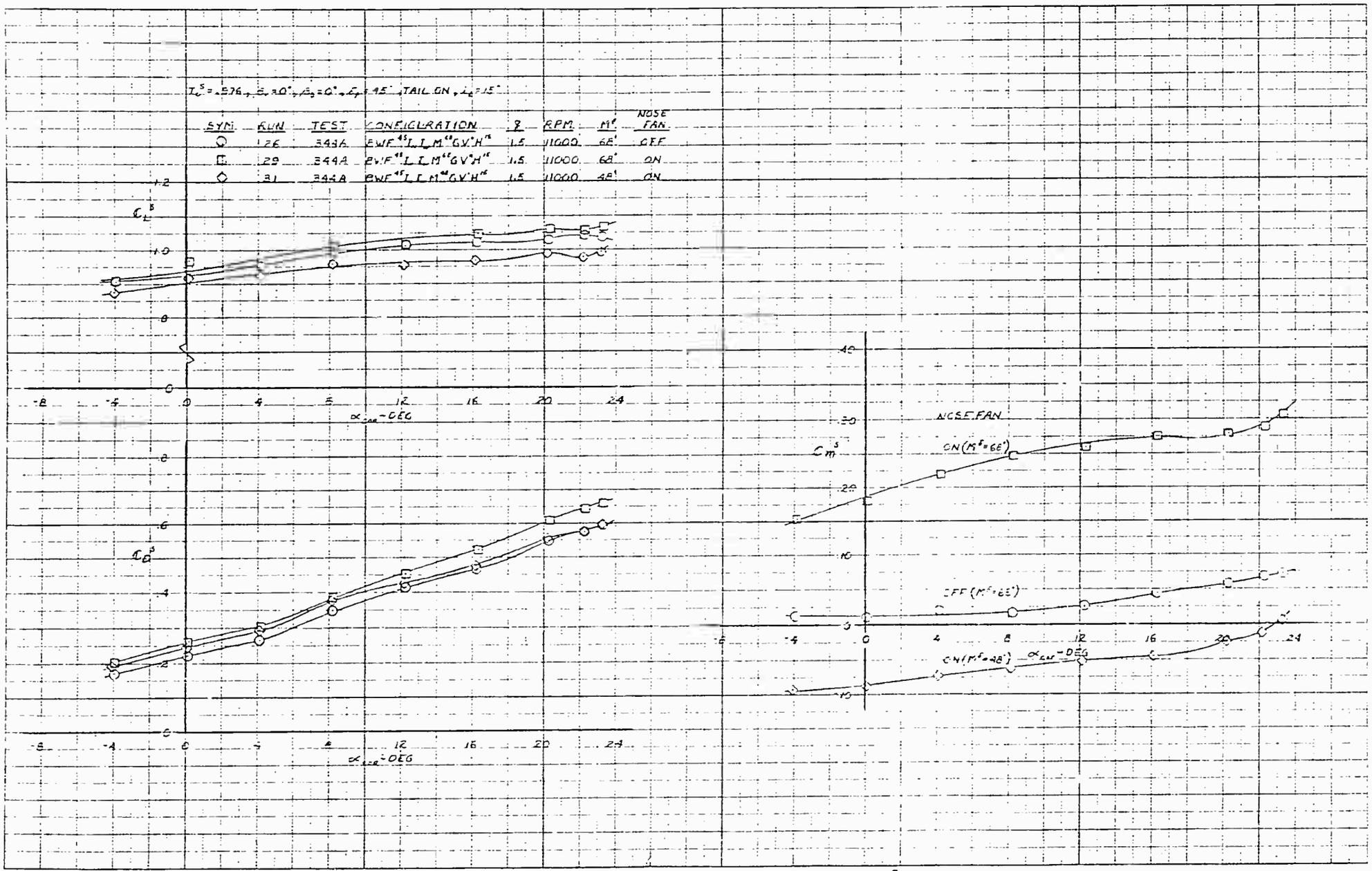

Figure 4.21 Effect of the Nose Fan on Longitudinal Characteristics, T_c^S = .976

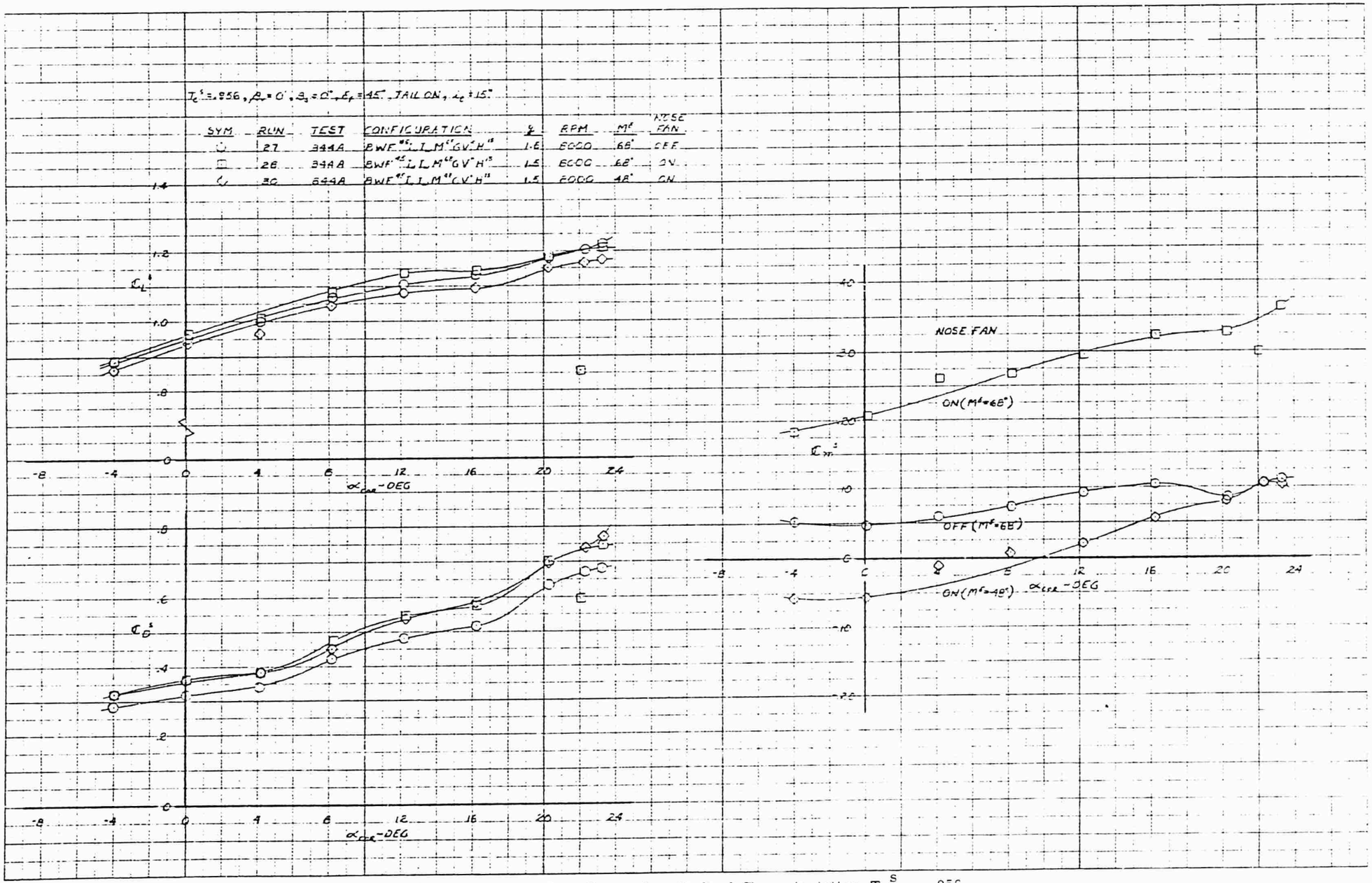

Figure 4.22 Effect of the Nose Fan on Longitudinal Characteristics, T_c^s = .956

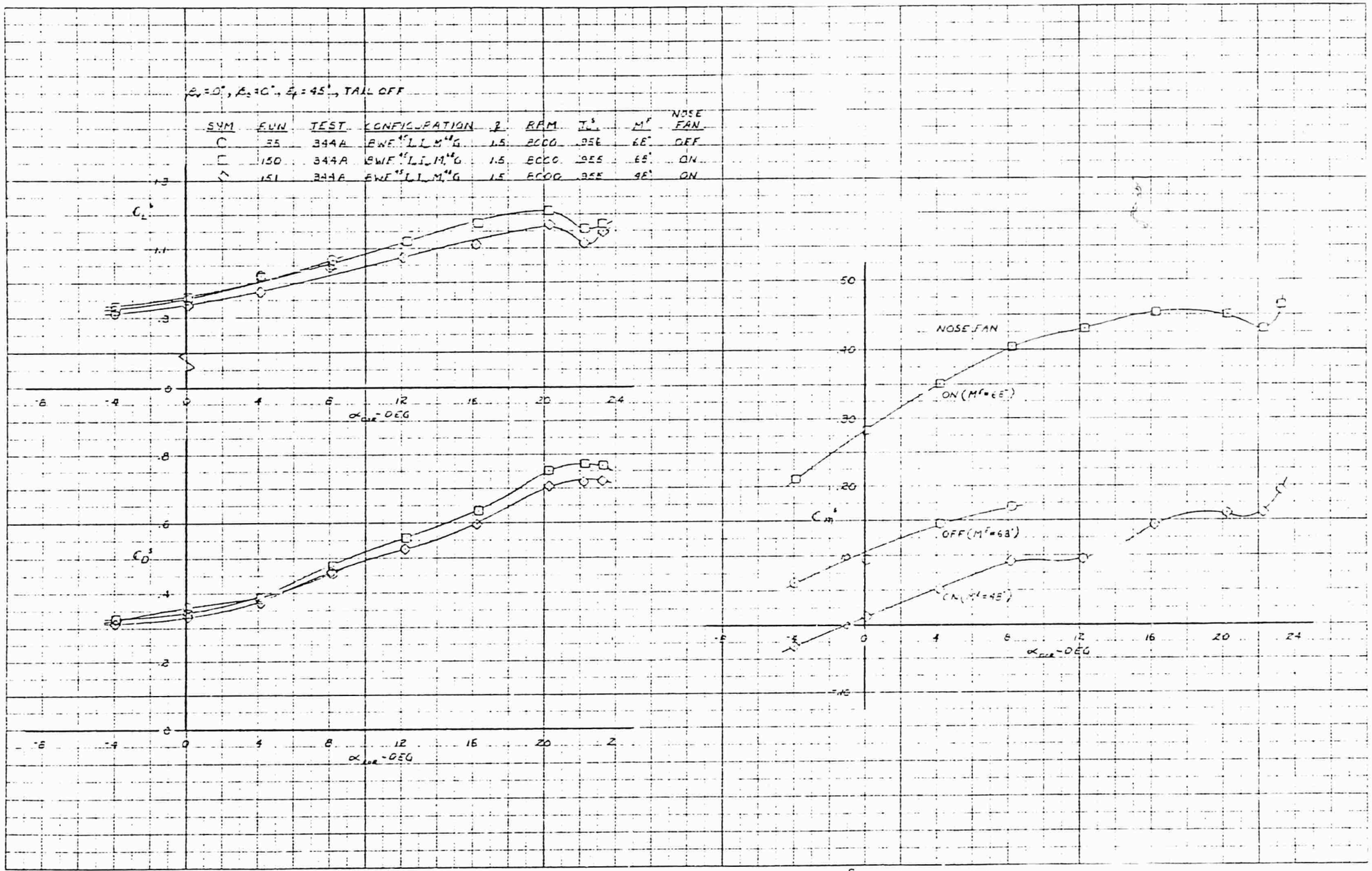

Figure 4.23 Effect of the Nose Fan on Longitudinal Characteristics, T_c^s = .955, Tail Off

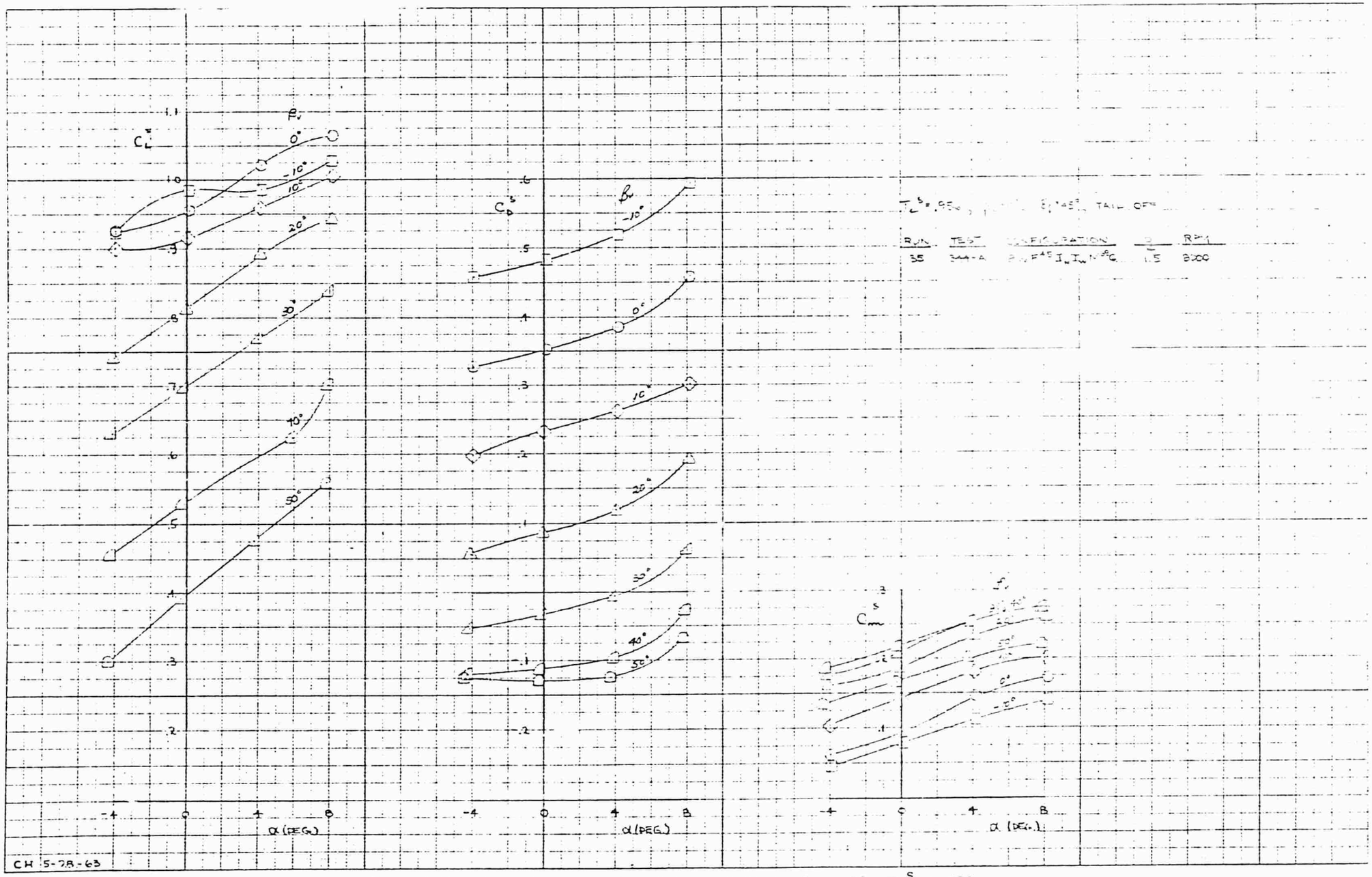

Figure 4.24 Effect of Vector Angle and Angle of Attack, $\beta_s = 0°$, $T_c^s = .956$

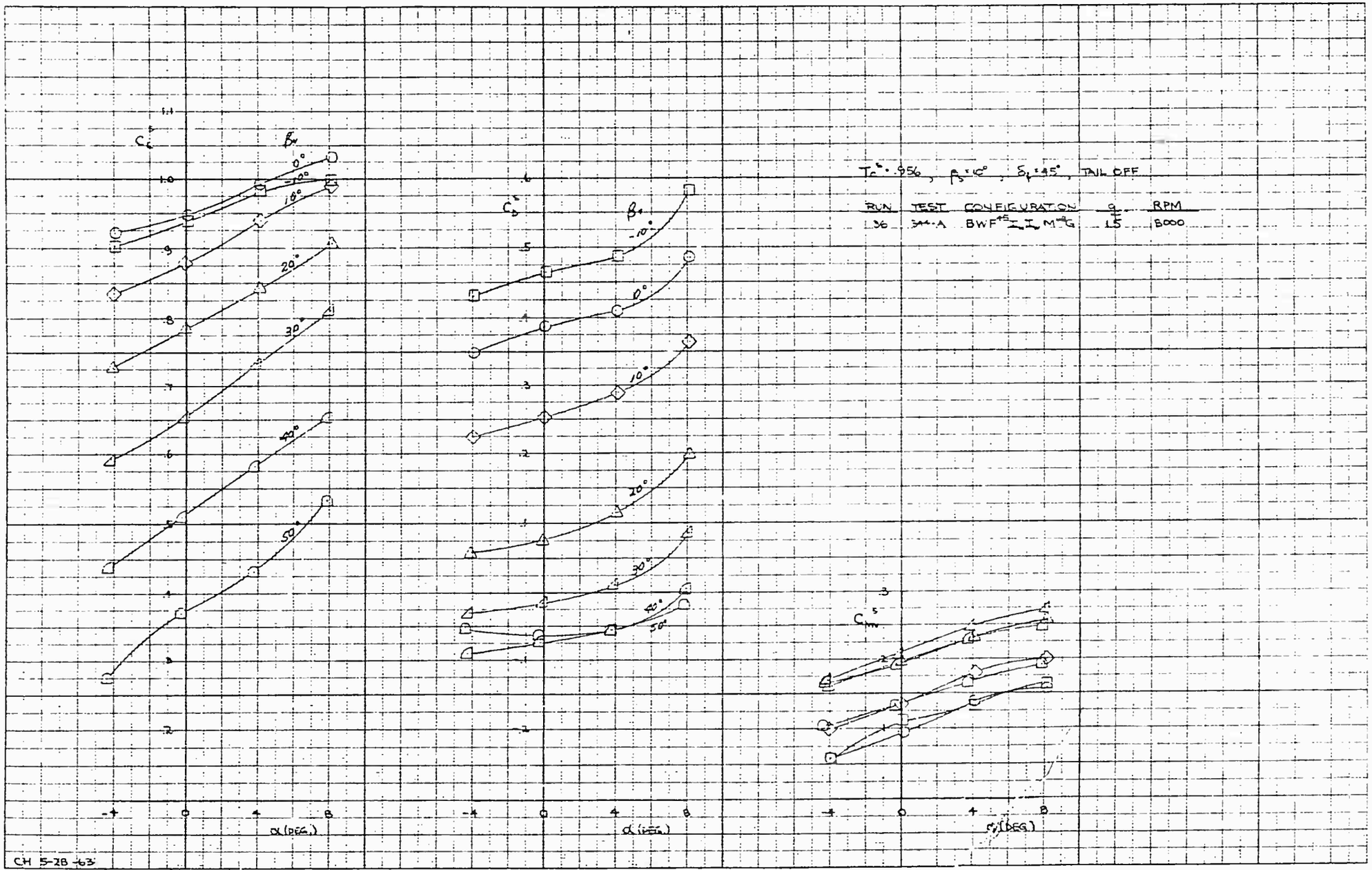

Figure 4.25 Effect of Vector Angle and Angle of Attack, β_s = 10°, T_c^s = .956

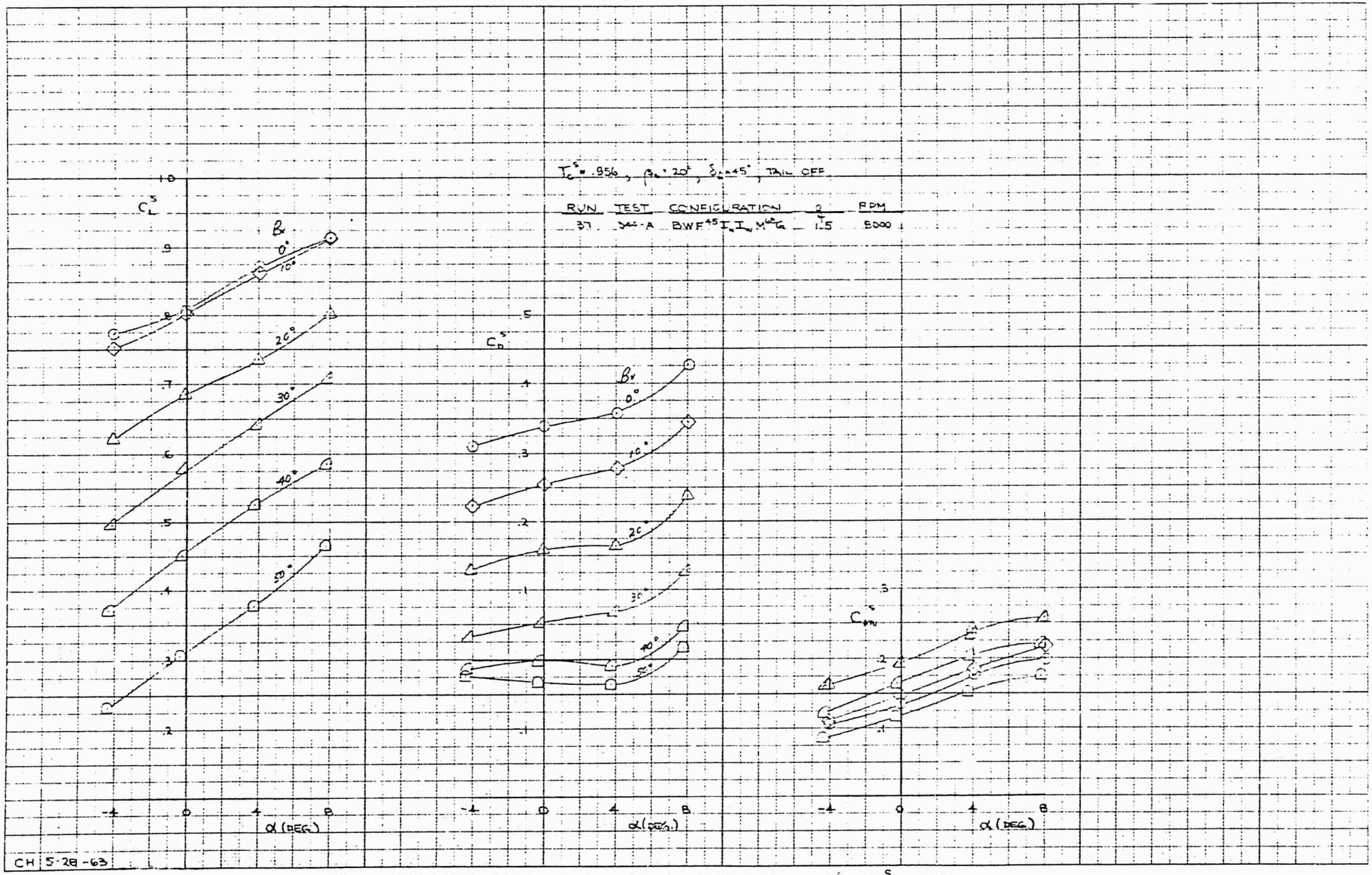

Figure 4.26 Effect of Vector Angle and Angle of Attack, β_s = 20°. T_c^s = .956

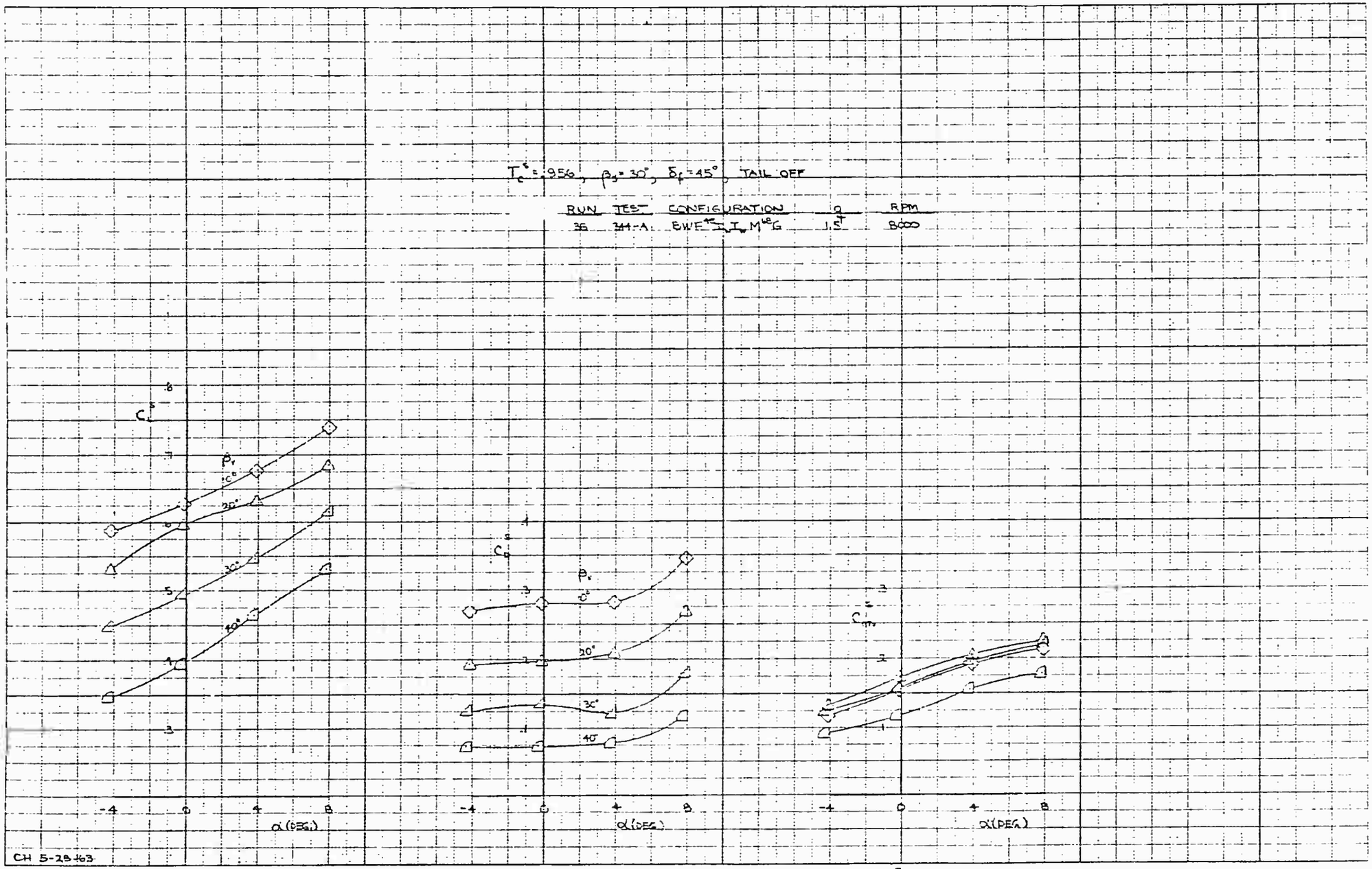

Figure 4.27 Effect of Vector Angle and Angle of Attack, β_s = 30°, T_c^s .956

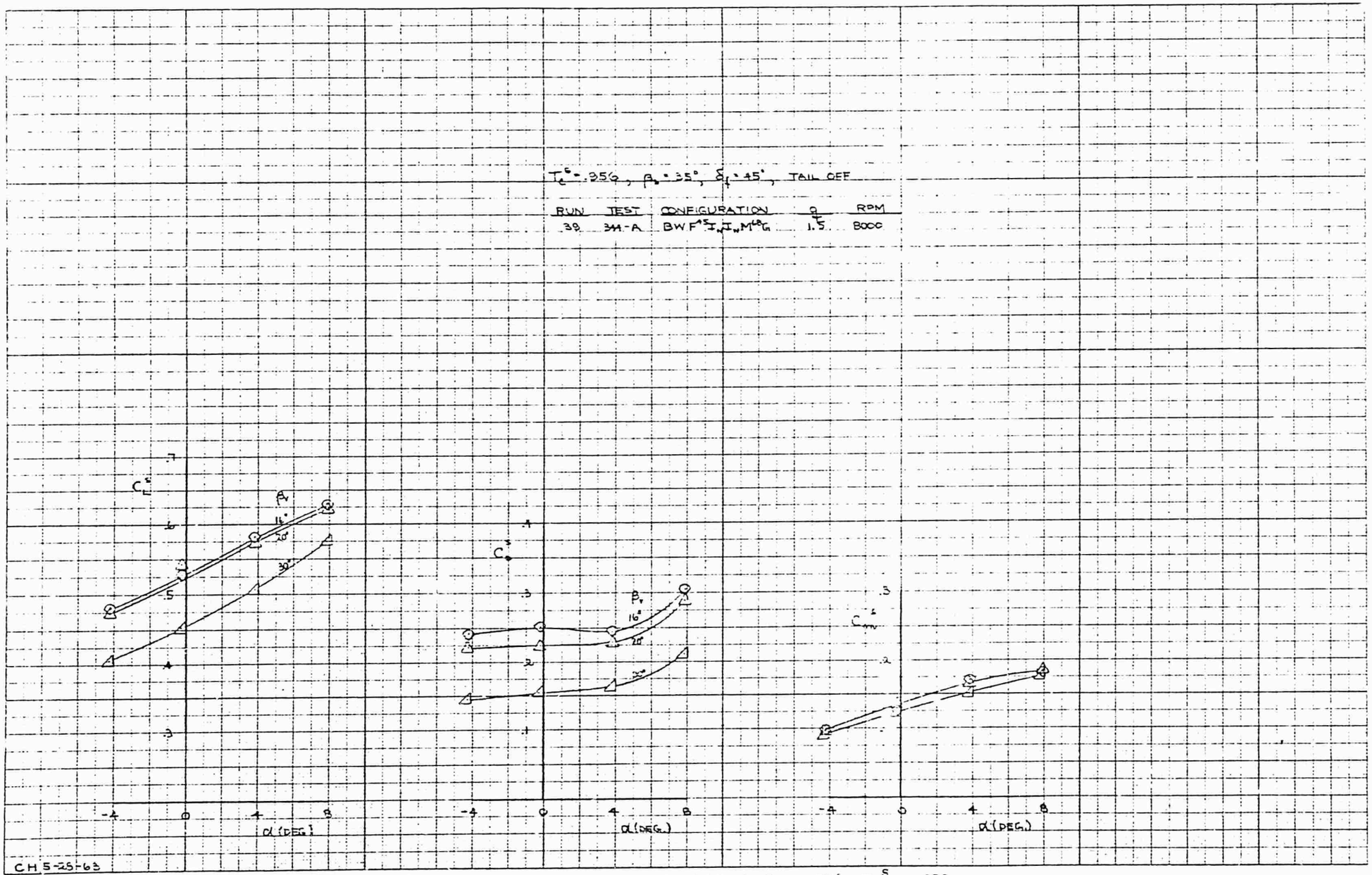

Figure 4.28 Effect of Vector Angle and Angle of Attack, β_s = 35°, T_c^s = .956

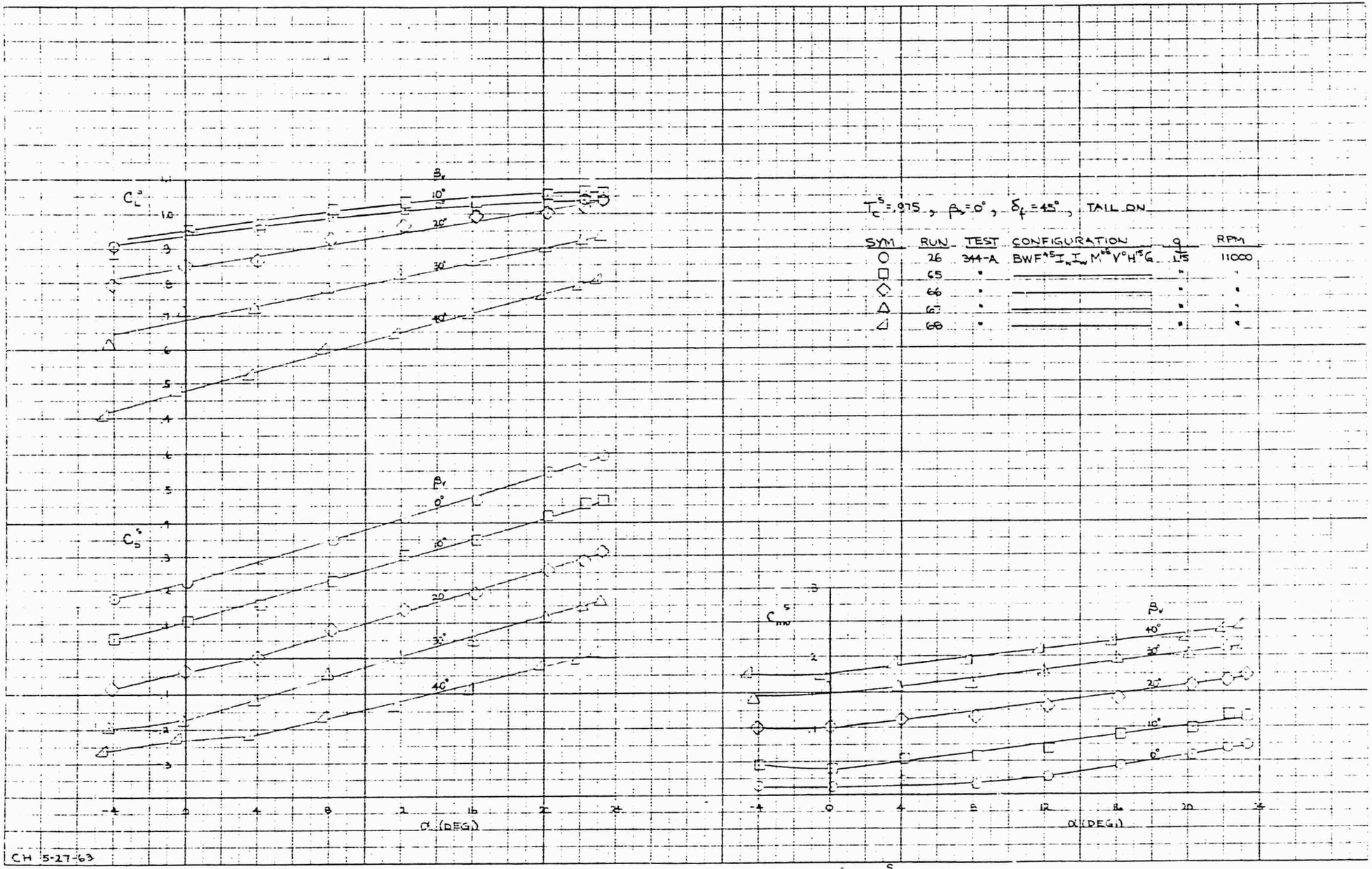

Figure 4.29 Effect of Vector Angle and Angle of Attack, β_s = 0°, T_c^s .975

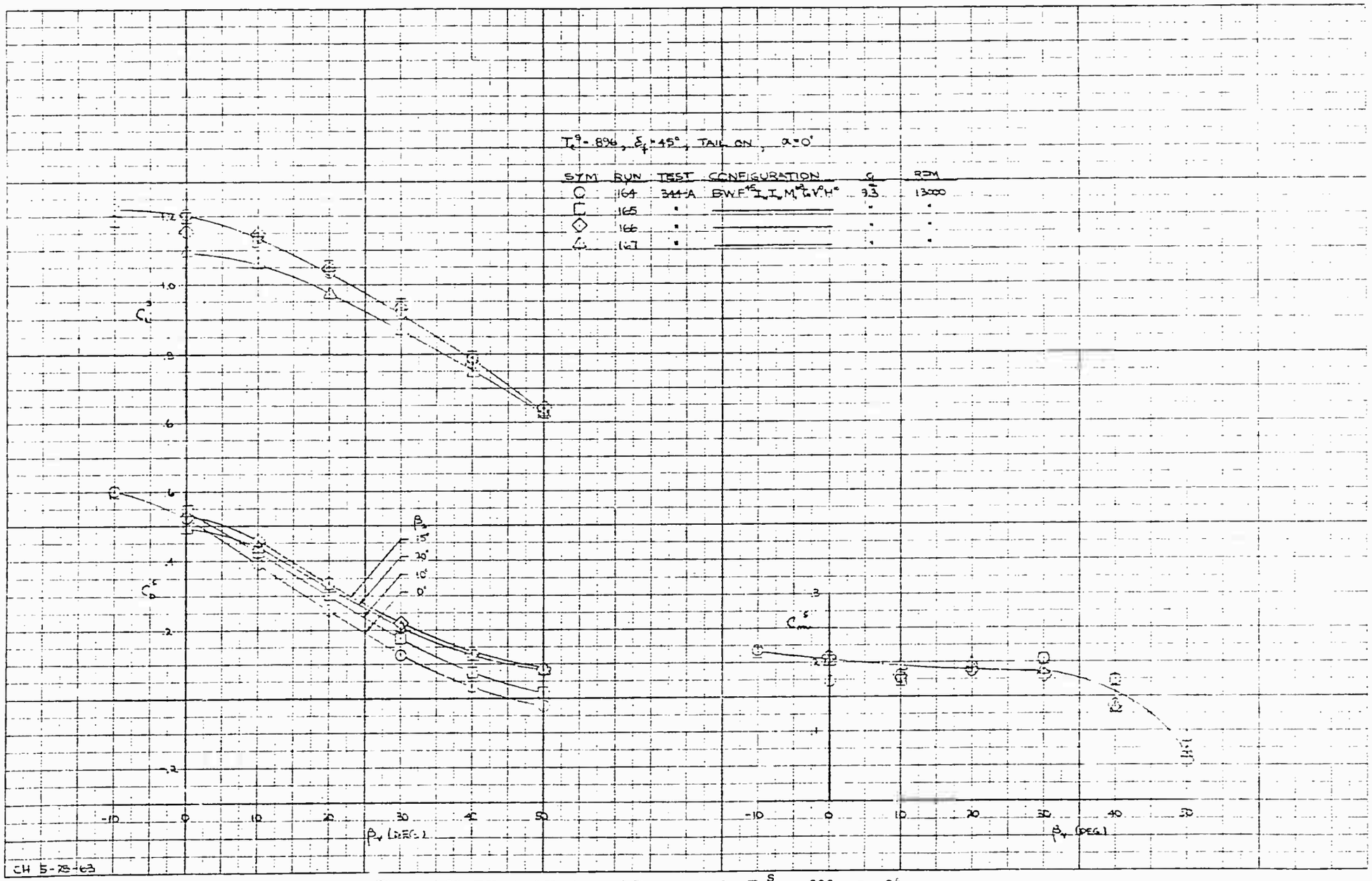

Figure 4.30 Effect of Vector and Stagger Angle, T_c^s = .896, = 0°

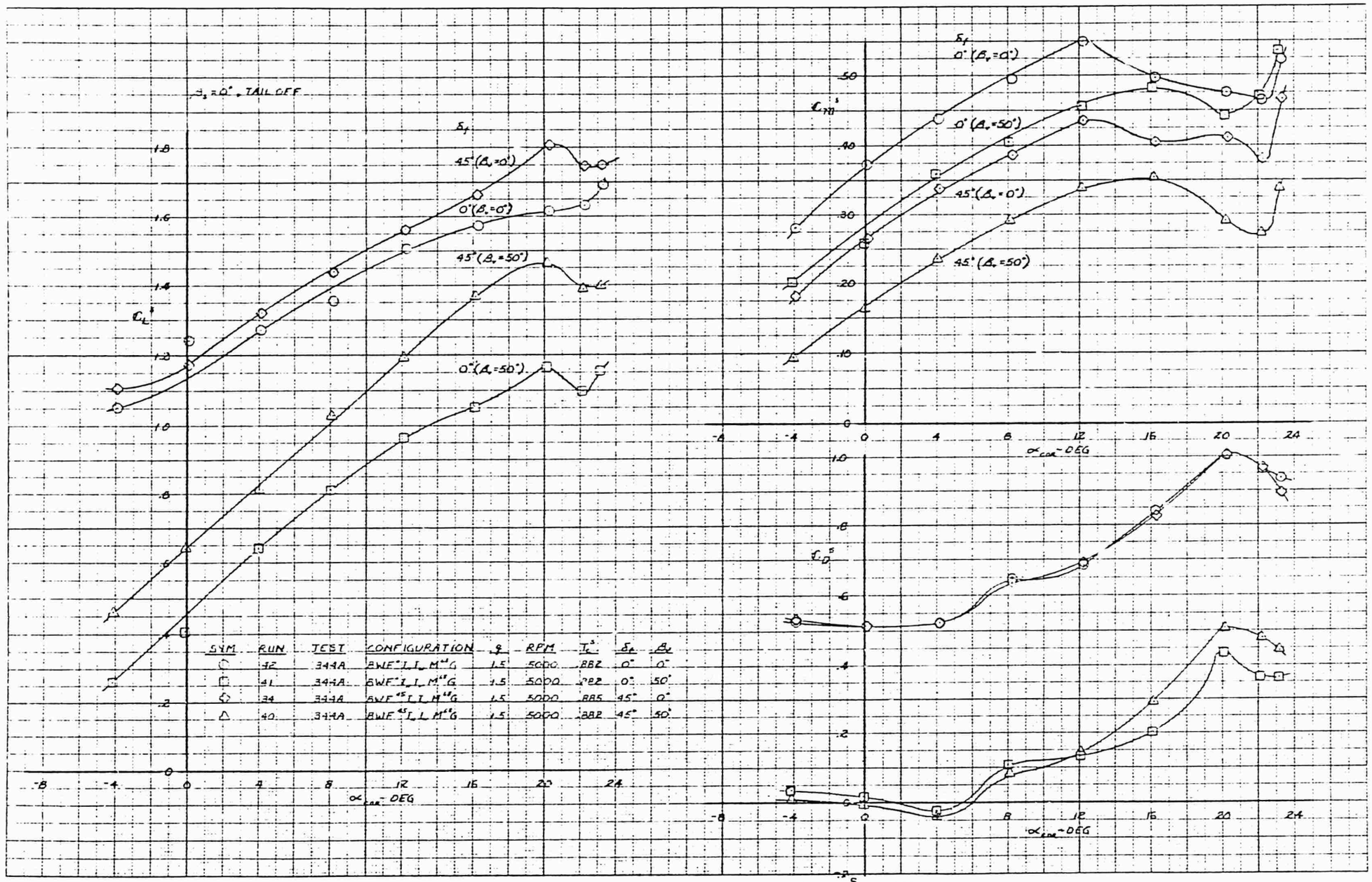

Figure 4.31 Variation of Flap Effectiveness with Vector Angle, T_c^s = .882

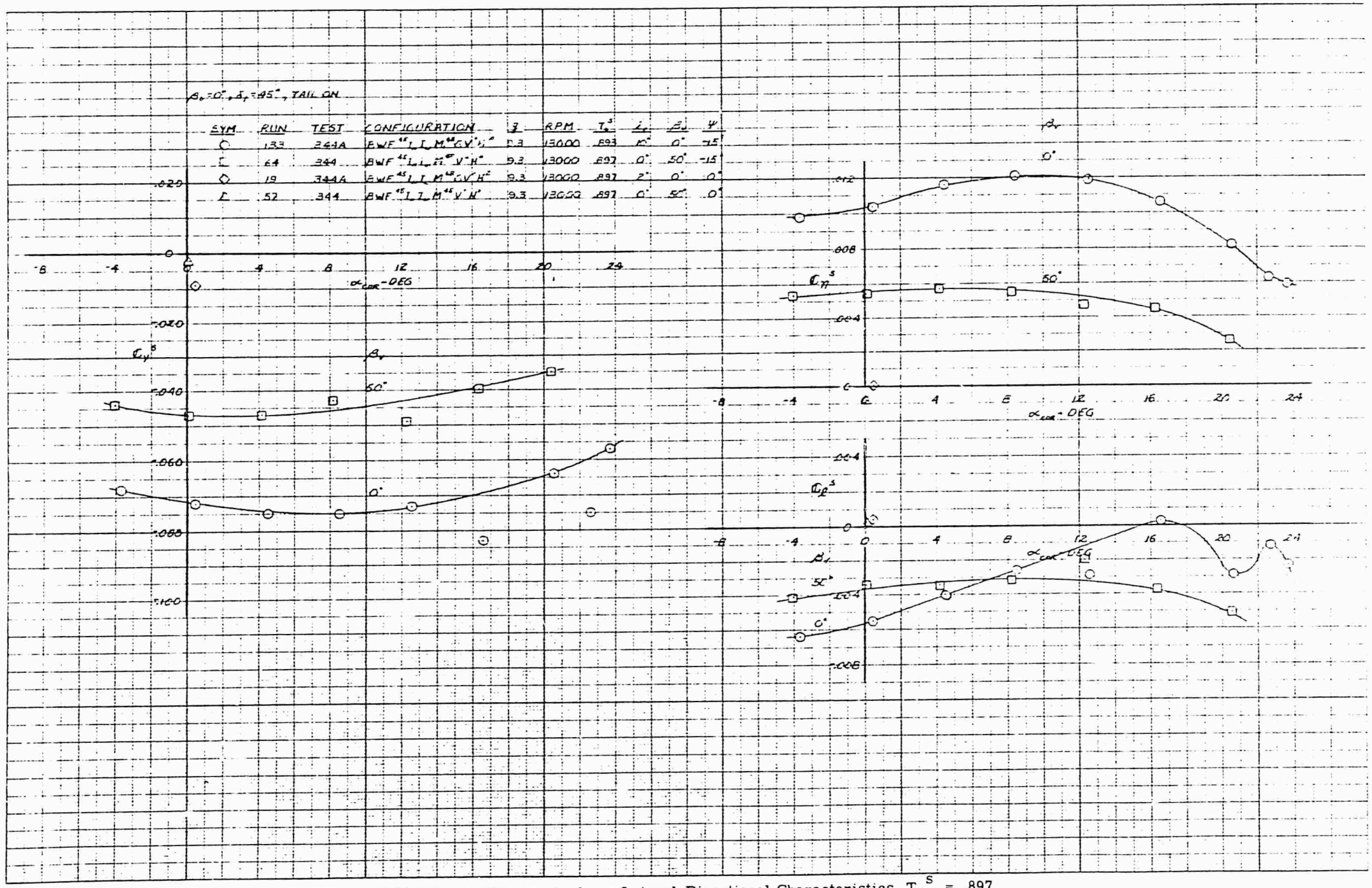

Figure 4.32 Effect of Vector Angle on Lateral-Directional Characteristics, T_c^s = .897

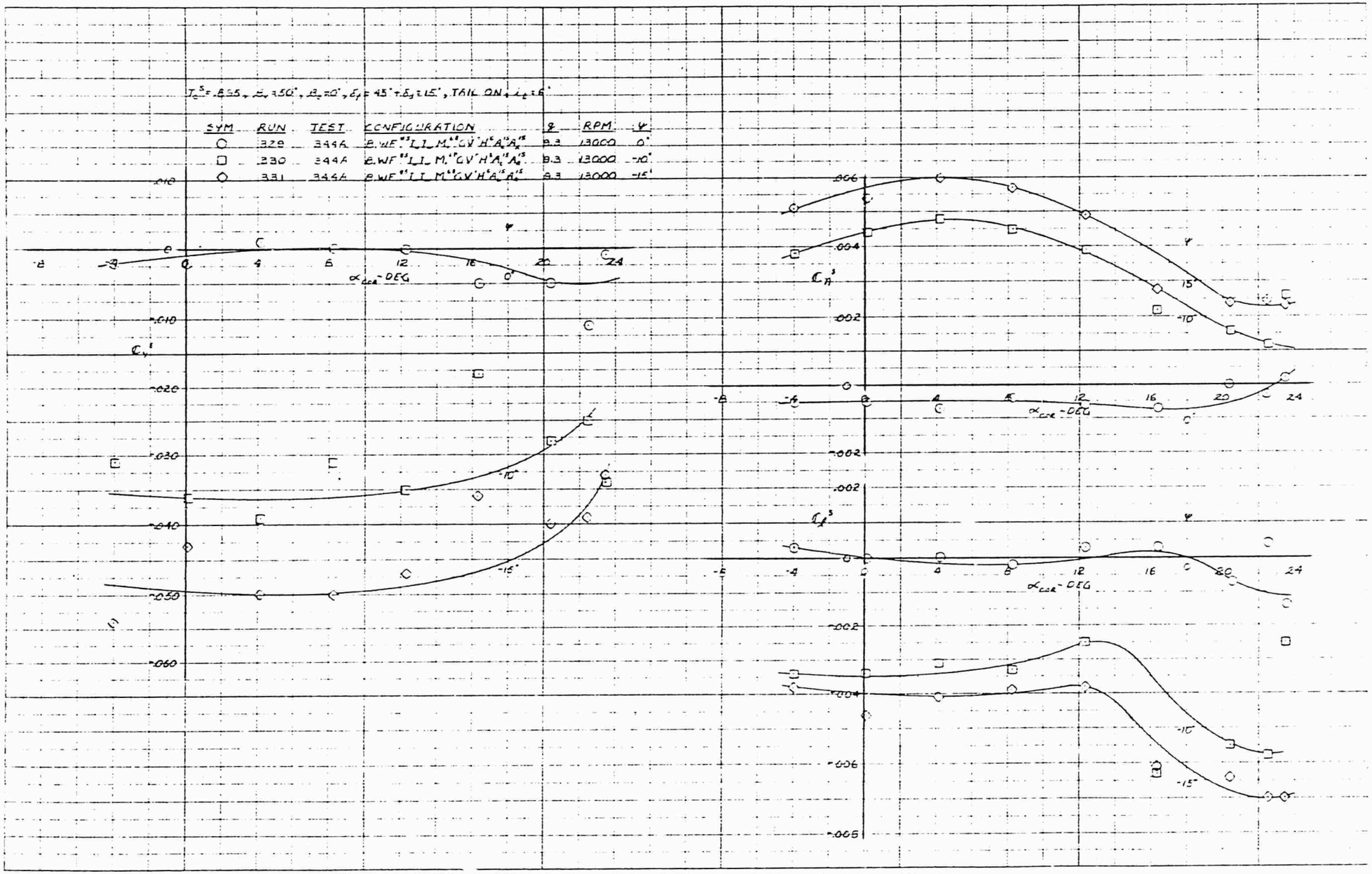

Figure 4.33 Effect of Yaw Angle on Lateral-Directional Characteristics, Ailerons Drooped 15°. T_c^S = .895

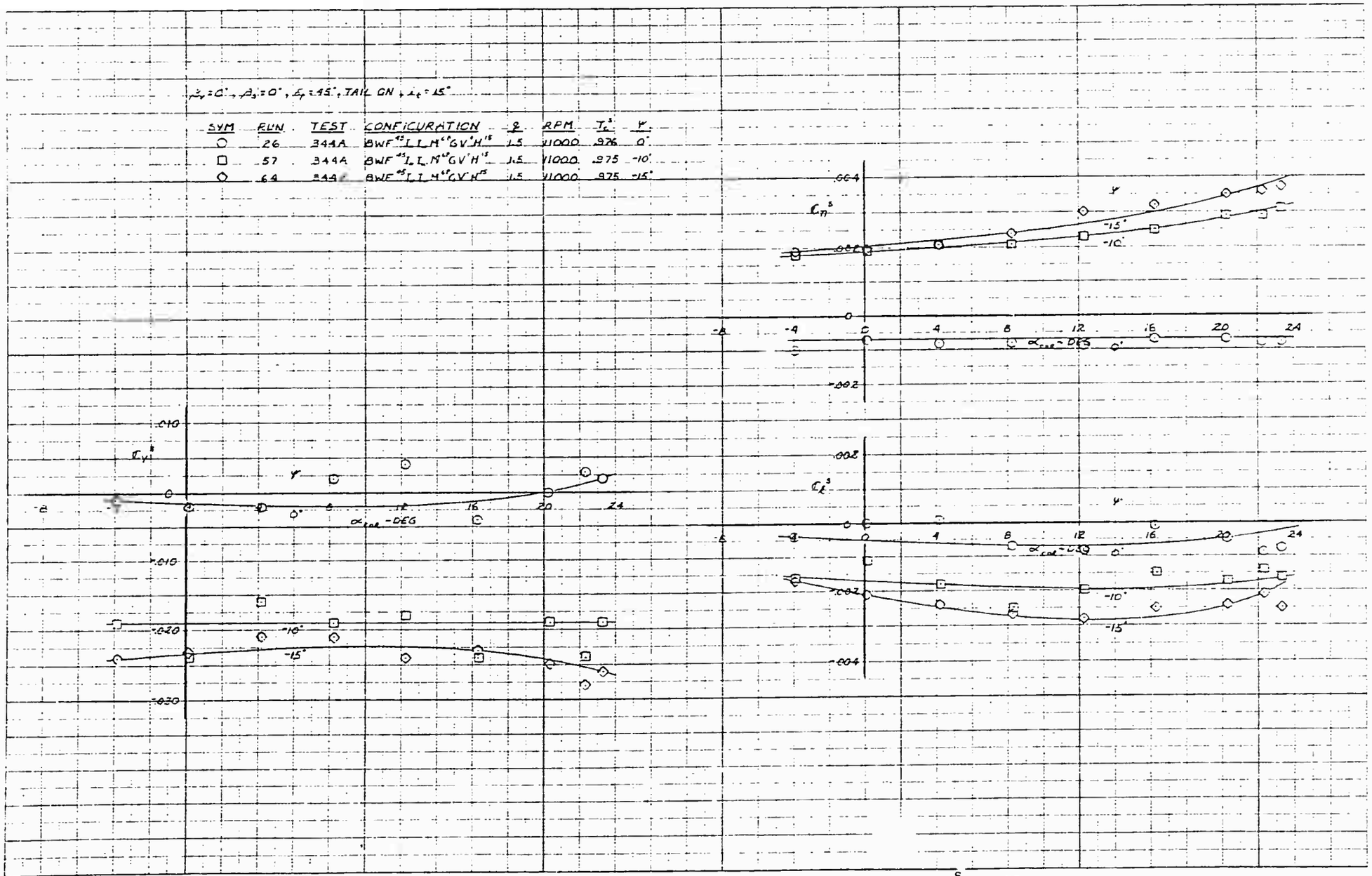

Figure 4.34 Effect of Yaw Angle on Lateral-Directional Characteristics, T_c^s = .975

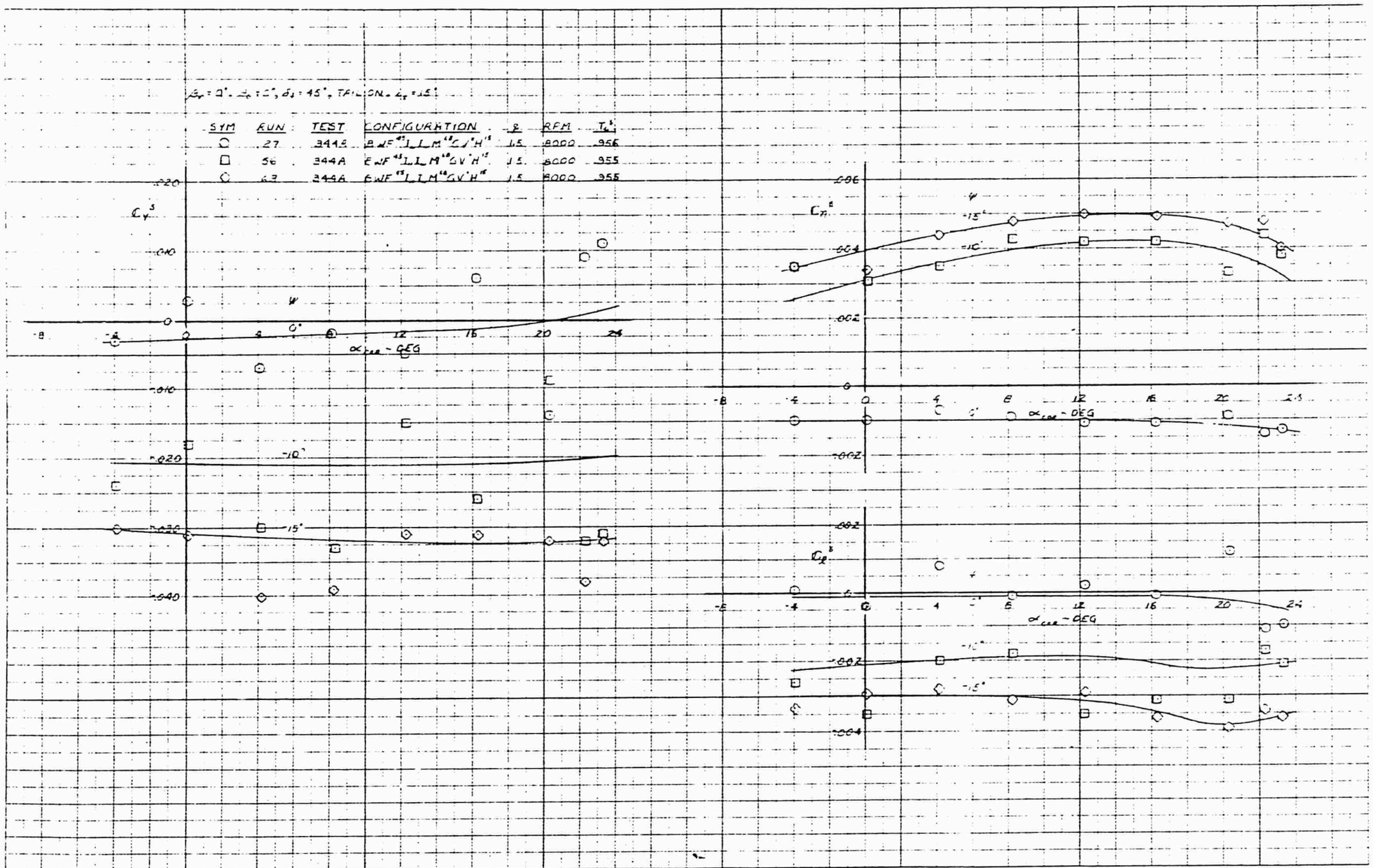

Figure 4.35 Effect of Yaw Angle on Lateral-Directional Characteristics, T_C^S = .955

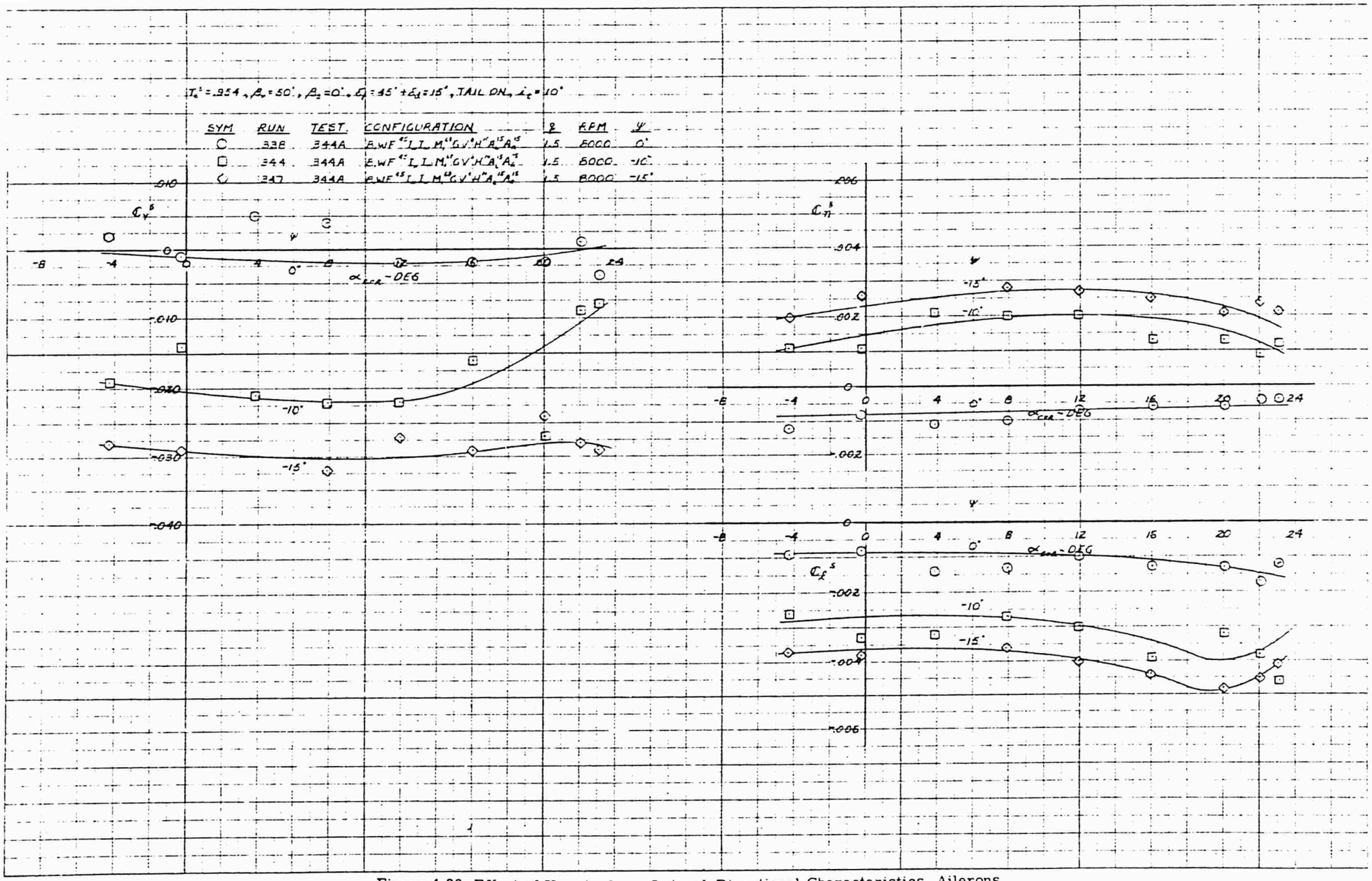

Figure 4.36 Effect of Yaw Angle on Lateral-Directional Characteristics, Ailerons Drooped 15°, T_c^s = .954

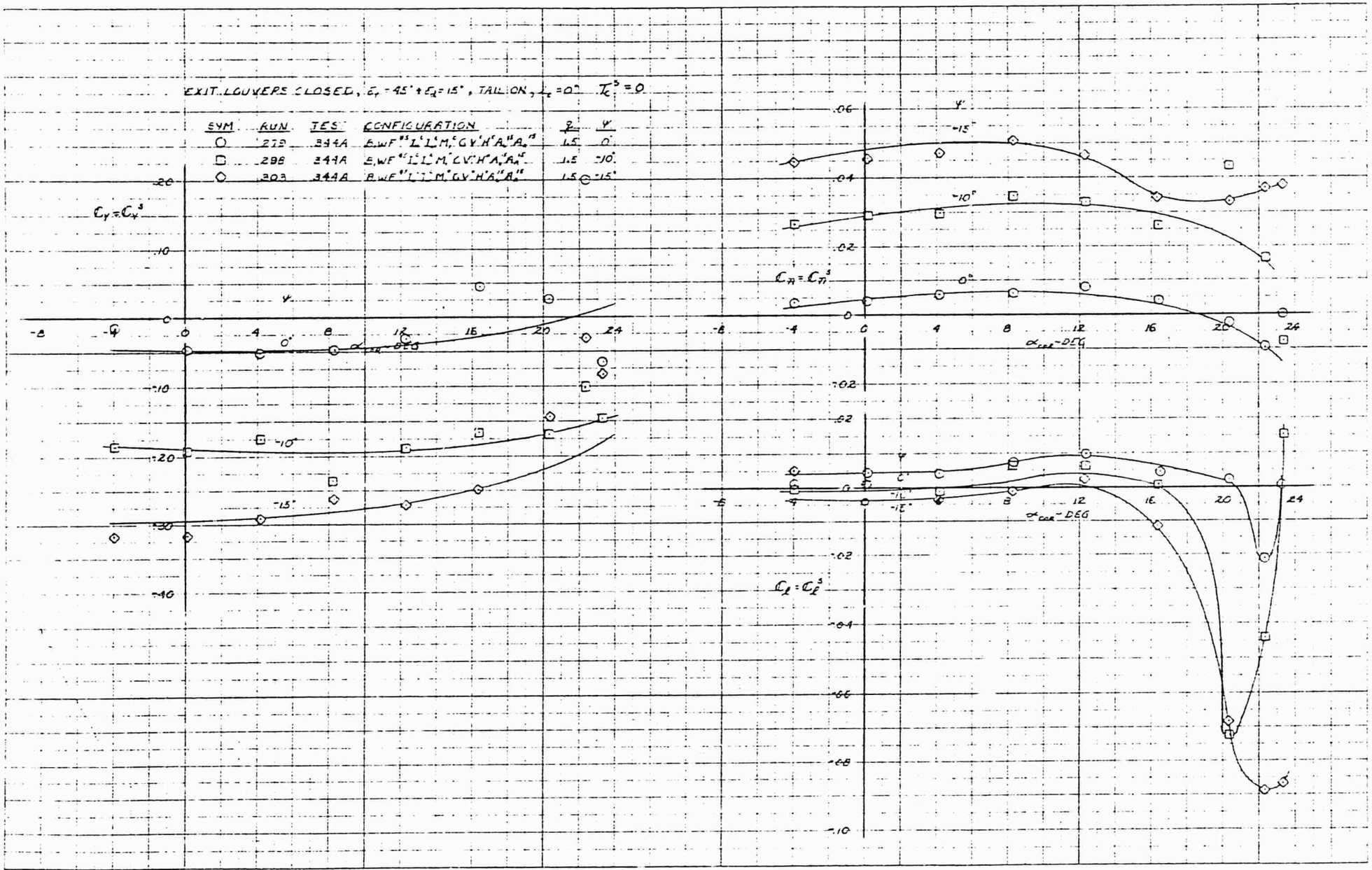

Figure 4.37 Effect of Yaw Angle - Power Off, Ailerons Drooped 15

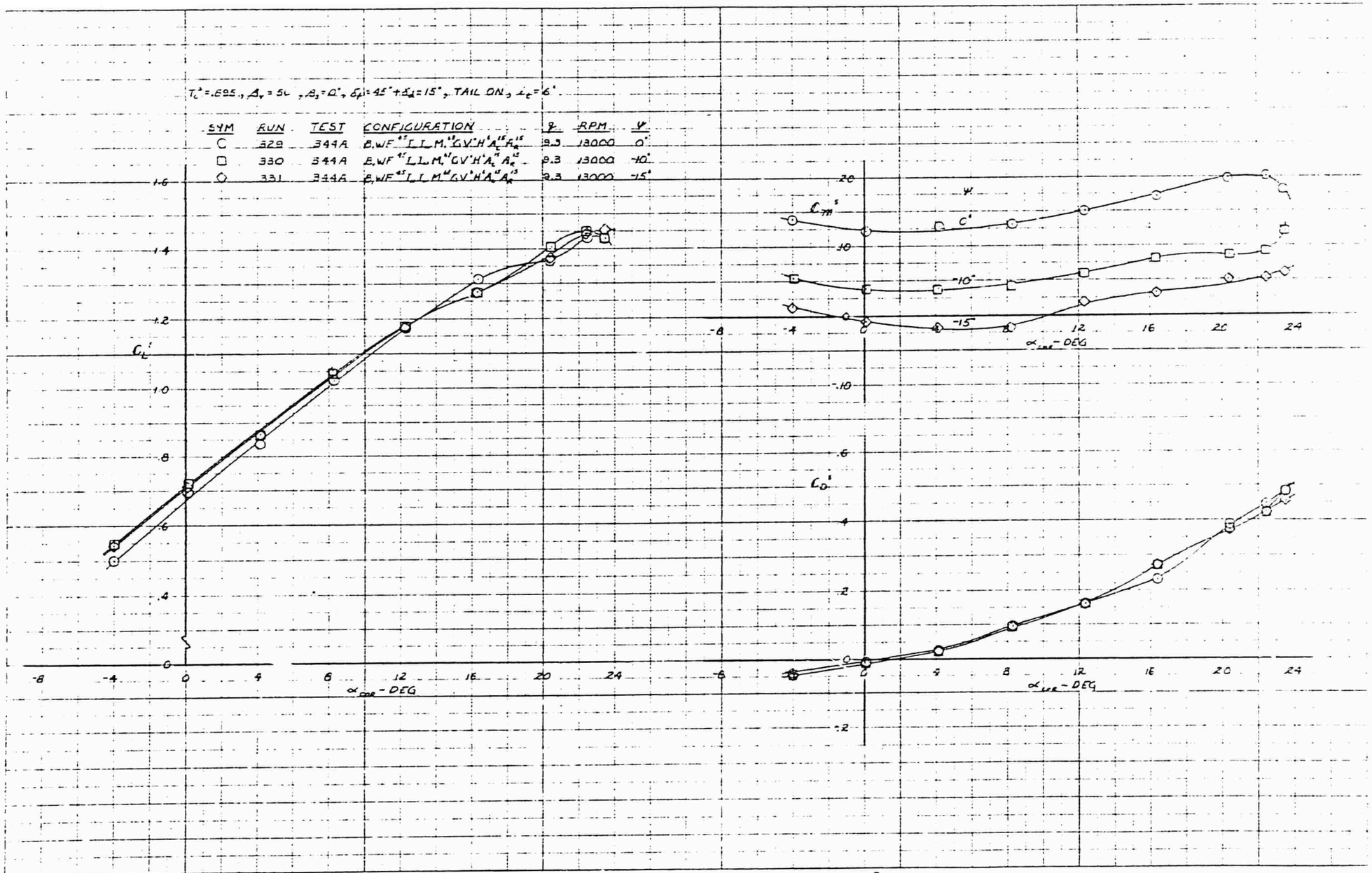

Figure 4.38 Effect of Yaw Angle on Longitudinal Characteristics. T_c^s = .895

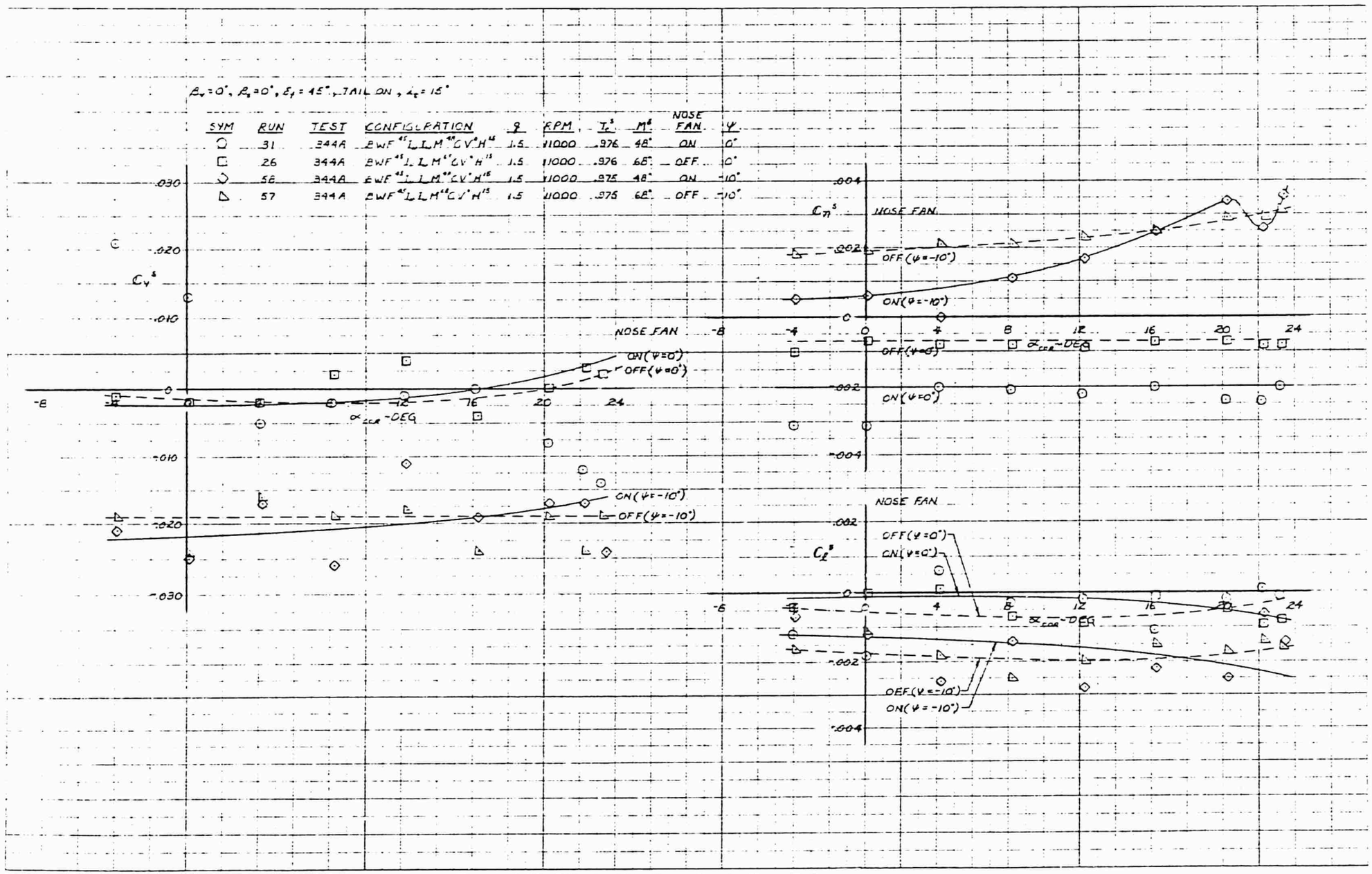

Figure 4.39 Effect of the Nose Fan in Yaw, T_c^s = .976

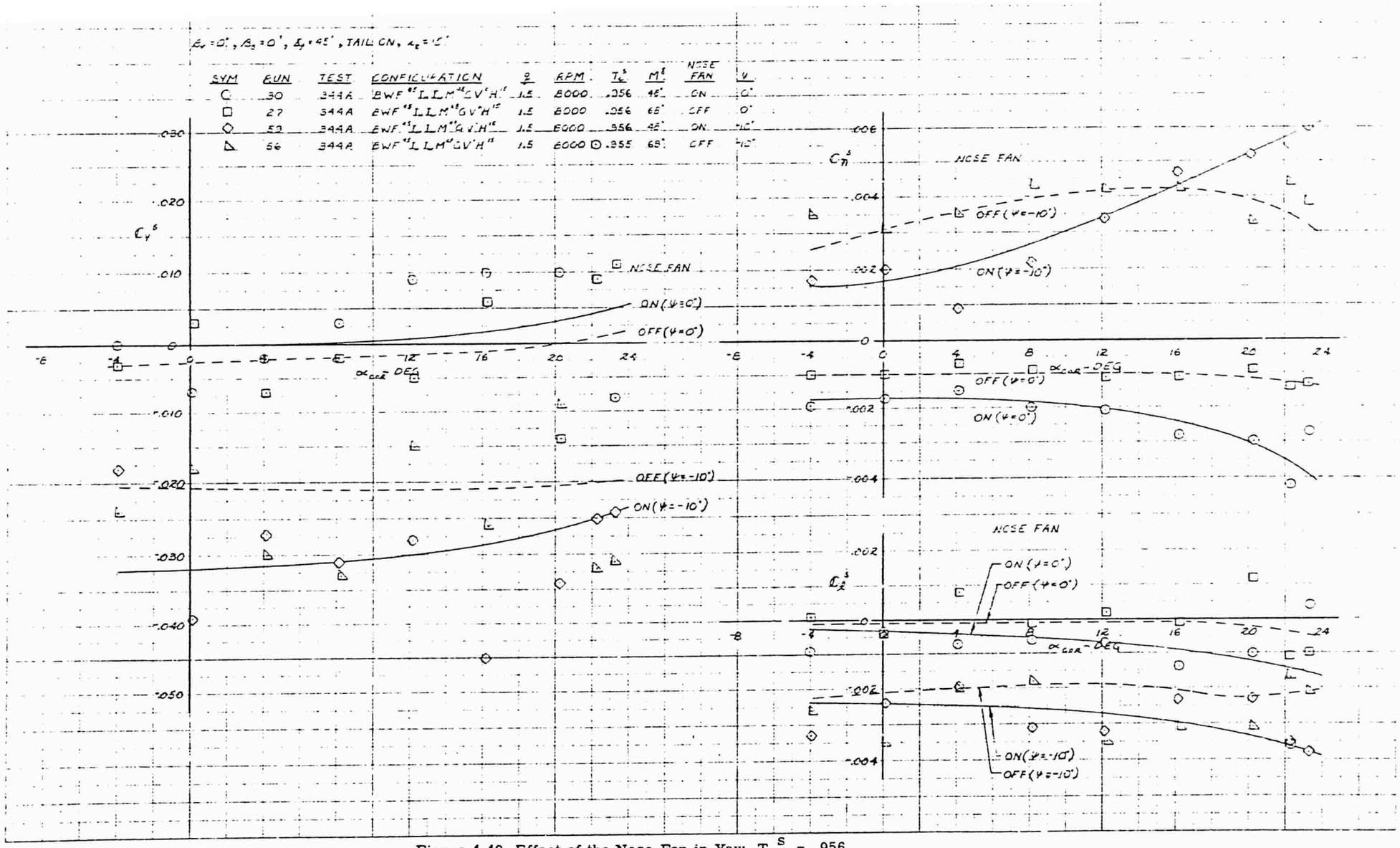

Figure 4.40 Effect of the Nose Fan in Yaw, T_c^s = .956

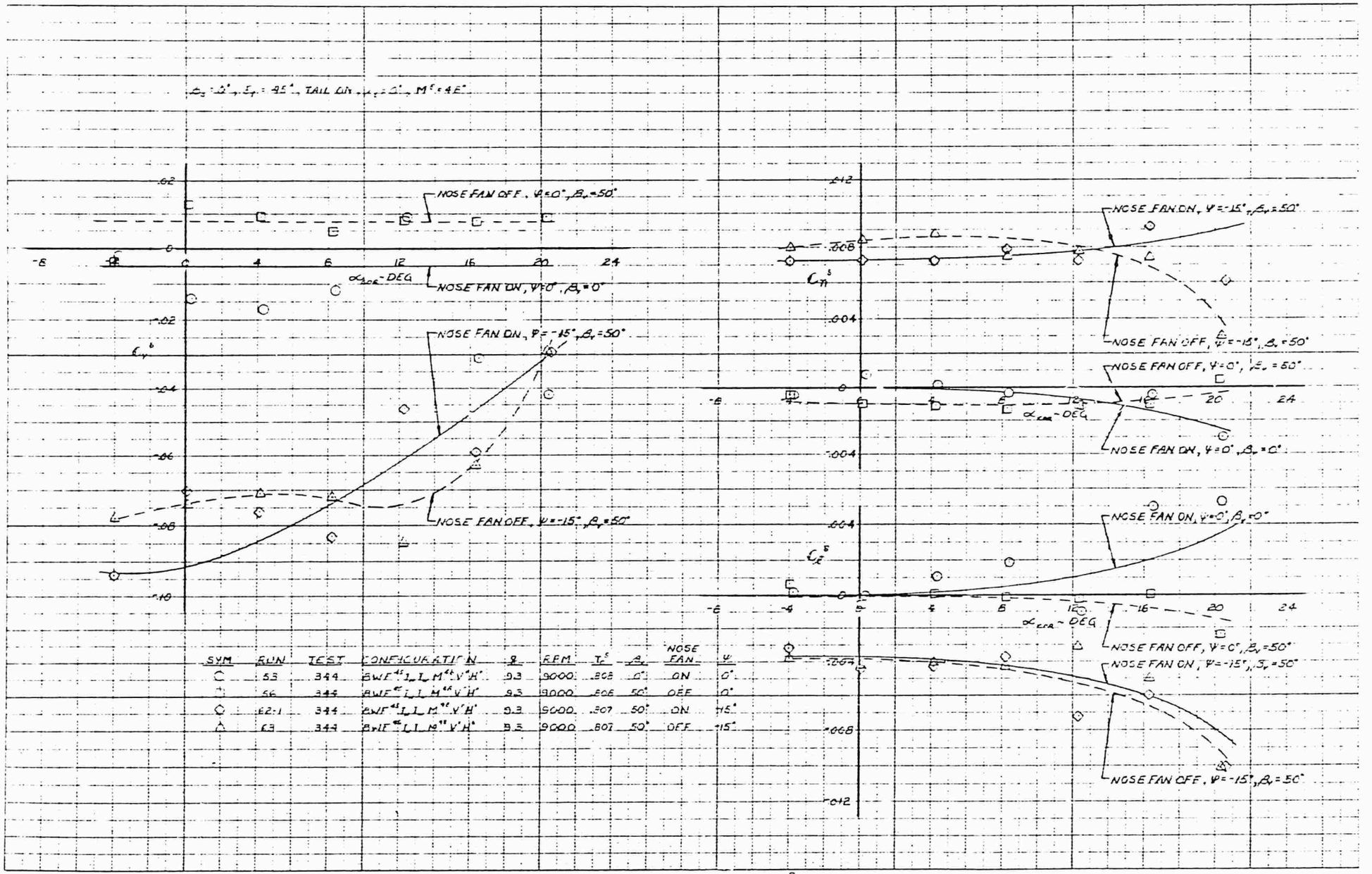

Figure 4.41 Effect of the Nose Fan in Yaw, T_c^s = .808

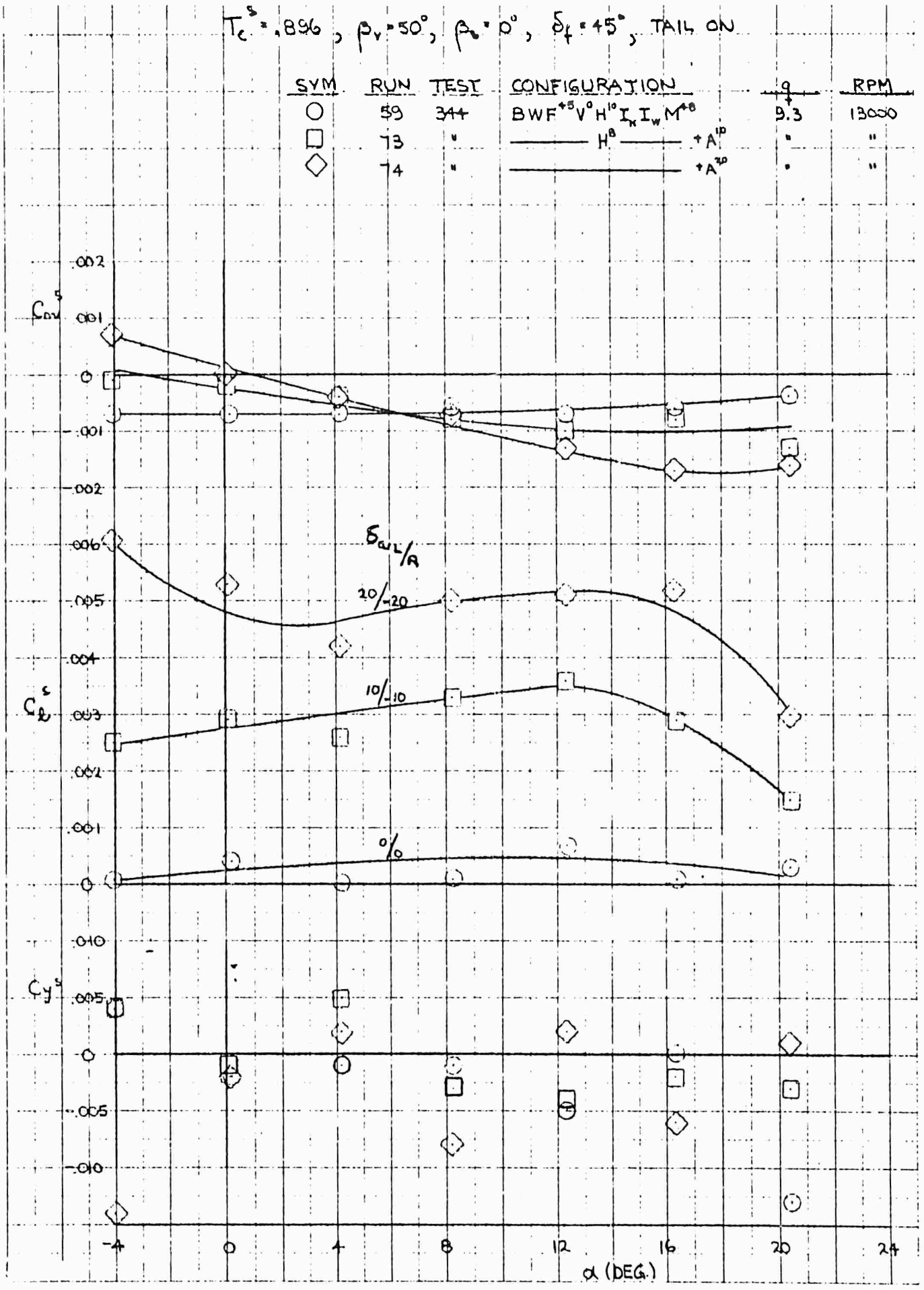

Figure 4.42 Effect of Aileron Deflection, T_c^s = .896

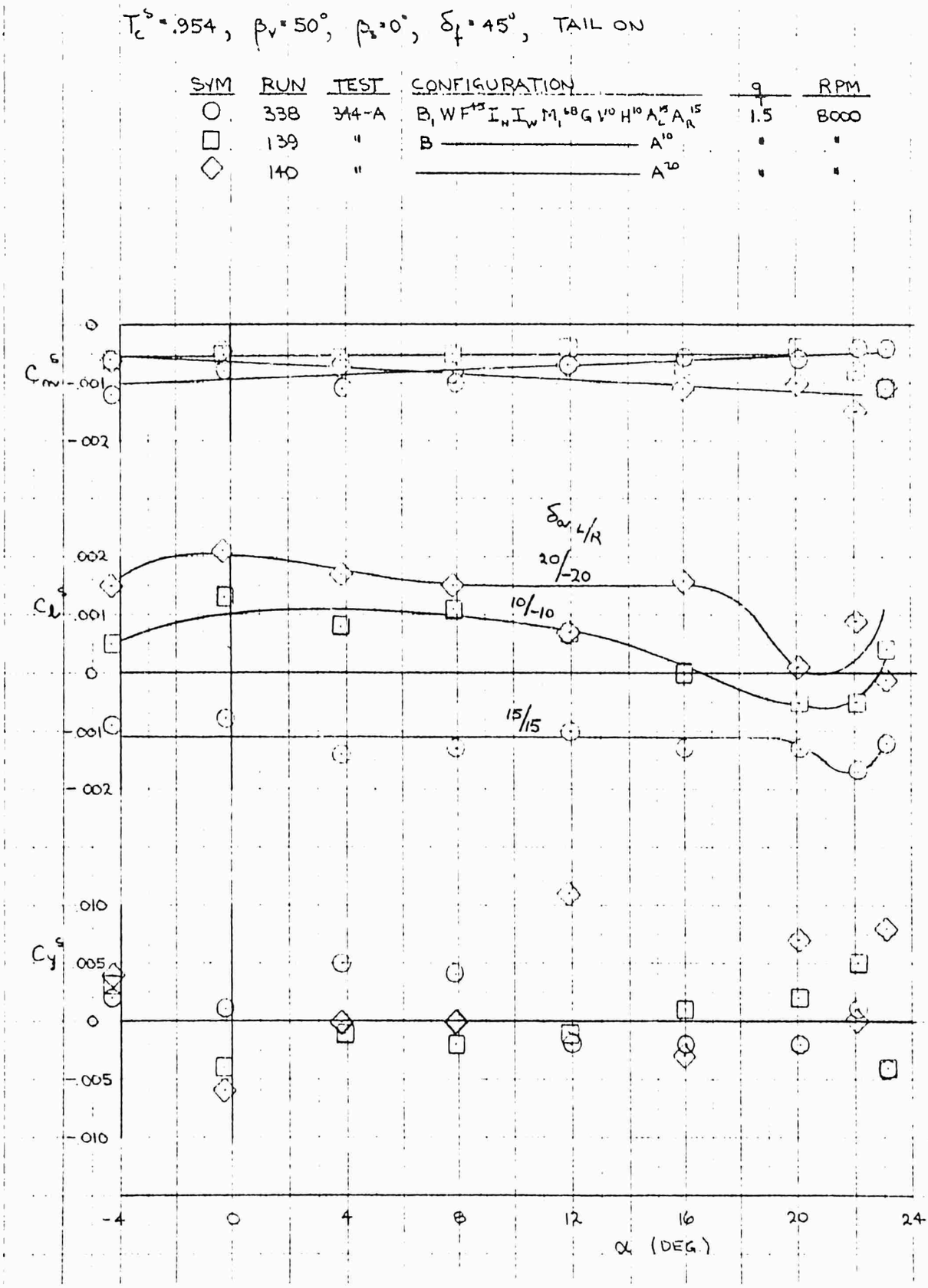

Figure 4.43 Effect of Aileron Deflection, T_c^S = .954

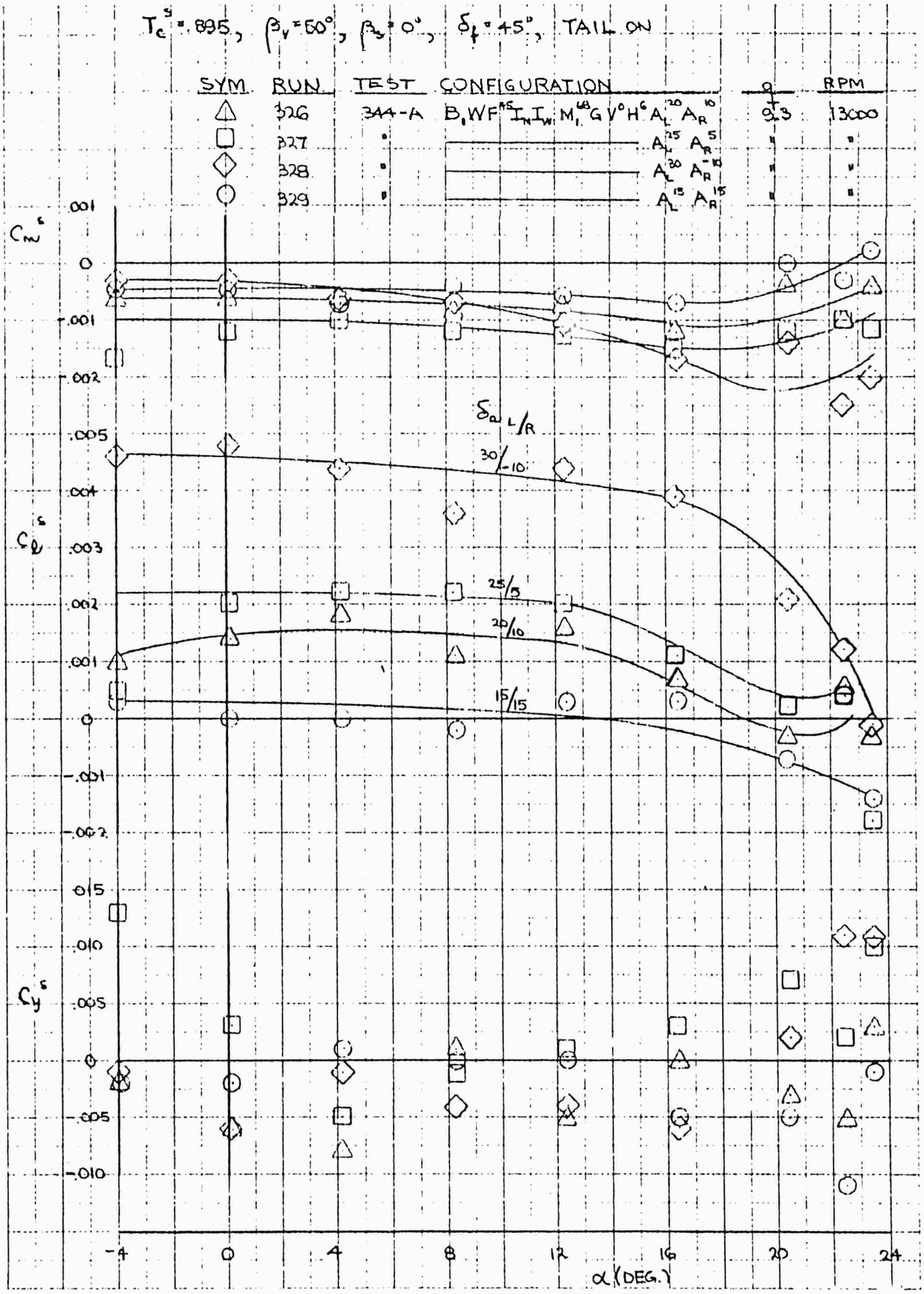

Figure 4.44 Effect of Aileron Deflection from 15° Droop Position, T_c^s = .895

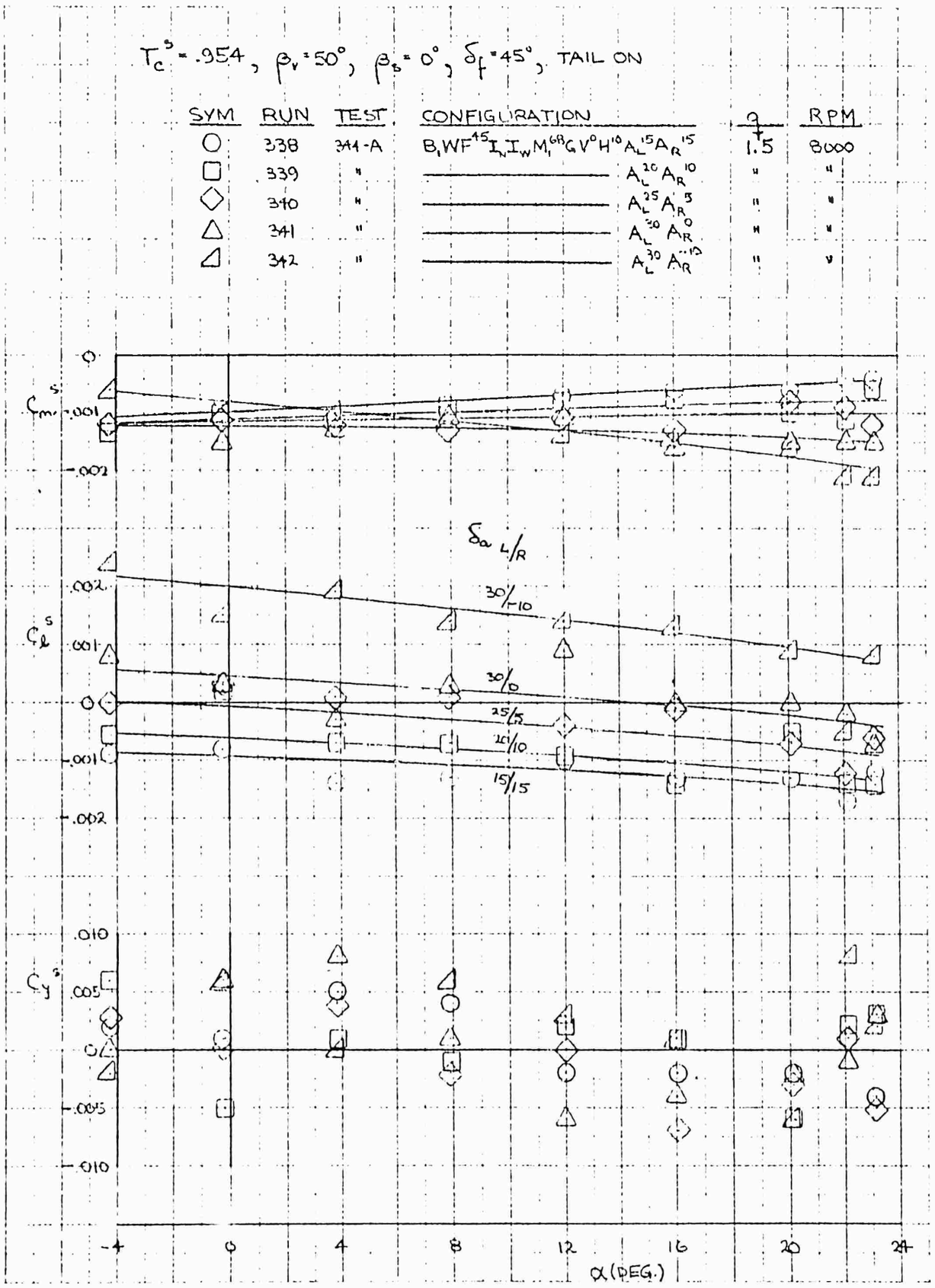

Figure 4.45 Effect of Aileron Deflection from 15° Droop Position, $T_c^s = .954$

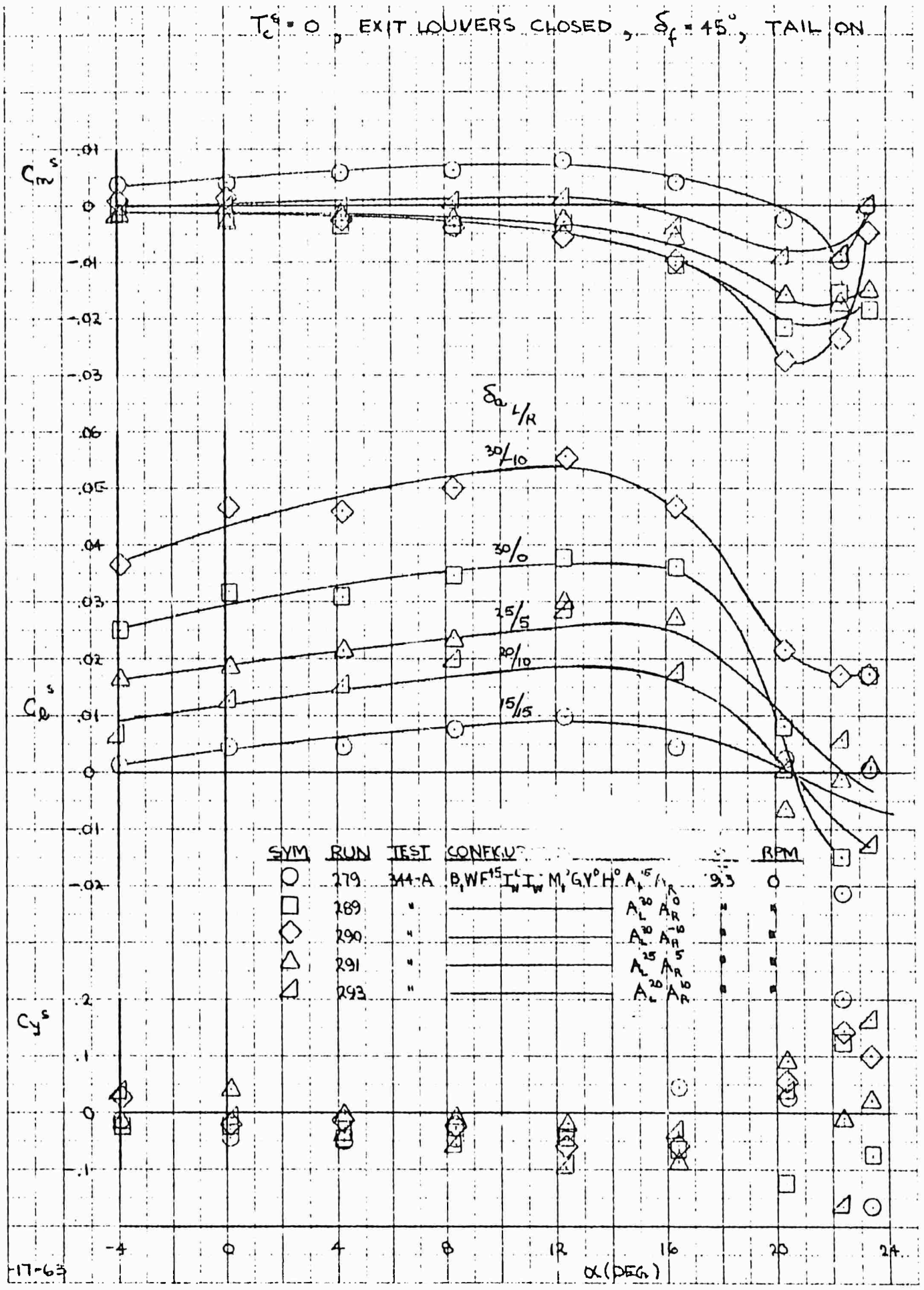

Figure 4.46 Effect of Aileron Deflection from 15° Droop Position, $T_c^s = 0$, $\delta_f = 45°$

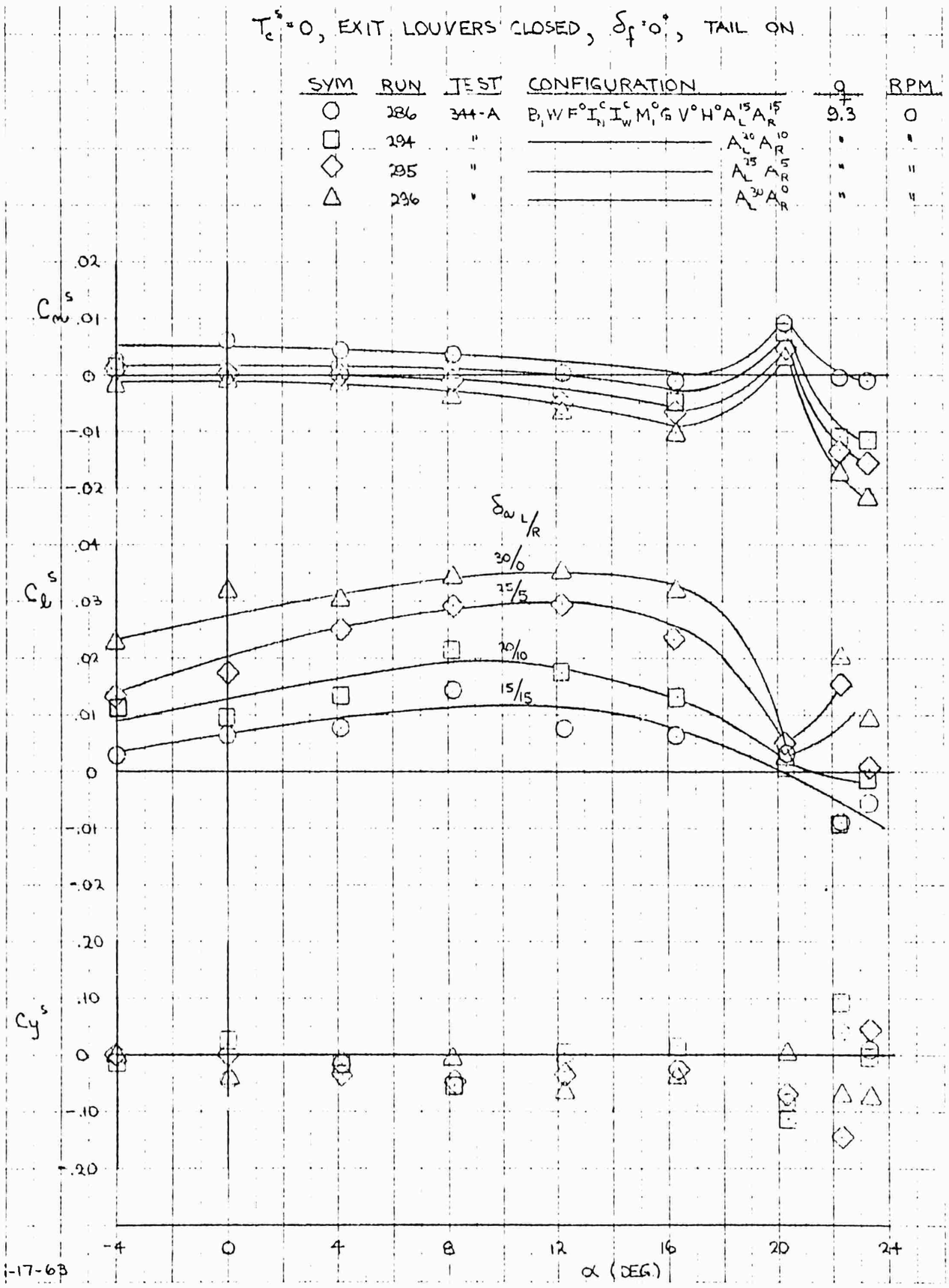

Figure 4.47 Effect of Aileron Deflection from 15° Droop Position, $T_c^s = 0$, $\delta_f = 0°$

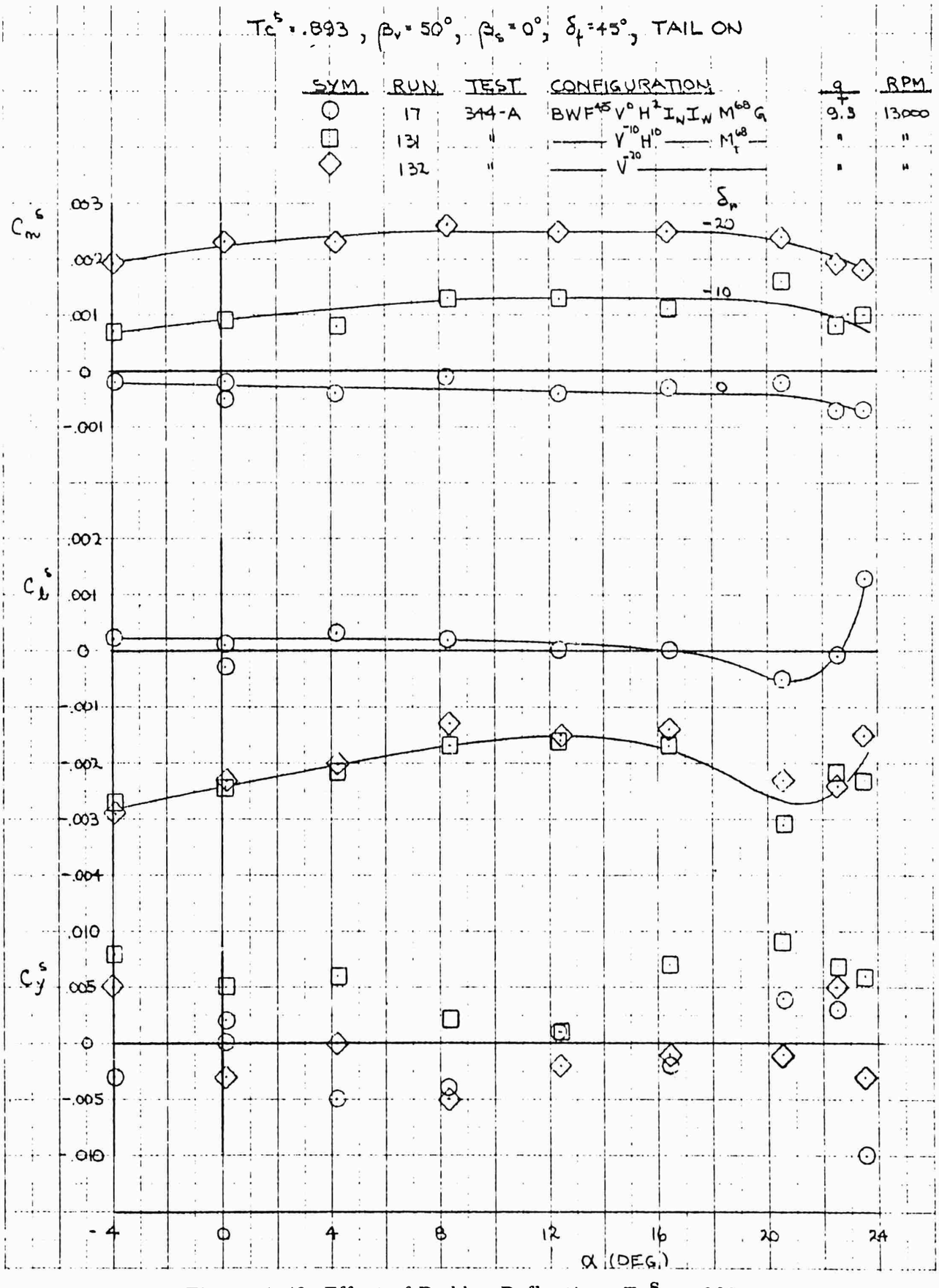

Figure 4.48 Effect of Rudder Deflection, T_c^s = .893

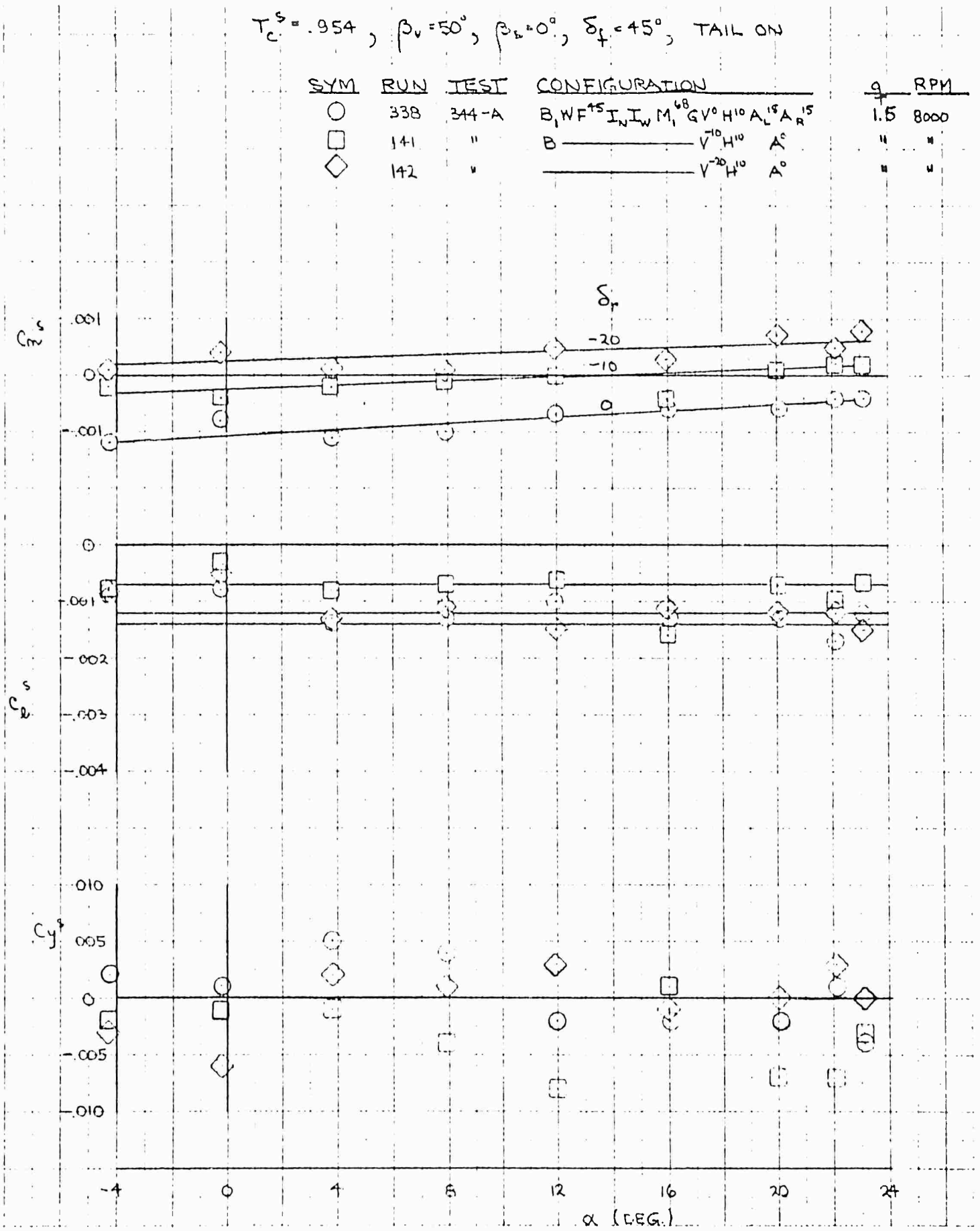

Figure 4.49 Effect of Rudder Deflection, $T_c^s = .954$

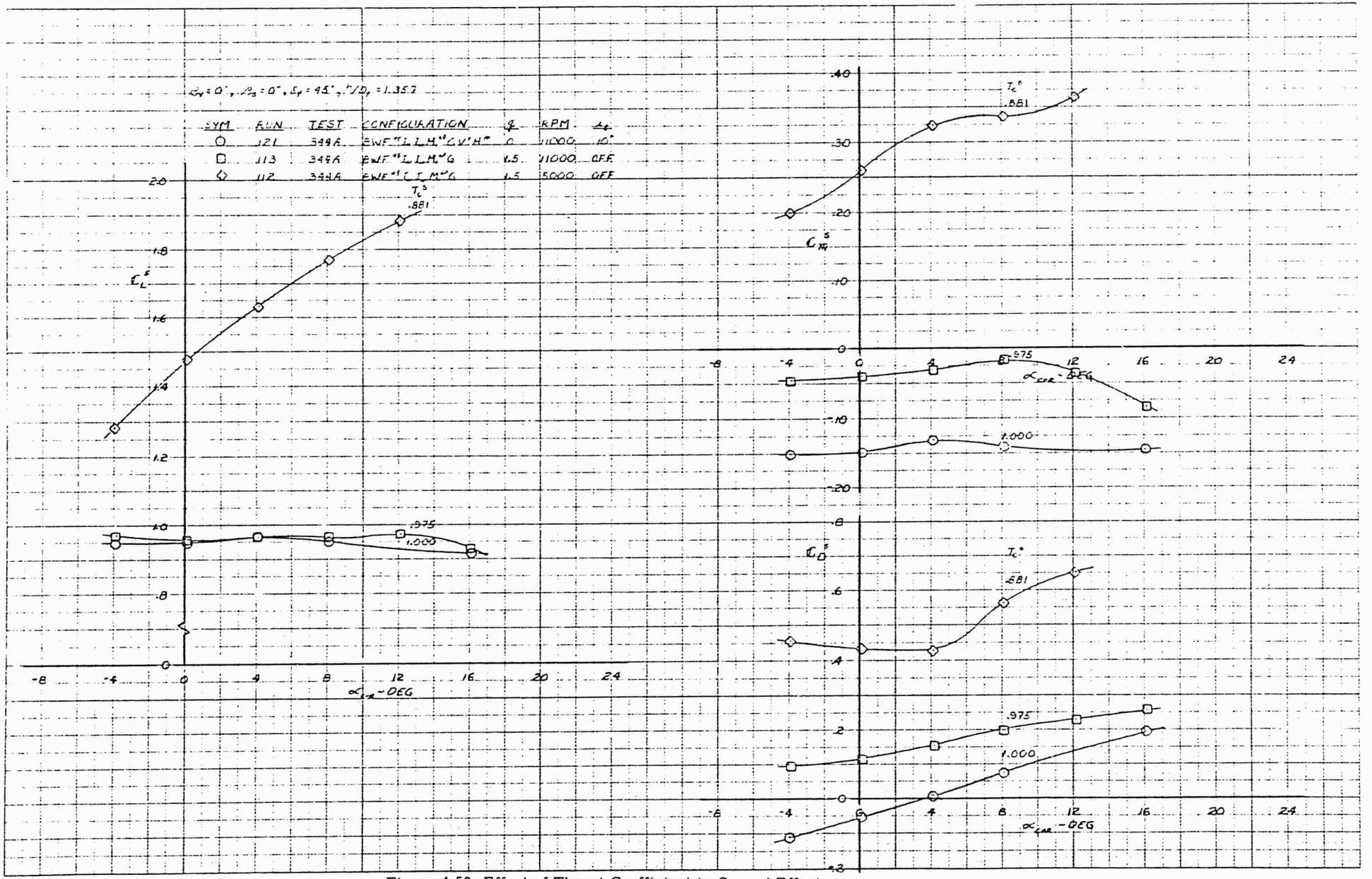

Figure 4.50 Effect of Thrust Coefficient in Ground Effect

$T_c^s = .925$, $\beta_v = 0°$, $\beta_3 = 0°$, $\delta_f = 45°$, $h/D_f = 1.357$.

SYM	RUN	TEST	CONFIGURATION	$\frac{q}{}$	RPM	i_t
○	113	344A	BWF^{45}L$_1$L$_1$M$_1^{45}$G	1.5	11000	OFF
□	107	344A	BWF^{45}L$_1$L$_1$M$_1^{45}$GV$^{\circ}$H^{6}	1.5	11000	6°
◇	108	344A	BWF^{45}L$_1$L$_1$M$_1^{45}$GV$^{\circ}$H^{15}	1.5	11000	15°

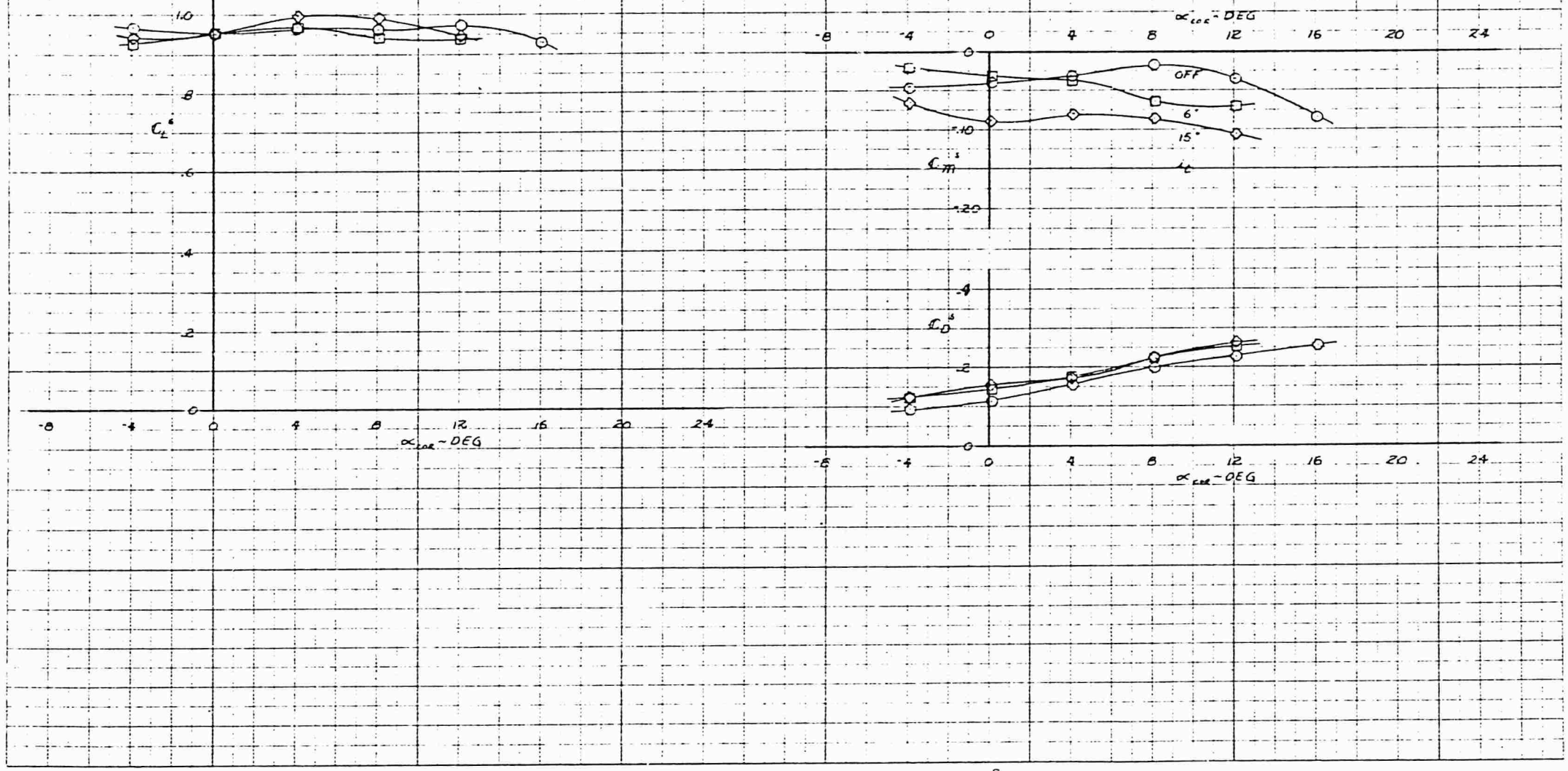

Figure 4.51 Horizontal Stabilizer Effectiveness in Ground Effect, $T_c^s = .975$

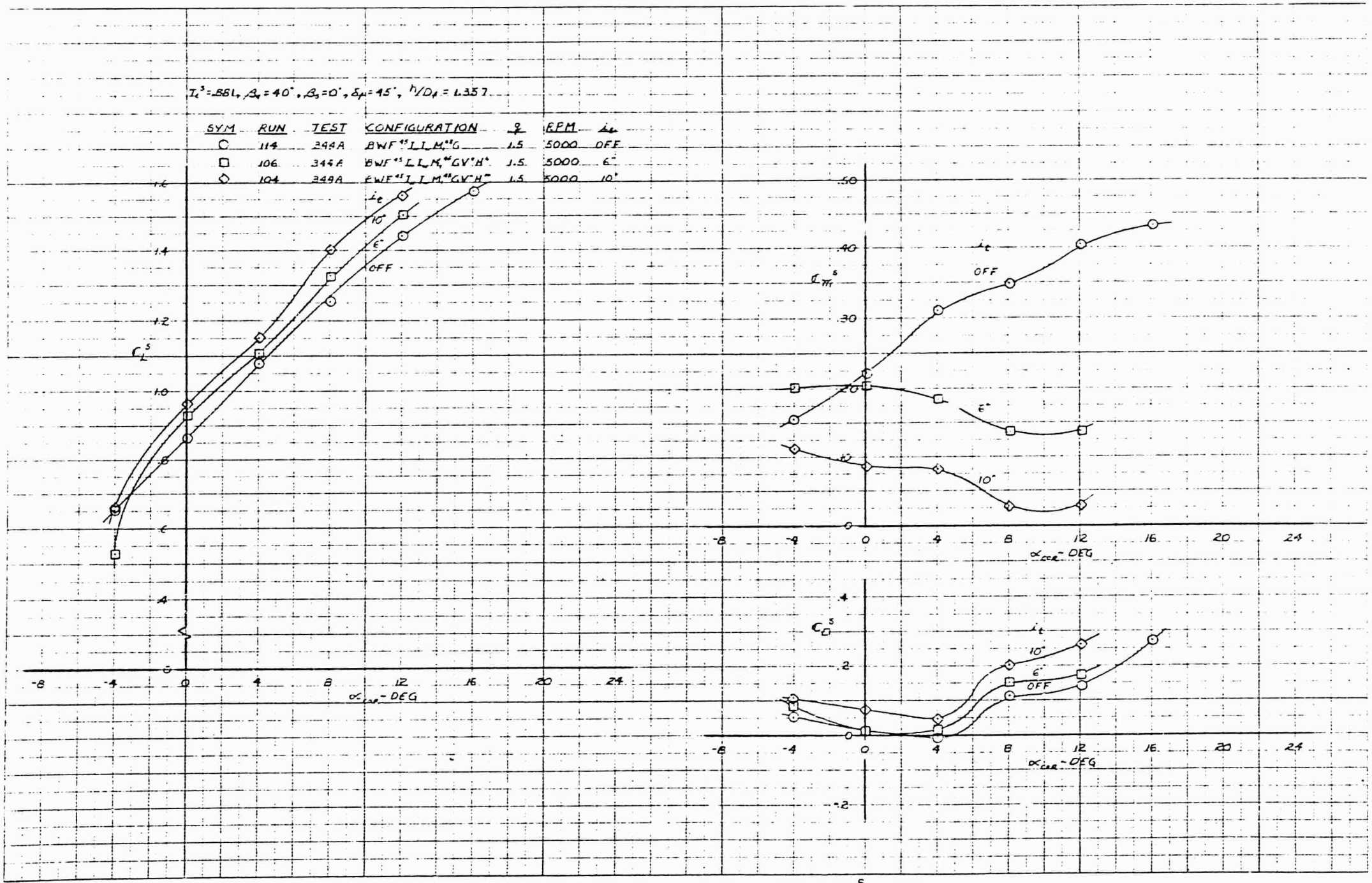

Figure 4.52 Horizontal Stabilizer Effectiveness in Ground Effect, T_C^S = .881

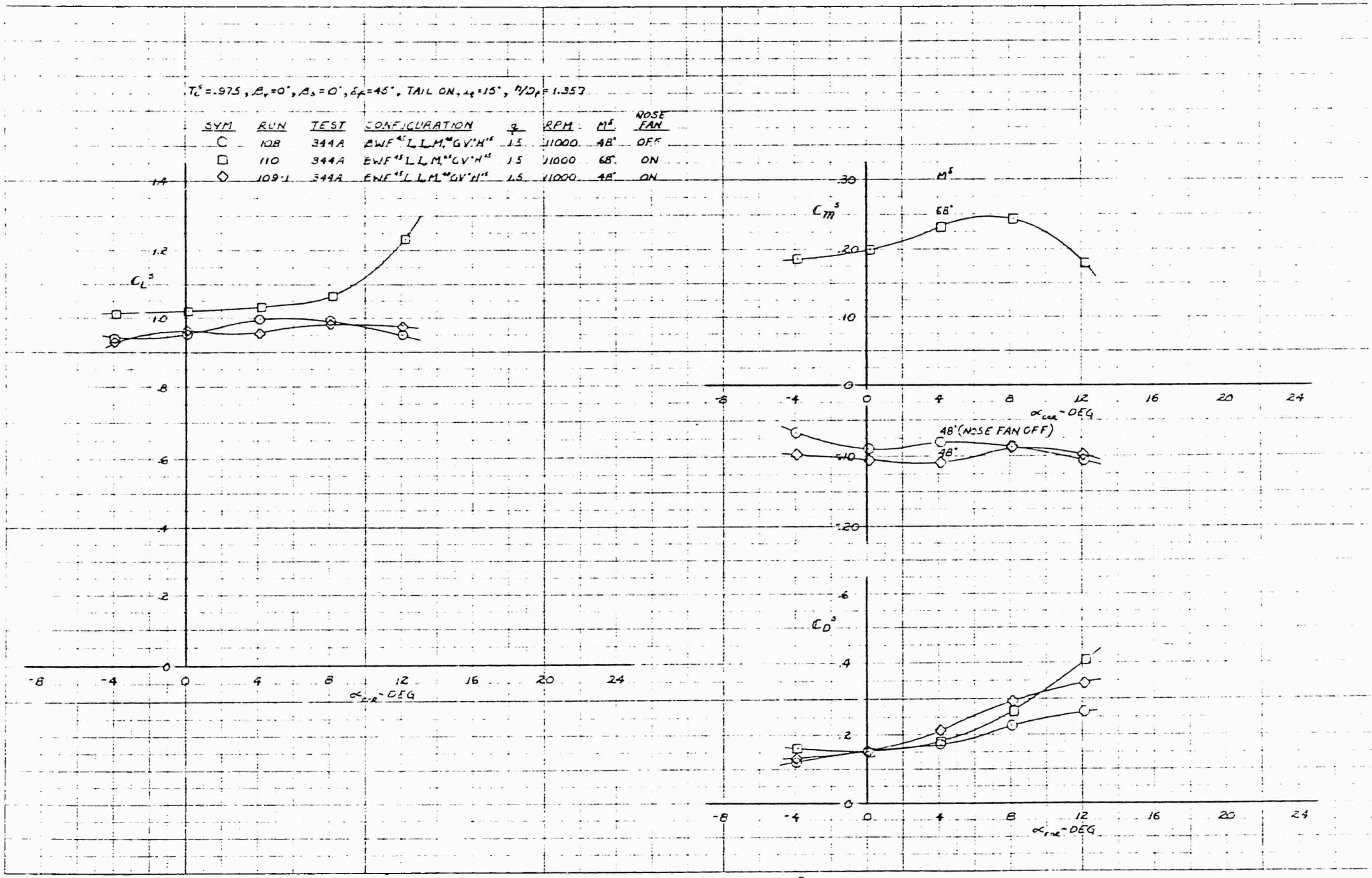

Figure 4.53 Effect of The Nose Fan in Ground Effect, T_C^S = .975

T_c^s = .881, ϕ_f = 0°, β_s = 0°, δ_f = 45°, TAIL ON, i_t = 10°, h/D_p = 1.357

SYM	RUN	TEST	CONFIGURATION	δ_e	RPM	M^f	NOSE FAN
○	101	344A	BWF^{65} L L M,^{45} GV H"	1.5	5000	66°	OFF
□	102	344A	BWF^{65} L L M,^{45} GV H"	1.5	5000	66°	ON
◇	103	344A	BWF^{65} L L M,^{45} GV H"	1.5	5000	46°	ON

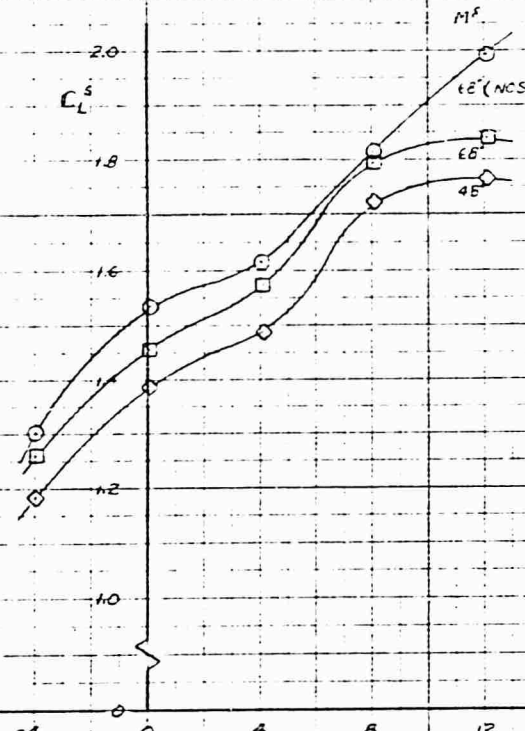

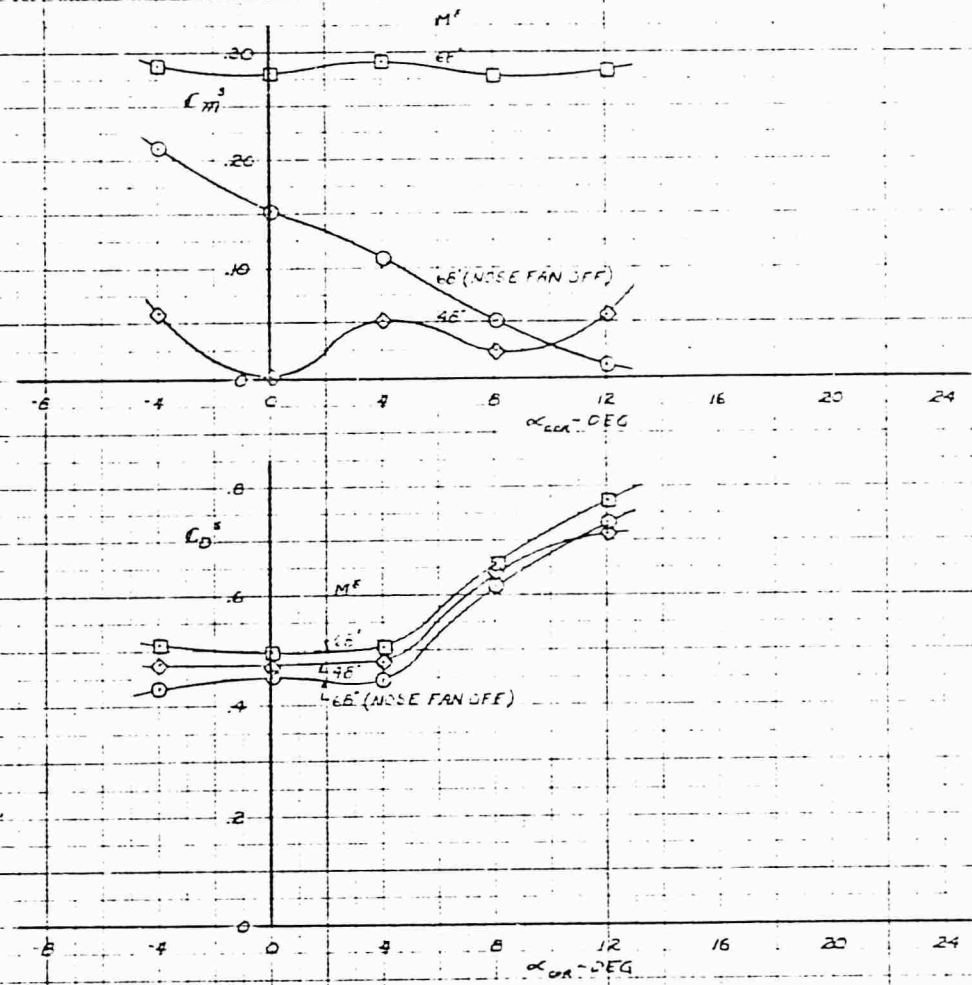

Figure 4.54 Effect of The Nose Fan in Ground Effect, T_c^s = .881

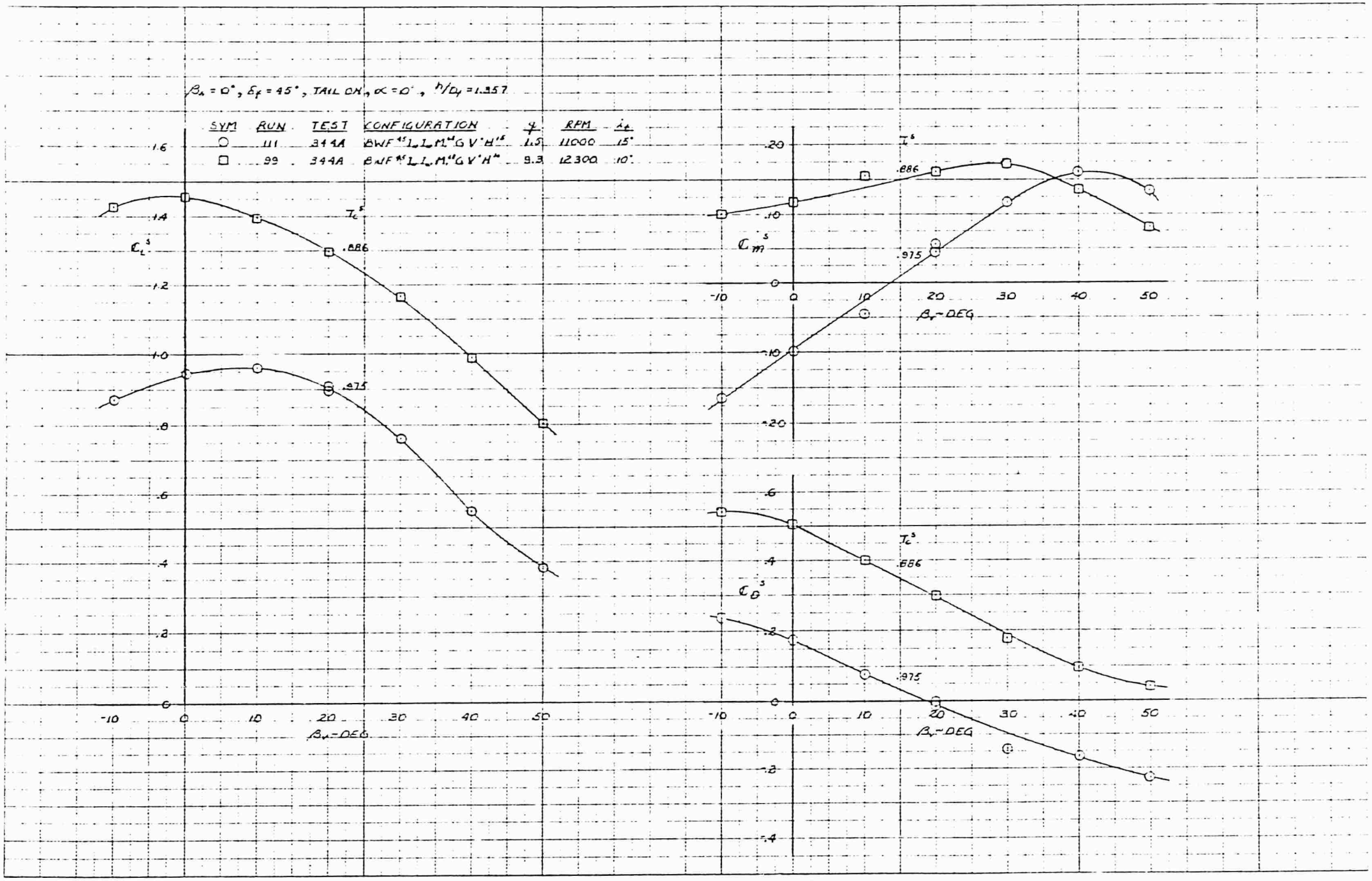

Figure 4.55 Vector Effectiveness in Ground Effect

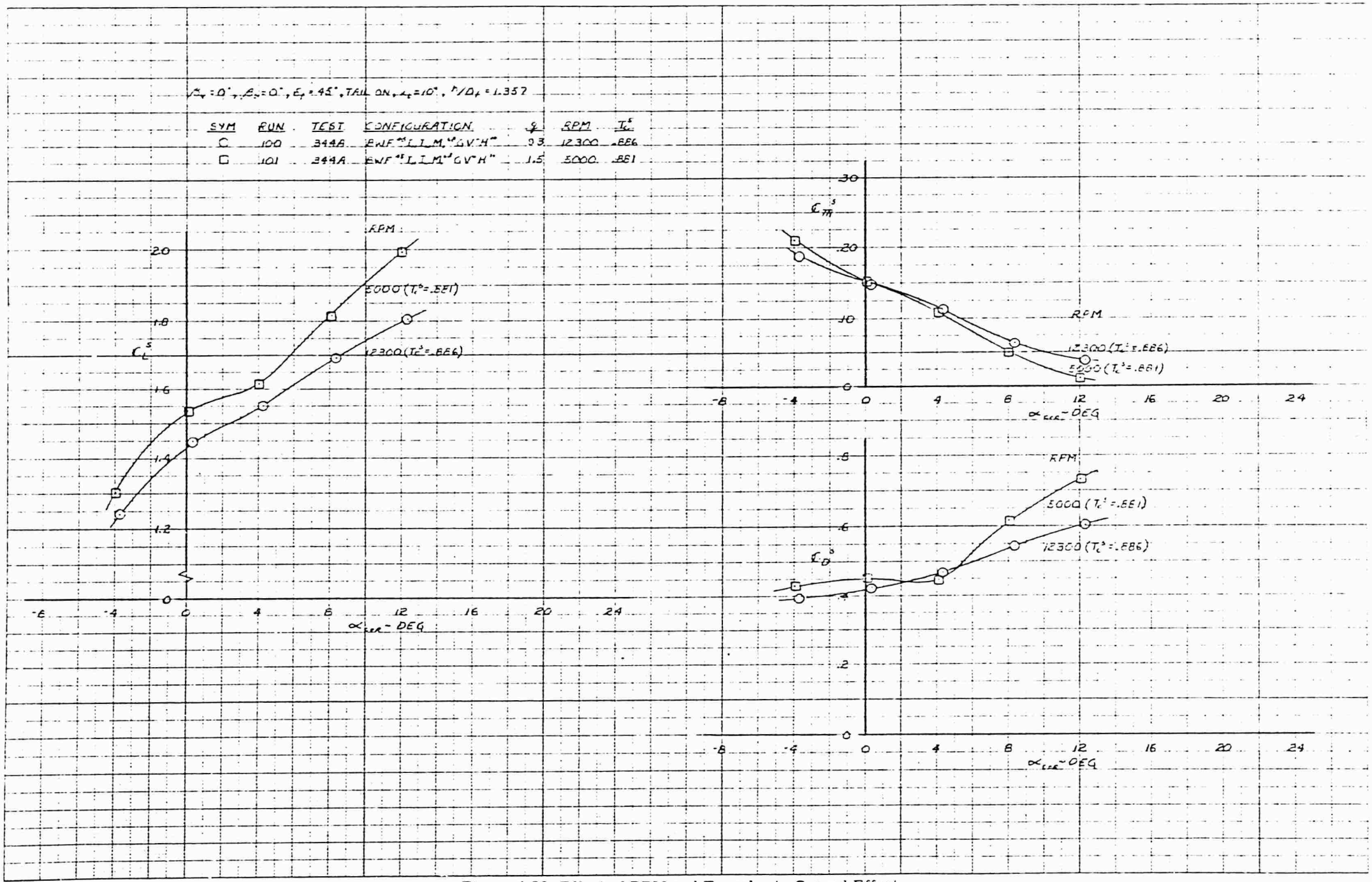

Figure 4.56 Effect of RPM and Tunnel q in Ground Effect

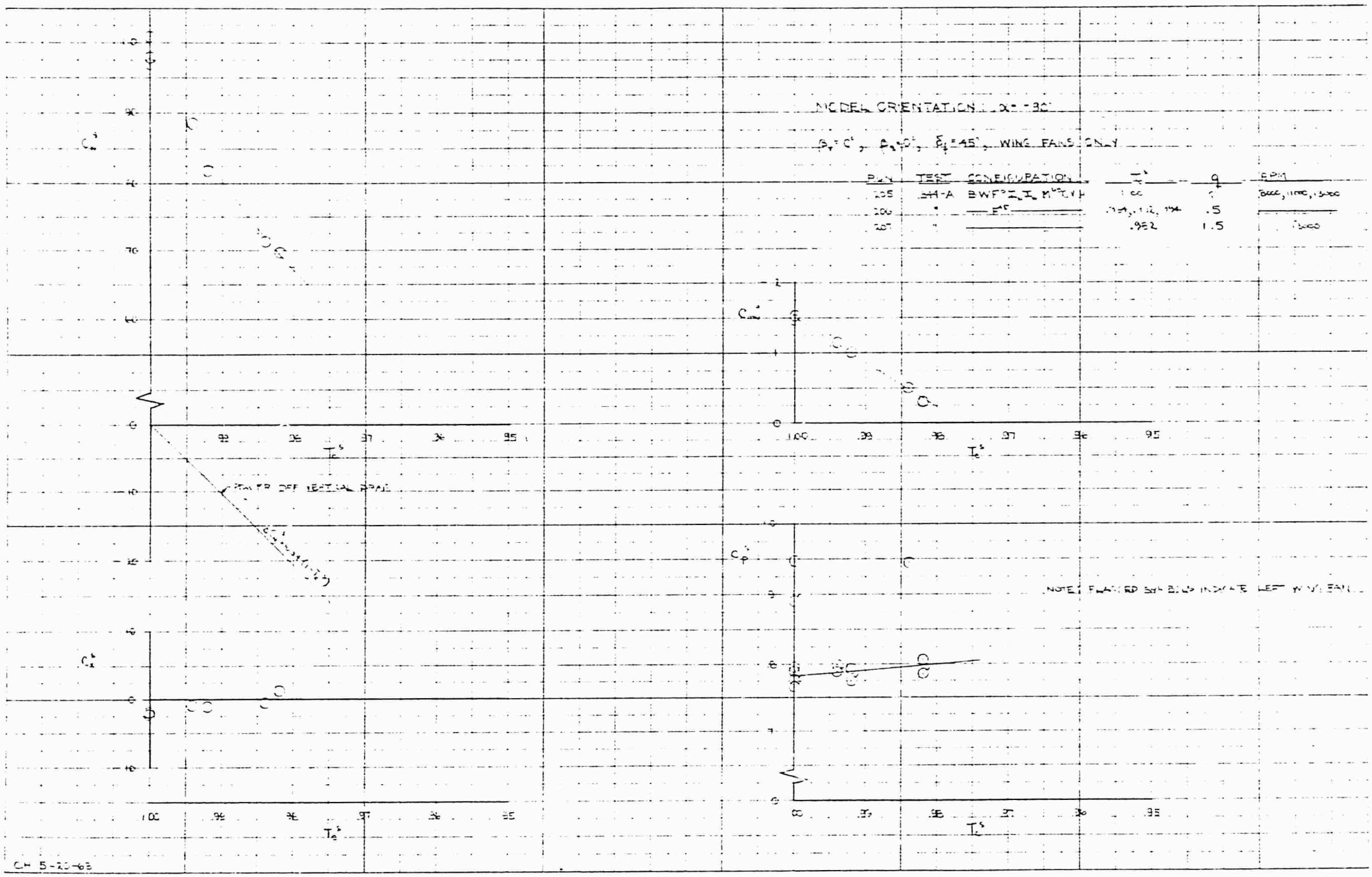

Figure 4.57 Effect of Velocity in Vertical Ascent

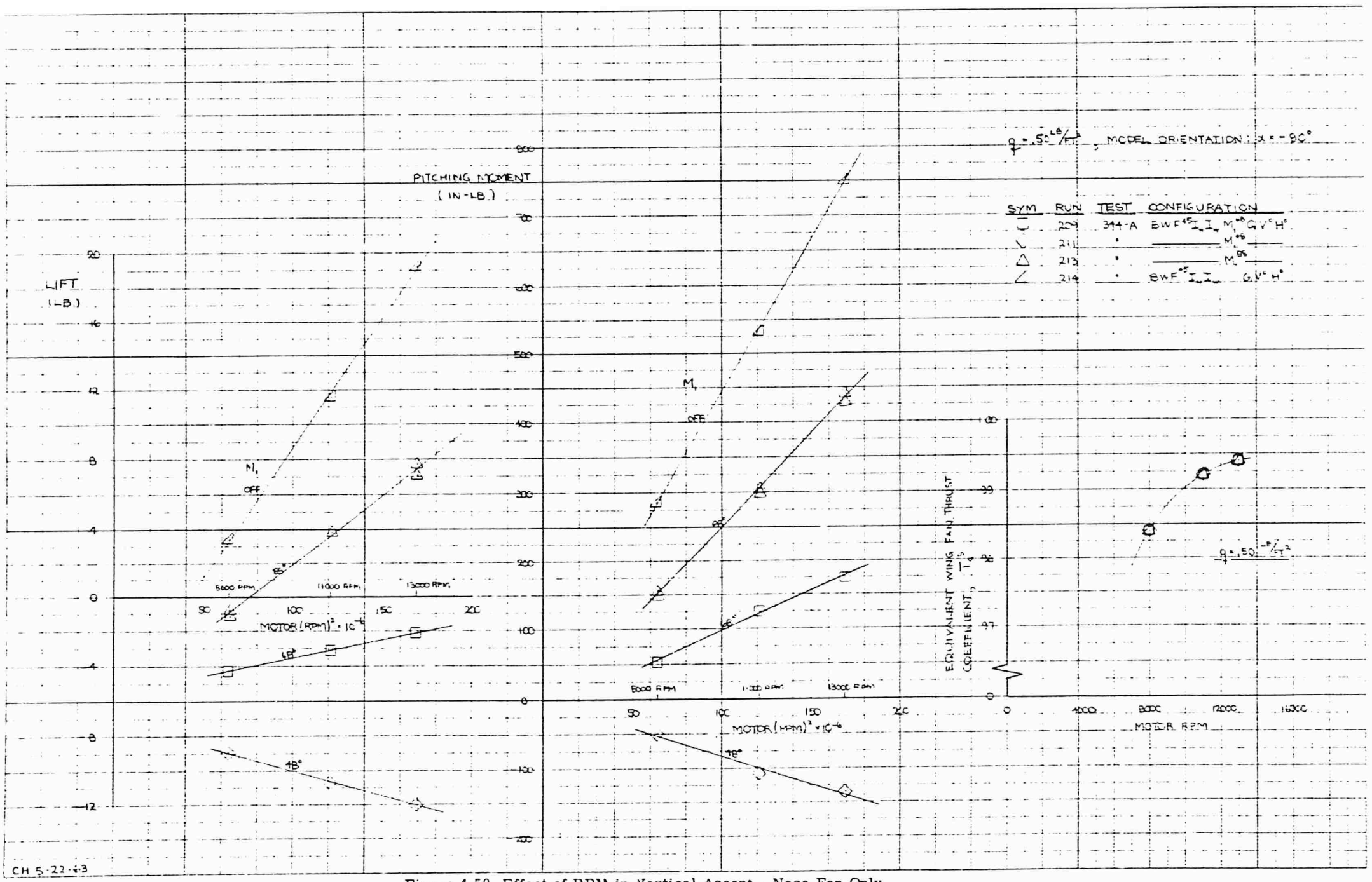

Figure 4.58 Effect of RPM in Vertical Ascent - Nose Fan Only

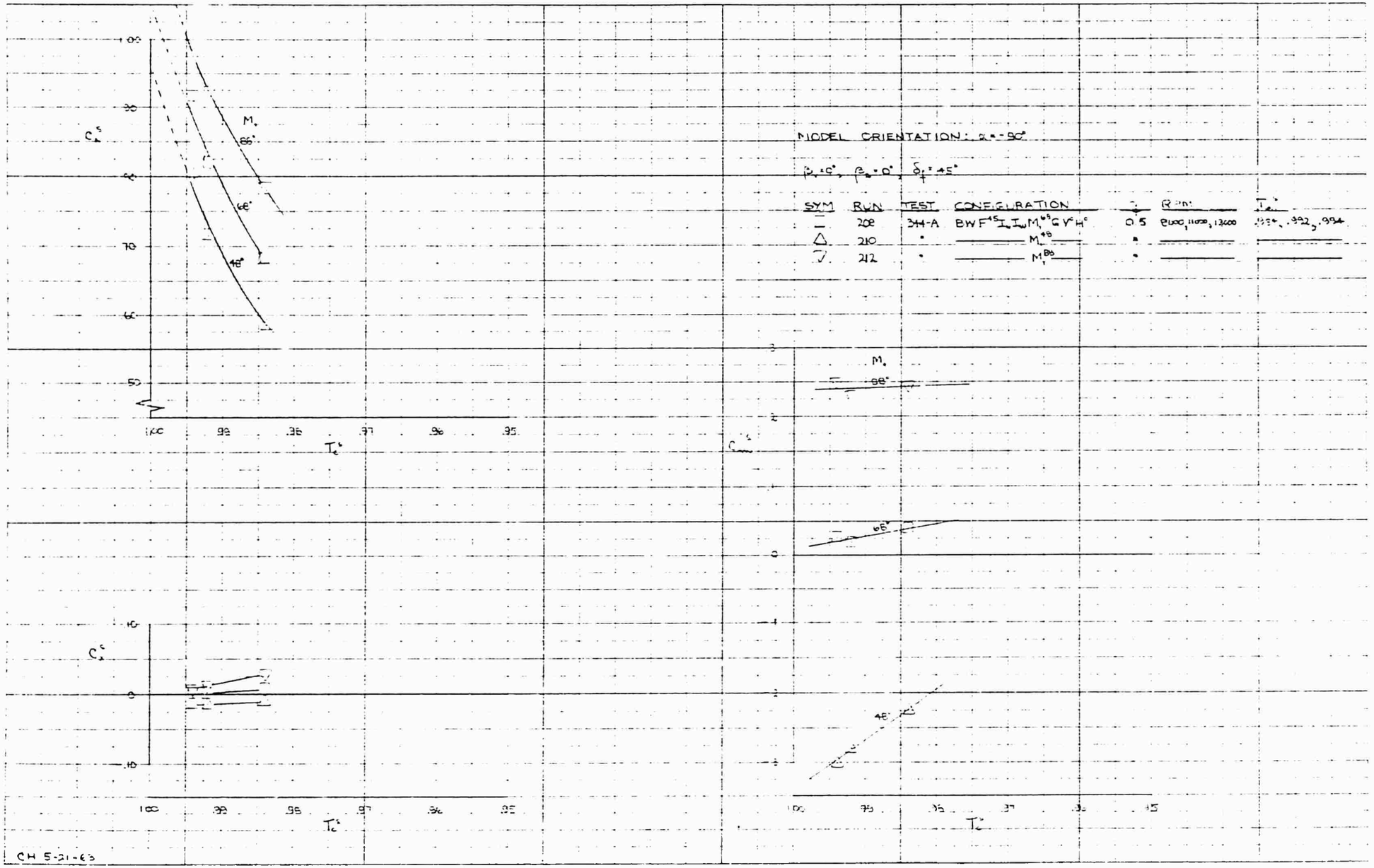

Figure 4.59 Effect of Velocity in Vertical Ascent, Wing Fans and Nose Fan

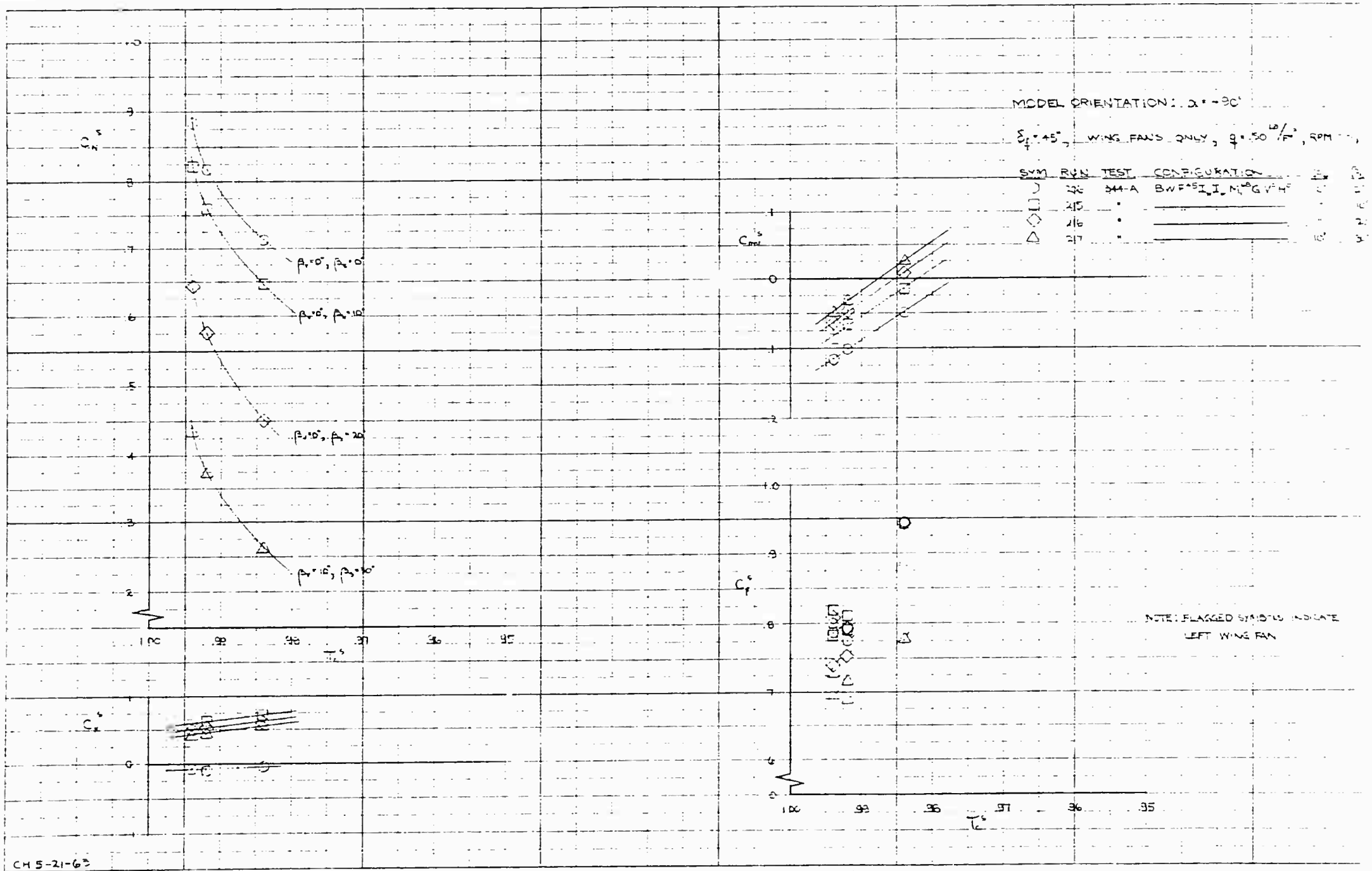

Figure 4.60 Effect of Stagger Angle in Vertical Ascent

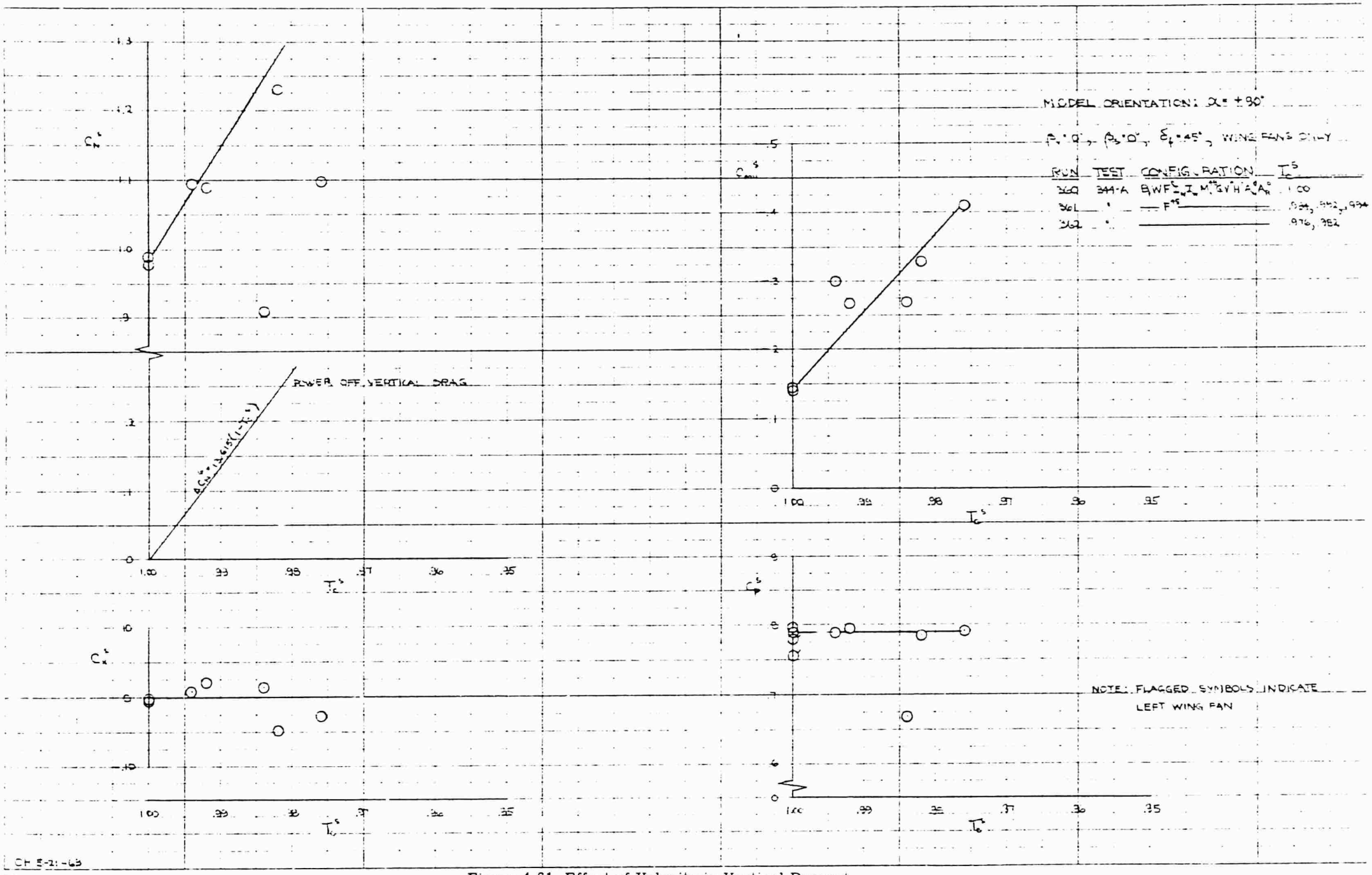

Figure 4.61 Effect of Velocity in Vertical Descent

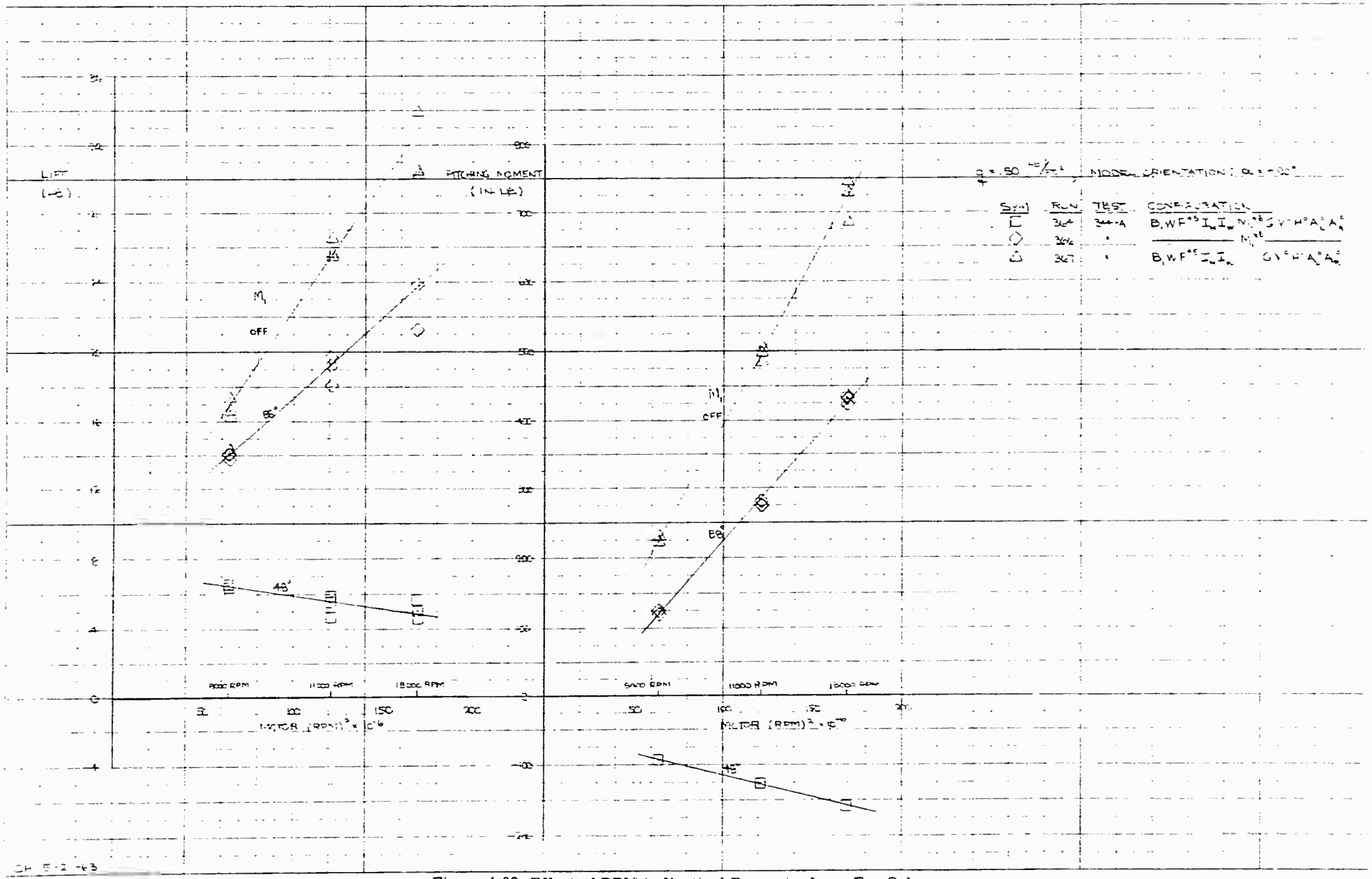

Figure 4.62 Effect of RPM in Vertical Descent - Nose Fan Only

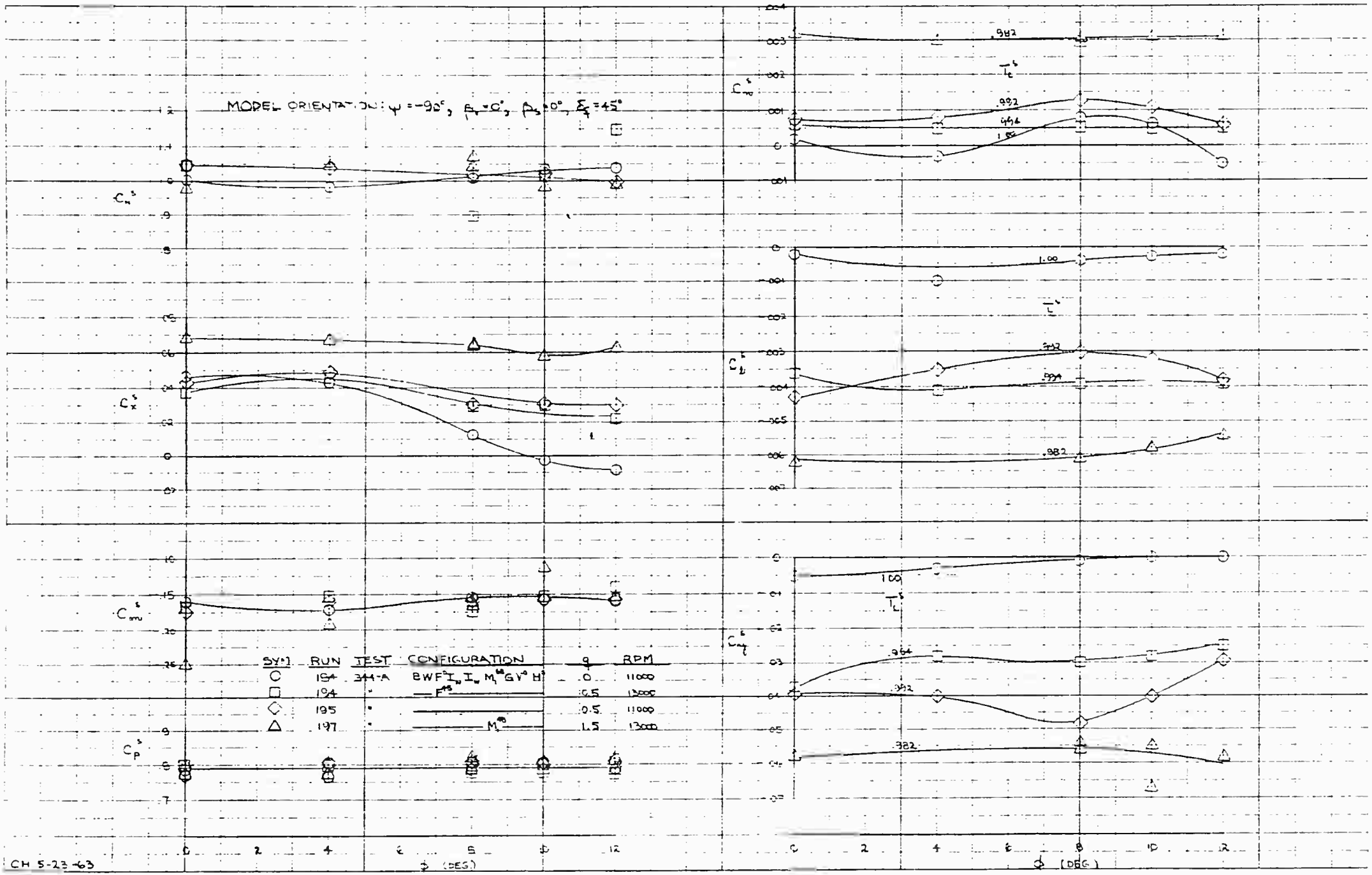

Figure 4.63 Effect of Velocity in Lateral Transition

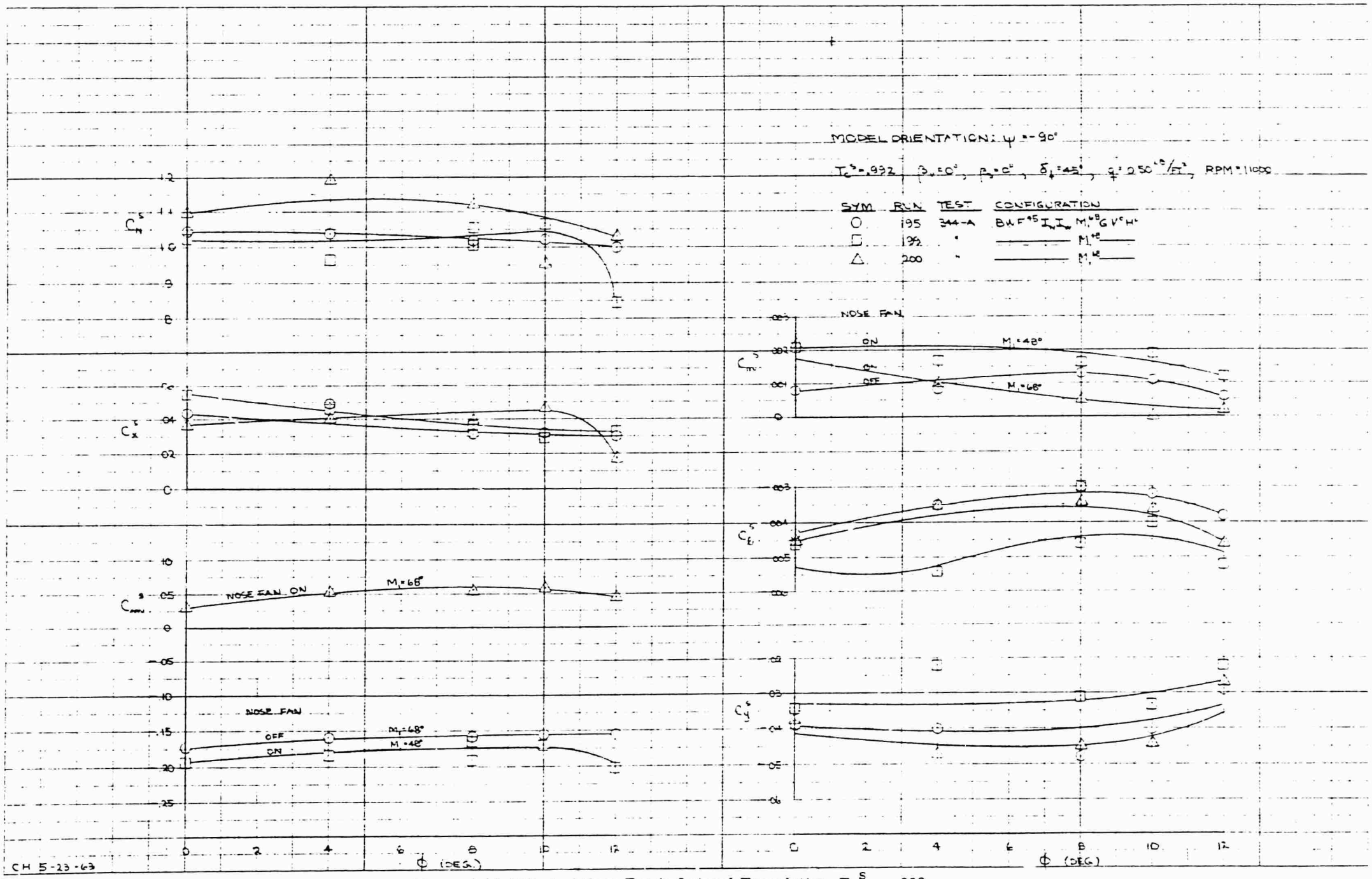

Figure 4.64 Effect of Nose Fan in Lateral Translation, T_c^s = .992

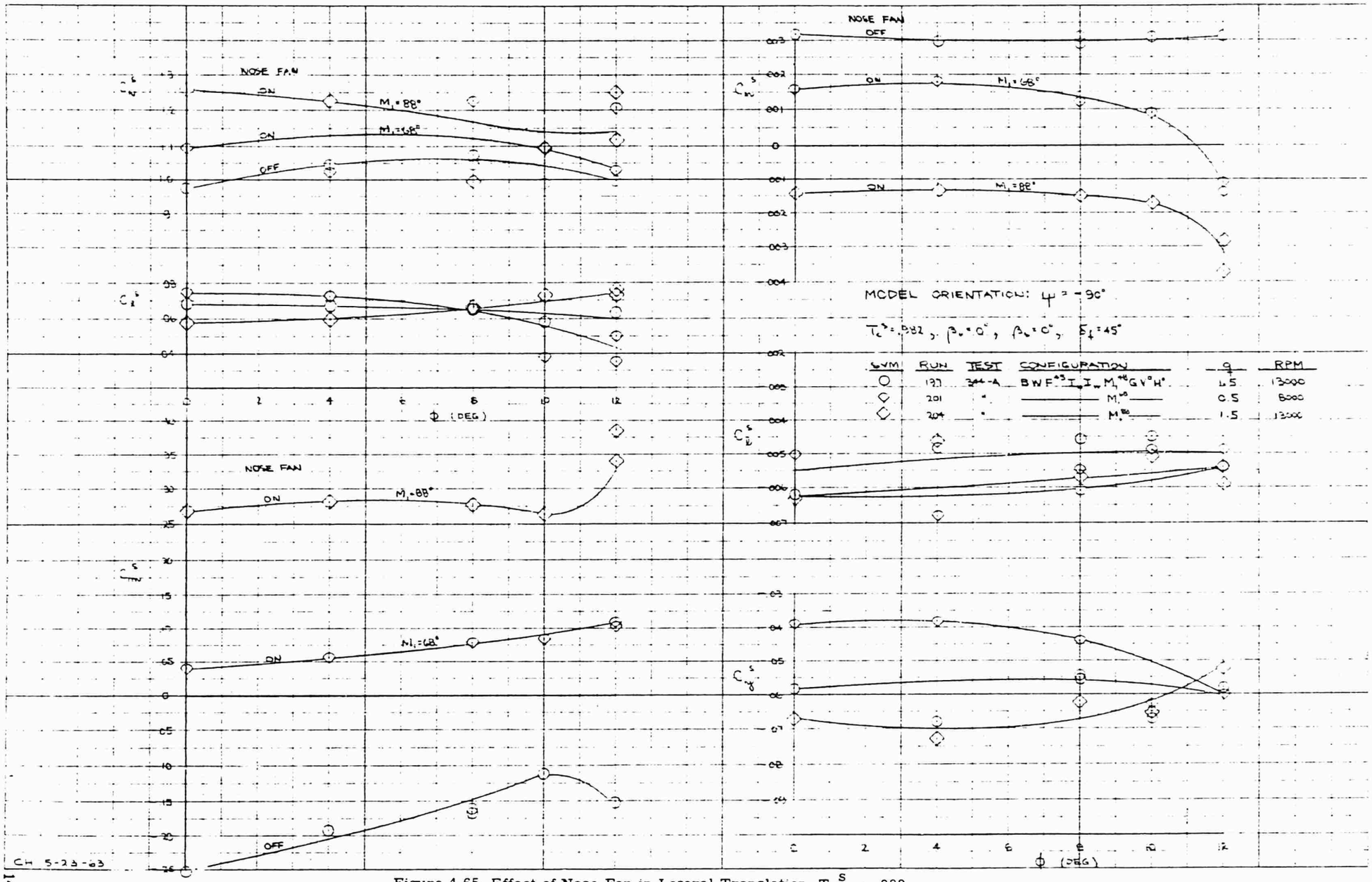

Figure 4.65 Effect of Nose Fan in Lateral Translation, T_c^s = .982

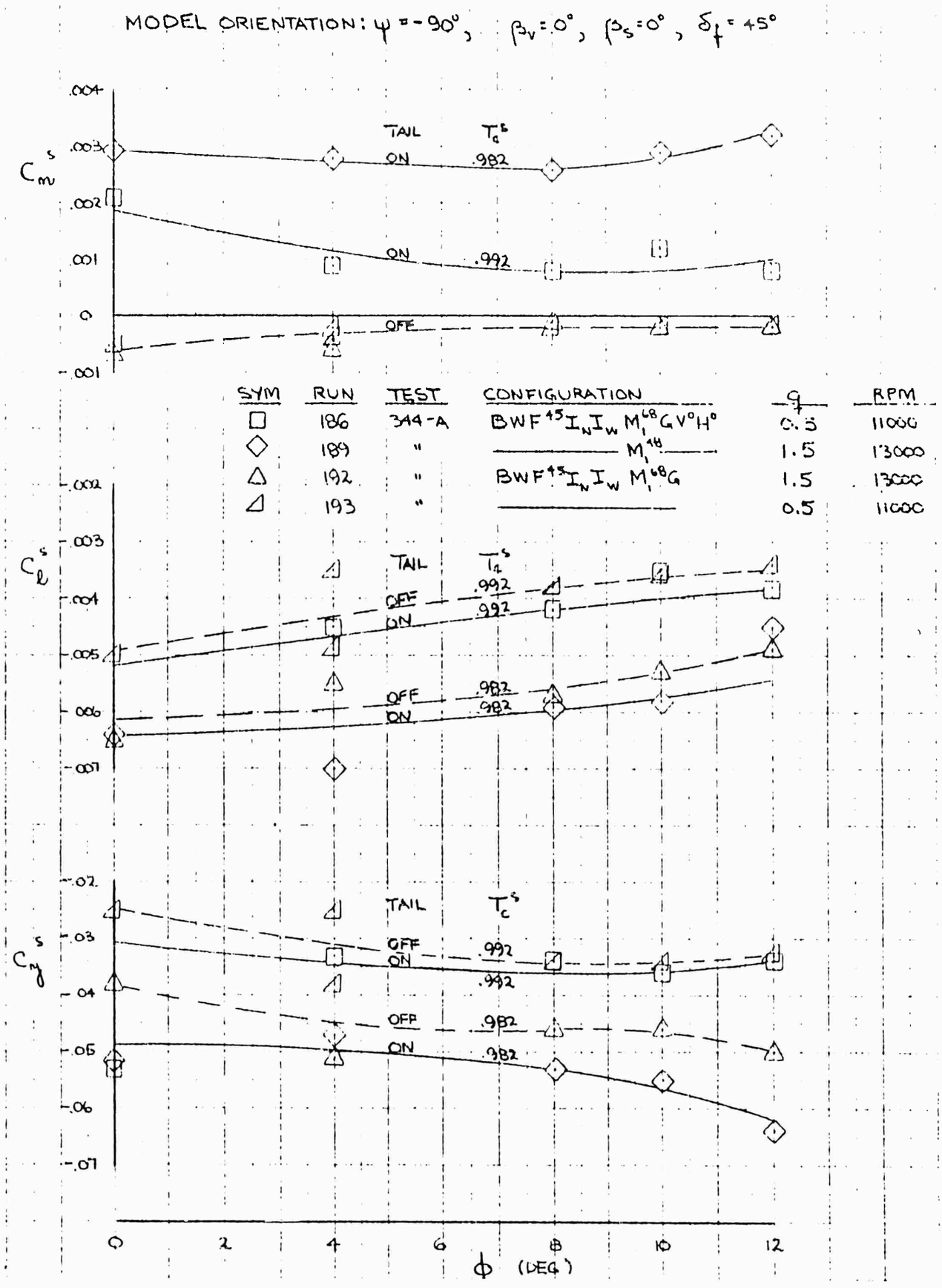

Figure 4.66 Effect of the Vertical and Horizontal Tail in Lateral Translation

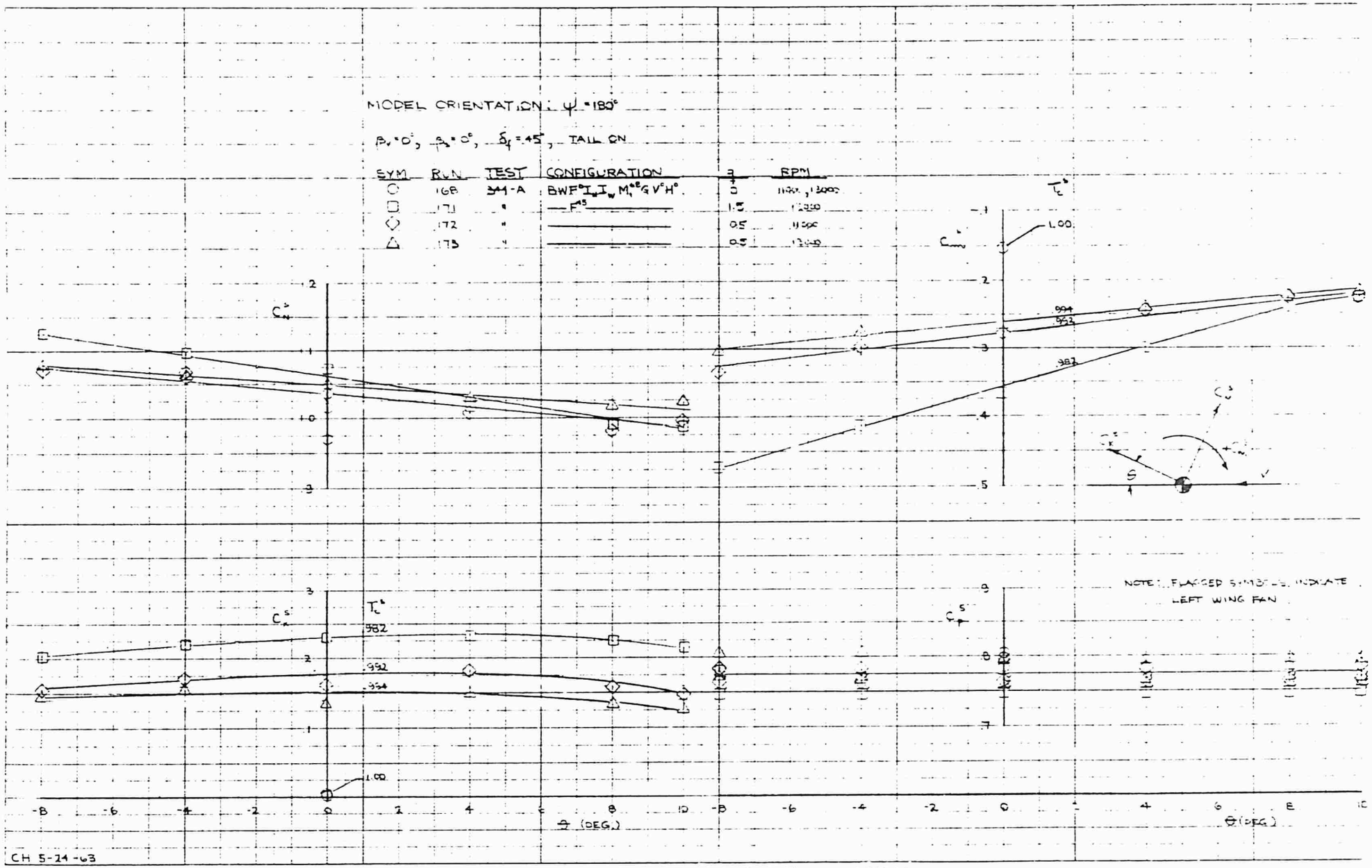

Figure 4.67 Effect of Velocity and Pitch Angle in Rearward Flight

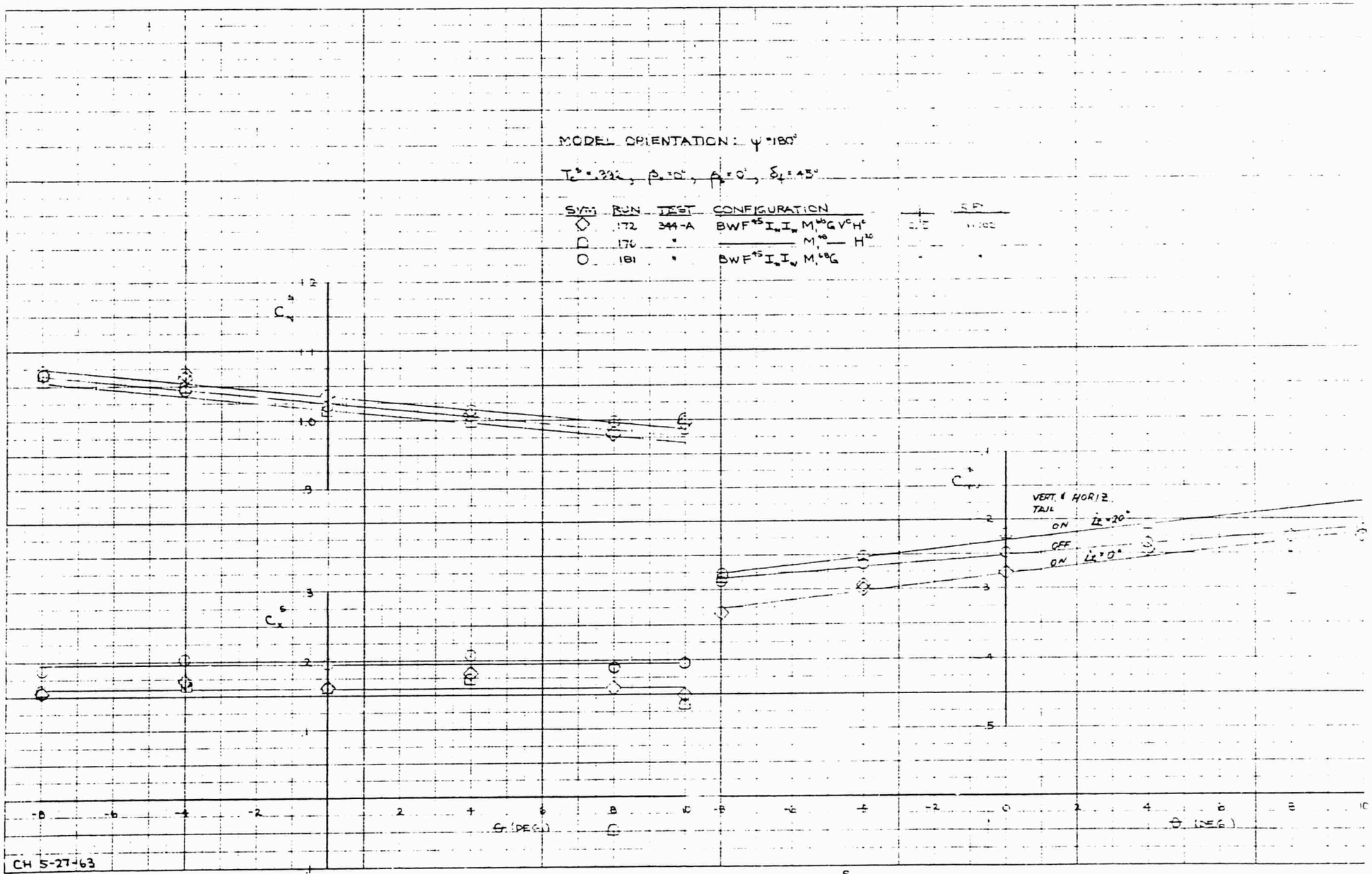

Figure 4.68 Effect of Horizontal Tail in Rearward Flight, T_c^S = .992

MODEL ORIENTATION: ψ = 150°

T_c^S = .982 → β_s = 0°, β_w = 0°, δ_f = 45°

SYM	RUN	TEST	CONFIGURATION	q	RPM
□	171	344-A	BWF^{45} I_w I_w M_1^{45} G V^c H^c	1.5	13,000
◇	177	"	——— M_2^{45} ——— H^{50}	"	"
○	182	"	BWF^{45} I_w I_w M_1^{45}	"	"

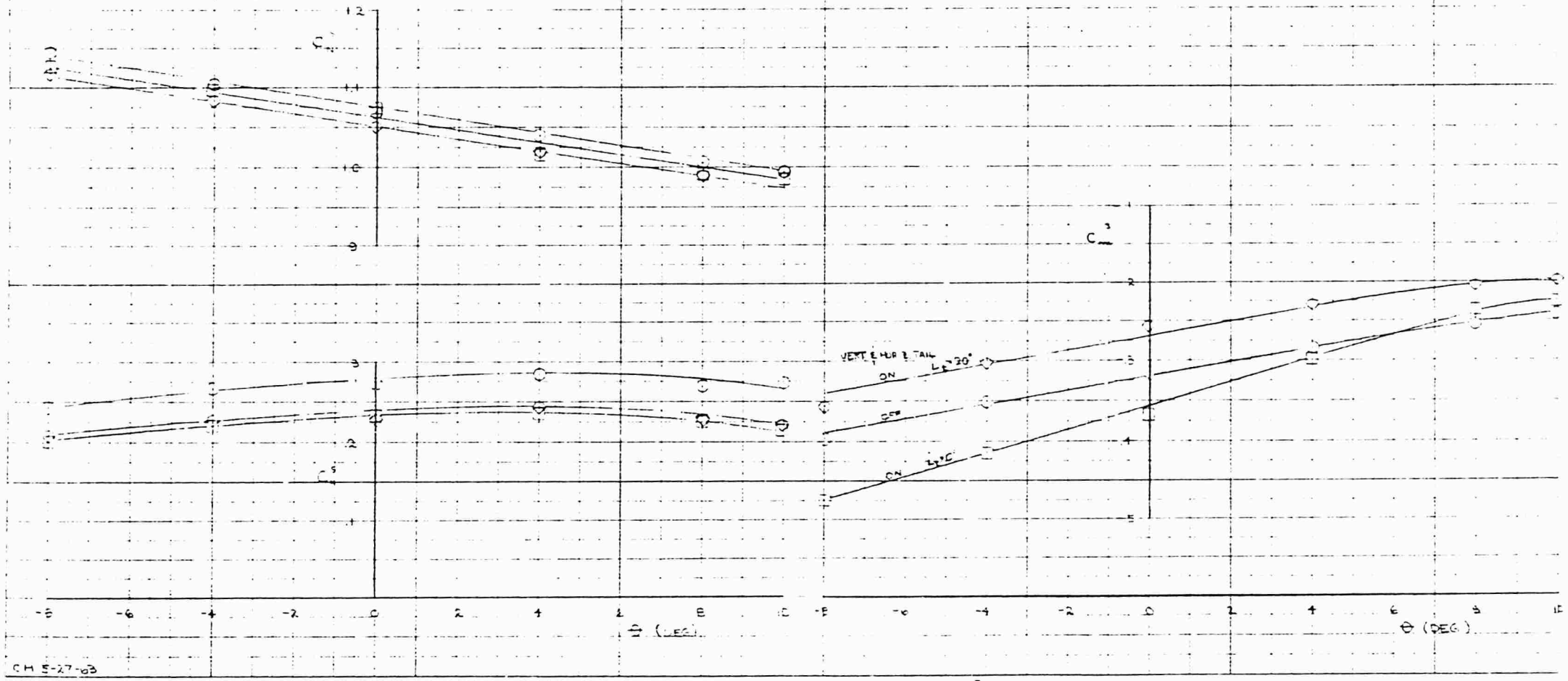

Figure 4.69 Effect of Horizontal Tail in Rearward Flight, T_c^S = .982

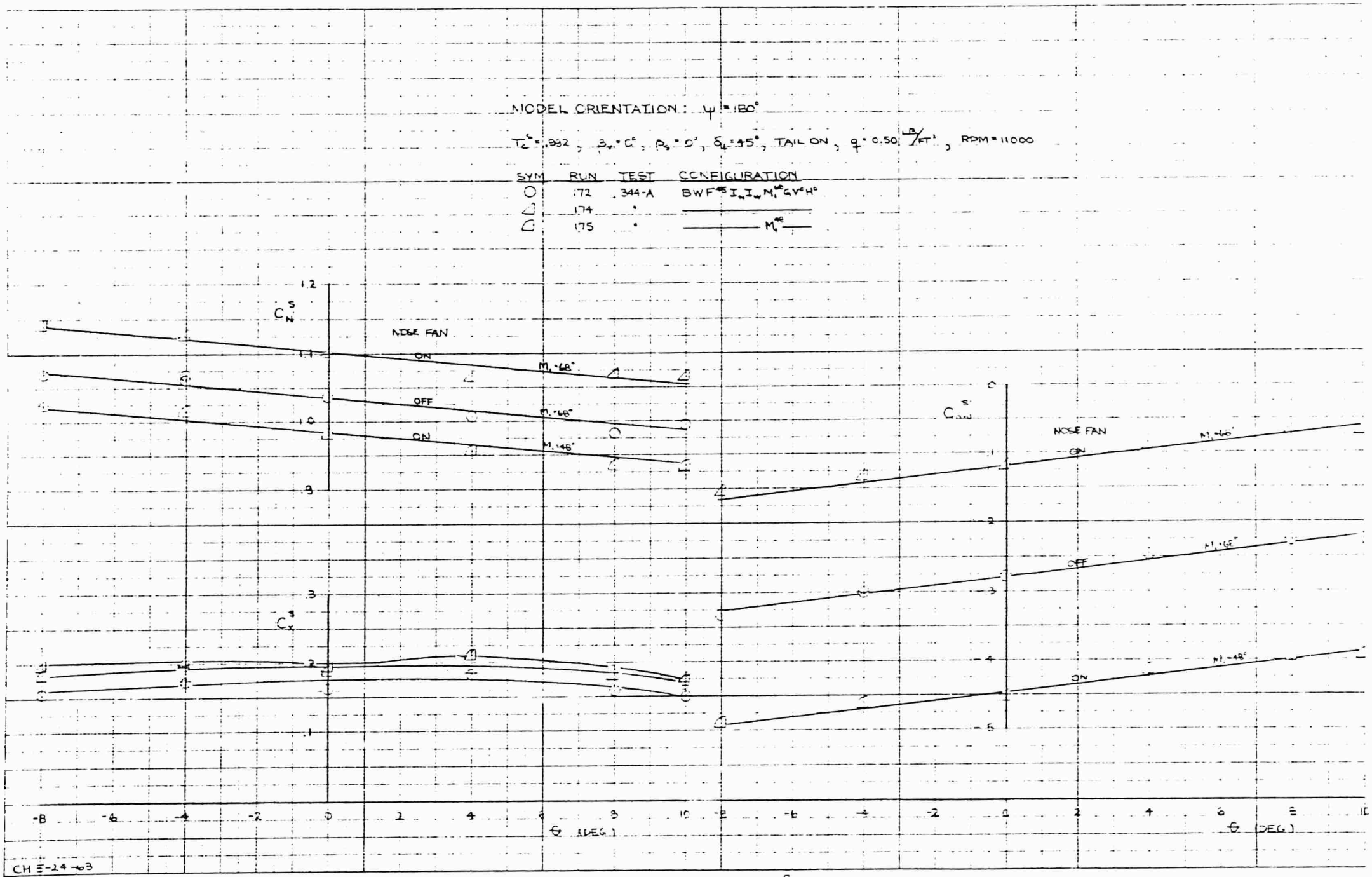

Figure 4.70 Effect of Nose Fan in Rearward Flight, T_c^s = .992

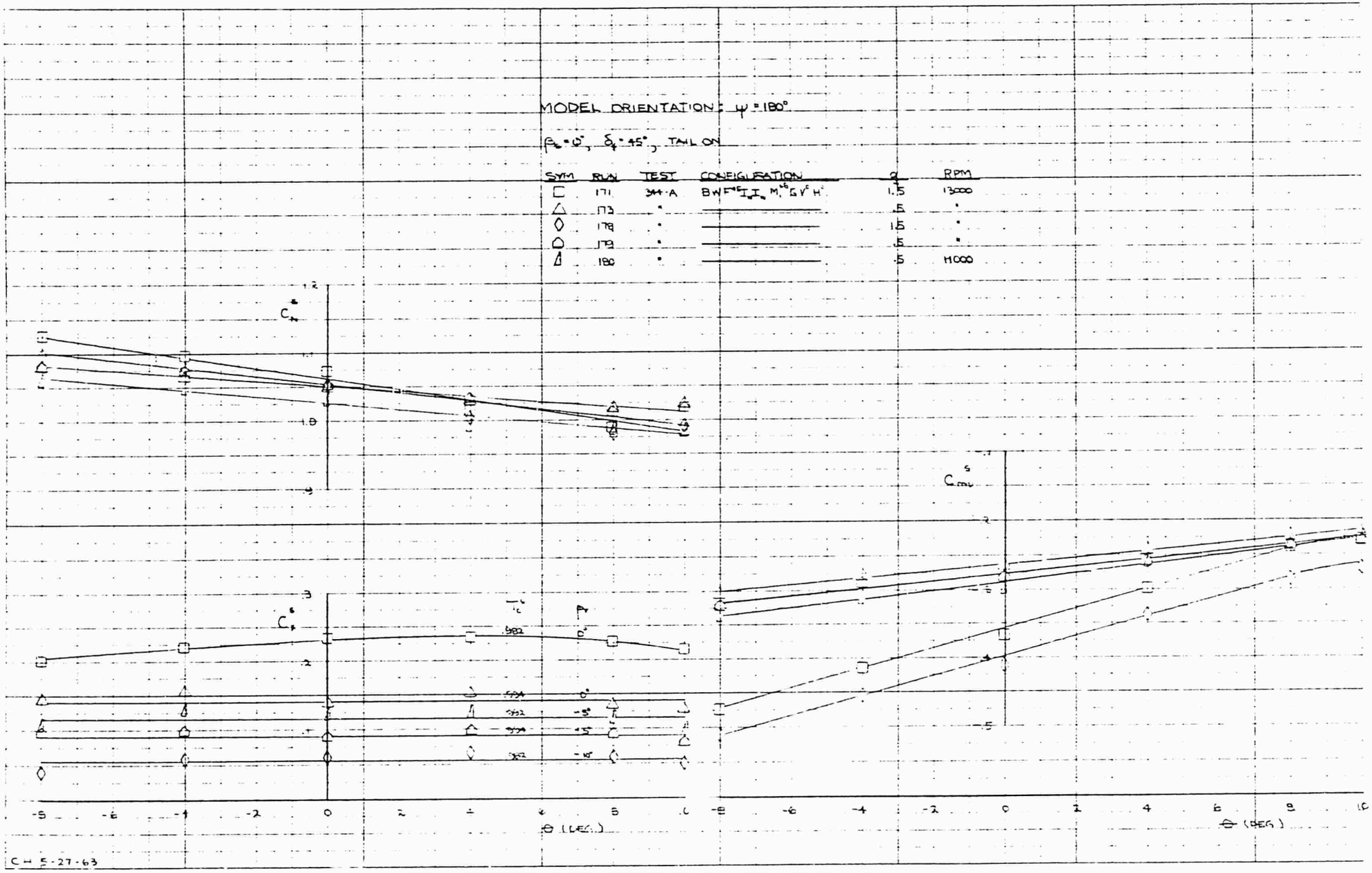

Figure 4.71 Effect of Negative Vectoring in Rearward Flight

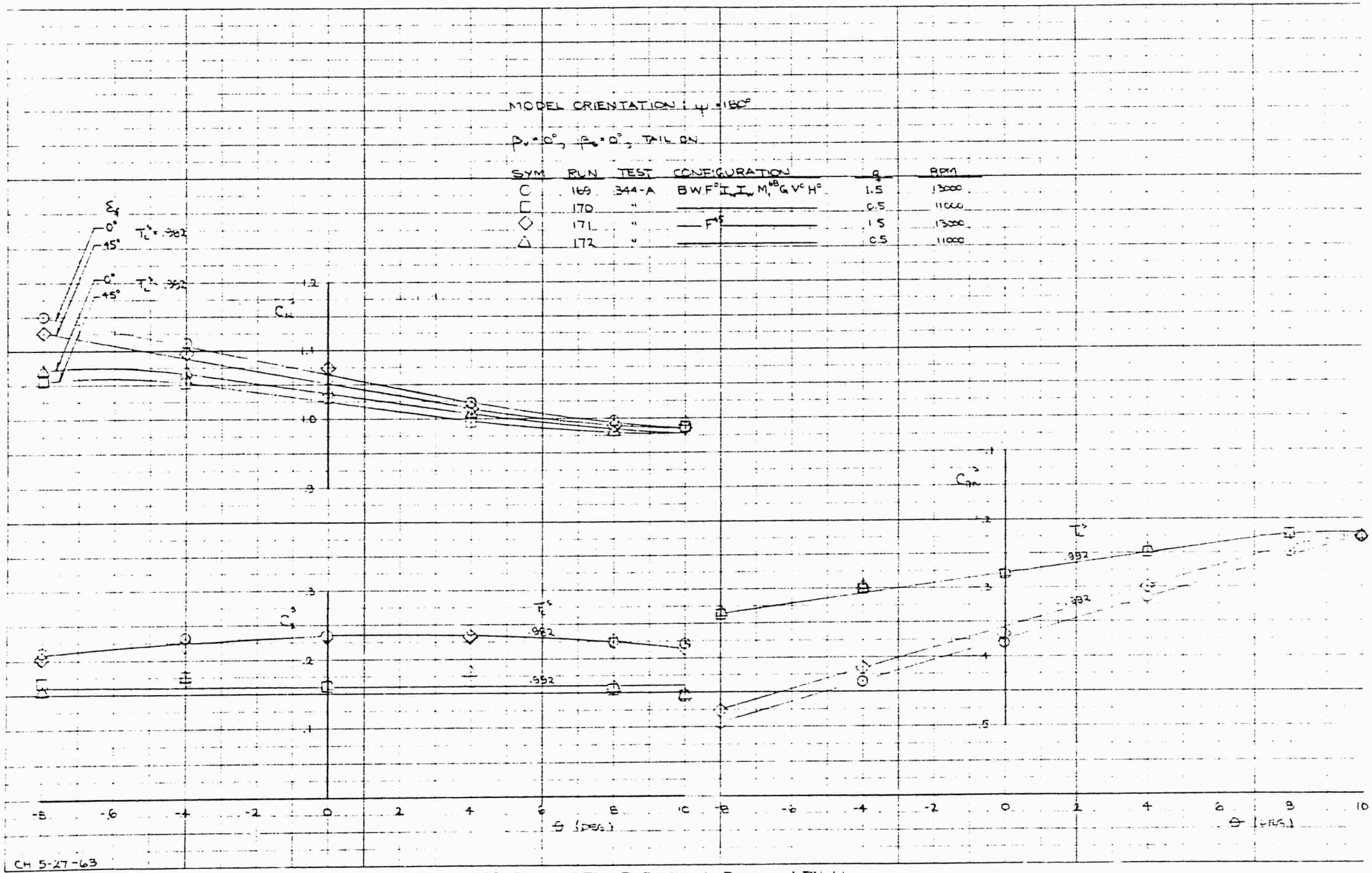

Figure 4.72 Effect of Flap Deflection in Rearward Flight

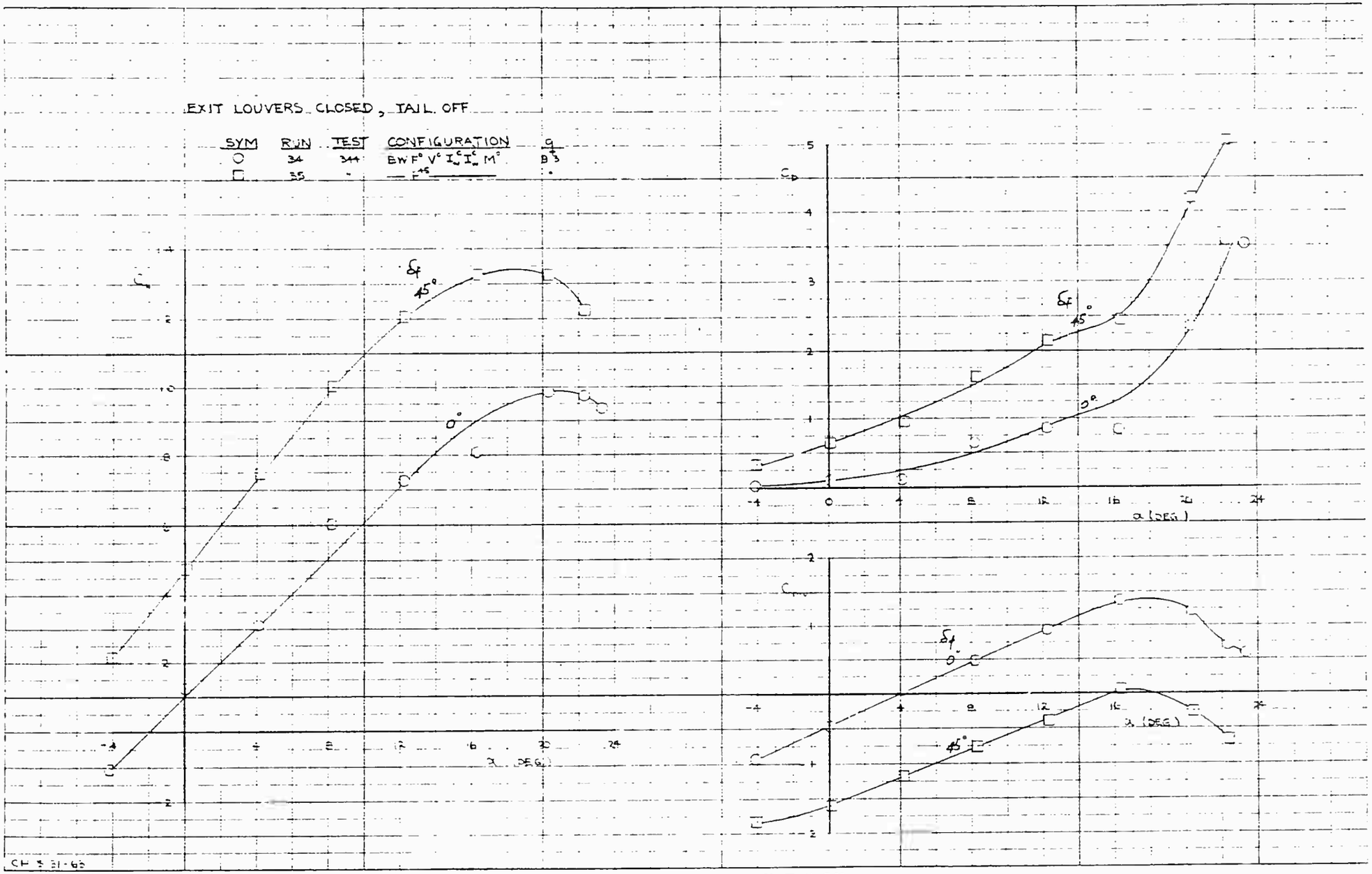

Figure 4.73 Flap Effectiveness- Power Off, Tail Off

EXIT LOUVERS CLOSED, TAIL ON

SYM	RUN	TEST	CONFIGURATION	q
○	25	344	BWF V° H° i_t^c i_w^c M°	9.3
□	26	"	— F^{30} —	"
◇	27	"	— F^{45} —	"

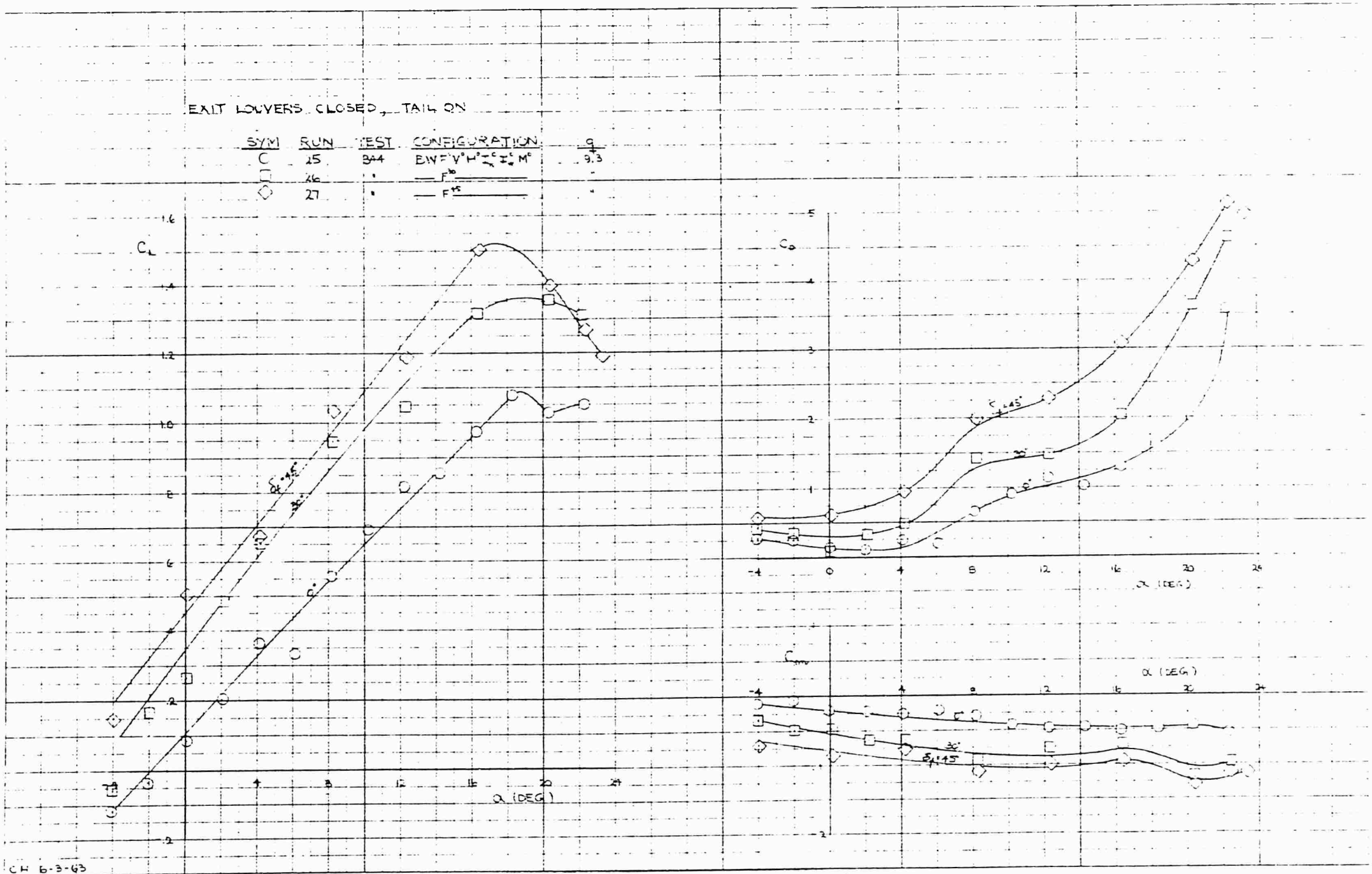

Figure 4.74 Flap Effectiveness - Power Off, Tail On

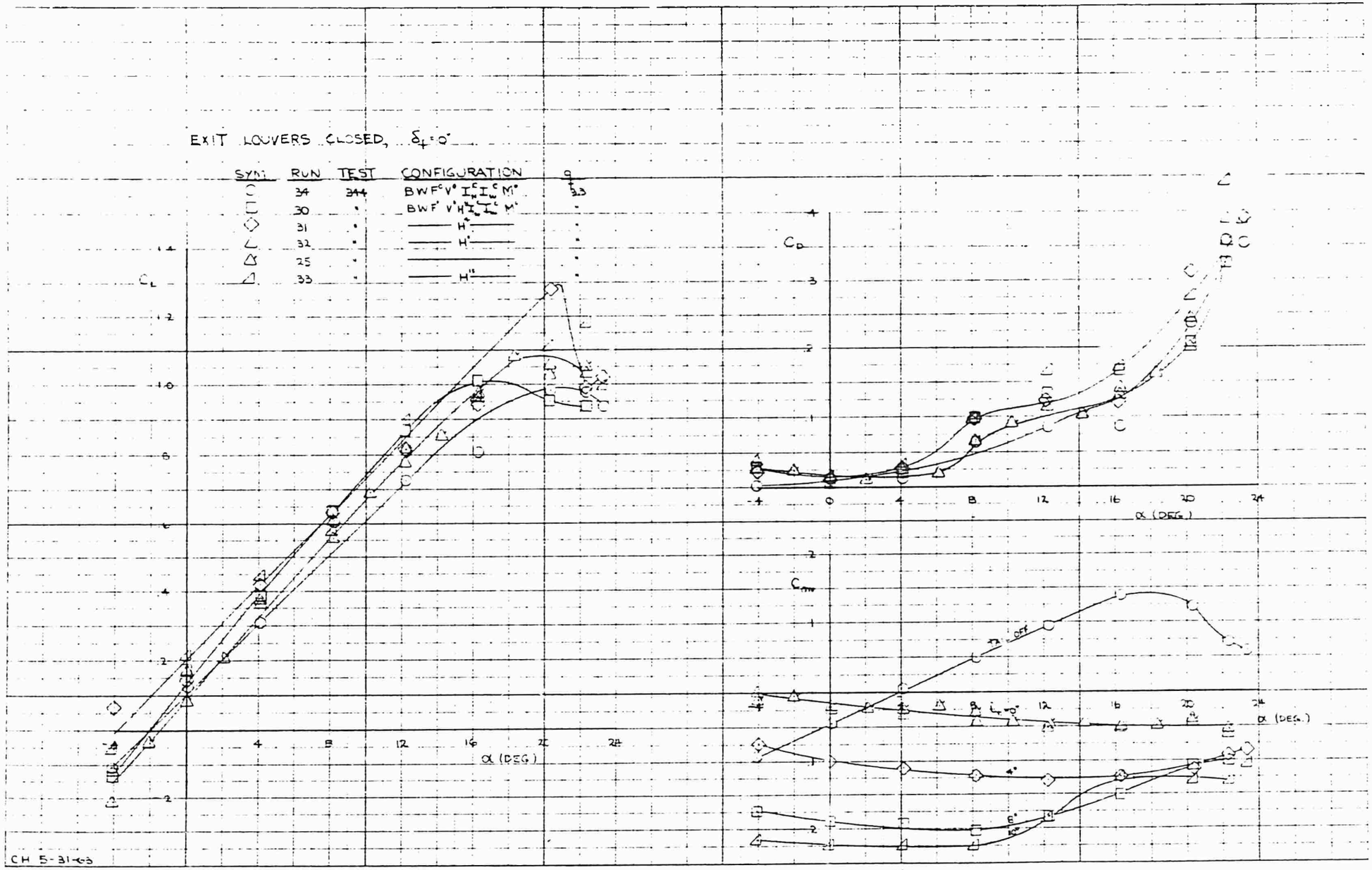

Figure 4.75 Horizontal Tail Effectiveness - Power Off, $\delta_f = 0°$

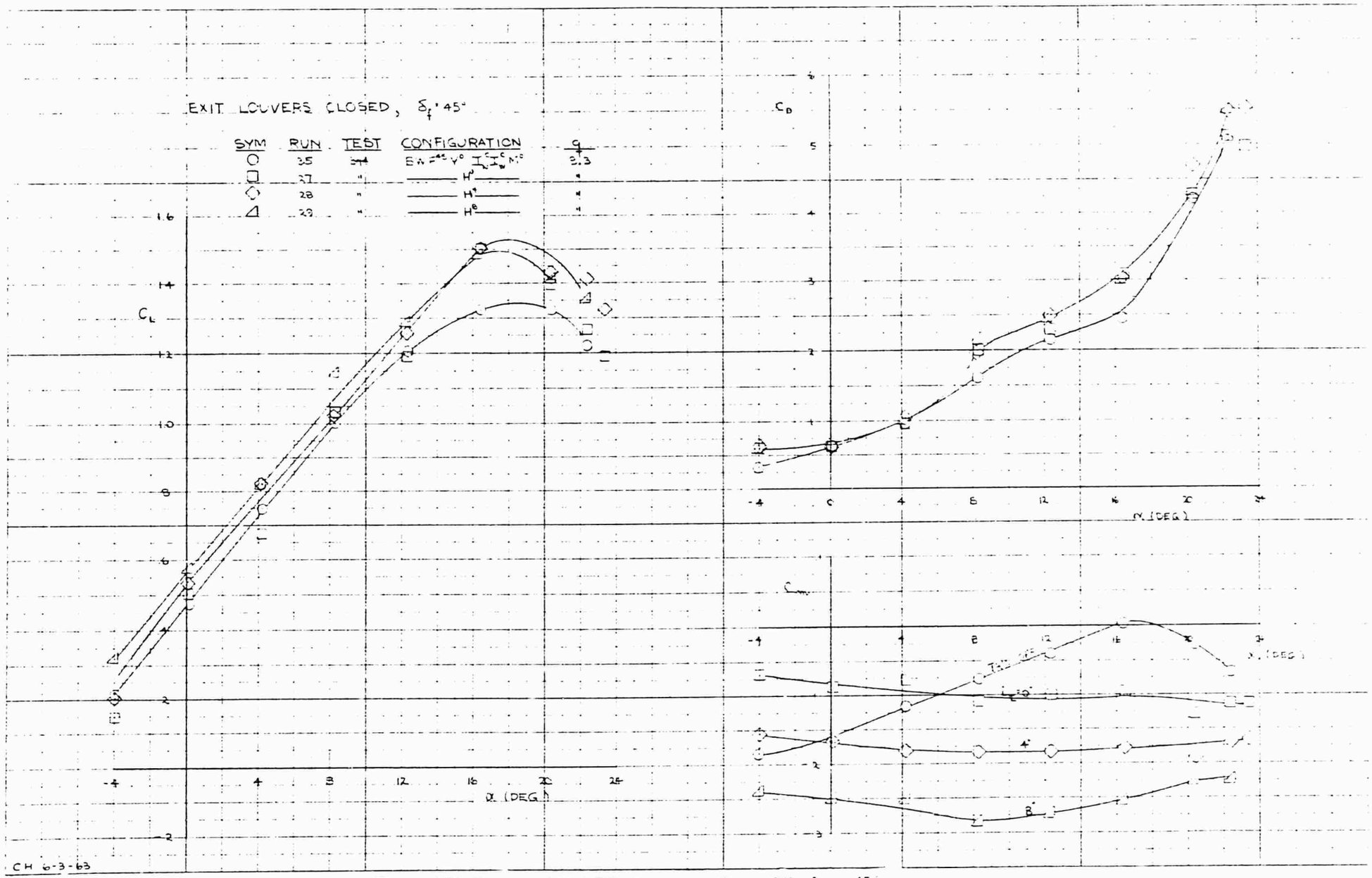

Figure 4.76 Horizontal Tail Effectiveness - Power Off. δ_f = 45°

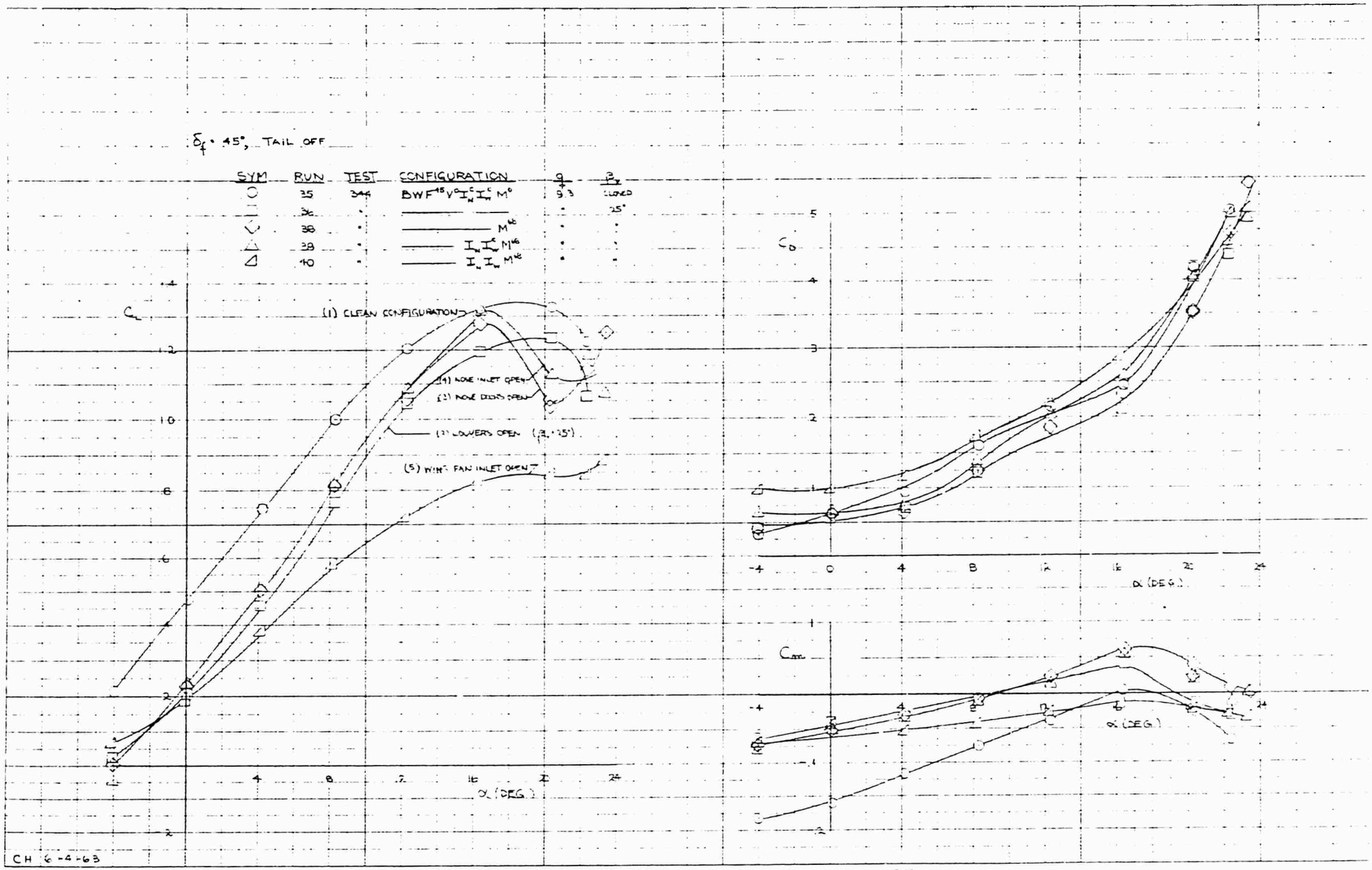

Figure 4.77 Effect of Conversion Sequence Configurations - Power Off

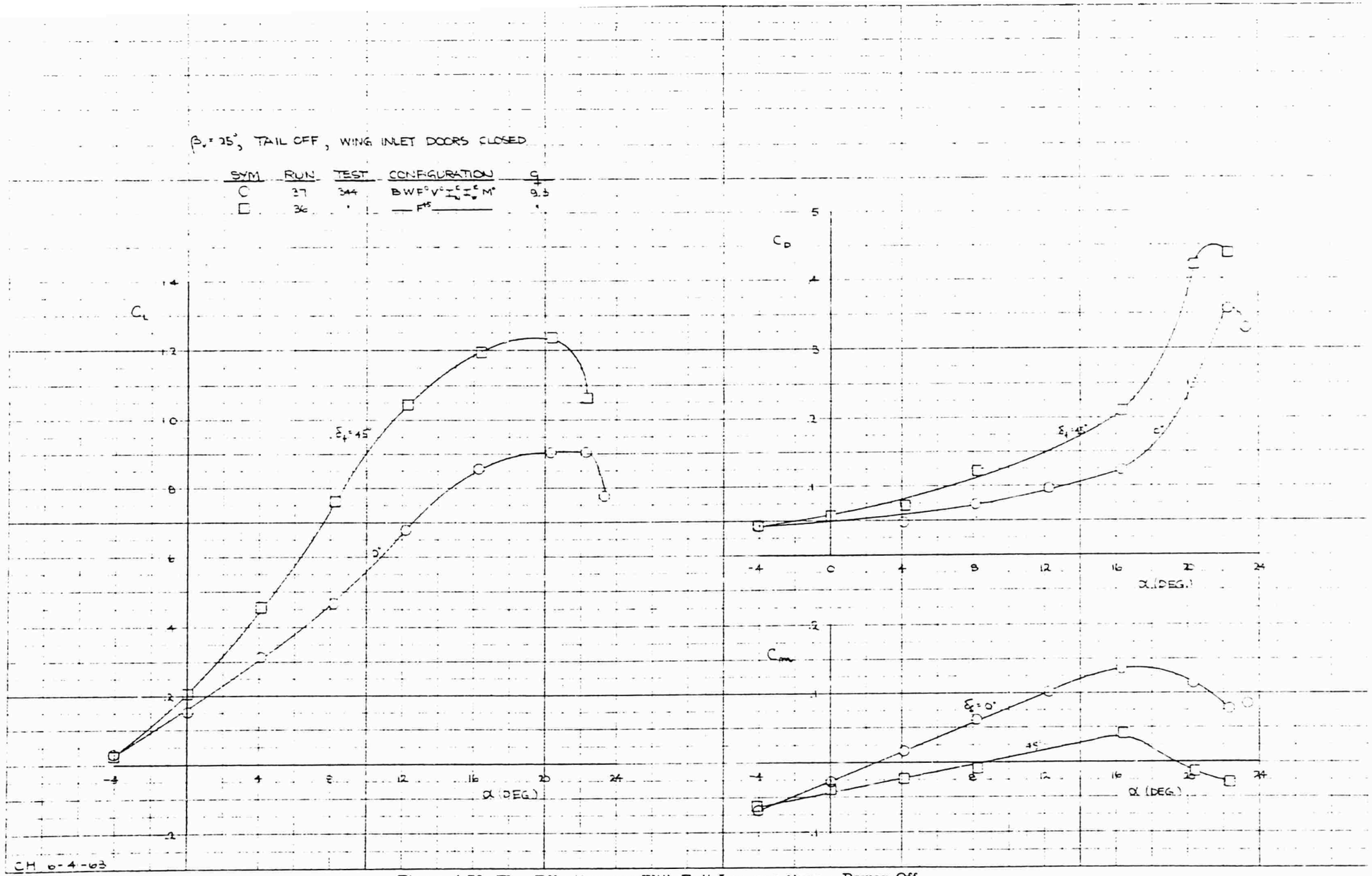

Figure 4.78 Flap Effectiveness With Exit Louvers Open - Power Off

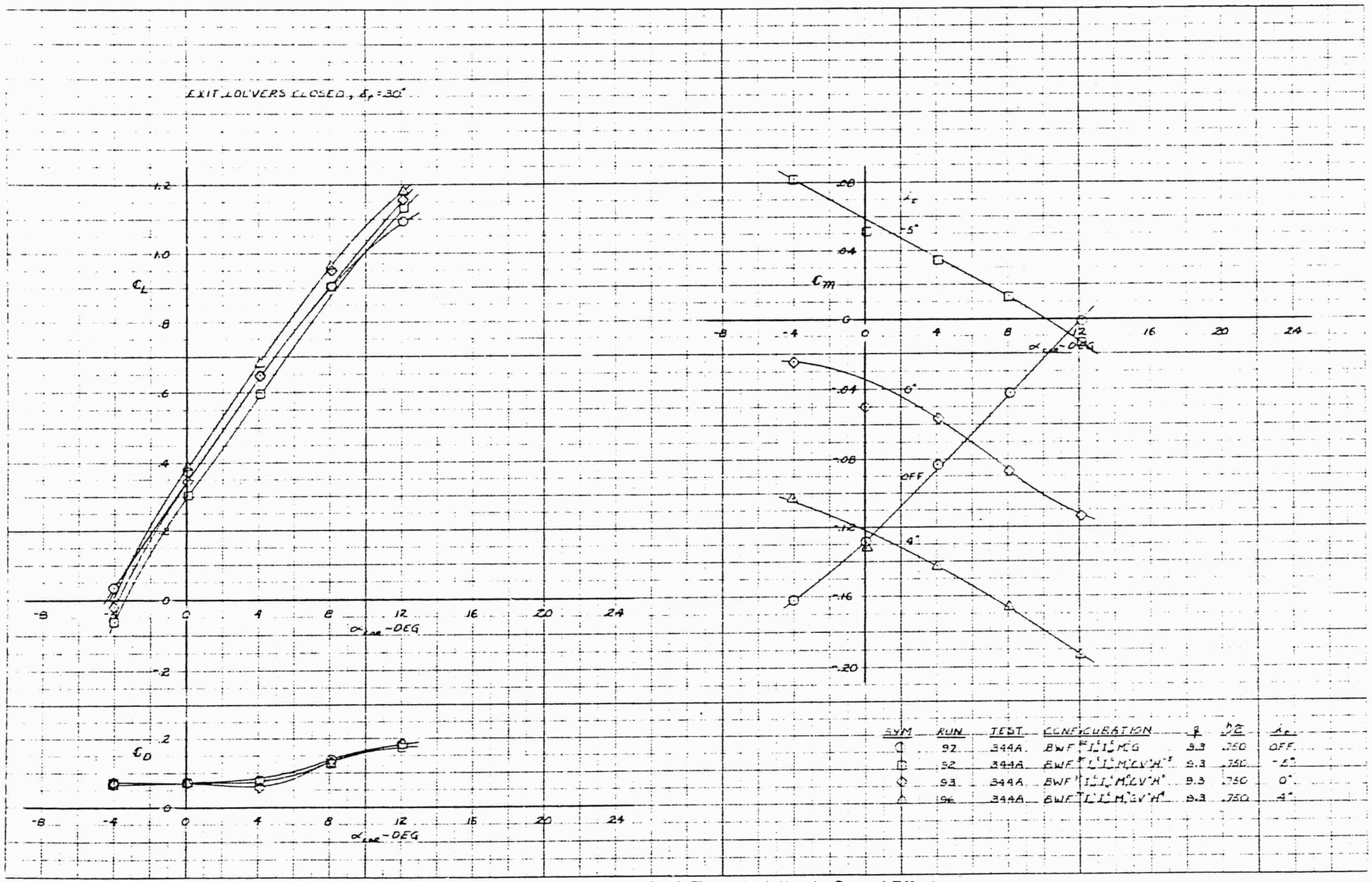

Figure 4.79 Power-Off Longitudinal Characteristics in Ground Effect, δ_f = 30°

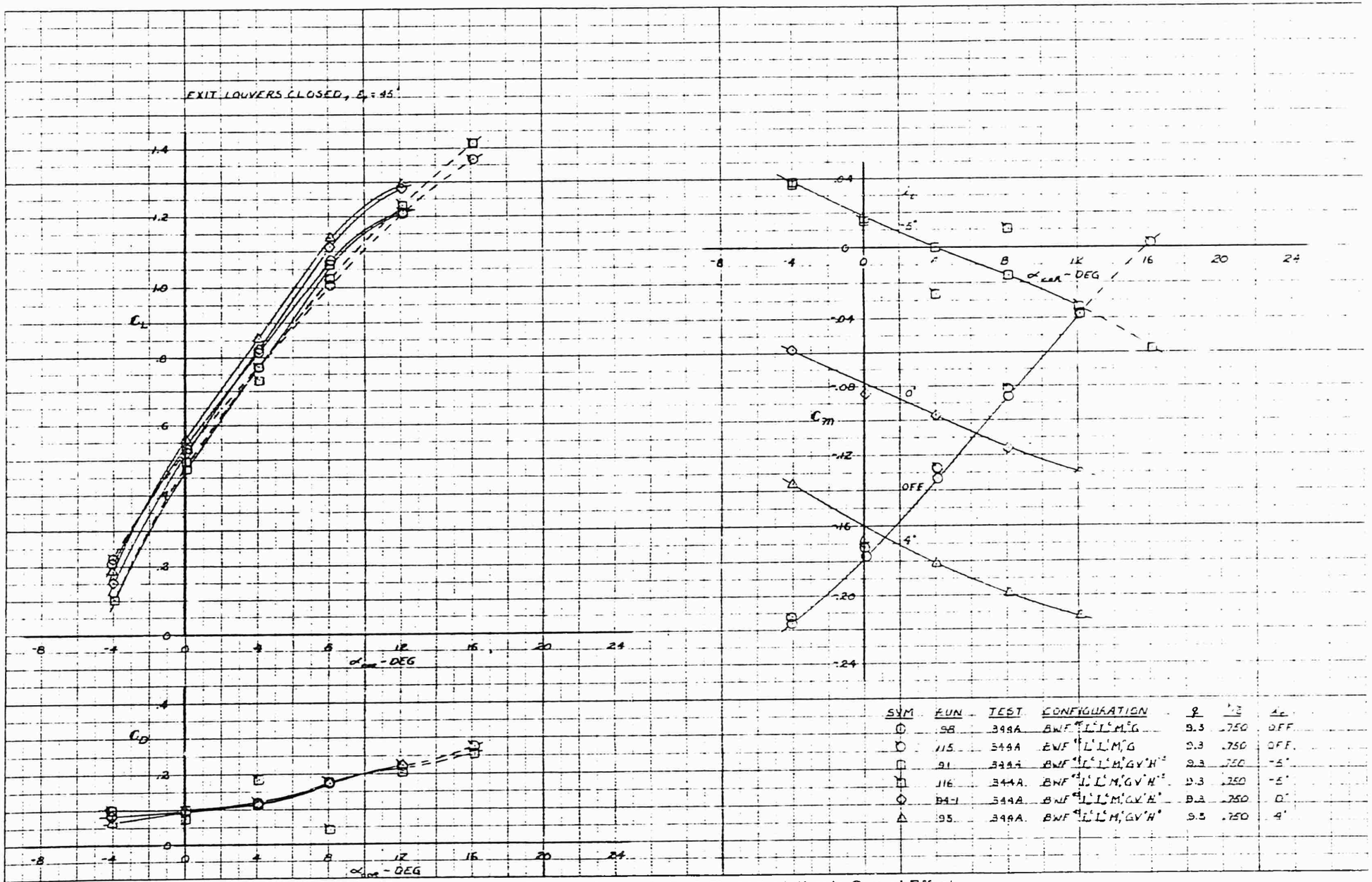

Figure 4.80 Power-Off Longitudinal Characteristics in Ground Effect, $\delta_f = 45°$

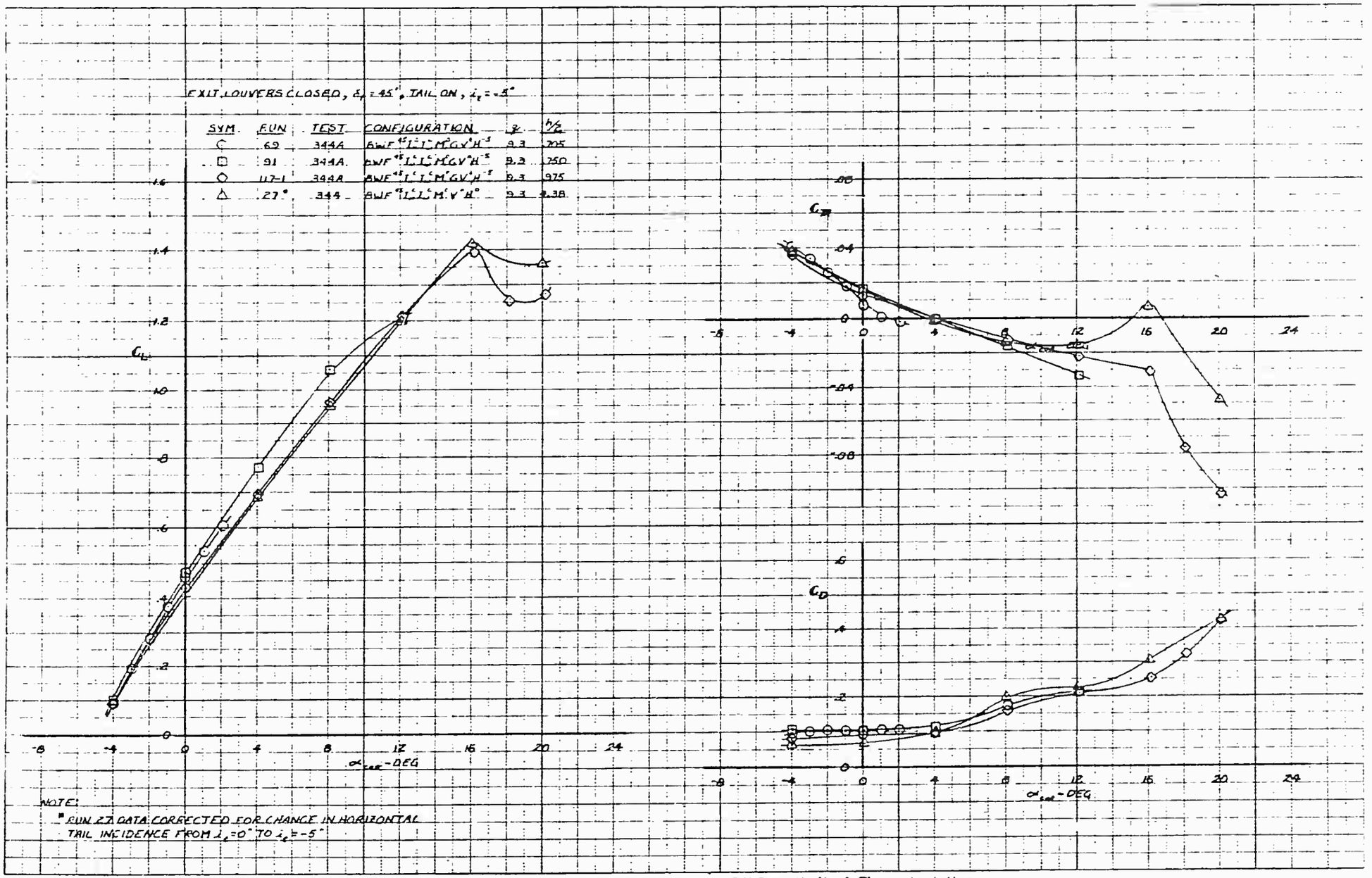

Figure 4.81 Effect of Ground Height On Power-Off Longitudinal Characteristics

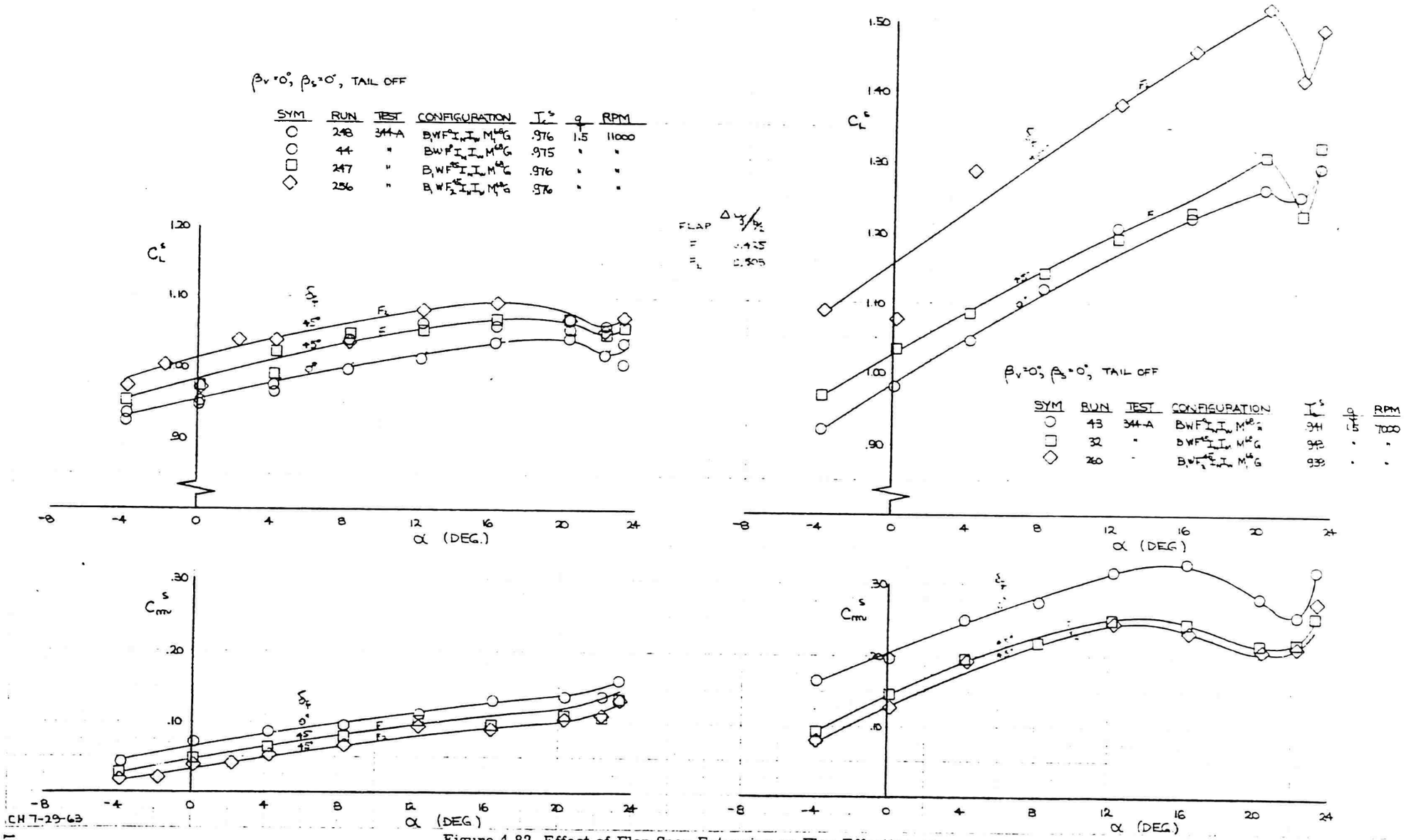

Figure 4.82 Effect of Flap Span Extension on Flap Effectiveness

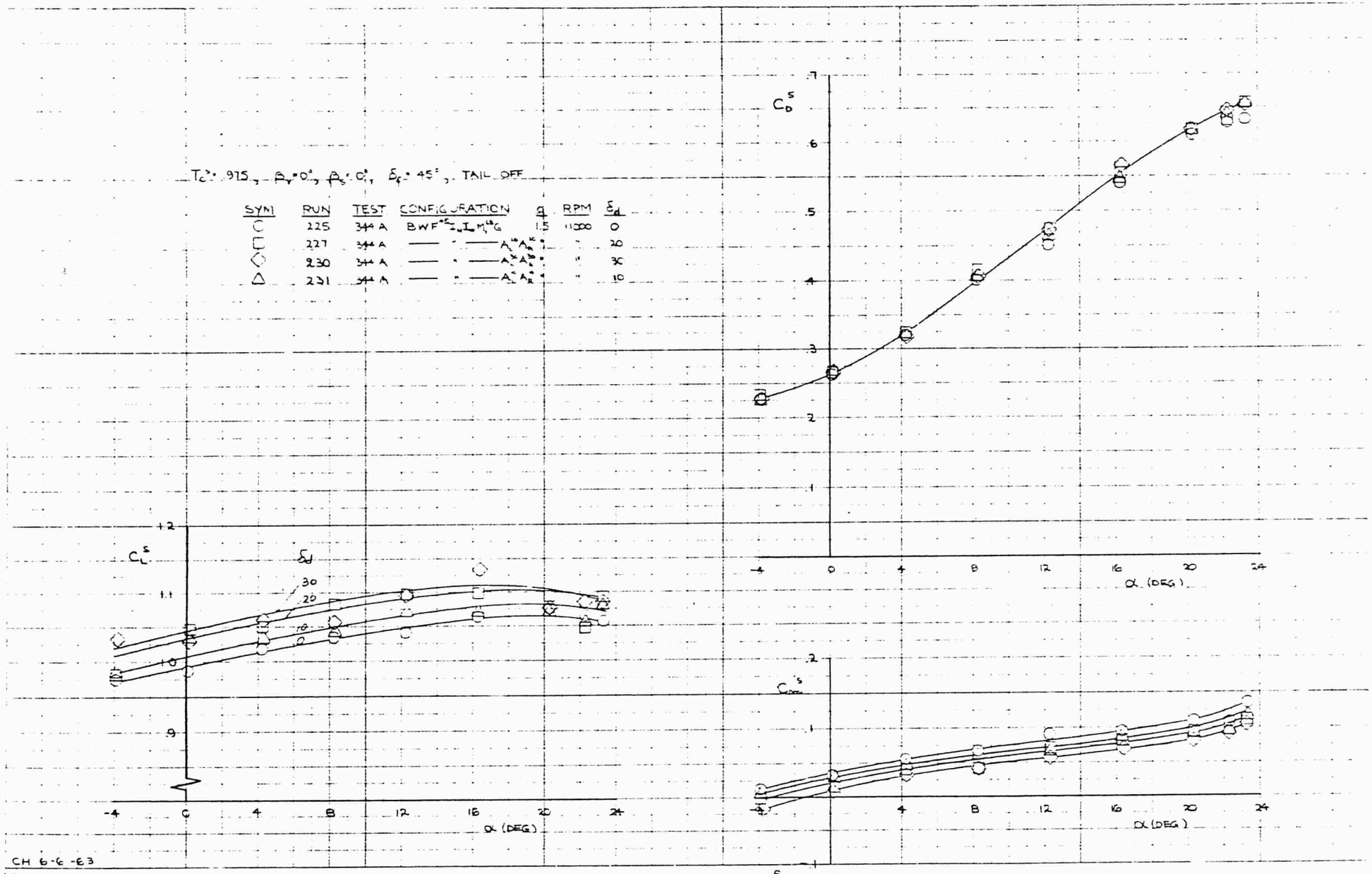

Figure 4.83 Effect of Aileron Droop, T_c^s = .975

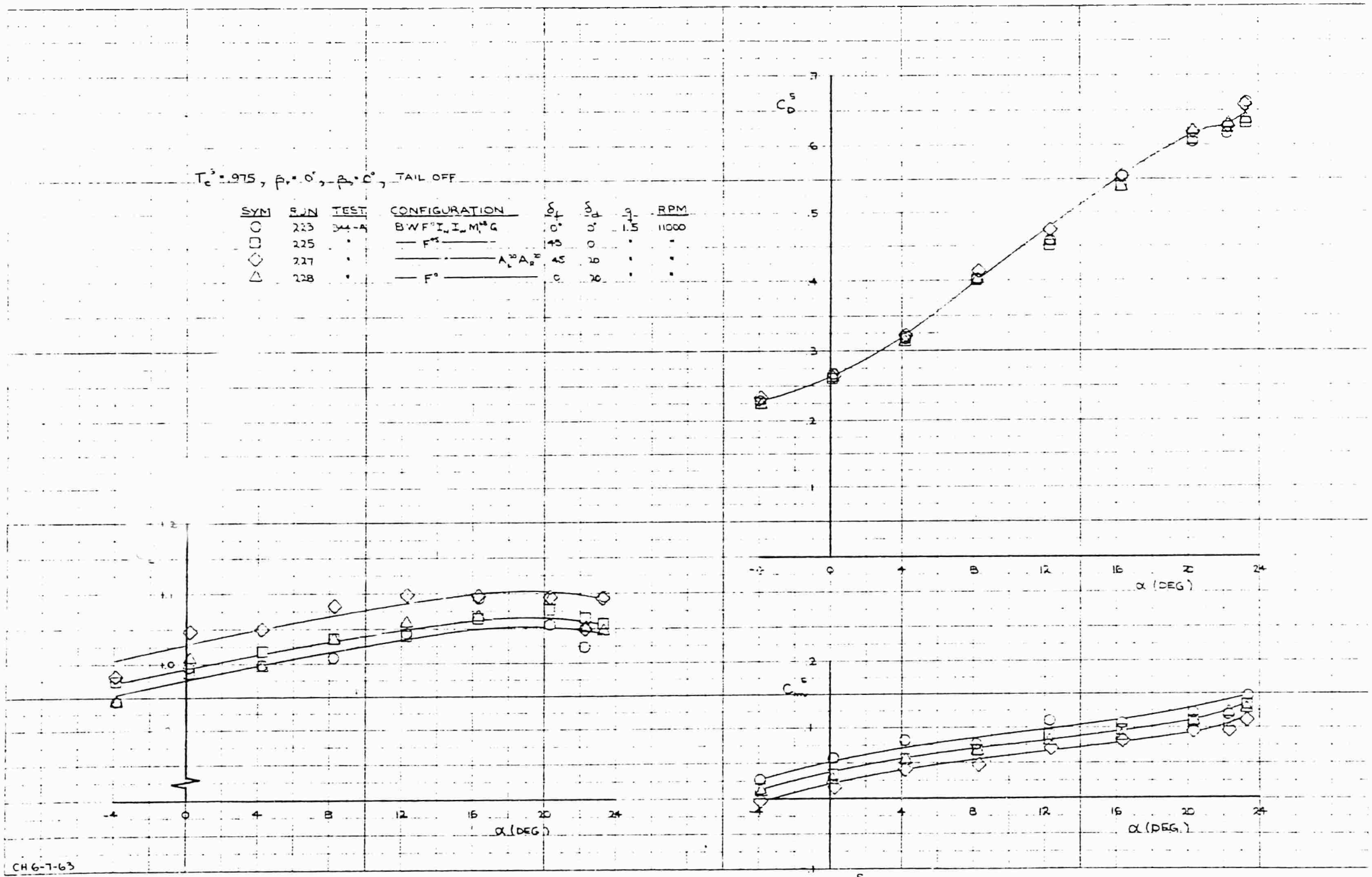

Figure 4.84 Effect of Aileron Droop on Flap Effectiveness, T_c^s = .975

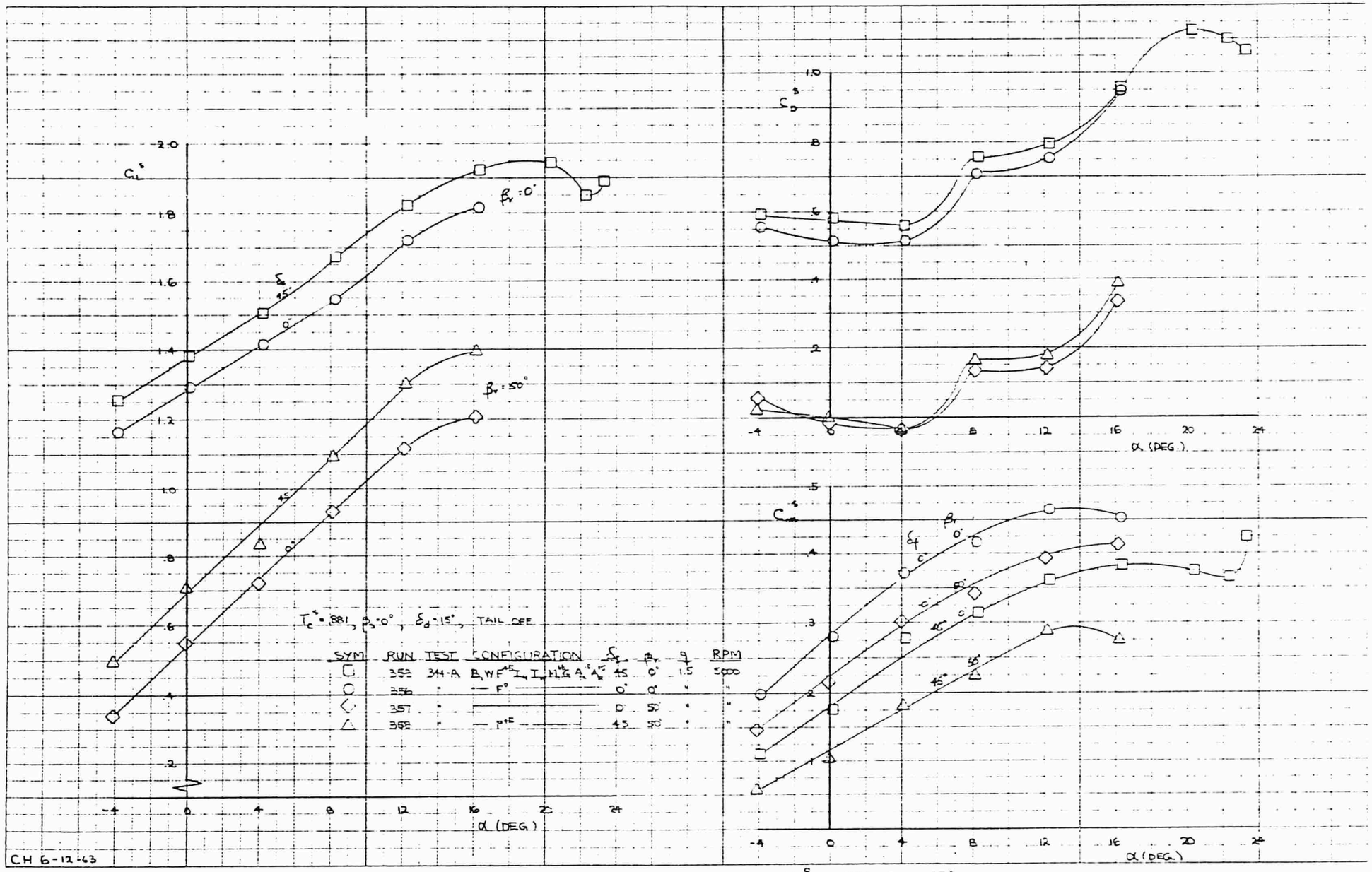

Figure 4.85 Effect of Vector Angle on Flap Effectiveness, $T_c^S = .881$, $\delta_d = 15°$

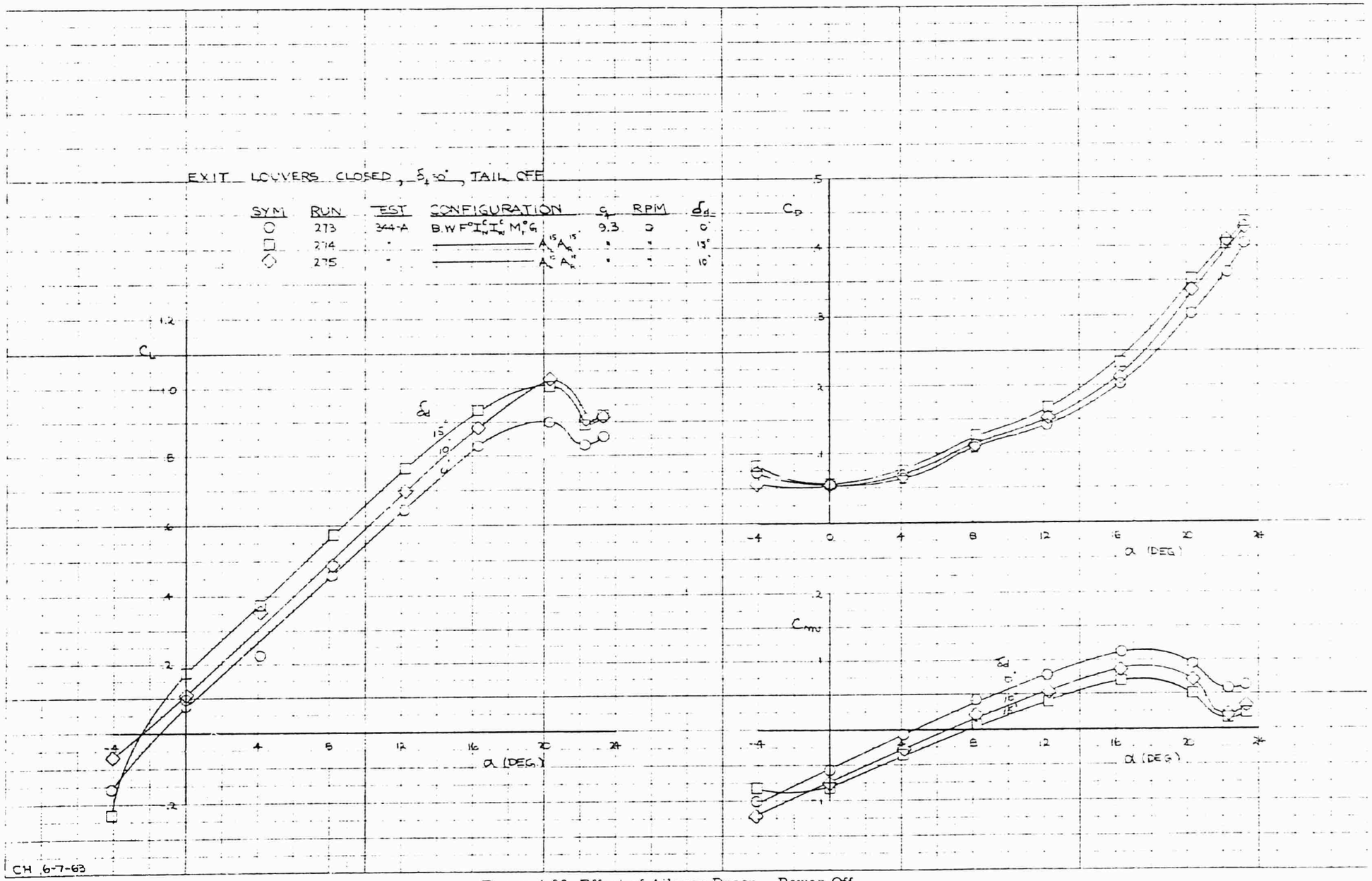

Figure 4.86 Effect of Aileron Droop - Power Off

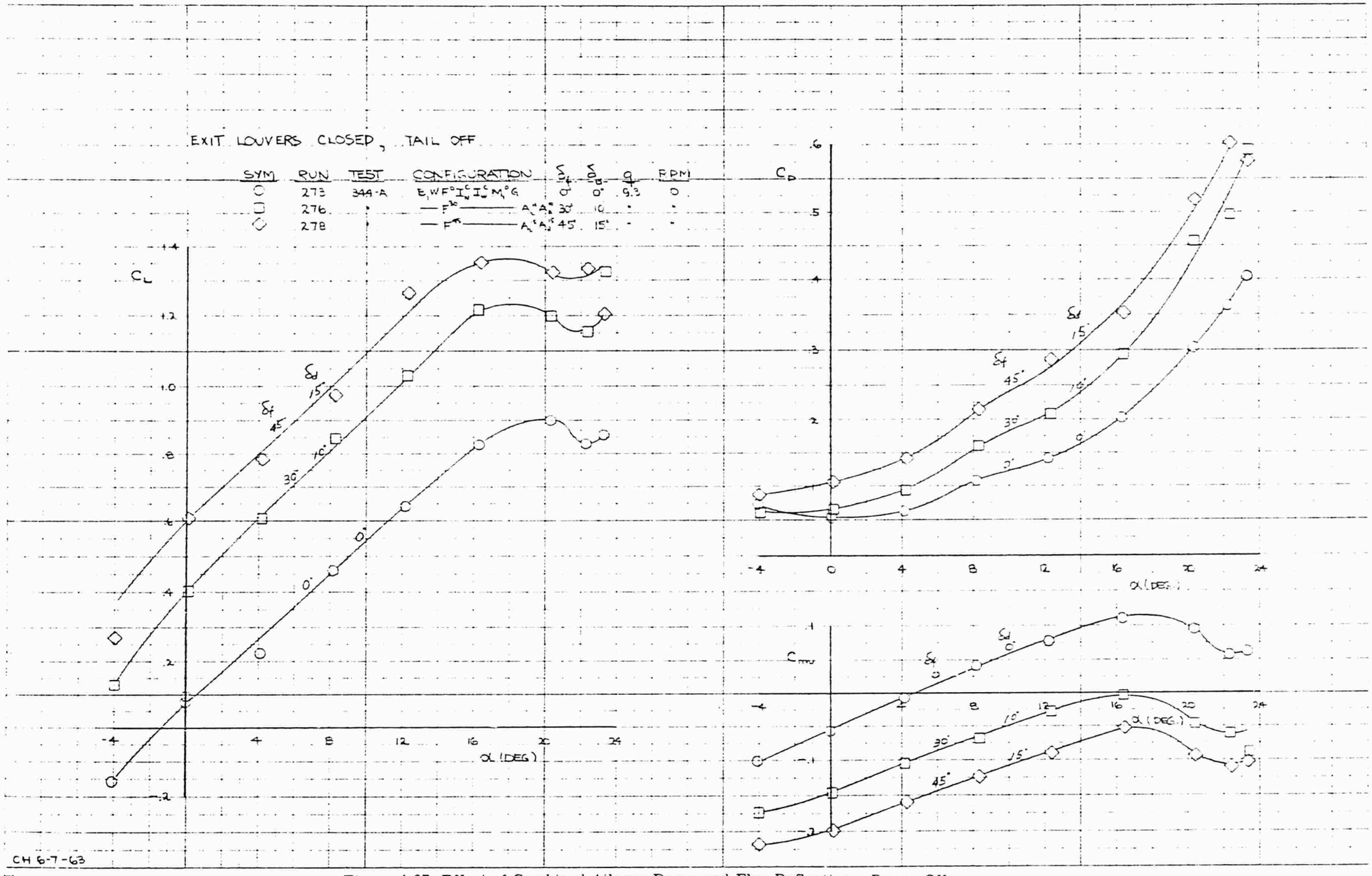

Figure 4.87 Effect of Combined Aileron Droop and Flap Deflection - Power Off

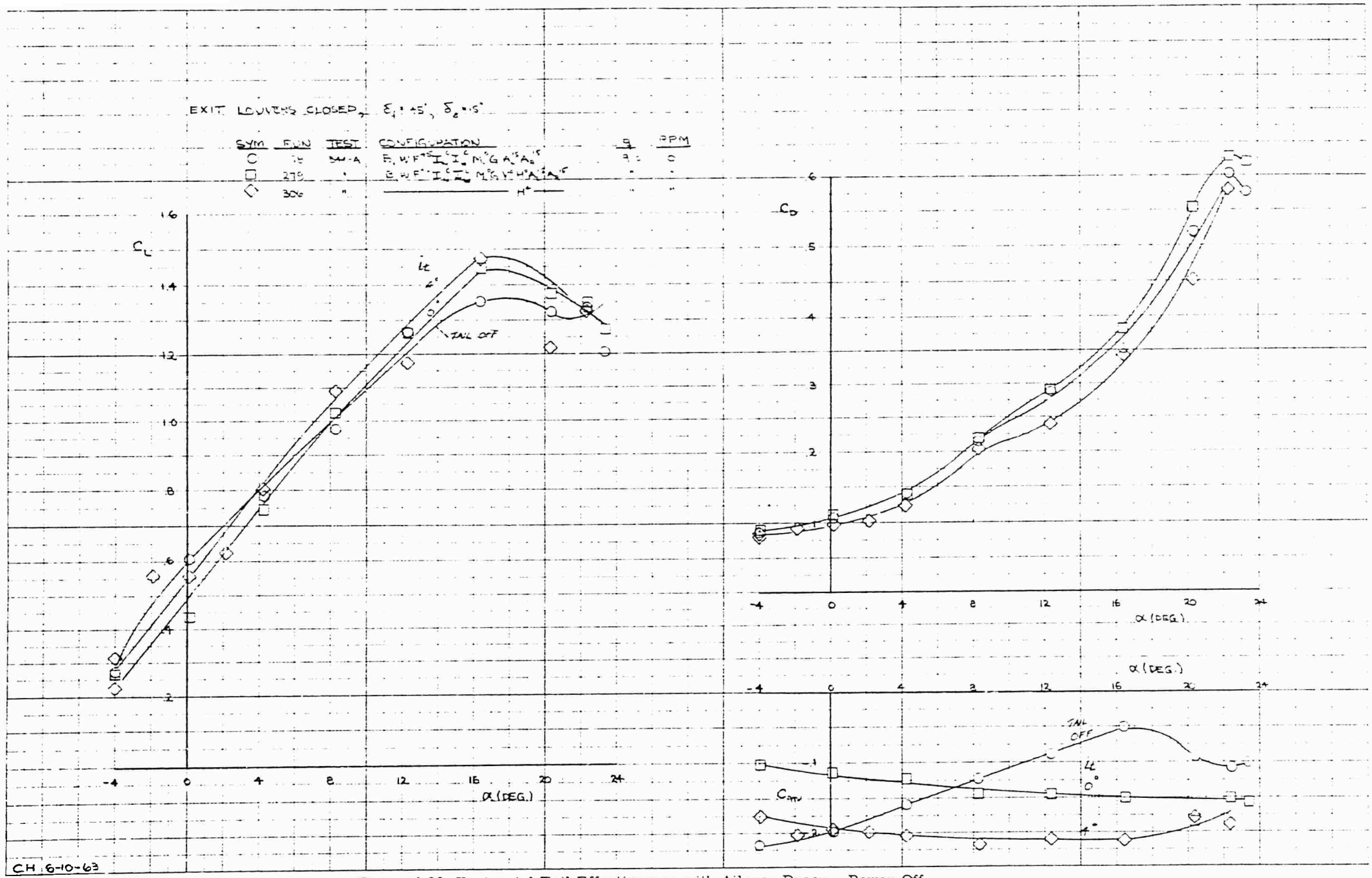

CH 6-10-63

Figure 4.88 Horizontal Tail Effectiveness with Aileron Droop - Power Off

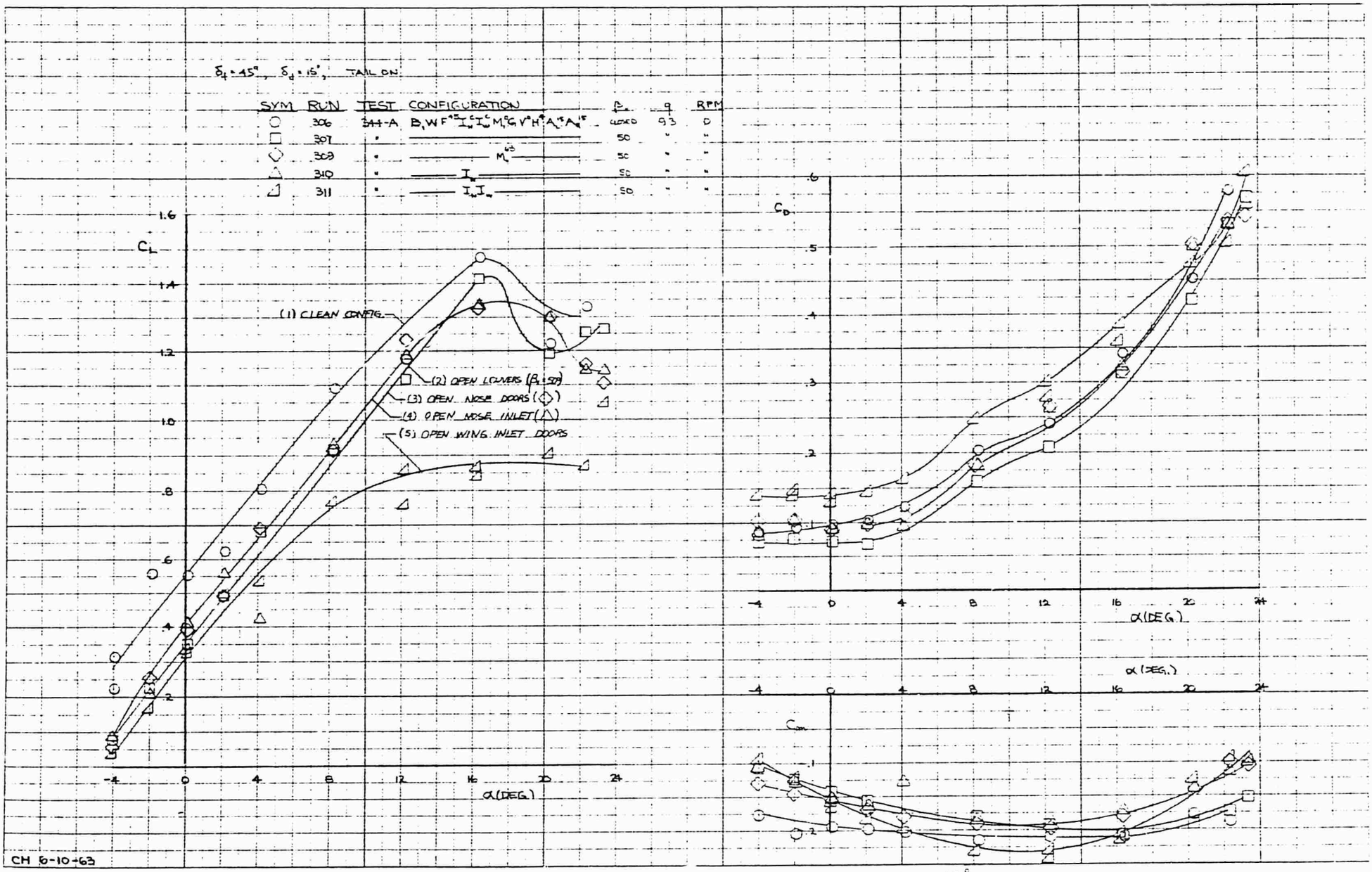

Figure 4.89 Effect of Conversion Sequence Configurations - Power Off, δ_d = 15°

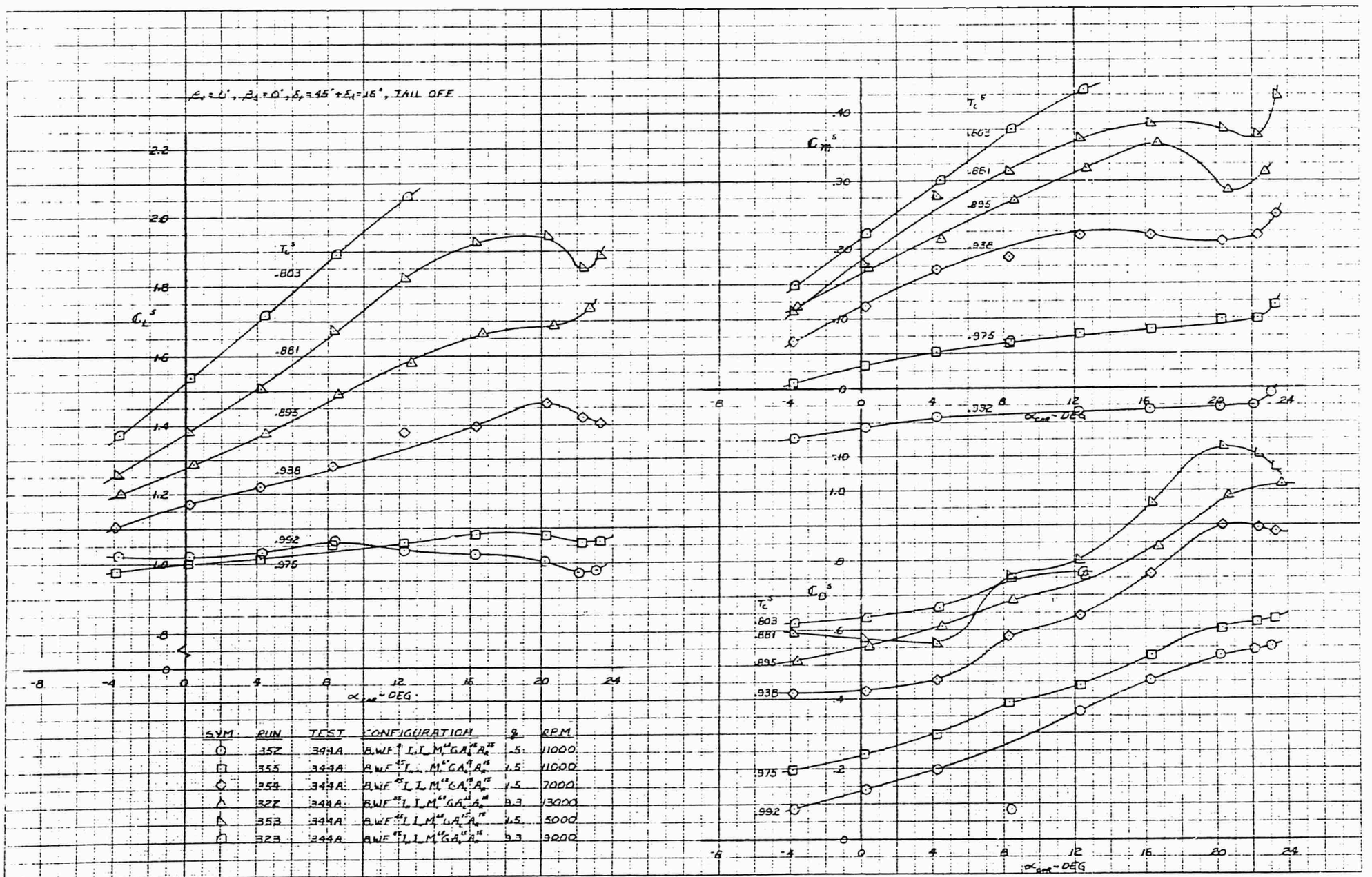

Figure 4.90 Effect of Thrust Coefficient With 15 Aileron Droop, $\beta_v = 0°$

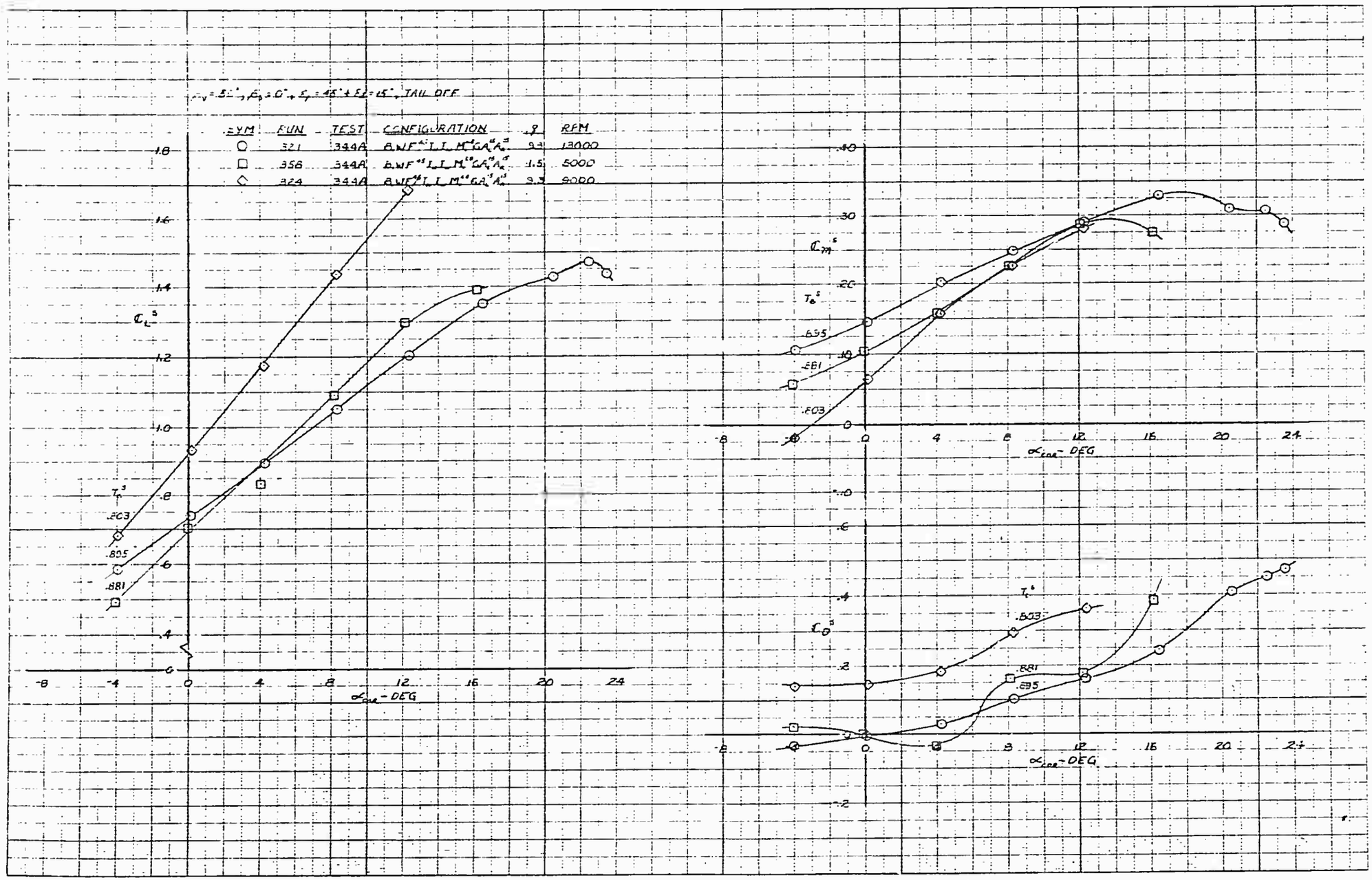

Figure 4.91 Effect of Thrust Coefficient With 15 Aileron Droop, β_V = 50°

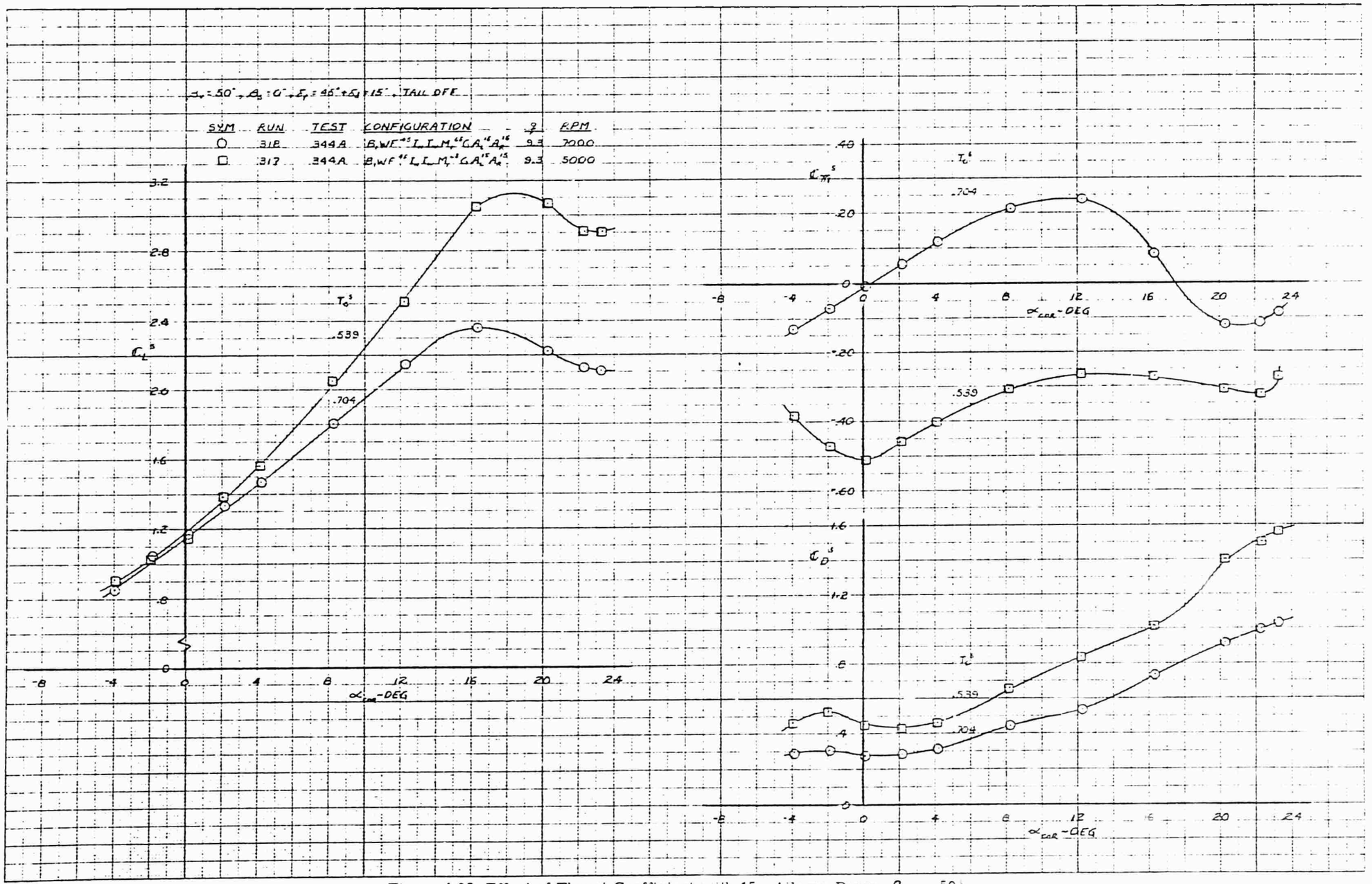

Figure 4.92 Effect of Thrust Coefficient with 15 Aileron Droop, β_v 50

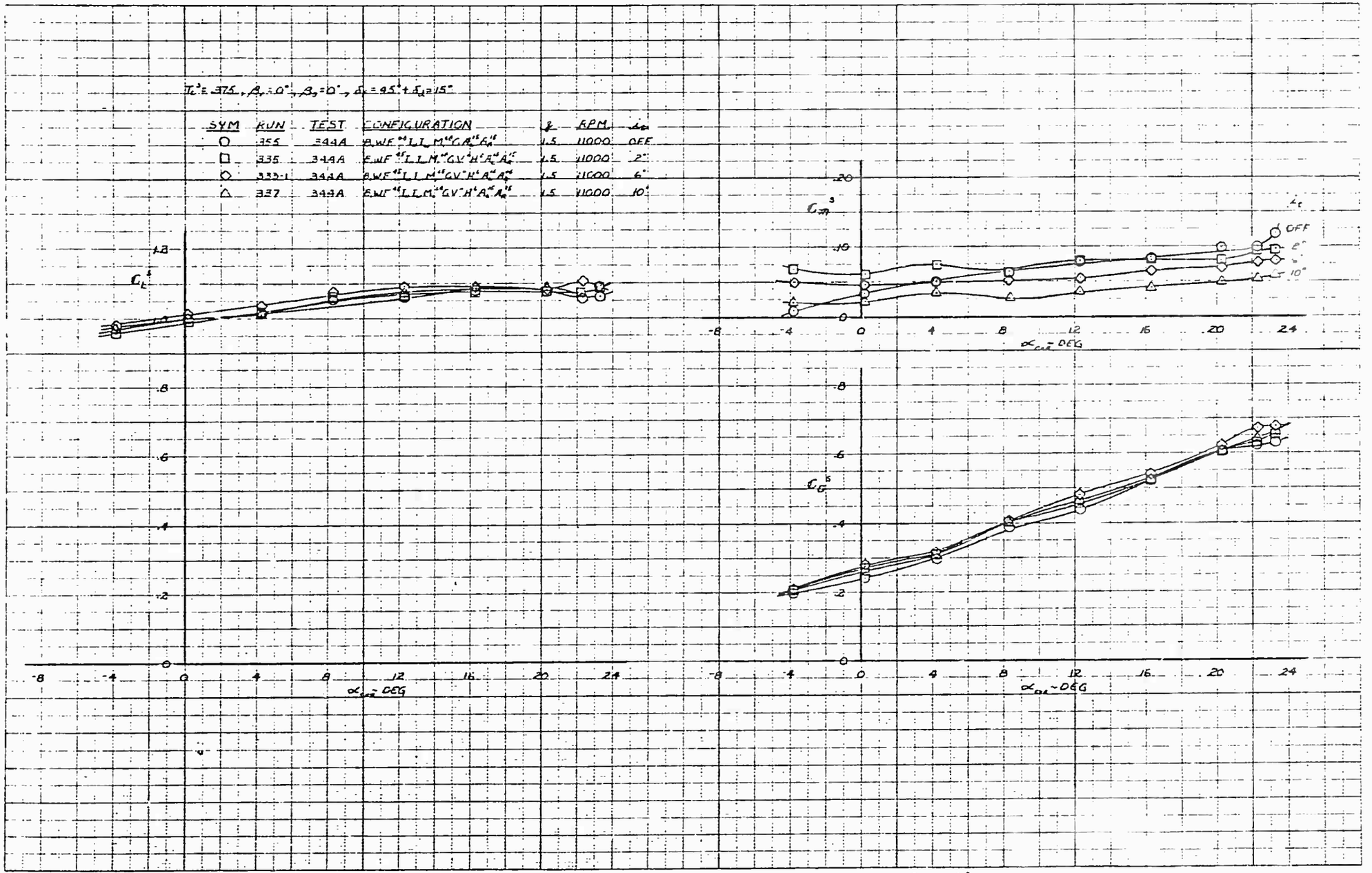

Figure 4.93 Horizontal Stabilizer Effectiveness With 15 Aileron Droop, β_v = 0°
T_c^s = .975

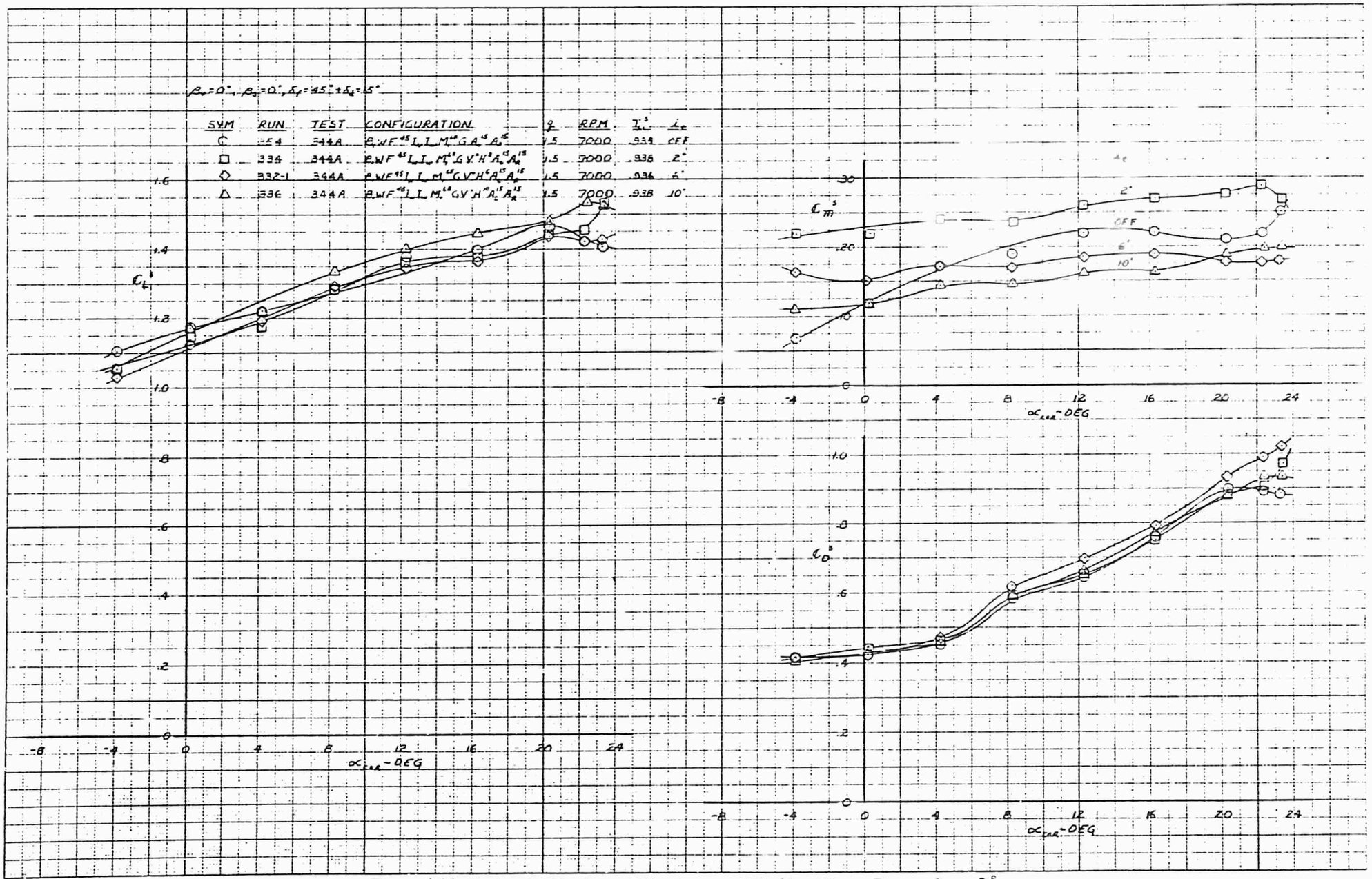

Figure 4.94 Horizontal Stabilizer Effectiveness With 15 Aileron Droop, $\beta_V = 0,^{\circ}$
$T_C^S = .938$

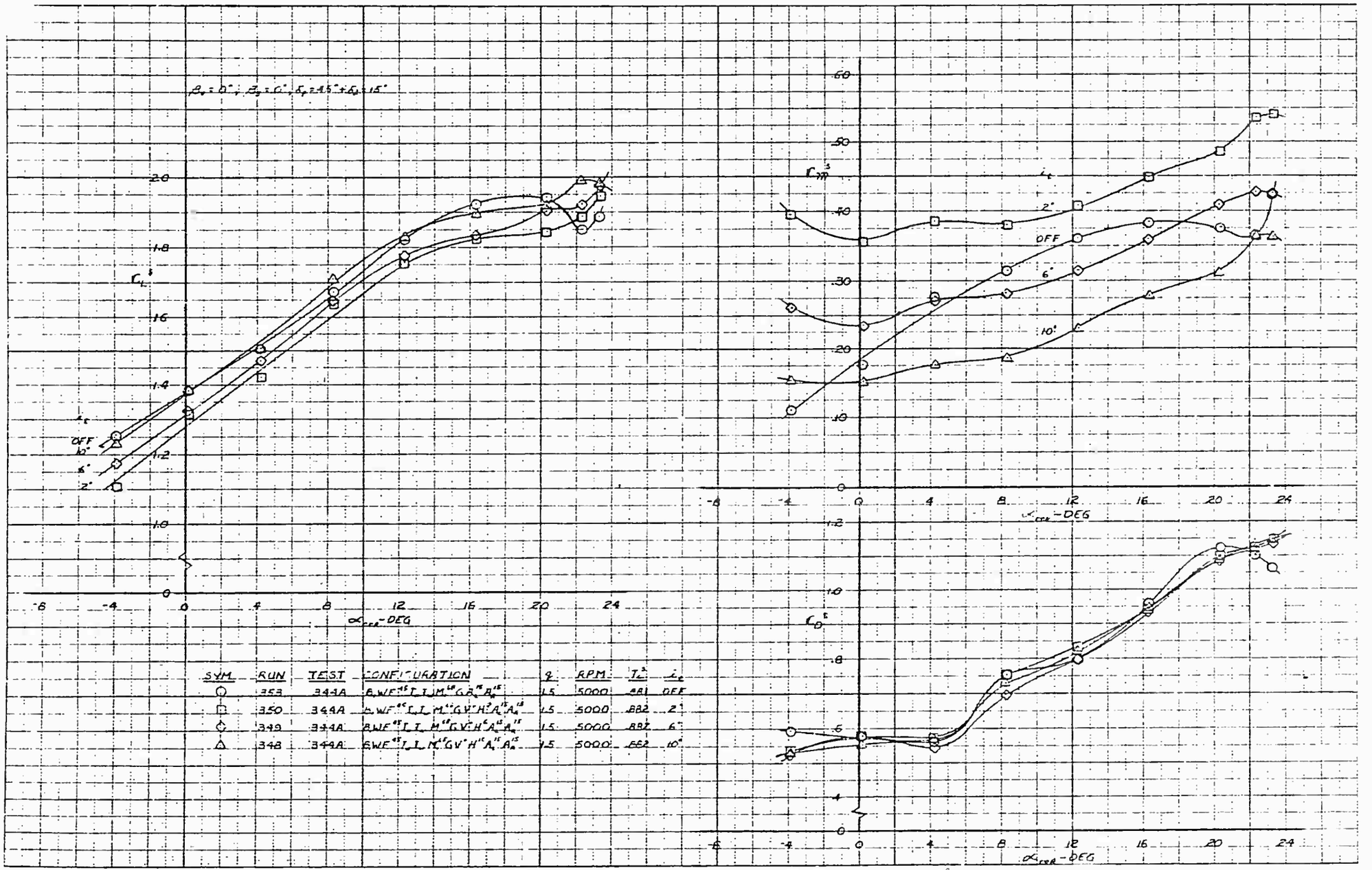

Figure 4.95 Horizontal Stabilizer Effectiveness With 15 Aileron Droop, $\beta_v = 0°$, $T_c^S = .882$

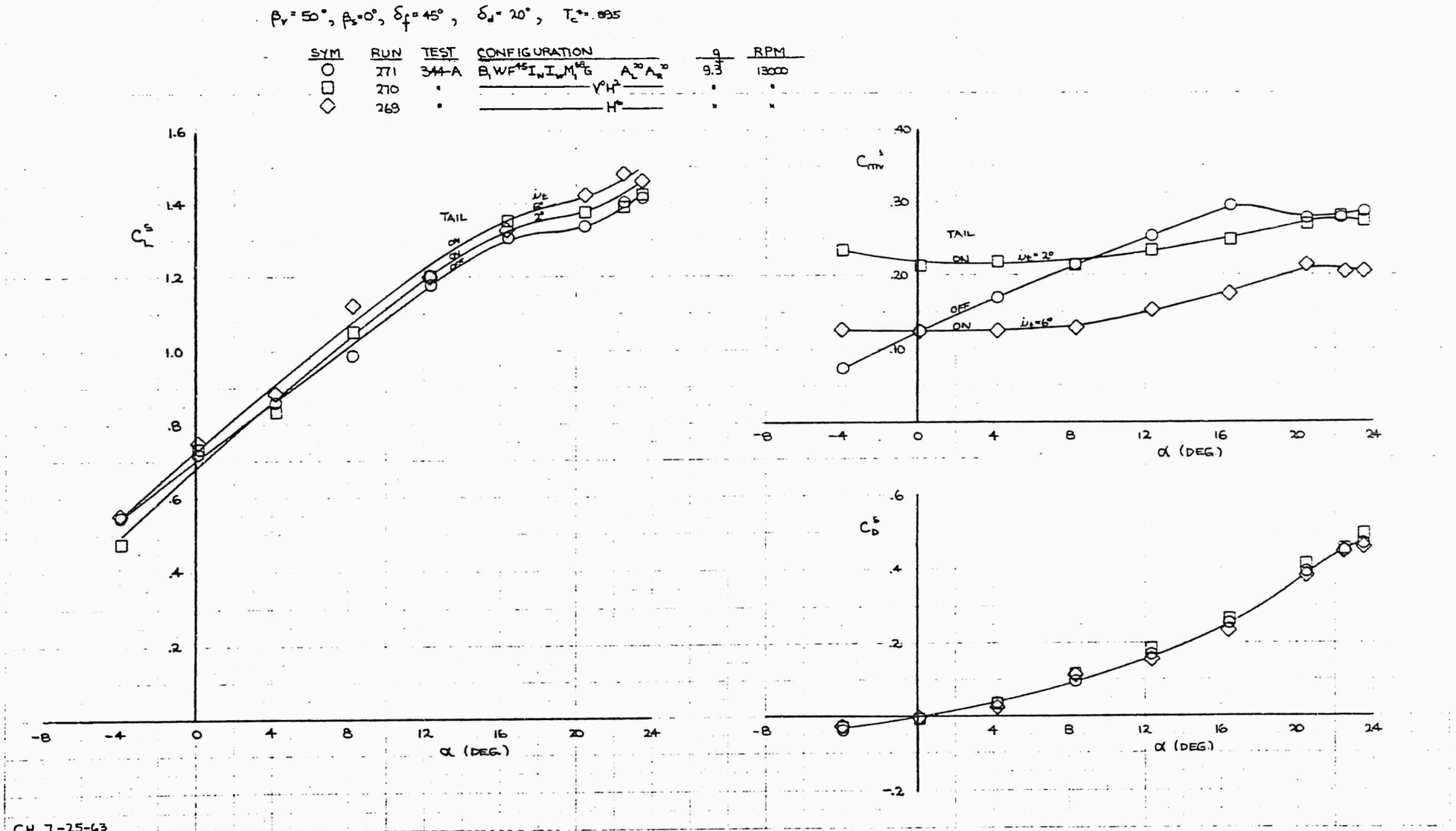

Figure 4.96 Horizontal Stabilizer Effectiveness With 15 Aileron Droop, $\beta_v = 50°$, $T_c^s = .895$

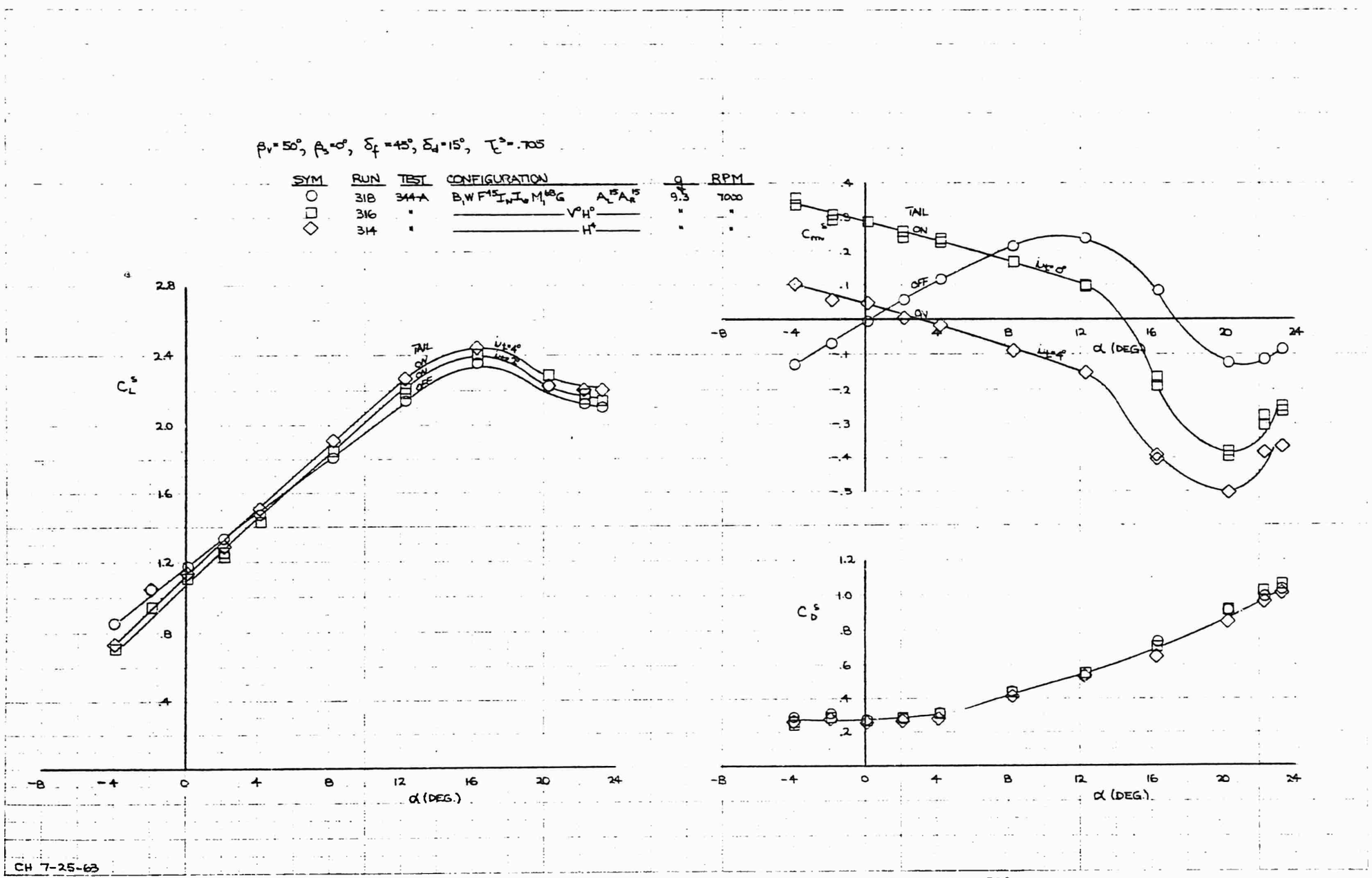

Figure 4.97 Horizontal Stabilizer Effectiveness With 15 Aileron Droop, β_v = 50°, T_c^s = .705

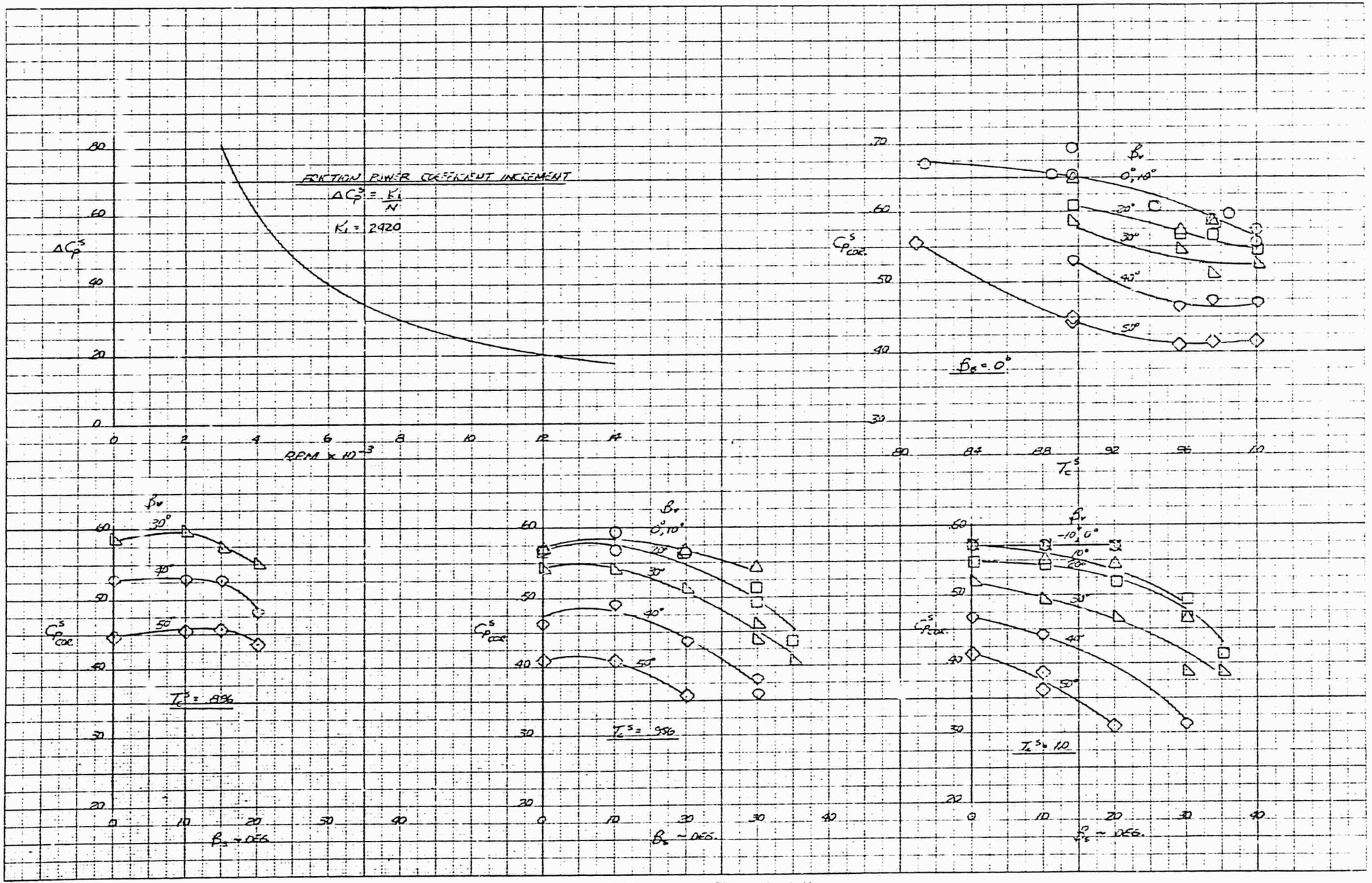

Figure 4.98 Fan Power Characteristics

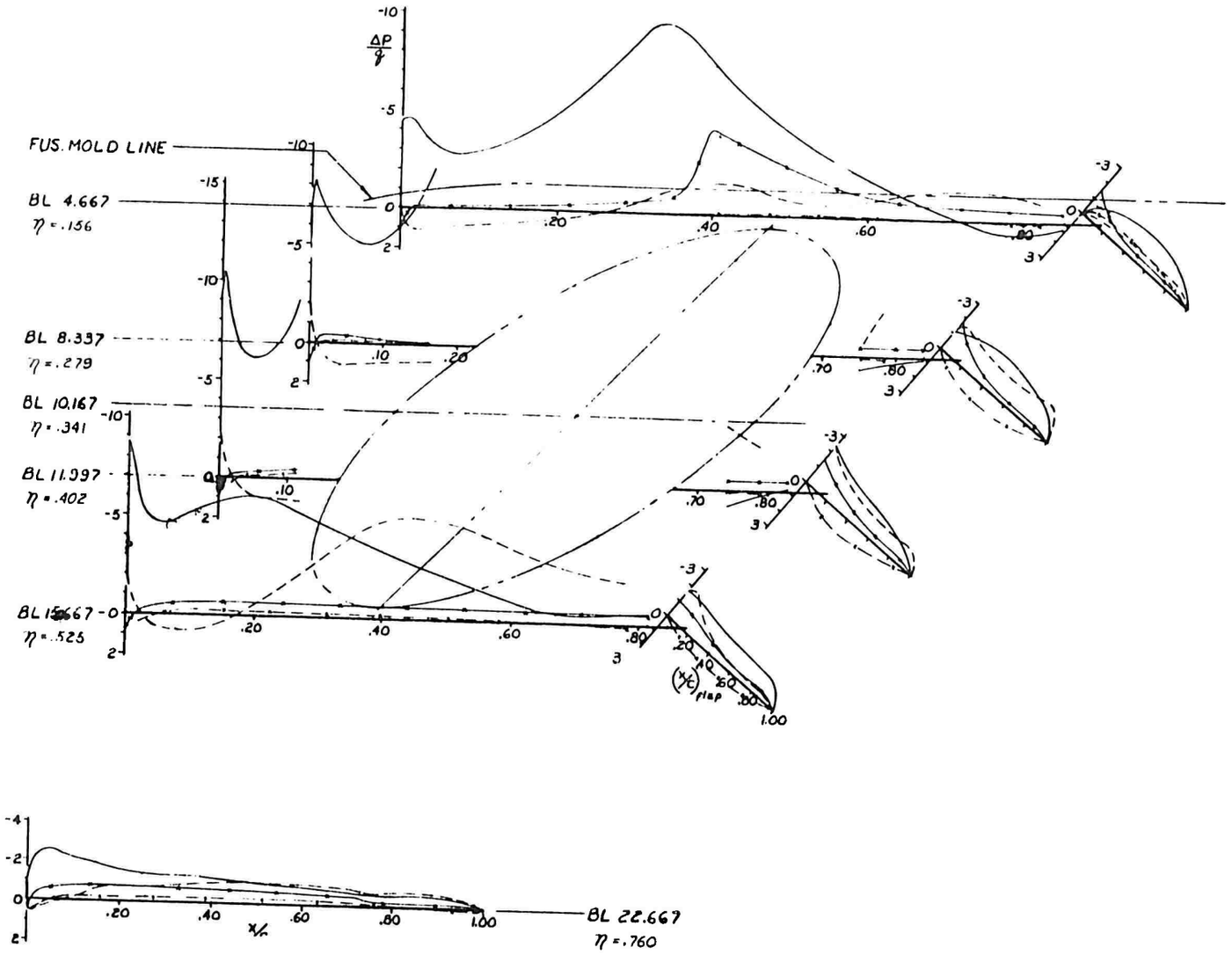

$\delta_f = 45°$, TAIL-ON, $\alpha = 0°$

RUN	TEST	CONFIGURATION	q	RPM	T_c'	NOSE FAN	C_L'	C_L	β_v	β_s	i_t
28	344A	$BWF^{45}I_wI_wM^{45}GV'H'^{8}$	1.6	8000	.956	ON	.969	—	0°	0°	15°
27	344	$BWF^{45}I_w'I_w'M'V'H'$	9.3	OFF	0.0	OFF	—	.506	CLOSED		0°

CODE	SURFACE	RUN
———	UPPER	28
- - - - -	LOWER	28
—x—x—x—	UPPER	27
-x- -x- -x-	LOWER	27

Figure 4.99 Effect of Power On Wind Static Pressure Distribution

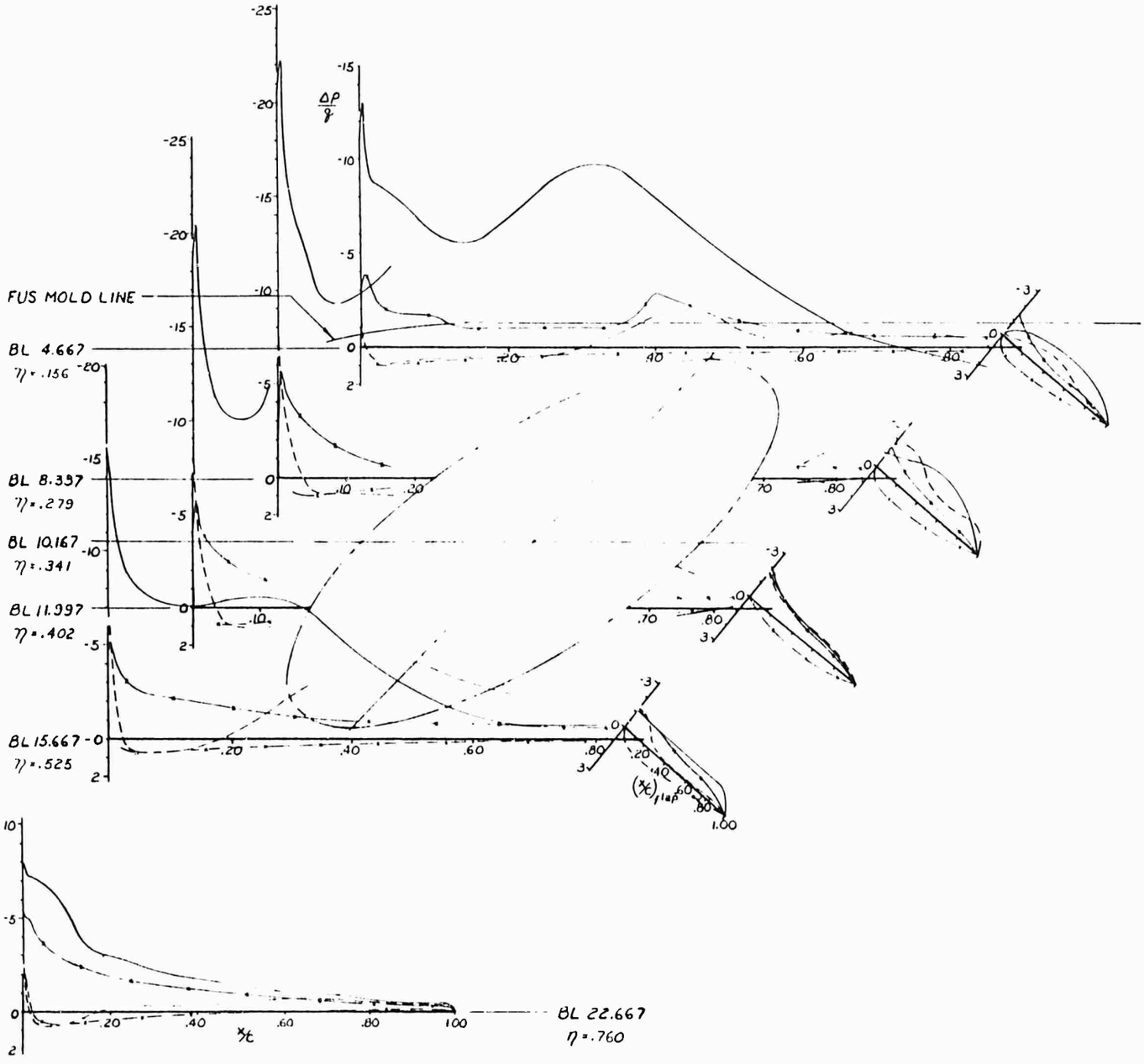

$\delta_f = 45°$, TAIL-ON, $\alpha = 16°$

RUN	TEST	CONFIGURATION	$\frac{T}{q}$	RPM	T_c[1]	NOSE FAN	C_L[2]	C_L	β_v	β_s	δ_t
28	344A	BWF[45] I, L, M[45] GV' H[45]	1.5	8000	.956	ON	1.141	—	0°	0°	15°
27	344	BWF[45] L' L' M' V' H'	93	OFF	0.0	OFF	—	1.305	CLOSED		0°

CODE	SURFACE	RUN
———	UPPER	28
- - -	LOWER	28
—*—*—*—	UPPER	27
-*- -*- -*-	LOWER	27

Figure 4.100 Effect of Power On Wing Static Pressure Distribution

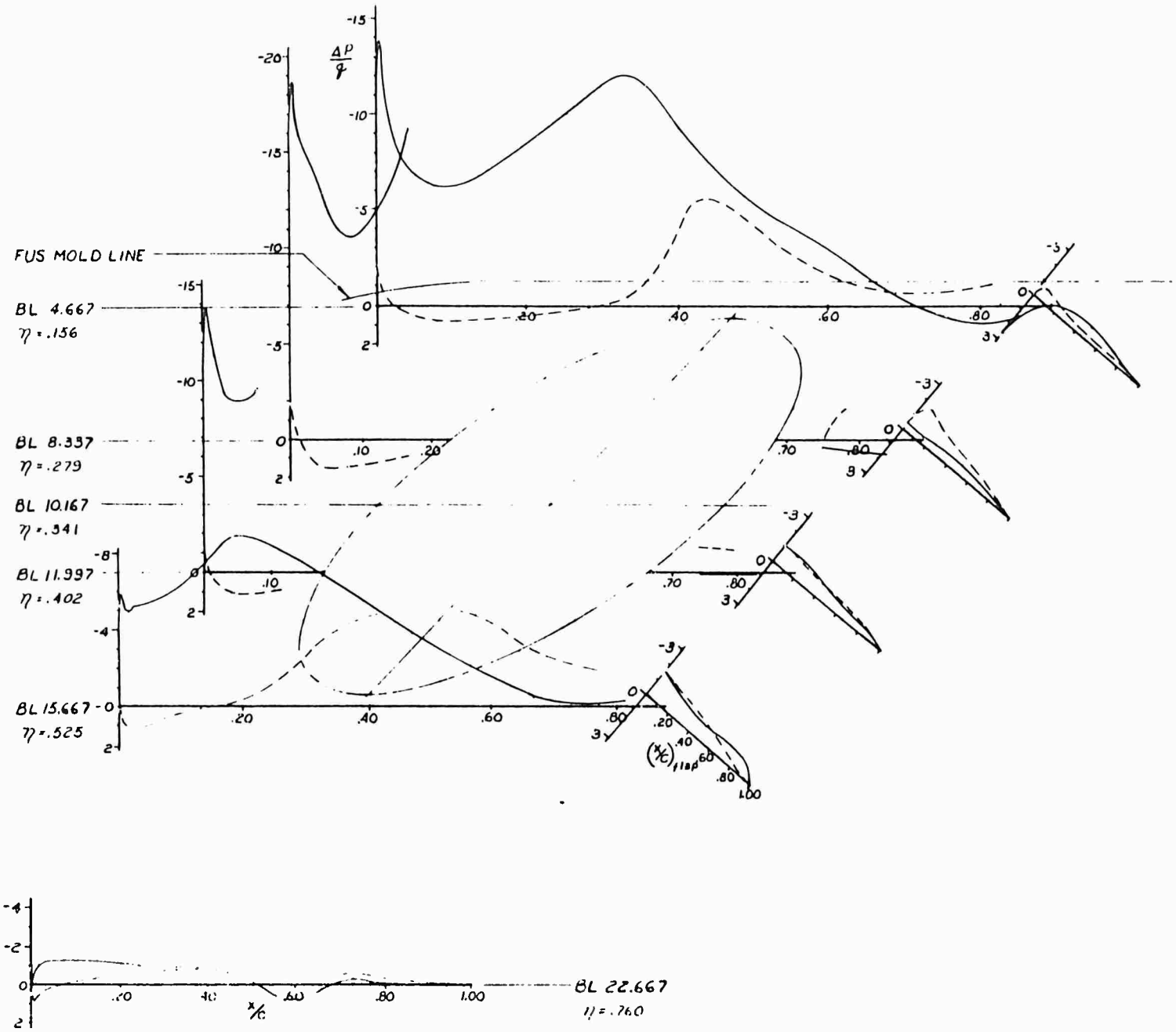

$\beta_V = 20°$, $\beta_s = 0°$, $\delta_f = 45°$, TAIL-ON, $i_t = 15°$, $\alpha = 0°$,

RUN	TEST	CONFIGURATION	$\bar{q}$	RPM	T_c^s	NOSE FAN	C_L^s
154	344A	BWF "S" I_w I_w M "GV" H"	1.3	11000	.975	ON	.818

CODE	SURFACE
———	UPPER
- - - - - -	LOWER

Figure 4.101 Wing Pressure Distribution For Trimmed Condition in Transition, $\beta_V = 20°$

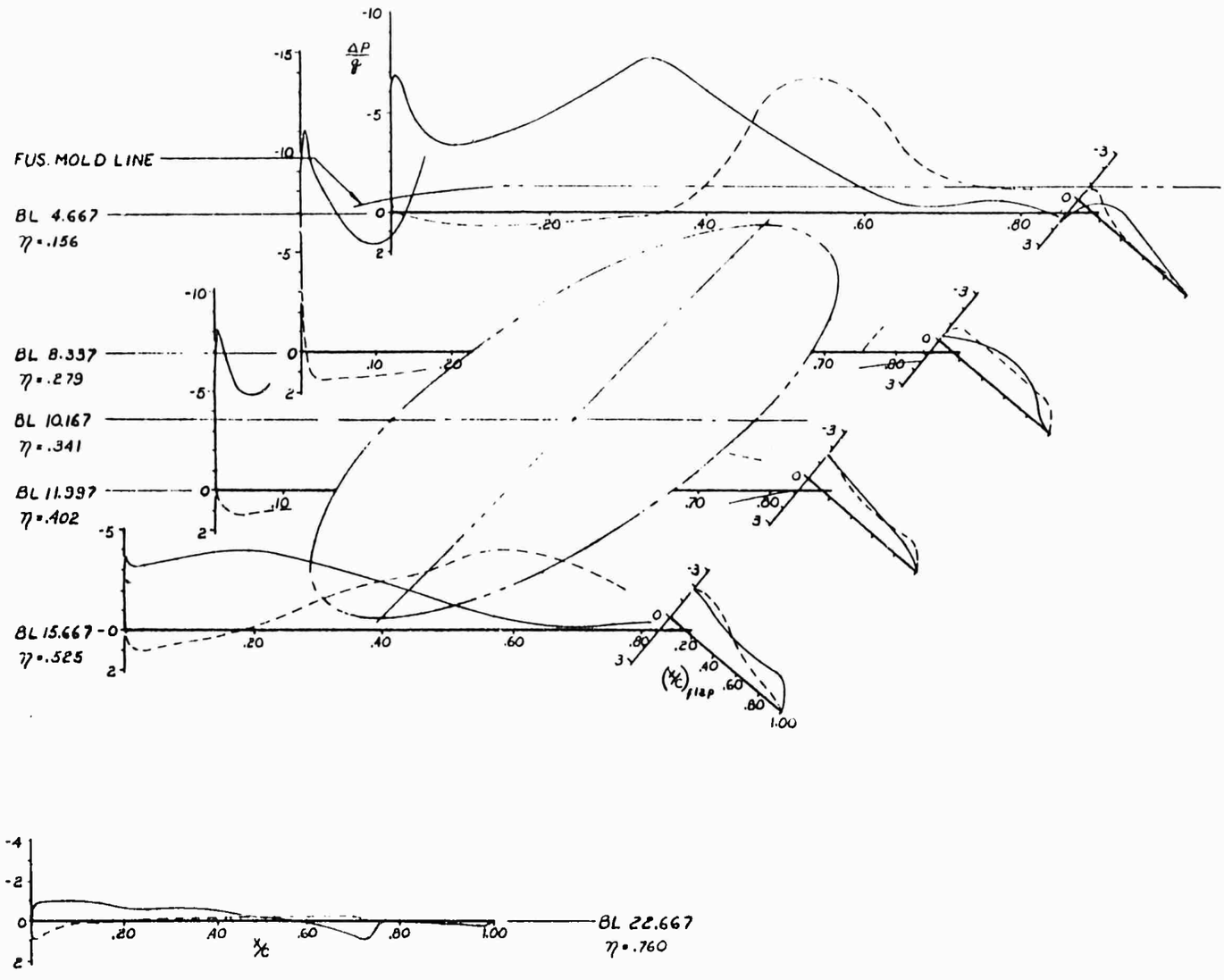

$\beta_v = 30°$, $\beta_s = 0°$, $\delta_f = 45°$, TAIL-ON, $i_t = 15°$, $\alpha = 0°$

RUN	TEST	CONFIGURATION	q	RPM	T_c'	NOSE FAN	C_L'
152	344A	BWF^{45} I_w I_w M_1^{40} G V H^{15}	1.5	8000	.955	ON	.682

CODE	SURFACE
———	UPPER
- - - - - -	LOWER

Figure 4.102 Wing Pressure Distribution For Trimmed Condition in Transition, $\beta_V = 30°$

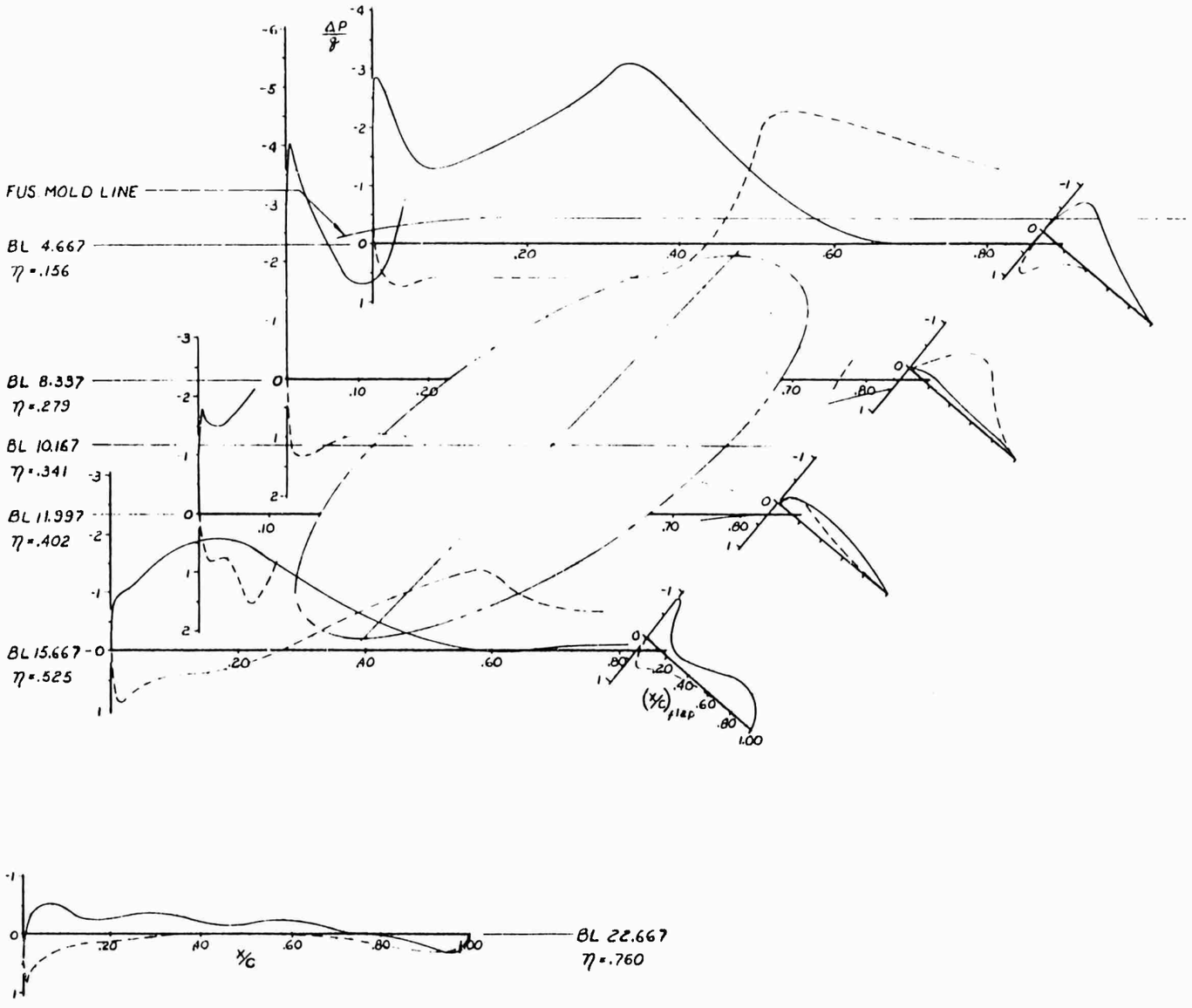

$\beta_v = 45°$, $\beta_3 = 0°$, $\delta_f = 45°$, TAIL-ON, $i_t = 10°$, $\alpha = 0°$

RUN	TEST	CONFIGURATION	q	RPM	T_c^s	NOSE FAN	C_L^s
156	344A	BWF^{48} I_w I_w M_1^{48}GV^{10}H	1.5	5000	.882	ON	.646

CODE	SURFACE
———	UPPER
- - - - - - -	LOWER

Figure 4.103 Wing Pressure Distribution For Trimmed Condition in Transition, $\beta_V = 45°$

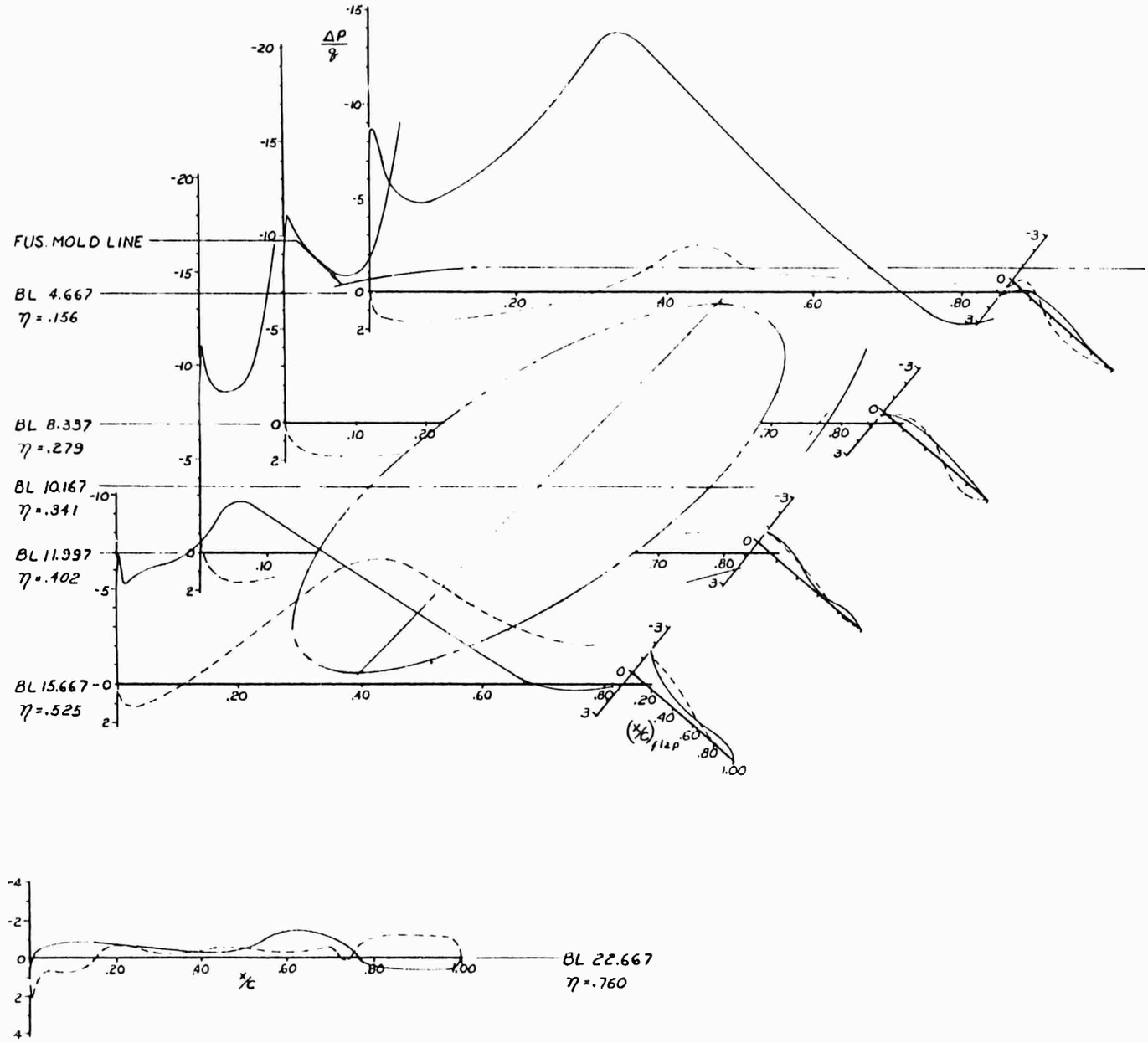

$\beta_v = 0°, \beta_3 = 0°, \delta_f = 45°$, TAIL-OFF, $\alpha = 0°$ $\delta_d = 0°$

RUN	TEST	CONFIGURATION	q	RPM	T_c[4]	C_L[5]
243	344A	BWF[13] $I_w I_t M_t$[14] $G A_s A_4$	1.5	11000	.976	.997

CODE	SURFACE
———	UPPER
- - - - -	LOWER

Figure 4.104 Wing Pressure Distribution With 0° Aileron Droop

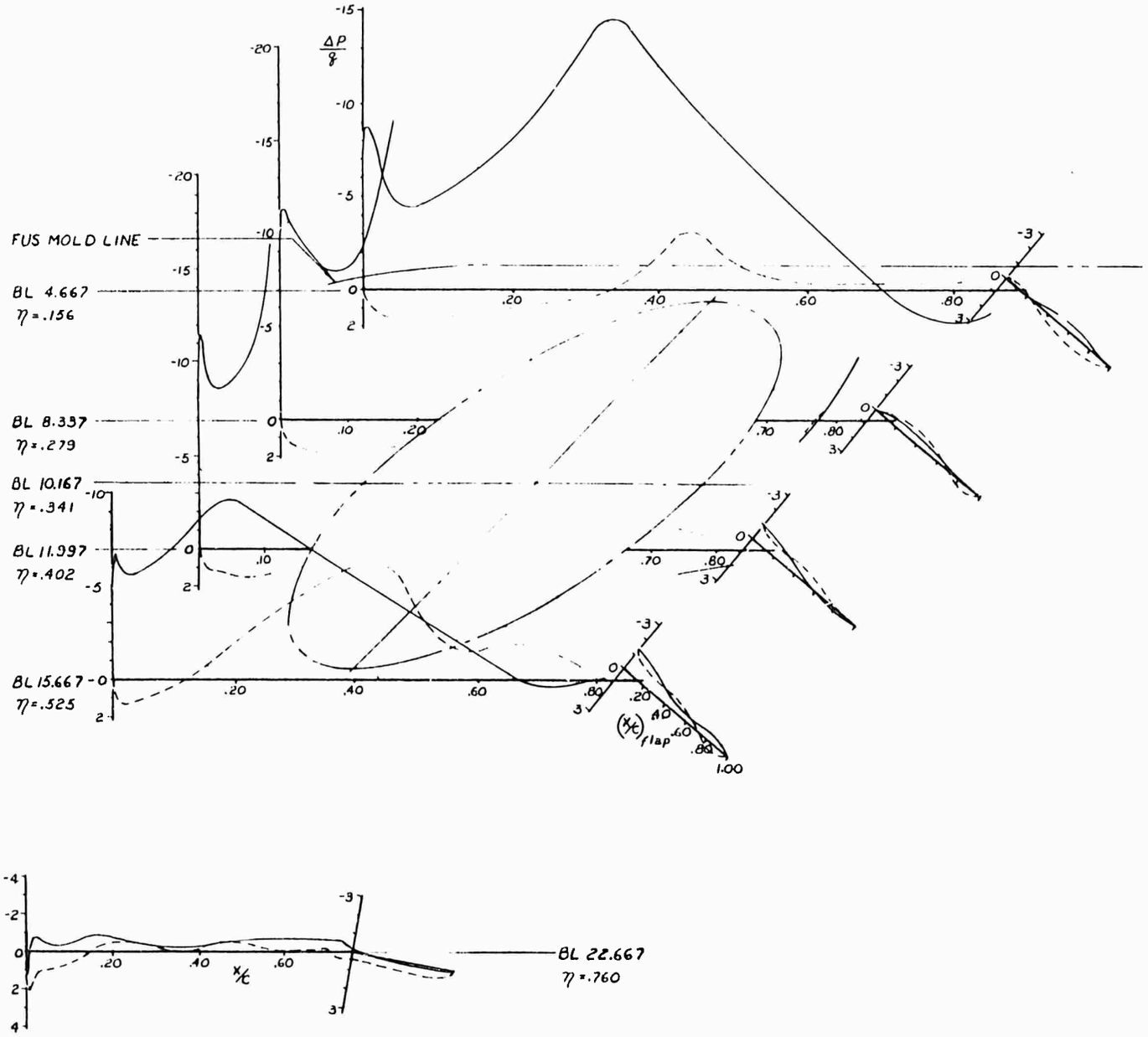

$\beta_v = 0°, \beta_s = 0, \delta_f = 45° + \delta_a = 10°$, TAIL-OFF, $\alpha = 0°$

RUN	TEST	CONFIGURATION	$\frac{g}{}$	RPM	T_c^s	C_L^s
244	344A	BWF^{45} I_w I_w $M_1^{.48}$ GA_L^{10} A_a^{10}	1.5	11000	.976	1.015

CODE	SURFACE
———	UPPER
- - - - - -	LOWER

Figure 4.105 Wing Pressure Distribution With 10° Aileron Droop

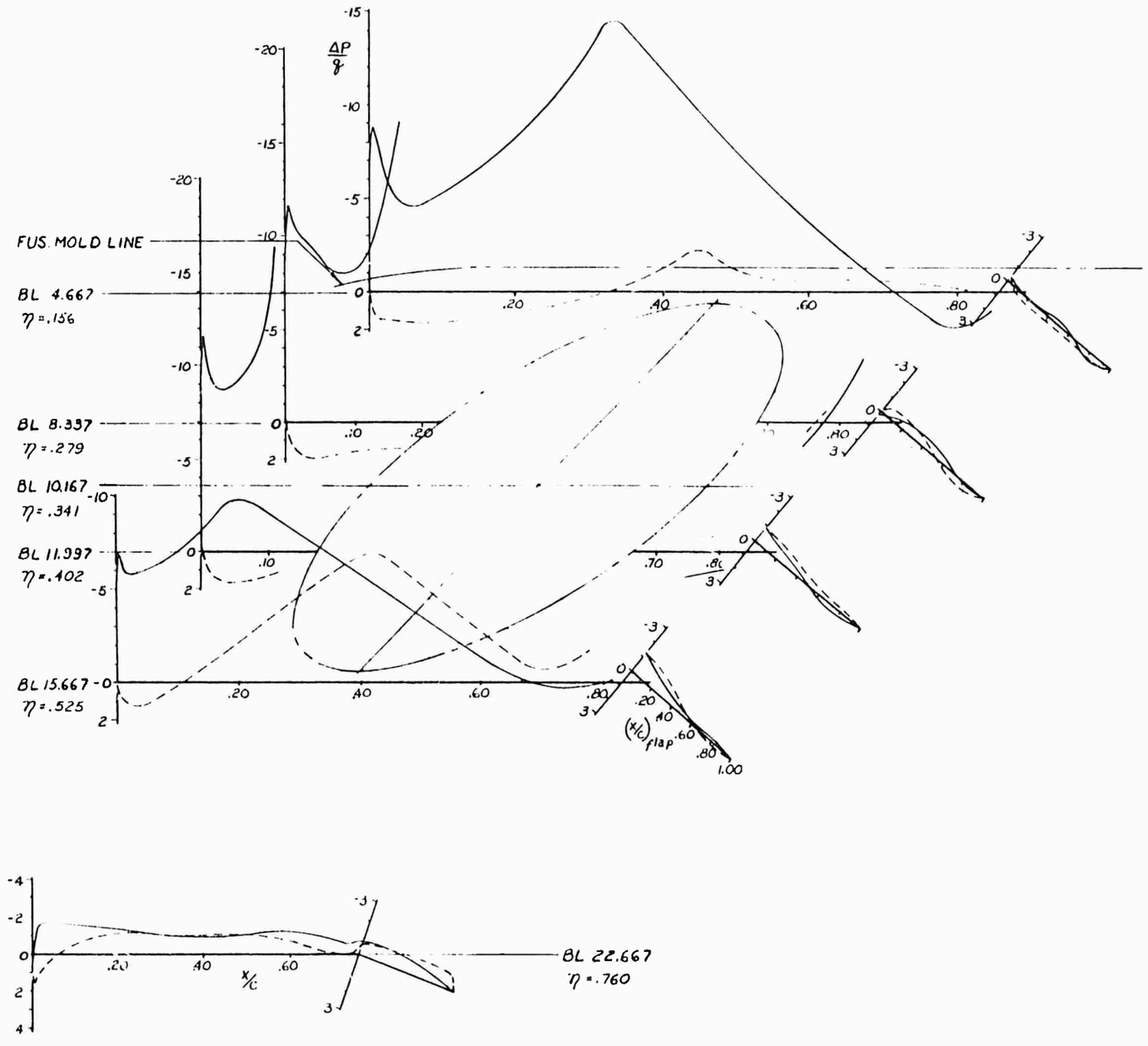

$\beta_v = 0$, $\beta_3 = 0°$, $\delta_f = 45° + \delta_d = 20°$, TAIL-OFF, $\alpha = 0°$

RUN	TEST	CONFIGURATION	γ	PPM	T_c^5	C_L^3
246	344A	BWF^{43} I_w I_w H_t^{18} $G A_L^{24} A_A^{7°}$	1.5	11000	.976	1.028

CODE — SURFACE
———— UPPER
- - - - - - LOWER

Figure 4.106 Wing Pressure Distribution With 20° Aileron Droop

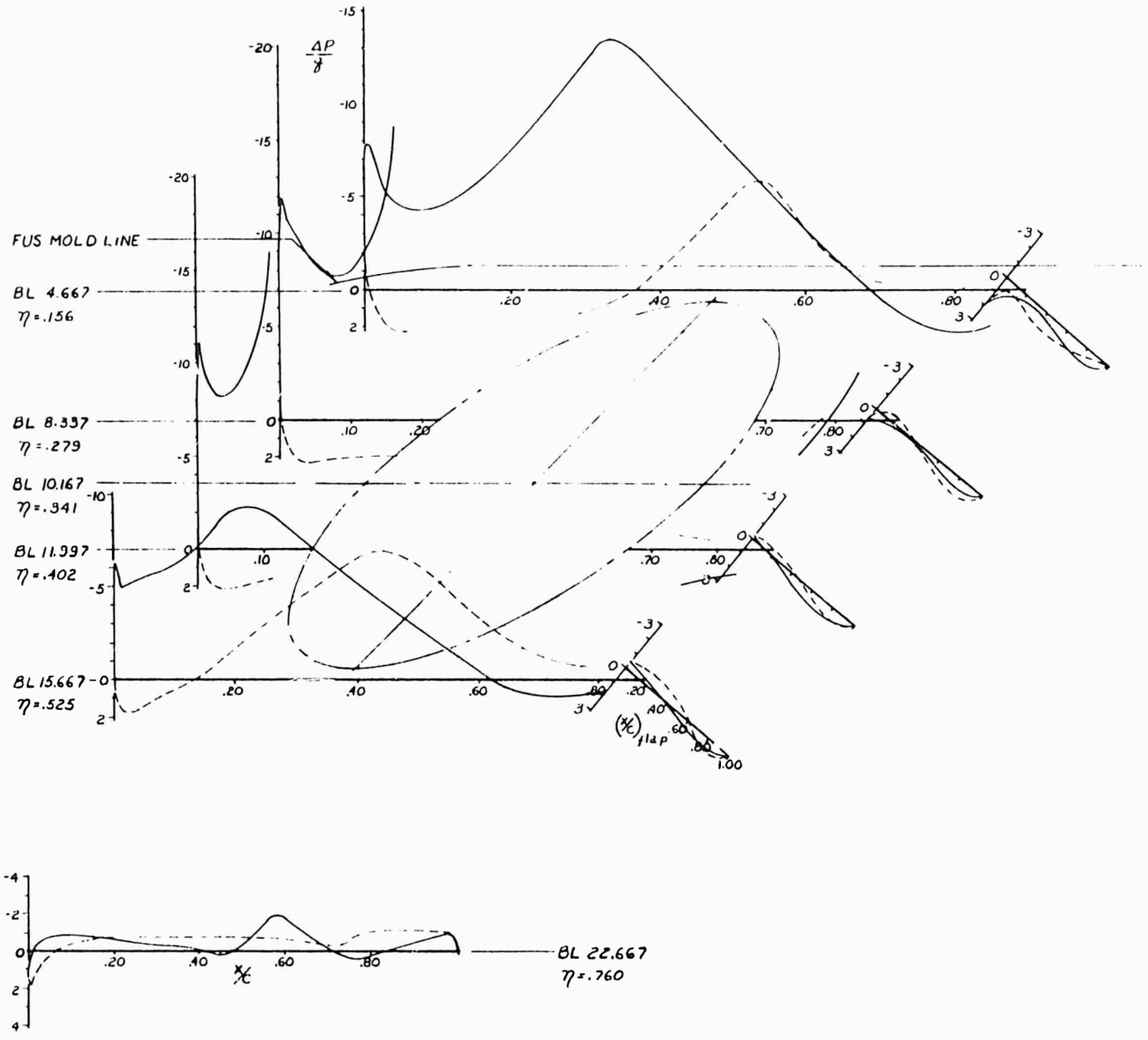

$\beta_v = 0°$, $\beta_s = 0°$, $\delta_f = 45°$, TAIL-OFF, $\alpha = 0°$

RUN	TEST	CONFIGURATION	q	RPM	T_c^s	C_L^s
254	344A	B, WF_a^{44} I_w I_w M_1^{69} G	1.5	11000	.976	1.010

CODE	SURFACE
———	UPPER
- - - - - -	LOWER

Figure 4.107 Wing Pressure Distribution With Extended Flap Span

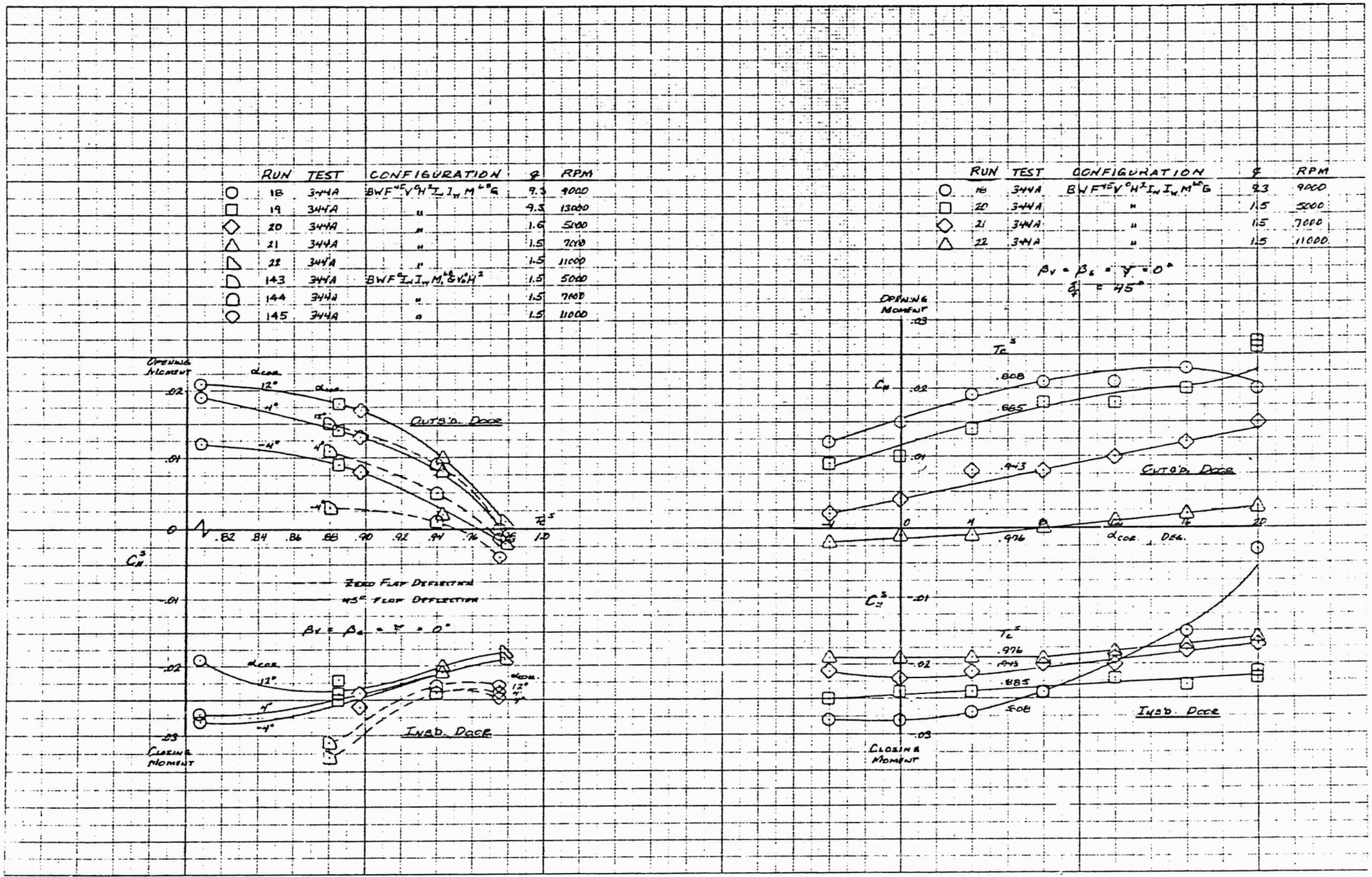

Figure 4.108 Variation of Wing Fan Door Hinge Moment Coefficients With T_c^S, α, and δ_f

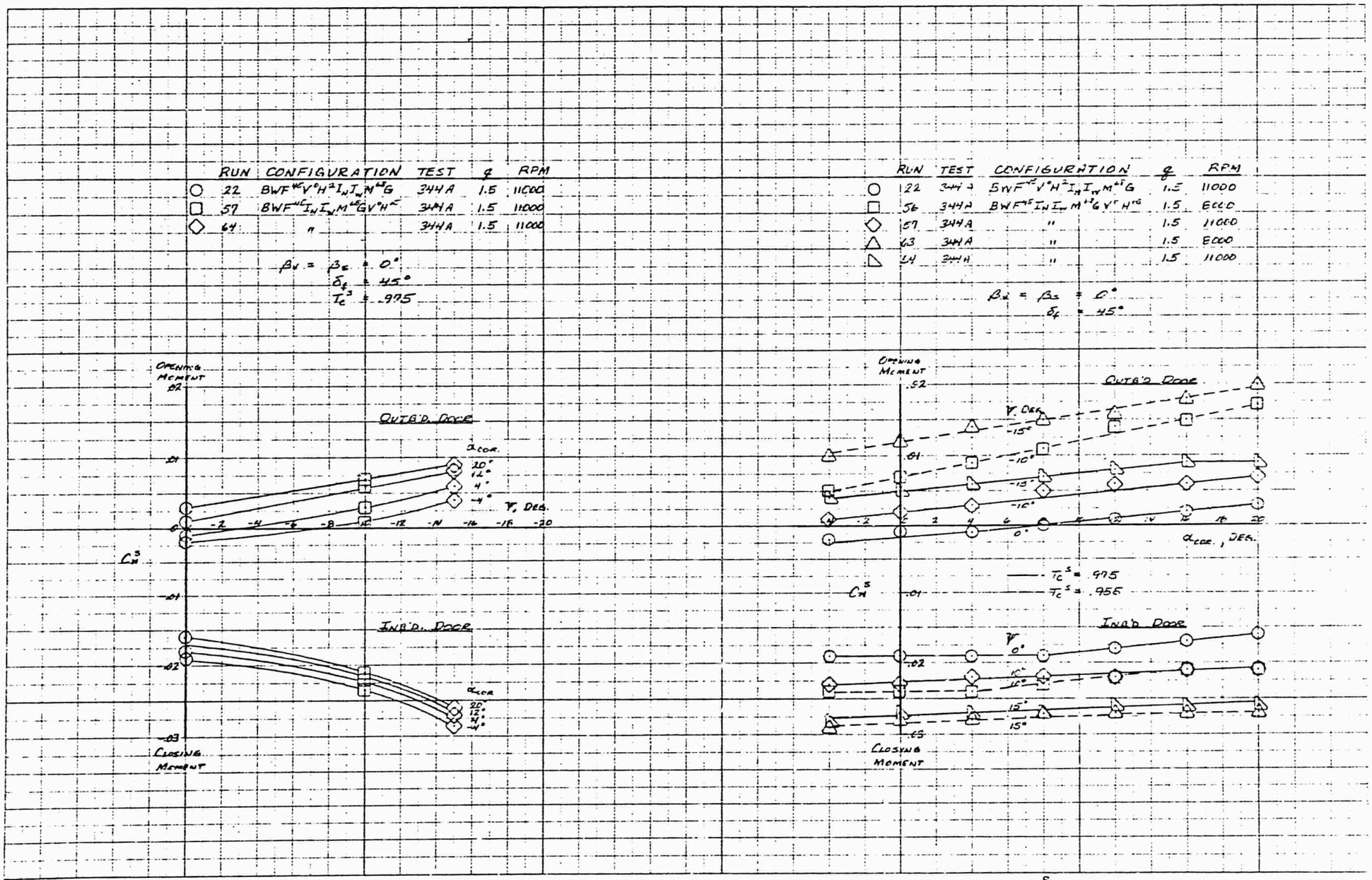

Figure 4.109 Variation of Wing Fan Door Hinge Moment Coefficients With α, ψ, and T_c^S

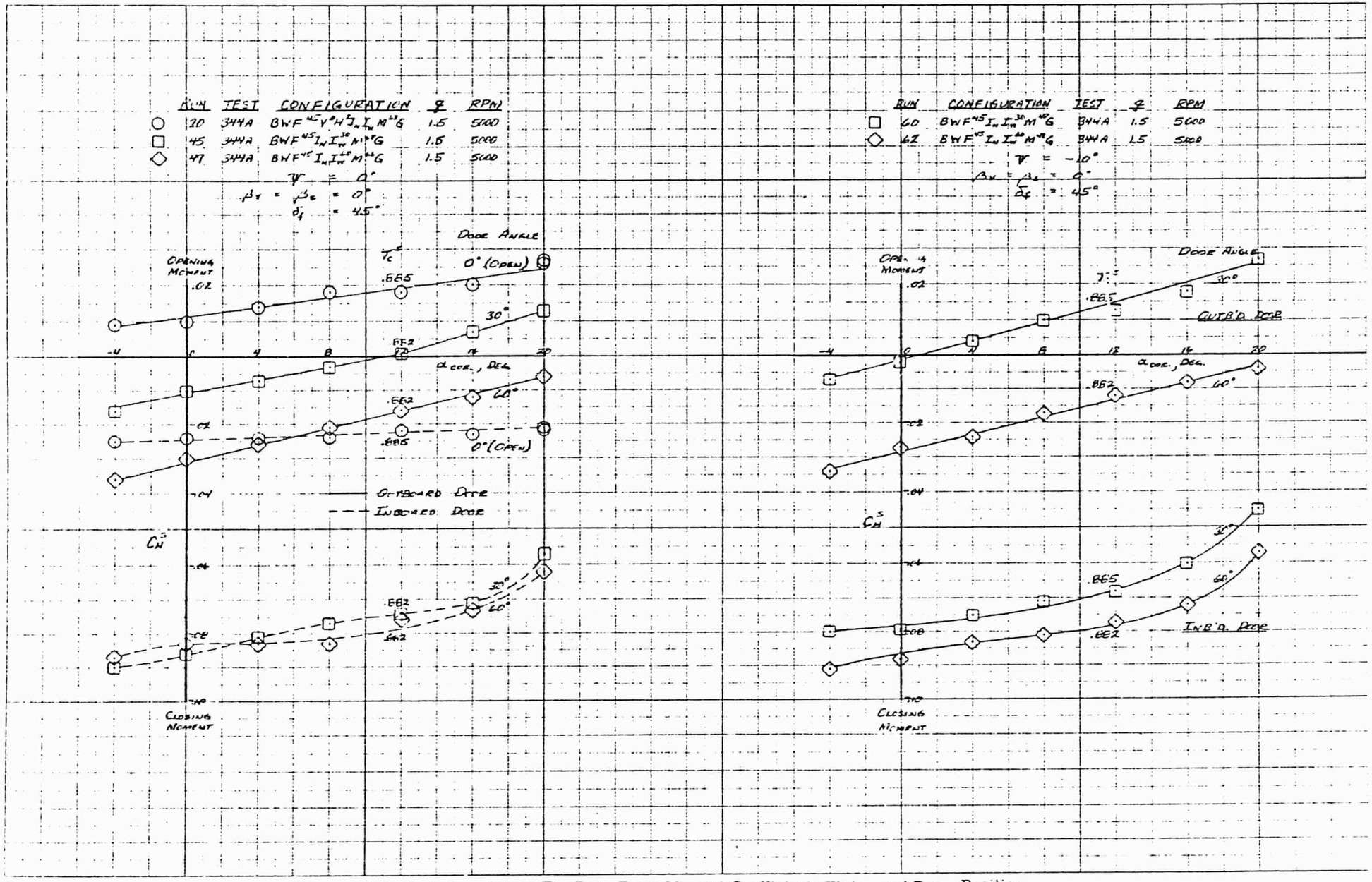

Figure 4.110 Variation of Wing Fan Door Hinge Moment Coefficients With and Door Position

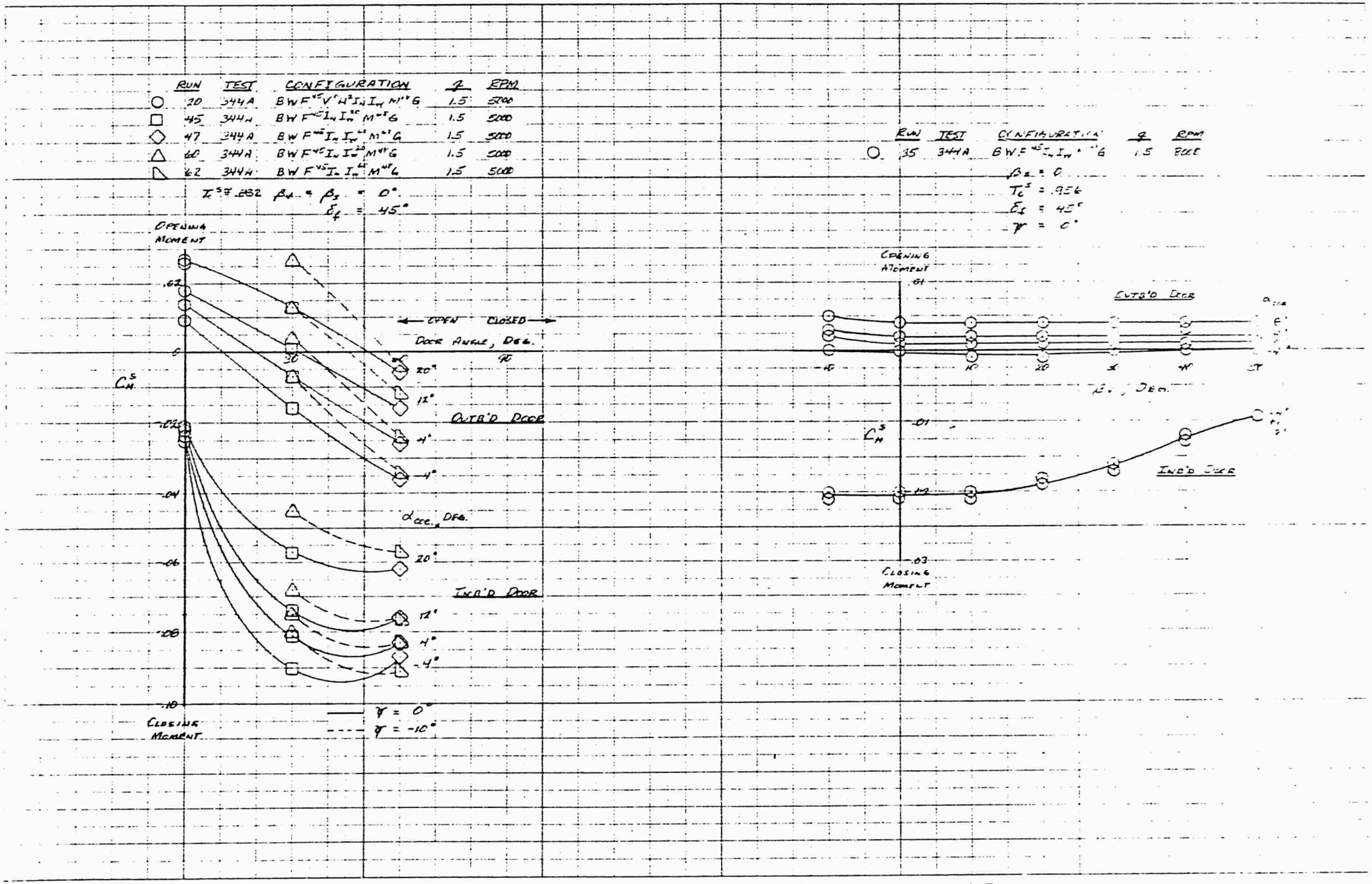

Figure 4.111 Variation of Wing Fan Door Hinge Moment Coefficients With α, ψ, Door Position, and β_v

5.0 CONCLUSIONS

The following conclusions are made based on the wind tunnel test results of a 1/6-scale powered model of the XV-5A Lift Fan Research Aircraft.

1. An adverse ground effect on static lift occurs at heights less than approximately two wing fan diameters at constant fan rotational speed. However, a corresponding reduction in fan power tends to compensate for the lift loss.

2. The effect of power is destabilizing longitudinally and the model exhibits a mild instability with respect to angle of attack in the transition speed range of thrust coefficient for a model moment center corresponding to the full-scale aft c.g. position of Sta. 246, W.L. 112.

3. Nose fan operation is destabilizing with respect to angle of attack at low speeds with the instability decreasing with reverse thrust nose fan door settings.

4. The horizontal tail, although located in a high downwash field due to fan operation, maintains an effectiveness which is independent of fan operating conditions.

5. The model configuration with -6° wing tip dihedral is statically stable in yaw for sideslip angles up to 15° for all values of thrust coefficient, with an increase in the stability parameters, C_{n_β} and C_{ℓ_β}, with increasing thrust coefficient.

6. Aileron and rudder control effectiveness are maintained independent of fan operating conditions.

7. A favorable ground effect on lift at a height of 1.3 wing fan diameters occurs at forward speeds, with lift increases as much as 22% above the out of ground effect data at thrust coefficients near STOL lift-off speed.

8. Rolling moment and sideforce variations with speed in lateral translational flight are similar to pitching moment and drag variations with low forward speeds, indicating similar fan center of lift and momentum drag for the two model attitudes.

9. Opening the exit louvers with the fan inlet doors closed results in a decrease in maximum power-off lift coefficient, ΔC_L, of approximately .12. No large trim changes occur due to opening the exit louvers and nose fan inlet and exit, with power off.

10. A lift coefficient decrease of approximately 5% from the static value occurs at low forward speeds and is at least in part caused by negative pressures on the wing lower surface in the region of the flap aft of the fan.

11. Extensions to the flap span, to obtain flap area outboard of the wing fans, or drooping the ailerons, raise the wing lower surface pressures with attendant increases in lift.

12. Increased flap effectiveness due to larger flap span (or droop) results in favorable nose-down pitching moment increments which help relieve the large nose-up pitching moment inherent in wing-lift fan configurations.

13. The gear driven wing fans, at constant RPM, show an increase in power absorption with increasing tunnel speed and a decrease in power absorption with either exit louver vector or stagger angle.

6.0 APPENDIX

6.1 REFERENCES

1. Reynolds, H.A.: Low Speed Wind Tunnel Tests of a 1/6-Scale Powered Model of the Ryan Model 143 Airplane to Evaluate the Static Performance of the Wing and Nose Fans and the Low Speed Aerodynamic Characteristics of the Model (Tested July 5 thru July 10, 1962), Convair Aeronautical Laboratory Report 344, April 15, 1963.

2. Reynolds, H.A.: Additional Low Speed Wind Tunnel Tests of a 1/6-Scale Model of the Ryan Model 143 Airplane to Investigate Static Performance and Low Speed Aerodynamic Characteristics at a Variety of Model Attitudes and Test Conditions (Tested Sept. 7 thru Oct. 16, 1962), Convair Aeronautical Laboratory Report 344-A, July 15, 1963.

3. Liggett, H.G.: Low Speed Wind Tunnel Tests of a 1/8-Scale Conventional Model of the Ryan Model 143 Airplane to Determine Longitudinal and Directional Characteristics, Duct Internal Flow, Wing and Fuselage Pressures, and Control Surface Cavity Pressures and Hinge Moments (Tested June 6-19, 1962), Convair Aeronautical Laboratory Report 343, April 12, 1963.

6.2 LIST OF SYMBOLS

A_F — Wing fan area of both fans, $\frac{\Pi}{2} D_F^2$, ft^2

b — Wing span, ft.

C_D — Drag coefficient, D/qS

C_D^s — Drag coefficient, $D/q^s A_F$

C_L Lift coefficient, L/qS

C_L^s Lift Coefficient, L/q^sA_F

C_m Pitching Moment coefficient, $M/qS\bar{c}$

C_m^s Pitching Moment coefficient, $M/q^sA_FD_F$

C_ℓ Rolling Moment coefficient, L/qSb

C_ℓ^s Rolling Moment coefficient, L/q^sSb

C_N^s Normal force coefficient, N/q^sA_F

C_n Yawing Moment coefficient, N/qSb

C_n^s Yawing Moment coefficient, N/q^sSb

C_Y Side force coefficient, Y/qS

C_Y^s Side force coefficient, Y/q^sS

C_p^s Power coefficient, $\dfrac{P\rho^{1/2}}{\left[\left(\dfrac{T_{ooo}}{A_F}\right)\left(\dfrac{T_{std}}{p_{std}}\right)\left(\dfrac{p_o}{T_o}\right)\right]^{3/2}\dfrac{A_F}{2}}$

C_X^s Longitudinal force coefficient X/q^sA_F

C_H^s Wing fan closure door hinge moment coefficient, $\dfrac{HM}{q^sA_{F/2}D_F}$

c Local wing chord with flap retracted, ft.

$\bar{c}$	Wing mean aerodynamic chord, ft.
D	Drag, lb.
D_F	Wing fan diameter, ft.
h	Reference height of model above ground board, measured to Waterline 16.667, inches.
i_t	Horizontal stabilizer incidence angle, deg.
L	Lift force, lb., or rolling moment, ft./lb.
M	Pitching moment, ft./lb.
N	Normal force, lb. or yawing moment, ft./lb.
P	Wing fan drive motor output power, per motor, ft. lb./sec.
p	Measured local static pressure.
p_o	Wind tunnel test section static pressure.
p_{std}	Standard atmosphere sea level static pressure, (29.921 in. Hg).
$\frac{\Delta p}{q}$	Pressure coefficient, $\frac{p - p_o}{q}$
q	Wind tunnel free stream dynamic pressure, $\rho\frac{V^2}{2}$, lb/ft.^{2}
q^s	Slipstream dynamic pressure, $q + \left(\frac{T_{ooo}}{A_F}\right)\left(\frac{p_o}{p_{std}}\right)\left(\frac{T_{std}}{T_o}\right)$
S	Projected wing area, ft^2.
T_{ooo}	Model static lift force with $\beta_v = 0$, $\beta_s = 0$, corrected to sea level std. day atmospheric conditions, lb.

T_c^s Wing fan thrust coefficient, $\dfrac{T_{ooo}\left(\dfrac{p_o}{p_{std}}\right)\left(\dfrac{T_{std}}{T_o}\right)}{q^s A_F}$

T_o Wind tunnel test section temperature, ^oR

T_{std} Standard atmosphere sea level temperature (518.4° R)

V Wind tunnel free stream velocity, ft/sec.

X Longitudinal force along the body X axis, positive forward, lb.

x Chordwise distance measured from wing or flap leading edge

Y Sideforce, lb.

y Spanwise distance measured from plane of symmetry

α, α_{cor} Model angle of attack, deg.

β Wing fan exit louver angle in degrees, measured between louver chord plane and a plane parallel to fan axis, positive trailing edge aft.

β_s Exit louver stagger angle, measured between the chord planes of any even numbered louver and the adjacent odd numbered louver, i.e., $\beta_s = \beta_8 - \beta_7$.

β_v Exit louver vector angle determined from the average angle formed by adjacent even and odd numbered louvers, i.e., $\beta_v = \dfrac{\beta_8 + \beta_7}{2}$

δ Control surface angular deflection, deg.

θ Model pitch angle, positive nose up, deg.

φ Model roll angle, positive right wing down, deg.

ψ, $\psi_{cor.}$	Model yaw angle, positive nose right, deg.
ρ	Air mass density in test section, slug/ft^3
η	Nondimensional spanwise distance, y/b/2

Subscripts

a	Aileron
d	Aileron-droop
f	Wing trailing edge flap
r	Rudder
s	Stagger
t	Horizontal stabilizer
v	Vector
L	Left-hand
R	Right-hand

Abbreviations

cor.	Corrected
c. g.	Center of gravity
RPM	Motor rotational speed in revolutions per minute
mac	Mean aerodynamic chord

6.3 MODEL COMPONENT DESIGNATIONS

Symbol	Description
B	Fuselage with faired (plugged) engine inlet and incorporating pitch control fan in nose section.

Symbol	Description
B_1	Basic fuselage, B, with a wax fairing added to the wing lower surface-fuselage juncture increasing fuselage width approx. 1.6 inches at the wing root 50% chord point and fairing smoothly to the fuselage at the wing root leading and trailing edge.
W	Wing incorporating 2 lift fans with exit louver system.
F^{δ}	Single slotted wing trailing edge flap at deflection δ in deg., positive trailing edge down.
F_2^{δ}	Basic trailing edge flap, F, with 2.50 inch span extension on each flap.
A^{δ}	Aileron at deflection δ in deg. A_L^{20}/A_R^{10} indicates the left hand aileron deflected 20° (positive trailing edge down) and the right hand aileron deflected 10°.
H^{δ}	Horizontal stabilizer at deflection δ in degs., positive leading edge up.
V^{δ}	Vertical tail incorporating adjustable rudder. Superscript δ denotes rudder deflection in deg., positive trailing edge left.
M^{δ}	Nose fan thrust modulator doors which fair into sides of fuselage nose section when in the closed position. Superscript δ denotes deflection in degs. from the closed position.
M_1^{δ}	Nose fan thrust modulator doors with 1/16" balsa wood trip strips located on door outer surface near hinge line.
I_n	Nose fan inlet louvers. Seven louvers and nose fan hub fairing located at the nose fan inlet. Closed configuration denoted by superscript c was simulated by replacing louvers with sheet metal cover.
I_w	Wing fan inlet doors including chordwise support strut. Doors were adjustable for angular settings between the open vertical position and the closed faired position. Closed position denoted by superscript c.

Symbol	Description
G	Main landing gear and gear well doors attached to fuselage, representing the conventional take-off landing gear position.
WING FAN INLET VANE	Fixed inlet vanes consisting of a circular vane concentric with fan inlet bellmouth and eight spanwise vanes between fan hub and circular vane.

TABLE 6.1

MODEL GEOMETRIC CHARACTERISTICS

WING

Projected Area	7.231	sq. ft.
Aspect ratio	3.42	
Taper ratio		
Inboard panel	.752	
Outboard panel	.395	
Span	59.667	in.
Chord length		
Root (BL 0.00)	24.17	in.
At break of quarter chord line(BL 16.79)	18.17	in.
Tip (BL 29.83)	7.17	in.
Mac	18.82	in.
Dihedral		
Inboard panel	0.00	deg.
Outboard panel (from BL 17.72)	-6.00	deg.
Sweep of quarter chord line		
Inboard panel	15.00	deg.
Outboard panel	28.34	deg.
Geometric twist		
Inboard panel	0.00	deg.
Outboard panel (from BL 16.79 to BL 28.34)	-3.00	deg.
Incidence, with respect to fuselage reference line, at root chord	0.00	deg.
Aileron (basic configuration)		
Projected area (aft of hinge line, per side)	.282	sq. ft.
Spanwise location	.563 to 1.00	b/2
Chord ratio		
BL 16.79	.188	$c_{a/c}$
BL 29.83	.392	$c_{a/c}$

Deflection limits (adjustable in 5 deg. increments, positive deflection trailing edge down)	-15.0 to +30.0	deg.
Type of balance - radius nose, unsealed		
Flap (basic configuration)		
Projected area (per side)	.347	sq. ft.
Spanwise location	.138 to .563	b/2
Chord ratio		
BL 4.12	.174	$c_{f/c}$
BL 16.79	.217	$c_{f/c}$
Deflection limits (adjustable in 5 deg. increments, positive deflection trailing edge down)	0.0 to +60.0	deg.
Type - single slotted		
Modified Flap (F_2)		
Projected area (per side)	.416	sq. ft.
Spanwise location	.138 to .647	b/2
Chord ratio		
BL 4.12	.174	$c_{f/c}$
BL 19.29	.242	$c_{f/c}$
Deflection limits (adjustable in 5 deg. increments, positive deflection trailing edge down)	0.0 to +60.0	deg.
Type - single slotted over original span, modified plain flap over extended span.		

WING FAN

Rotor area (per wing fan, including hub)	.59	sq. ft.
Rotor diameter	10.40	in.
Hub diameter	5.20	in.
Fus. Sta. of fan centerline	42.67	
BL of fan center line	10.22	
Fan rotation (viewed from above)		
Right hand - clockwise		
Left hand - counterclockwise		
Louver deflection limits		
Simple vector	-10.0 to +50.0	deg.

Simple stagger	0.0 to 35.0	deg.
Motor to fan gear ratio	1.46-1.00	

NOSE FAN

Rotor area (including hub)	.213	sq. ft.
Rotor diameter	6.25	in.
Hub diameter	3.12	in.
Fus. Sta. of fan centerline	9.83	
BL of fan centerline	0.00	
Nose fan thrust reverser doors positions (measured from closed position)	28, 48, 68 and 88	deg.
Motor to fan gear ratio	.74-1.00	

HORIZONTAL TAIL

Projected area	1.407	sq. ft.
Aspect ratio	3.01	
Taper ratio	.500	
Span	24.70	in.
Chord length		
Root (BL 0.00)	10.94	in.
Tip (BL 12.35)	5.47	in.
Mac	8.51	in.
Airfoil section	NACA 64A012	
Dihedral	0.00	deg.
Sweep of quarter chord line	8.44	deg.
Incidence settings available with respect to fuselage reference line (positive, leading edge up)	-5, -2, 0, +2, +4, +6 +8, +10, +15, and +20	deg.
Fus. Sta. of horizontal tail pivot point (WL 33.50)		82.76

VERTICAL TAIL

Projected area (excluding dorsal)	1.416	sq. ft.
Aspect ratio	1.18	
Taper ratio	.520	
Chord length (// to WL 16.67)		
Root (WL 18.83)	17.32	in.
Tip (WL 34.33)	9.00	in.
Mac	13.60	in.
Airfoil Section		
WL 18.83	NACA 64A(012)-016.5	
WL 34.33	NACA 64A012	

Sweep of quarter chord line	29.51	deg.
Rudder		
Projected area (aft of hinge line)	.155	sq. ft.
Span (// to hinge line)	8.99	in.
Spanwise location at hinge line	.139 to .701	b
Chord ratio	.180	$c_{r/c}$
Deflection limits (adjustable in 5 deg. increments, positive deflection trailing edge left)	±25.0	deg.

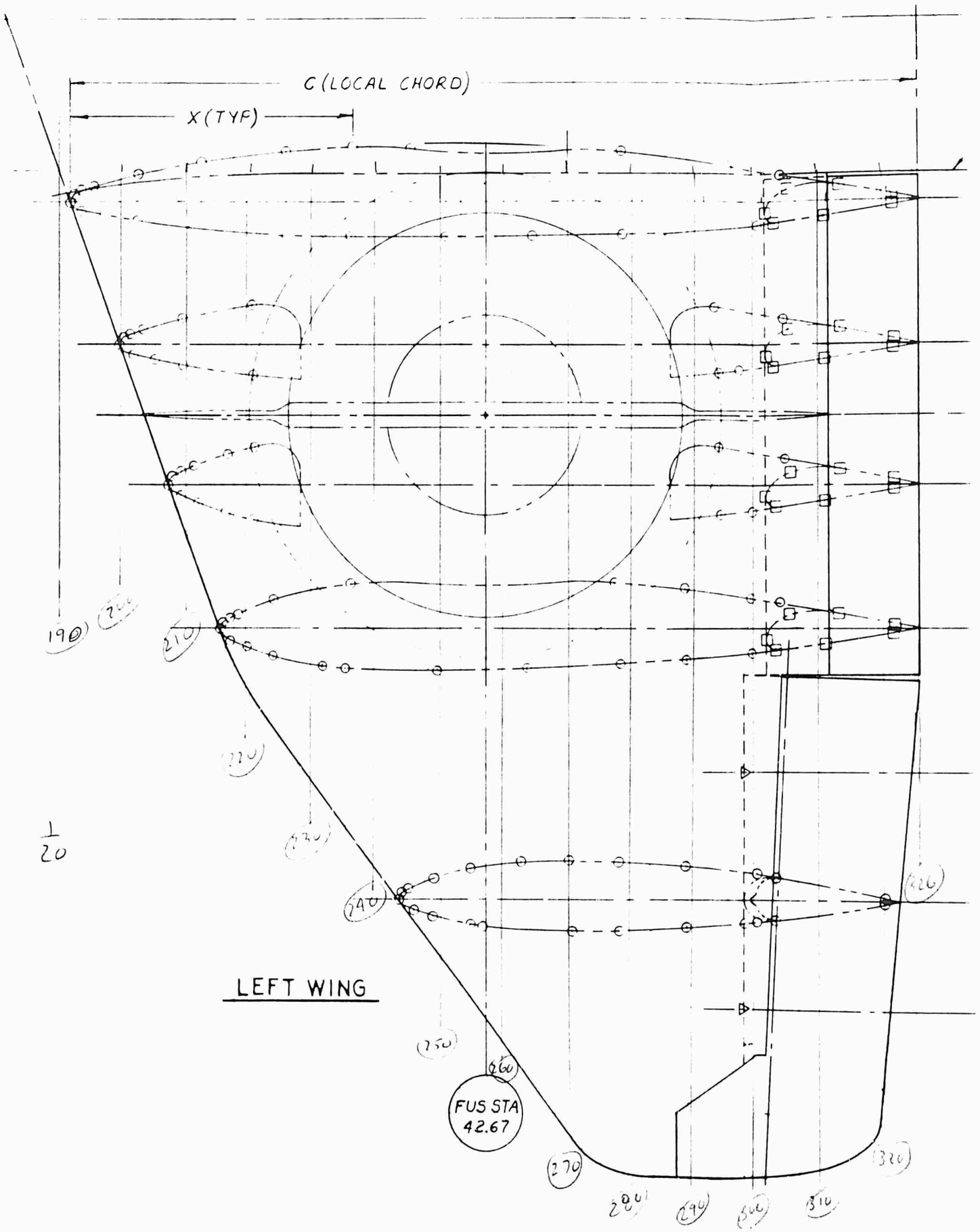
C (LOCAL CHORD)
X (TYP)
190
200
210
220
230
240
250
260
FUS STA
42.67
270
280
290
300
310
320
330
1/20
LEFT WING

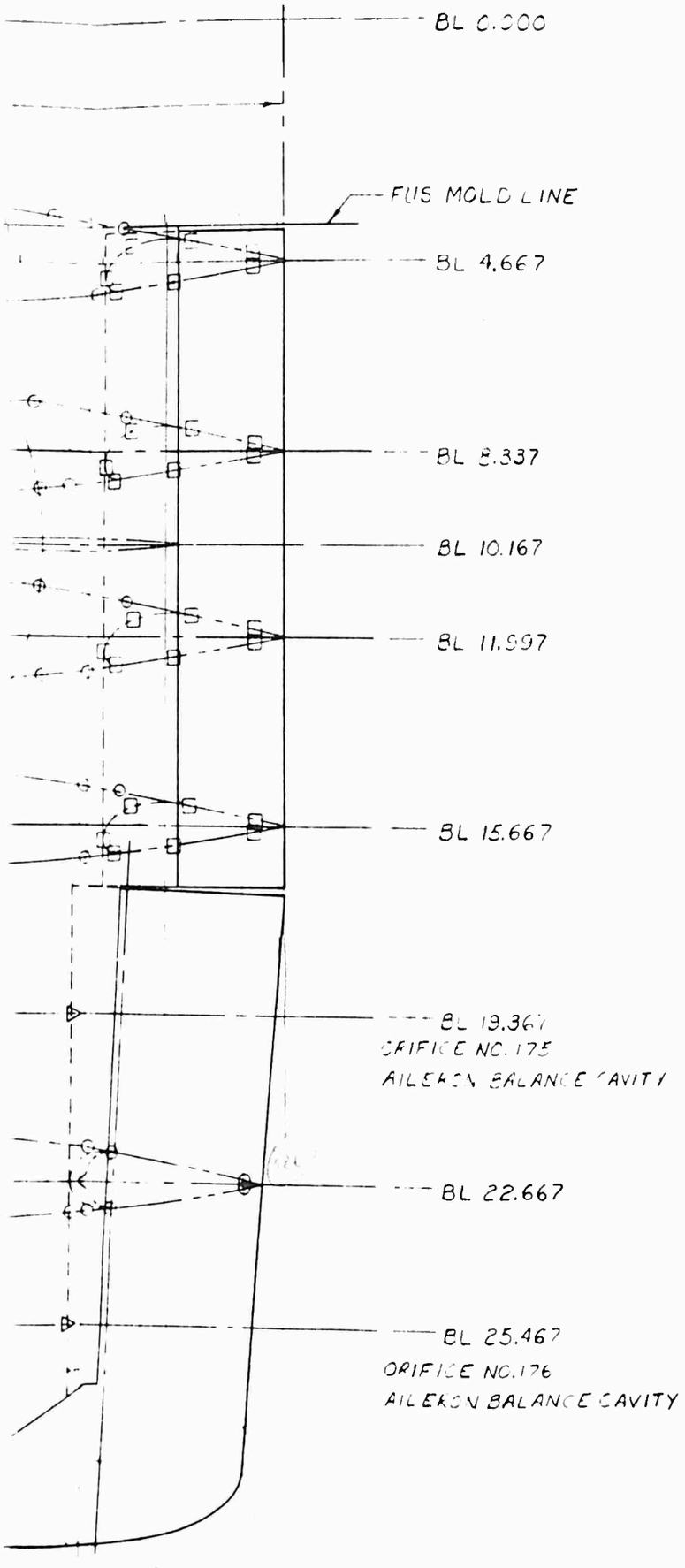

C WING CHORDW

BL 4.667

ORIFICE NO.	UPPER SURF. X/C	ORIFICE NO.	LOWER SURF. X/C
180	.000	1	.016
13	.004	2	.040
14	.017	3	.079
15	.029	4	.254
16	.078	5	.331
17	.153	6	.439
18	.254	7	.543
19	335	8	.647
20	.400	9	.811
21	.647		
22	.774		
23	.844		

BL 8.337

ORIFICE NO.	UPPER SURF. X/C	ORIFICE NO.	LOWER SURF. X/C
181	.000	28	.017
37	.005	29	.042
38	.012	30	.079
39	.030	31	.165
40	.079	32	.752
41	165	33	.780
42	.747		
43	.835		

BL 11.997

ORIFICE NO.	UPPER SURF. X/C	ORIFICE NO.	LOWER SURF. X/C
182	.000	48	.015
57	.003	49	.041
58	.015	50	.075
59	.033	51	.111
60	.078	52	.738
61	.112	53	.785
62	.738		
63	.824		

C WING CHORDWISE ORIFICE LOCATIONS

7
E

UPPER SURF. X/C	ORIFICE NO.	LOWER SURF. X/C
.000	1	.016
.004	2	.040
.017	3	.079
.029	4	.254
.078	5	.331
.153	6	.439
.254	7	.543
335	8	.647
.400	9	.811
.647		
.774		
.844		

7
E

UPPER SURF. X/C	ORIFICE NO.	LOWER SURF. X/C
.000	28	.017
.005	29	.042
.012	30	.079
.030	31	.165
.079	32	.752
165	33	.780
.747		
.835		

97
E

UPPER SURF. X/C	ORIFICE NO.	LOWER SURF. X/C
.000	48	.015
.003	49	.040
.015	50	.075
.033	51	.111
.078	52	.738
.112	53	.785
.738		
.824		

BL 15.667

ORIFICE NO.	UPPER SURF. X/C	ORIFICE NO.	LOWER SURF. X/C
81	.000	68	.015
82	.008	69	.040
83	.015	70	.077
84	.027	71	.152
85	.078	72	.181
86	.130	73	.312
87	.566	74	.442
88	.668	75	.573
89	.768	76	.668
90	.810	77	.769

BL 22.667

ORIFICE NO.	UPPER SURF. X/C	ORIFICE NO.	LOWER SURF. X/C
183	.000	95	.007
108	.007	96	.032
109	.019	97	.069
110	.063	98	.145
111	.146	99	.169
112	.246	100	.346
113	.345	101	.445
114	.444	102	.576
115	.577	103	.632
117	.722	104	.721
118	.760	105	.761
119	.972	106	.972

Figure 6.1 Left Wing I

C

ATIONS

.67

E UPPER SURF. X/C	ORIFICE NO.	LOWER SURF. X/C
.000	68	.015
.003	69	.040
.015	70	.077
.027	71	.152
.078	72	.181
.190	73	.312
.566	74	.442
.668	75	.573
.768	76	.668
.810	77	.769

.67

E UPPER SURF. X/C	ORIFICE NO.	LOWER SURF. X/C
.000	95	.007
.007	96	.032
.019	97	.069
.069	98	.145
.146	99	.169
.246	100	.346
.345	101	.445
.444	102	.576
.577	103	.632
.722	104	.721
.760	105	.761
.372	106	.972

C WING FLAP CHORDWISE ORIFICE LOCATIONS

BL 4.667

ORIFICE NO.	UPPER SURF. X/C	ORIFICE NO.	LOWER SURF. X/C
24	.000	10	.065
25	.162	11	.400
26	.510	12	.850
27	.850		

BL 8.337

ORIFICE NO.	UPPER SURF. X/C	ORIFICE NO.	LOWER SURF. X/C
44	.000	34	.058
45	.161	35	.395
46	.506	36	.848
47	.855		

BL 11.997

ORIFICE NO.	UPPER SURF. X/C	ORIFICE NO.	LOWER SURF. X/C
64	.000	54	.063
65	.170	55	.334
66	.510	56	.851
67	.850		

BL 15.667

ORIFICE NO.	UPPER SURF. X/C	ORIFICE NO.	LOWER SURF. X/C
91	.000	78	.061
92	.161	79	.396
93	.499	80	.845
94	.856		

NOTE:
FLAP PRESSURE ORIFICE LOCATIONS ARE BASED ON LOCAL FLAP CHORD 'X' BEING MEASURED FROM LEADING EDGE OF FLAP.

Figure 6.1 Left Wing Pressure Orifice Locations

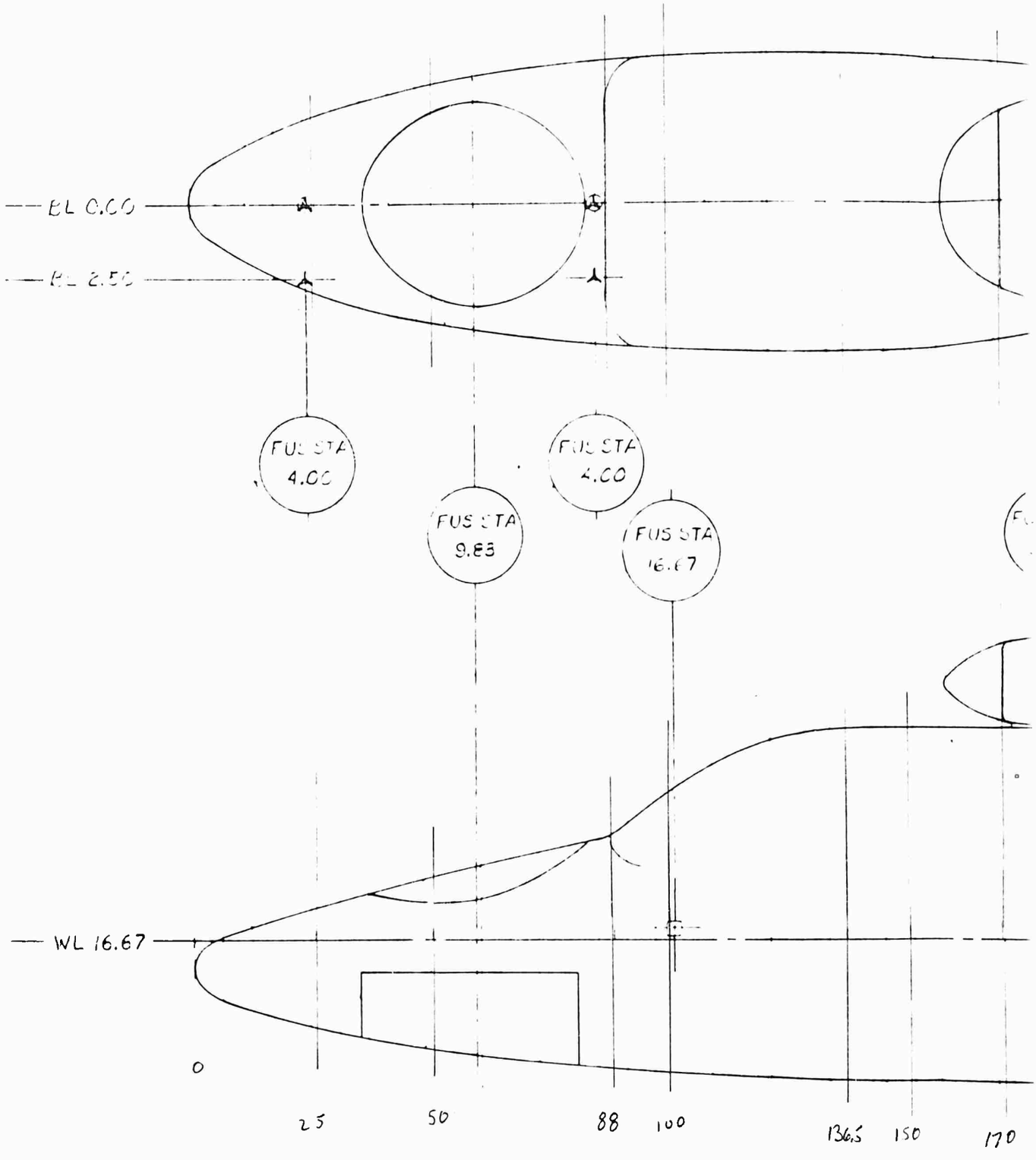
EL 0.00
EL 2.50
FUS STA 4.00
FUS STA 9.83
FUS STA 4.00
FUS STA 16.67
WL 16.67
0
25
50
88
100
136.5
150
170

A

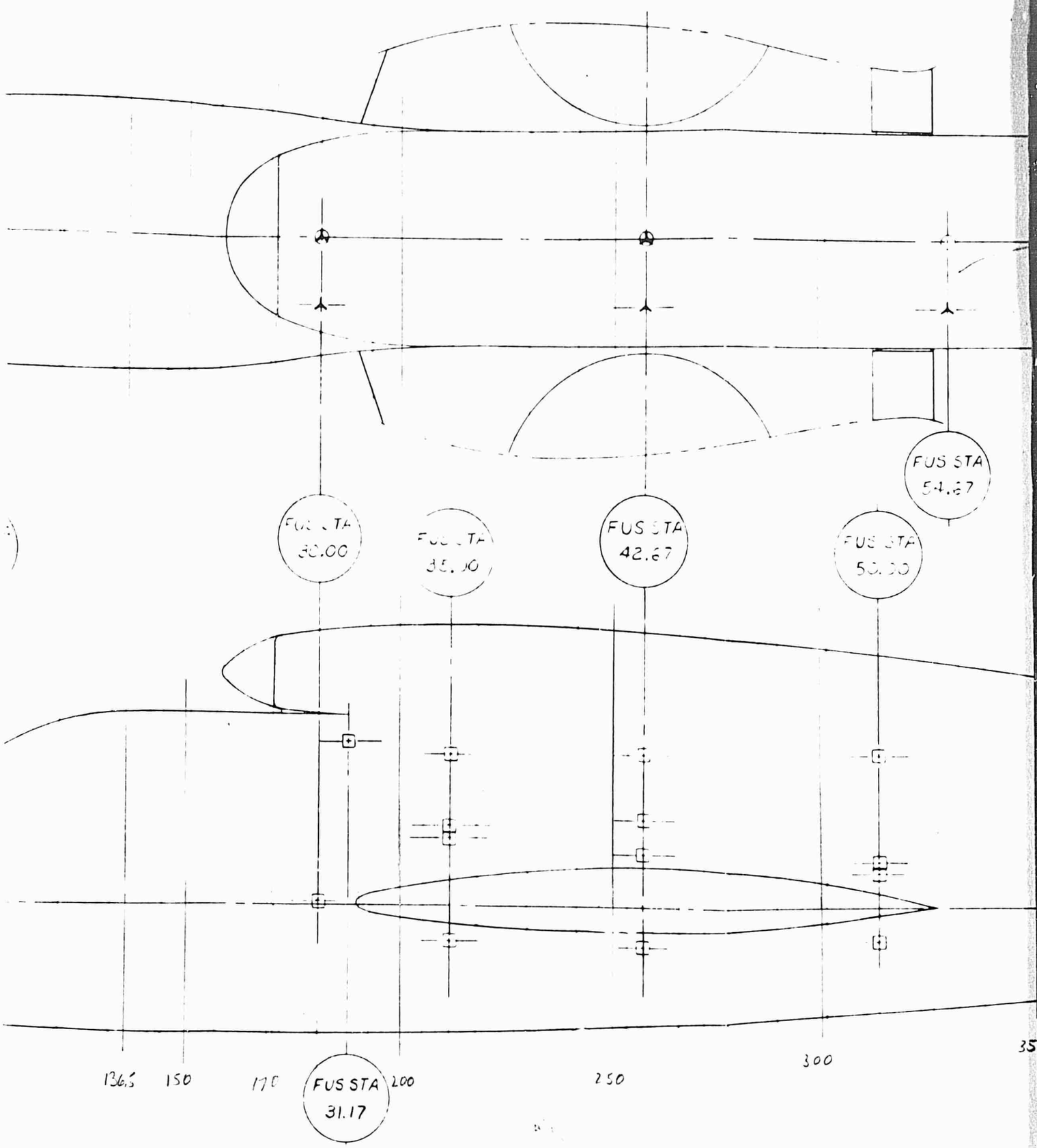
FUS STA
54.67
FUS STA
42.67
FUS STA
50.00
FUS STA
30.00
136.5
150
170
FUS STA
31.17
200
250
300
35

B

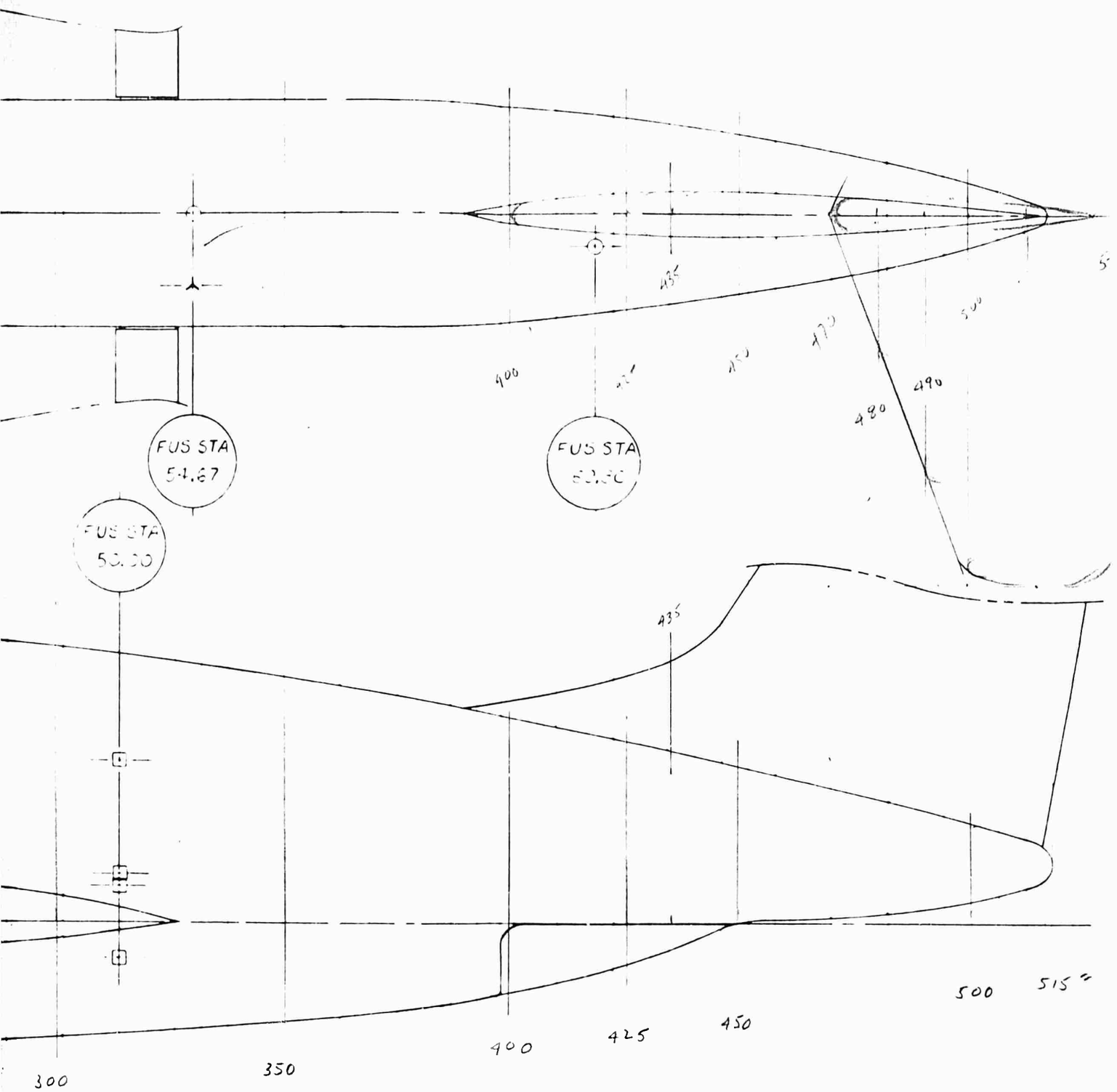

$\frac{1}{30} \times 10 =$ actual in.

C

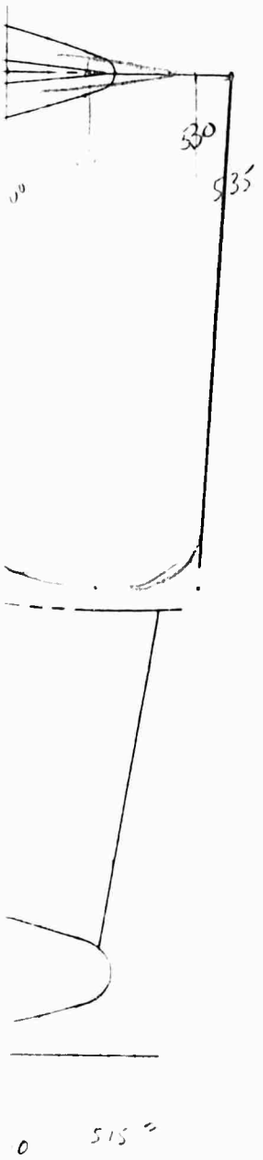

FUSELAGE ORIFICE LOCATIONS

ORIFICE NO.	FUS STA	W L	B L	LOCATION
201	4.00		0.00	
202	14.00		0.00	
203	30.00		0.00	TOP OF FUSELAGE
204	42.67		0.00	
205	54.67		0.00	
206	66.00		.75	
207	4.00		0.00	
208	14.00		0.00	
209	30.00		0.00	
210	42.67		0.00	
213	4.00		2.50	BOTTOM OF FUSELAGE
214	14.00		2.50	
215	30.00		2.50	
216	42.67		2.50	
217	54.67		1.50	
218	16.67	17.00		
219	30.67	18.40		
220	35.00	9.70		
220-A	35.00	22.33		
221	35.00	13.26		
222	35.00	5.55		
223	42.67	9.95		
223-A	42.67	22.33		RT SIDE OF FUSELAGE
224	42.67	18.66		
225	42.67	15.15		
226	50.00	14.28		
226-A	50.00	22.33		
227	50.00	10.34		
228	50.00	15.37		
229-A	31.17	22.50		

NOTE:

1- ORIFICE NUMBERS 220 223 & 226 WERE REPLACED FOR TEST IVAL 344A BY 220-A 223-A, & 226-A RESPECTIVELY.

2- ORIFICE NUMBER 229-A ADDED FOR TEST IVAL 344A.

Figure 6.2 Fuselage Pressure Orifice Locations

D

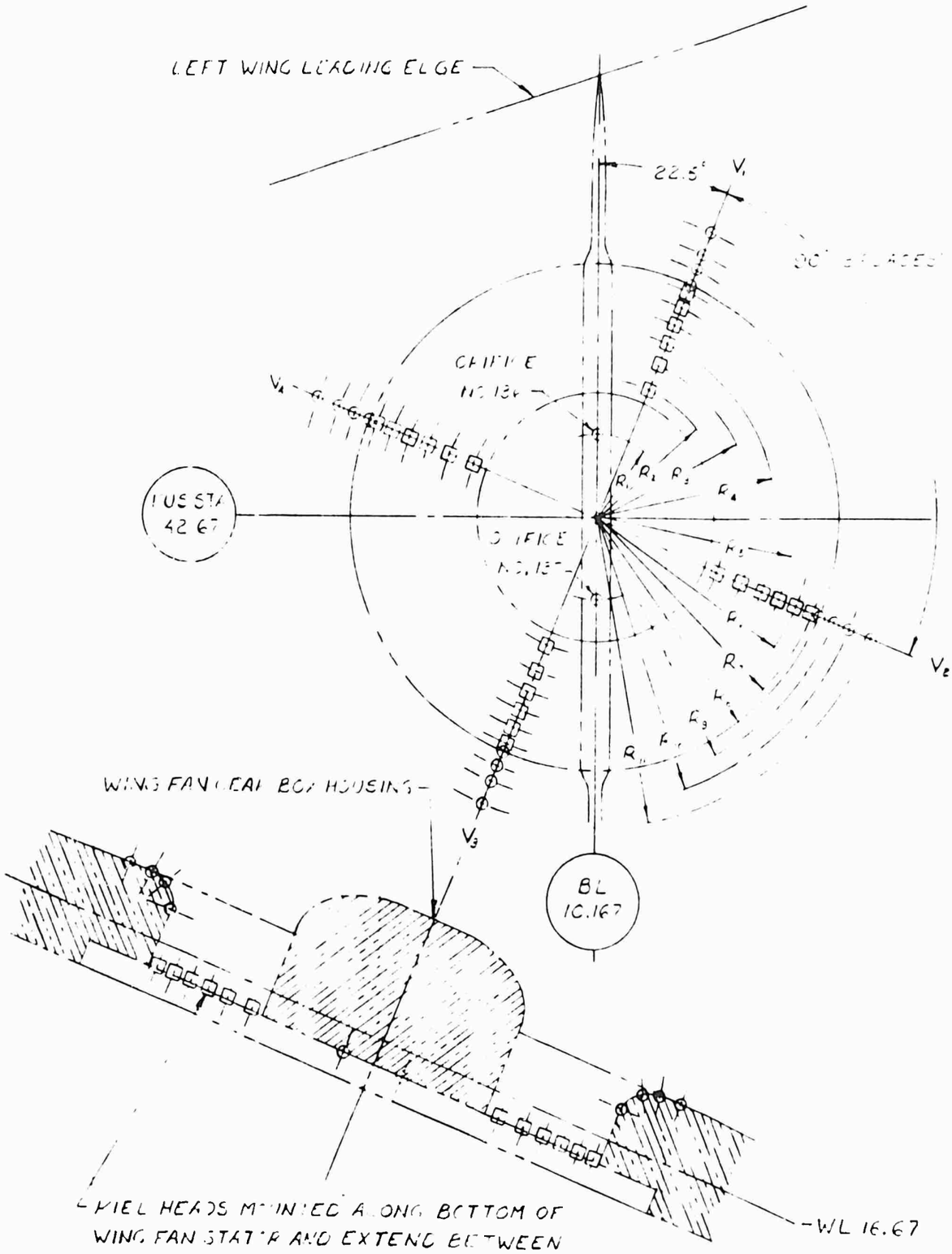

PAGE 11
P
P2
P3
P4
P5
P6
P7
P8
P9
P10
P11

PIEL T
NO.
151
152
153
154
155
156
157
158
159
160
161
162

ORIFI
NO
120
121
122
123
124
125
126
127

A

LEFT WING FAN

RADII	(IN.)
R	1.65
R_2	2.87
R_3	3.41
R_4	3.88
R_5	4.30
R_6	4.68
R_7	5.03
R_8	5.20
R_9	5.51
R_{10}	5.82
R_{11}	6.33

BL 0.000

□ PIEL TUBE LOCATIONS

PIEL TUBE NO.	RADIUS VECTOR		PIEL TUBE NO.	RADIUS VECTOR	
151	R_7	V_1	163	R_7	V_3
152	R_6	V_1	164	R_6	V_3
153	R_5	V_1	165	R_5	V_3
154	R_4	V_1	166	R_4	V_3
155	R_3	V_1	167	R_3	V_3
156	R_2	V_1	168	R_2	V_3
157	R_7	V_2	169	R_7	V_4
158	R_6	V_2	170	R_6	V_4
159	R_5	V_2	171	R_5	V_4
160	R_4	V_2	172	R_4	V_4
161	R_3	V_2	173	R_3	V_4
162	R_2	V_2	174	R_2	V_4

○ STATIC ORIFICE LOCATIONS

ORIFICE NO.	RADIUS VECTOR		ORIFICE NO.	RADIUS VECTOR	
120	R_{11}	V_1	128	R_{11}	V_3
121	R_{10}	V_1	129	R_{10}	V_3
122	R_9	V_1	130	R_9	V_3
123	R_8	V_1	131	R_8	V_3
124	R_{11}	V_2	132	R_{11}	V_4
125	R_{10}	V_2	133	R_{10}	V_4
126	R_9	V_2	134	R_9	V_4
127	R_8	V_2	135	R_8	V_4

NOSE FAN

RADII	(IN.)
R_{12}	2.45
R_{13}	3.12
R_{14}	3.45

◇ KIEL TUBE LOCATIONS

KIEL TUBE NO.	RADIUS
147	R_{12}
148	R_{12}
43	R_{12}
150	R_{12}

△ STATIC ORIFICE LOCATIONS

ORIFICE NO.	RADIUS
139	R_{14}
140	R_{14}
141	R_{14}
142	R_{14}
143	R_{13}
144	R_{13}
145	R_{13}
146	R_{13}
231	R_{13}
232	R_{13}
233	R_{13}
234	R_{13}

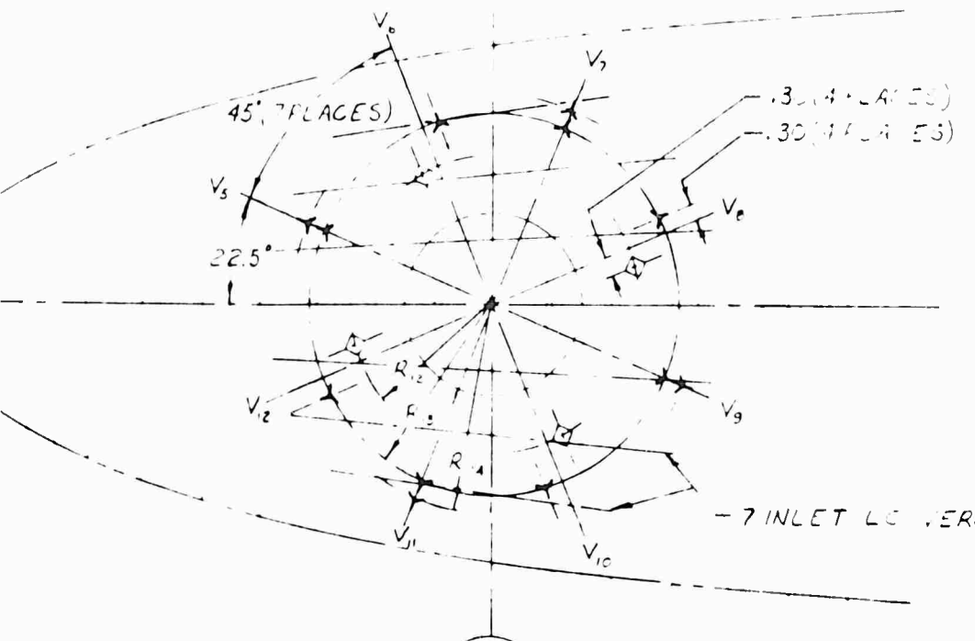

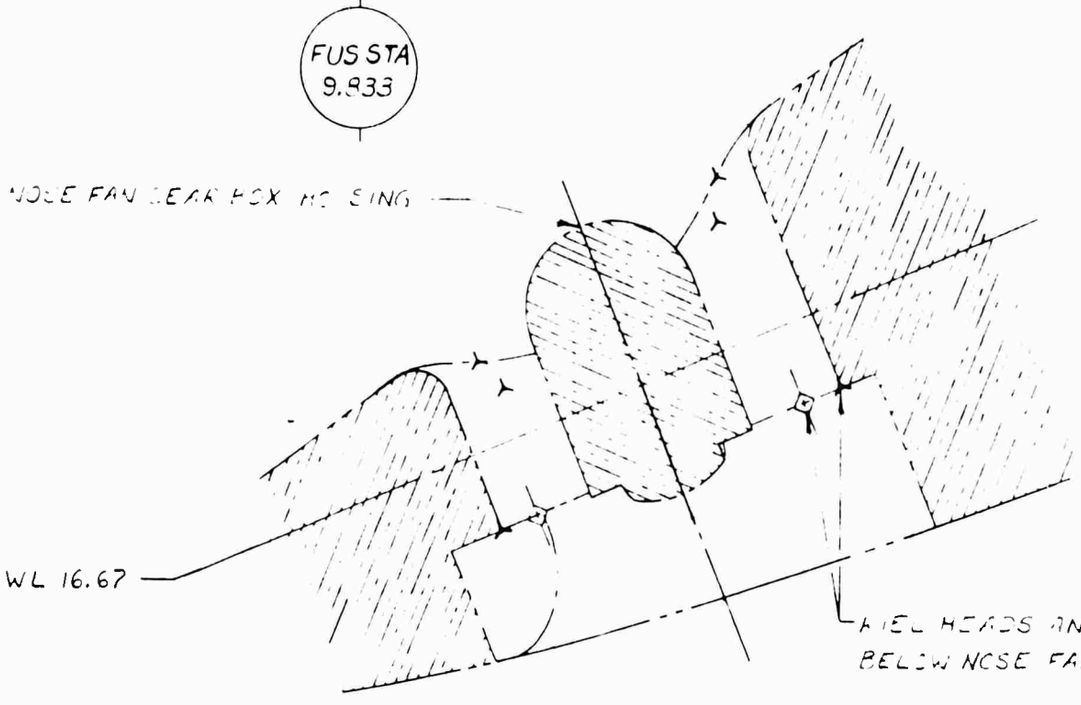

C

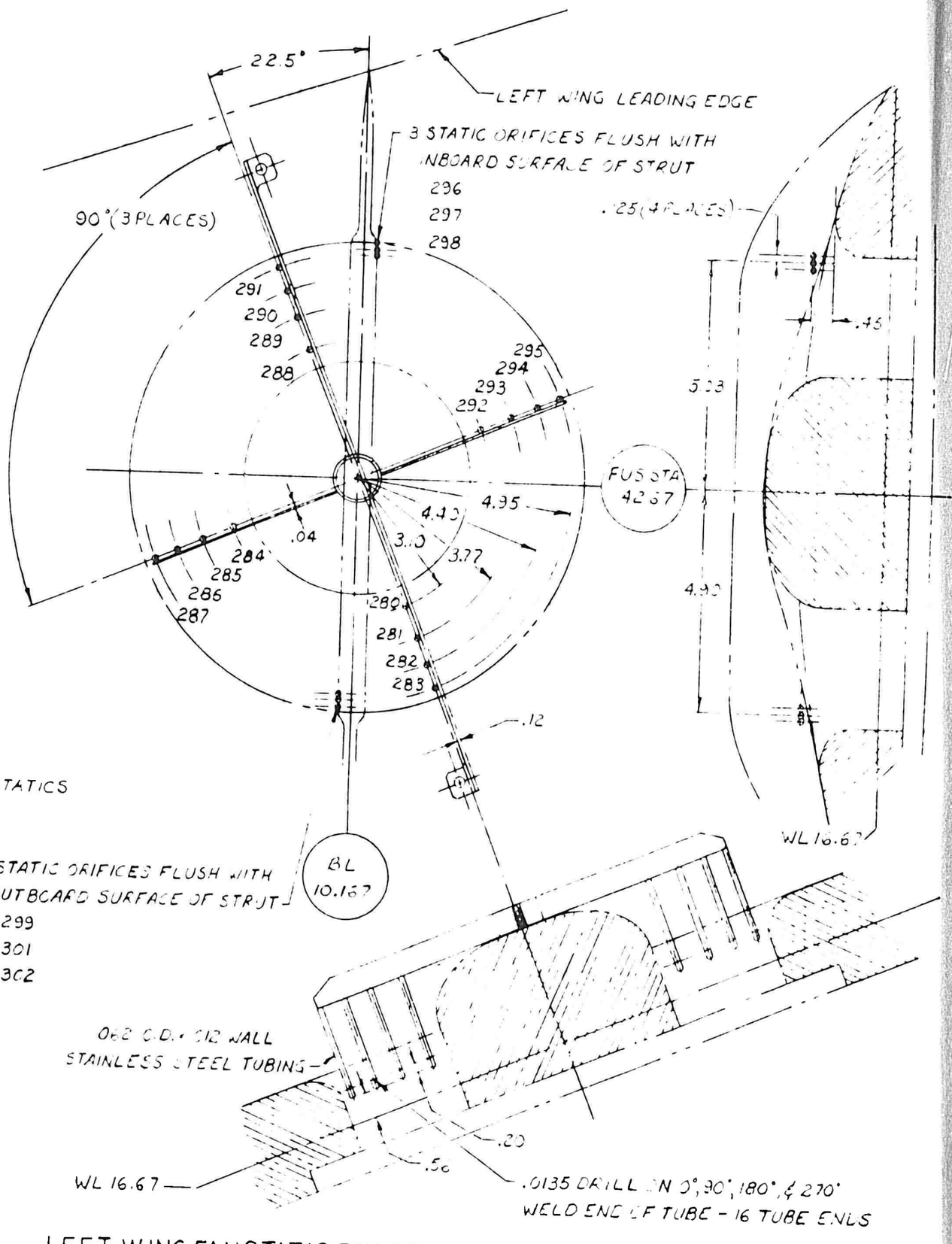

LEFT WING FAN STATIC PRESSURE INLET RAKE & STRUT ORIFICES

Figure 6.3 Left Wing Fan and Nose Fan Pressure Orifice Locations